Load-deflection response of prestressed concrete beams strengthened with FRP: a comprehensive perspective

by

Kimberly Waggle Kramer

B.S., Kansas State University, 1989
M.E., University of Texas at Arlington, 1999

AN ABSTRACT OF A DISSERTATION

submitted in partial fulfillment of the requirements for the degree

DOCTOR OF PHILOSOPHY

Department of Civil Engineering
Carl R. Ice College of Engineering

KANSAS STATE UNIVERSITY
Manhattan, Kansas

2020

Abstract

Currently, degradation of pretensioned prestressed reinforced concrete (PRC) bridge structures is a serious problem in the United States of America. Since 2000, the use of fiber-reinforced polymer (FRP) is well studied and has become an accepted method to rehabilitate concrete bridges. Design engineers use the *ACI 440.2R-17* to determine strength requirements. Additionally, evaluating the deflection of strengthened PRC members is required during the restoration/strengthening design. *ACI 440.2R-17* relies on *ACI 318-19* for deflection calculations and limits prestressing from yielding under service load levels. This dissertation examines the application of the effective moment of inertia equation given in *ACI 318-19* for the determination of deflection after cracking of PRC beams externally strengthened with carbon fiber reinforced polymers (CFRP).

The results reported in this dissertation deal with the behavior of partially prestressed concrete beams strengthened with high strength composites. The three major parts discussed are experimental work, analytical investigations, and a parametric study. Experimental results obtained by other researchers were used to verify the results of the analytical procedures developed. The parametric study provides information on the moment-curvature and load-deflection behavior of strengthened pretensioned prestressed concrete flexural members externally strengthened with fiber-reinforced polymers that can be obtained for various concrete strengths, reinforcement ratios, and varying cross-sections.

An analytical model was developed to predict the flexural rigidity of pretensioned, partially prestressed concrete beams that are externally strengthened with high strength composites. CFRP sheets were used for the derivation of equations. The proposed model is based on principles of mechanics and the sectional equations available for the analysis of

partially prestressed beams. The model is applicable to the full range of prestressed concrete members covering partially and fully prestressed concrete, straight or harped strands, with or without supplemental mild-reinforcing steel, and varying loading conditions. The procedure can be used to generate the entire load-deflection response and through performing the moment-curvature analysis and estimation of stresses and strains in addition to computing the effective flexural stiffness of the strengthened prestressed member. Comparisons of experimental and analytical results show that deflection can be predicted with good accuracy using the developed modified effective moment of inertia equation.

The parametric investigation was conducted on the effect of the basic variables namely, cross-section, concrete compressive strength, prestressing steel ratio, amount of carbon fibers, modulus of elasticity of prestressing steel-to-modulus of elasticity of CFRP ratio, modulus of elasticity of carbon fiber composite, spans, and shear span-to-span ratios. The goal of this investigation was conducted to understand the effect of CFRP strengthening to the flexural stiffness. Rectangular cross-sections with straight bonded prestressing tendons strengthened with 1 to 5 layers of unidirectional carbon sheets were analyzed in the parametric study.

Lastly, the application of the proposed effective moment of inertia equation to bonded, pretensioned prestressed members, with harped strands depressed at midspan, externally strengthened with CFRP is examined in comparison with the experimental and analytical response curves.

Load-deflection response of prestressed concrete beams strengthened with FRP: a comprehensive perspective

by

Kimberly Waggle Kramer

B.S., Kansas State University, 1989
M.E., University of Texas at Arlington, 1999

A DISSERTATION

submitted in partial fulfillment of the requirements for the degree

DOCTOR OF PHILOSOPHY

Department of Civil Engineering
Carl R. Ice College of Engineering

KANSAS STATE UNIVERSITY
Manhattan, Kansas

2020

Approved by:

Major Professor
Professor Hayder A. Rasheed

Copyright

Abstract

Currently, degradation of pretensioned prestressed reinforced concrete (PRC) bridge structures is a serious problem in the United States of America. Since 2000, the use of fiber-reinforced polymer (FRP) is well studied and has become an accepted method to rehabilitate concrete bridges. Design engineers use the *ACI 440.2R-17* to determine strength requirements. Additionally, evaluating the deflection of strengthened PRC members is required during the restoration/strengthening design. *ACI 440.2R-17* relies on *ACI 318-19* for deflection calculations and limits prestressing from yielding under service load levels. This dissertation examines the application of the effective moment of inertia equation given in *ACI 318-19* for the determination of deflection after cracking of PRC beams externally strengthened with carbon fiber reinforced polymers (CFRP).

The results reported in this dissertation deal with the behavior of partially prestressed concrete beams strengthened with high strength composites. The three major parts discussed are experimental work, analytical investigations, and a parametric study. Experimental results obtained by other researchers were used to verify the results of the analytical procedures developed. The parametric study provides information on the moment-curvature and load-deflection behavior of strengthened pretensioned prestressed concrete flexural members externally strengthened with fiber-reinforced polymers that can be obtained for various concrete strengths, reinforcement ratios, and varying cross-sections.

An analytical model was developed to predict the flexural rigidity of pretensioned, partially prestressed concrete beams that are externally strengthened with high strength composites. CFRP sheets were used for the derivation of equations. The proposed model is based on principles of mechanics and the sectional equations available for the analysis of

partially prestressed beams. The model is applicable to the full range of prestressed concrete members covering partially and fully prestressed concrete, straight or harped strands, with or without supplemental mild-reinforcing steel, and varying loading conditions. The procedure can be used to generate the entire load-deflection response and through performing the moment-curvature analysis and estimation of stresses and strains in addition to computing the effective flexural stiffness of the strengthened prestressed member. Comparisons of experimental and analytical results show that deflection can be predicted with good accuracy using the developed modified effective moment of inertia equation.

The parametric investigation was conducted on the effect of the basic variables namely, cross-section, concrete compressive strength, prestressing steel ratio, amount of carbon fibers, modulus of elasticity of prestressing steel-to-modulus of elasticity of CFRP ratio, modulus of elasticity of carbon fiber composite, spans, and shear span-to-span ratios. The goal of this investigation was conducted to understand the effect of CFRP strengthening to the flexural stiffness. Rectangular cross-sections with straight bonded prestressing tendons strengthened with 1 to 5 layers of unidirectional carbon sheets were analyzed in the parametric study.

Lastly, the application of the proposed effective moment of inertia equation to bonded, pretensioned prestressed members, with harped strands depressed at midspan, externally strengthened with CFRP is examined in comparison with the experimental and analytical response curves.

Table of contents

List of figures

List of tables

Acknowledgements

"Every great achiever is inspired by a great mentor." (Lailah Gifty Akita). I would like to thank my advisor, Dr. Hayder Rasheed, for his guidance and mentoring along with his patience throughout this research. I have become more technically competent and a better mentor because of your direction and knowledge. I would also like to thank Dr. Hani Melhem for his support on this endeavor and mentorship while I have been at Kansas State University. Additionally, I would like to thank Dr. Bill Zhang and Dr. Christopher Jones for serving on my advisory committee and review comments.

Dedication

"You don't choose your family. They are God's gift to you, as you are to them," Desmond Tutu. I dedicate this dissertation to my family. Kyle Kramer, you inspire me daily to be a better person. I have learned to enjoy life because of you. Darren Reynolds, your love, encouragement, and confidence in me made this possible. Letha Waggle, your example of a strong, independent women allowed me to overcome many adversities as a female structural engineer. Jerome Waggle, your example of work ethic and integrity has shaped who I am. Dr. Larry Waggle, your knowledge, wisdom, and encouragement through this was inspiring.

Notations

A_c cross-sectional area of the beam section with a width of b and a depth of h, in^2 (mm^2)

A_f area of fiber reinforced polymer (FRP) external reinforcement, equivalent area of fiber in composite, FRP plate area, in^2 (mm^2)

A_g gross area of concrete section neglecting reinforcing steel, in^2 (mm^2)

A_{gt} uncracked gross transformed area of the section including reinforcement, in^2 (mm^2)

A_i area of given shape in curvature diagram

A_{ps} area of prestressed longitudinal tension steel reinforcement, in^2 (mm^2)

A_s area of non-prestressed longitudinal tension steel reinforcement, in^2 (mm^2)

A'_s area of non-prestressed compression steel reinforcement, in^2 (mm^2)

b width of beam, in. (mm)

b_f width of beam flange, in. (mm)

b_w width of beam web, in. (mm)

C Compressive force of internal couple

c distance from the extreme compression fiber to neutral axis, in. (mm)

c_b distance from the center of gravity of the section to the extreme bottom fiber of the concrete

c_n depth of neutral axis measured from extreme compression fiber, in. (mm)

c_{nc} depth of neutral axis measured from extreme compression fiber when failure mode is concrete crushing, in. (mm)

c_{nr} depth of neutral axis measured from extreme compression fiber when failure mode is FRP rupture, in. (mm)

c_{nrd} depth of neutral axis measured from extreme compression fiber when failure mode is FRP rupture/debonding, in. (mm)

cgc center of gravity of the concrete

c_t distance from neutral axis of uncracked transformed section to extreme fiber in tension, in. (mm)

c_y depth of neutral axis measured from extreme compression fiber when at first yield (steel), in. (mm)

d distance from extreme compression fiber to centroid of non-prestressed tension steel reinforcement, in. (mm)

d' distance from extreme compression fiber to centroid of non-prestressed compression steel reinforcement, in. (mm)

d_f distance from extreme compression fiber to centroid of FRP reinforcement, in. (mm)

d_{ps} distance from extreme compression fiber to centroid of the longitudinal prestressing steel reinforcement, in. (mm)

E_c modulus of elasticity of concrete, $57000\sqrt{f_c'}$ in psi ($4700\sqrt{f'_c}$ in MPa)

E_f tensile modulus of elasticity of fiber reinforced polymer, psi (MPa)

E_i principle materials moduli of elasticity

EI flexural stiffness

E_{ps} modulus of elasticity of prestressed steel reinforcement, psi (MPa)

E_s modulus of elasticity of non-prestressed tension steel reinforcement, psi (MPa)

E'_s modulus of non-prestressed compression steel reinforcement, psi (MPa)

e eccentricity of the initial prestressed force from the neutral axis, in. (mm)

e_c eccentricity of prestressing force from the centroid of section at center of span, in. (mm)

e_e eccentricity of prestressing force from the centroid of section at end of span, in. (mm)

f compressive stress on the beam cross section, psi (MPa)

f_{bot} extreme fiber stress in the pre-compressed tension zone calculated at service loads using gross section properties after all prestress losses including eccentricity of prestressing strands, psi (MPa)

f'_c compressive strength of concrete at 28 days, psi (MPa)

f_f stress in FRP reinforcement, psi (MPa)

f_l stress due to the applied (service) live load, psi (MPa)

f_{pe} compressive stress in concrete due only to effective prestress forces, after allowance for all prestress losses, at extreme fiber of section of tensile stress is caused by externally applied loads, psi (MPa)

f_{ps} stress in the prestressing steel reinforcement at nominal flexural strength, psi (MPa)

f_{pu} ultimate tensile strength of prestressing steel reinforcement, psi (MPa)

f_{py} yield stress of prestressing steel reinforcement, psi (MPa)

f_r concrete modulus of rupture according to ACI 318-19, psi (MPa)

f_s' stress in compression reinforcing steel, psi (MPa)

f_{se} effective stress in the prestressing steel reinforcement after allowance for all prestress losses, psi (MPa)

f_t tensile stress, psi (MPa)

f_{tl} extreme fiber stress in the pre-compressed tension zone calculated at service loads using gross section properties after allowance for all prestress losses, psi (MPa)

f_{top} extreme fiber stress in the pre-compressed compression zone calculated at service loads using gross section properties after all prestress losses including eccentricity of prestressing strands, psi (MPa)

f_y yield strength of non-prestressed steel reinforcement, psi (MPa)

G_i shear modulus along a given axis

h total height of the cross-section, in. (mm)

I moment of inertia of the section

I_{cr} moment of inertia of the fully cracked transformed cross section neglecting reinforcement, in^4 (mm^4)

I_{crt} moment of inertia of the fully cracked transformed including reinforcement, in^4 (mm^4)

I_e effective moment of inertia for calculation of deflection, in^4 (mm^4)

I_{ey} effective moment of inertia at first yielding including slip bond, in^4 (mm^4)

I_g gross moment of inertia of gross concrete section about centroidal axis neglecting the steel reinforcement, in^4 (mm^4)

I_{gt} gross moment of inertia transformed including steel reinforcement, in^4 (mm^4)

I_n effective moment of inertia at ultimate strength, in^4 (mm^4)

kd depth of the concrete compression block in the elastic range

L span length

L_a shear span, distance from support to point of loading in four-point bending loading condition

L_g distance from support to location of external cracking moment

L_y distance from support to location of external yielding moment

M moment due to applied (service) loads

M_a applied (elastic) moment along the span

M_{cr} minimum moment at which the cracking takes place at a cross-section in the beam

M'_{cr} cracking moment from zero curvature in prestressing member

M_D moment caused by self-weight of the member

M_L moment caused by live-load

M_n external moment corresponding to failure of member

M_{SD} moment caused by super-imposed dead load

M_T total moment caused by super-imposed loads and self-weight

M_y external moment corresponding to first yield

m constant used in Branson's effective moment of inertia equation

n modulus of elasticity ratio

n_f ratio of the tensile modulus of elasticity of FRP to modulus of elasticity of the concrete

n_p ratio of the modulus of elasticity of the prestressing steel to modulus of elasticity of the concrete

n_s ratio of the modulus of elasticity of the non-prestressing steel to modulus of elasticity of the concrete

P external load for bending condition

P_e effective prestress force after all losses, equivalent prestressed force, kips (kN)

P_i initial prestressing force, kips (kN)

r radius of gyration of the cross section, $\sqrt{\frac{I_g}{A_c}}$, in. (mm)

S_t top section modulus of concrete section, in^3 (mm^3)

S_b bottom section modulus of concrete section, in^3 (mm^3)

S_{bt} bottom section modulus of concrete section including reinforcing steel, in^3 (mm^3)

T tension force of internal couple

t_f thickness of FRP sheet/plate, in. (mm)

v_i Poisson ratio along a given axis

w uniform load

x distance along the beam from a support

x_i distance from reference point to centroid of area on curvature diagram

y distance from the center of gravity of the section to the extreme fiber, in. (mm)

y_t distance from extreme fiber in tension to centroidal axis, in. (mm)

y_b distance from the center of gravity of the section to the extreme bottom fiber, in. (mm)

y_{bot} distance from the neutral axis to the extreme fiber in tension, in. (mm)

α constant used to convert the nonlinear stress-strain relationship into an equivalent rectangular distribution

β_1 factor relating depth of equivalent rectangular compressive stress block to depth of neutral axis

γ integration factor for loading and support conditions for Bischoff effective moment of inertia method

γ constant related to compression force contribution from concrete, neutral axis coefficient

γ_y constant related to compression force contribution from concrete at first yield

γ_{nc} constant related to compression force contribution from concrete at concrete crushing

γ_{nrd} constant related to compression force contribution from concrete at rupture/debonding of FRP

$\gamma_y c_y$ depth of the resultant force of concrete in compression at first yielding

$\gamma_{cn} c_{nc}$ depth of the resultant of concrete in compression at concrete crushing

Δ_{cr} deflection based on cracked moment of inertia (fully cracked section)

Δ_g deflection based on gross moment of inertia (uncracked section)

Δ_i deflection at given point along the length of the member

Δ_{mid} deflection at midspan

Δ_t total deflection based on cracked and uncracked deflection in bilinear method

δ_i deflection due to the uncracked, post-cracked, or post-yielded portion of the beam

ε strain

ε_b strain in the extreme bottom fiber of the beam

ε_c strain in the concrete at any concrete fiber

ε_{ce} strain in the strands due to initial eccentricity – decompression of the section at the level of the prestressing strands

ε'_c strain corresponding to f_c'

ε_{cf} maximum strain in concrete

ε_{cu} maximum strain in concrete at ultimate strength = 0.003

ε_f strain in FRP

ε_{fd} debonding strain of FRP

ε_{fu} ultimate rupture strain of FRP reinforcement

ε_{ps} strain in prestressing steel reinforcement corresponding to f_{ps}

ε'_s strain in non-prestressed compression steel reinforcement

ε_{se} strain in the prestress strands due to initial tension after losses

ε_t strain in the extreme top fiber of the beam

ε_0 effect of initial deformations due to service loads during beam strengthening the concrete extreme fiber tensile strain during strengthening, calculated according to the equations adopted by ACI 440.2R

ε_1 strain in the prestress strands due to initial tension after losses

ε_2 strain in the strands due to initial eccentricity – decompression of the section at the level of the prestressing strands

ε_3 strain in the prestress strands due to additional loading

η function of the ratio of the fully cracked section to the gross section moments of inertia

θ_A end rotation at support A

λ $A_f E_f / A_{ps} E_{ps}$

ρ_f reinforcement ratio of FRP = A_f / bd_{ps}

ρ_{ps} reinforcement ratio of prestressing steel = A_{ps} / bd_{ps}

ρ_s reinforcement ratio of non-prestressing steel = A_s / bd_{ps}

ρ'_s reinforcement ratio of non-prestressing compression steel = A'_s / bd_{ps}

ϕ curvature

ϕ_a curvature at the point of loading

ϕ_{cr} curvature expression for the cracking point

$\phi_{cr\text{-}y}$ curvature expression of the post-cracking region

ϕ_{in} maximum initial curvature due to prestressing

ϕ_{mid} curvature corresponding to span of member

ϕ_n curvature corresponding to failure of member

ϕ_{nc} curvature corresponding to failure of member due to concrete crushing

ϕ_{nrd} curvature corresponding to failure of member due to FRP rupture/debonding

ϕ_{pc} curvature expression of the post-cracked region

ϕ_{py} curvature expression of the post-yield region

ϕ_{un} curvature expression of the pre-cracking region

ϕ_y curvature corresponding to first yield, yielding of prestressing reinforcement

$\phi_{y\text{-}n}$ curvature expression of post-yielding regions

σ_c compression stress at extreme concrete fibers

χ shrinkage restraint factor, $X = 0.45$ for steel reinforcement and $X = 0.65$ for fiber reinforcement

ψ_f FRP strength reduction factor, equals 0.85 for flexure

Chapter 1 - Introduction

1.1 Overview

At the beginning of the twentieth century, *Prestressed Concrete* became the single most significant new direction in structural engineering (Billington, 2004). This unique concept gave the engineer the ability to control the actual structural behavior of a member to a higher degree than reinforced concrete (RC). Prestressing strands can be pretensioned or post-tensioned, bonded or unbonded, and straight, harped, or draped creating many variables that affect the prestressed reinforced concrete (PRC) member behavior. As the span increases and the members become shallower, an efficient design of PRC flexural members typically requires varying the strand eccentricity along the length of the member. One method is harping strands to reduce the strand eccentricity at the supports, which decreases the tensile and compressive stresses at the ends of girders.

From 1950 to 1990, the use of PRC bridges increased from zero percent to almost 50 percent of the market in the United States of America (USA). Almost a quarter of all highway bridges built during the 40-year period and currently in the National Bridge Inventory are of prestressed concrete (Dunker & Rabbat, 1992). Currently, degradation of bridge structures is a serious problem in the USA. Almost 40 percent of the bridges in the USA are at least half-century-old with approximately 55,000 structurally deficient in 2016 (ASCE, 2017). Since 2000, the use of fiber-reinforced polymer (FRP) to repair or rehabilitate concrete bridges has gained momentum across the USA indicating that strengthening of concrete members with external FRP has become common practice in the consulting engineering industry (Hamilton, 2011).

Strengthening of RC and PRC flexural members is well studied, and accepted design procedures are available to the design engineer using *ACI 440.2R: Guide for the Design and Construction of Externally Bonded FRP Systems for Strengthening Concrete Structures*. In addition to strength requirements, the retrofitted/strengthened concrete members need to meet serviceability requirements especially since PRC flexural members are typically shallower than non-prestressed RC members. Therefore, evaluating the deflection of strengthened PRC members is required during the restoration/strengthening design.

Rather than specifying a method to calculate the deflection of externally FRP strengthened RC and PRC flexural members, *ACI 440.2R* (ACI Committee 440, 2017) relies on *ACI 318: Building Code Requirements for Structural Concrete and Commentary* (ACI Committee 318, 2019) for deflection calculations and limits prestressing from yielding under service load levels. The *ACI 318* semi-empirical cubic effective moment of inertia (I_e) equation was developed by Dan Branson in 1963 (Branson, 1963) to compute the deflection after cracking of RC members. Branson and Trost (1982) further studied application of the I_e equation to the deflection of PRC flexural members; based on this research the *ACI 318* adopted the I_e equation for PRC members.

The deflection of RC beams strengthened with FRP is well studied (Rasheed and Charkas, 2009), but research on the deflection behavior of PRC beams strengthened with FRP is very limited. Since PRC elements tend to be shallower than RC members, it is critical to control their deflections, especially after cracking. The primary design of a PRC members strengthened with FRP (PRC-FRP) involves the determination of the amount of FRP needed to increase the flexural and shear capacity of the existing beam to meet ultimate loads. Then, the deflection of the PRC-FRP beam under service loads is verified to be within allowable short-term and long-

term deflection limits. Determination of instantaneous, short-term, deflections is the first step in calculating long-term deflections.

This dissertation evaluates the existing methods used for computing immediate deflection of cracked PRC-FRP flexural members with bonded, straight and/or harped strands under various load conditions. The members used in this study are from various research specimens with some of the evaluated members being in service for several years prior to rehabilitation/strengthening in the laboratory. Since the focus of this research is the load-deflection and moment-curvature behavior of PRC-FRP members in the cracking to yielding stage, all members can be considered *partially prestressed*. Partial prestressing is a prestressed concrete approach in which prestressed reinforcement or prestressed and non-prestressed reinforcement is used such that tension and cracking in concrete is allowed under service loads. Whereas prestressed concrete is concrete that has had internal stresses introduced to counteract, to the degree desired, the tensile stresses that will be imposed during service so that the section does not crack. The term "prestressed" is used in this document to encompass fully prestressed members and partially prestressed members that are externally strengthened with FRP for simplicity. Moreover, the effective prestress, f_{se}, accounts for the shrinkage, creep, and relaxation of the prestressing steel in addition to friction losses due to the harping of the strands. Time-dependent deflections under sustained load are not considered. The load-deflection response of PRC flexural members, with straight and/or harped prestressing strands, strengthened externally with FRP are evaluated and a proposed effective moment of inertia equation is presented.

1.2 Objectives

The presented research is aimed at developing generalized effective moment of inertia equation to be used for instantaneous deflection calculations of cracked PRC flexural members externally strengthened with FRP. Furthermore, parametric study is conducted to assess the effect of different aspects such as material properties, amount of prestressing steel, span, shear span-to-span ratio, and size of member.

1.3 Scope of dissertation

This dissertation consists of six chapters. The first chapter presents the introduction to the topic, objectives of this work and dissertation scope. Chapter 2 includes a literature review of topics related to the dissertation scope, such as behavior of PRC flexural members, nonlinear analysis of prestressed members including stress-strain curves of constituent materials, deflection of prestressed concrete members, and response of FRP materials. Analytical load-deflection behavior of prestressed concrete members strengthened with FRP is presented in Chapter 3. Chapter 4 offers a parametric study on the PRC members with straight strands to develop a deflection equation for PRC members externally strengthened with FRP. The parametric study is based on rectangular flexural members, but the resulting equation is compared to experimental rectangular and T-section members. PRC-FRP flexural members with harped strands are examined in Chapter 5. Conclusions are drawn and recommendations are provided in Chapter 6.

Some of the research presented in Chapter 3 and Chapter 4 has been published by Kramer and Rasheed; in 2018, Analytical Load Deflection Behavior of Prestressed Concrete Girders Strengthened with FRP that was published in the ACI Special Publication 327. Future publications are planned: a quad-linear formulation for partially prestressed-FRP strengthened

flexural members to be submitted to ACI Structural Journal; a manuscript quantifying the serviceability design checks for PRC-FRP members using the proposed Kramer and Rasheed effective moment of inertia equation to predict instantaneous deflection will be submitted to PCI journal; and the formulation of the load-deflection response of PRC-FRP members with harped strands will be submitted to Journal of Composites for Construction.

Chapter 2 - Literature review

2.1 Overview

An overview regarding the work conducted on the PRC flexural members unstrengthened and strengthened with FRP is introduced in this chapter. Work performed to describe the behavior of bonded PRC, fully prestressed and partially prestressed, members is presented in Section 2.2. Since the members evaluated in this dissertation consist of cracked pretensioned, bonded PRC, the focus in Section 2.2 is on fully and partially PRC members that have pretensioned and bonded prestressing reinforcement. Section 2.3 contains experimental and analytical research conducted to express the nonlinear analysis of PRC members including stress-strain curves of constituent materials. Literature describing the deflection response of prestressed members is given in Section 2.4. Since the presented research is aimed at developing a generalized effective moment of inertia equation to be used for instantaneous deflection calculations of cracked PRC flexural members externally strengthened with FRP, Section 2.5 contains experimental data, which describes the response of FRP materials.

2.2 Behavior of prestressed reinforced concrete members

Concrete is strong in compression but its tensile strength is approximately 10 percent of its compressive strength (Johnson, 1906). In order to prevent or reduce cracking, an eccentric force (prestressing) is imposed in the longitudinal direction of the flexural element (Magnel, 1954). This prestressing force prevents or reduces the cracks from developing or opening up by eliminating or considerably reducing the tensile stresses at the critical midspan and support sections at service load, thereby increasing the bending, shear, and torsional capacities of the sections. The prestressing force is delivered by the prestressed tendons or strands.

Prior to discussing the behavior of PRC flexural members some information on prestressing steel is given. Prestressing steel has evolved over the years from steel rods to low-relaxation tendons. The research mentioned in this section is to give a background on the evolution of prestressing reinforcement and is not all inclusive. Mandl (1896) stretched mild reinforcing rods with a permissible steel stress of 18 ksi (124 MPa) and a yield strength of roughly 33 ksi (227 MPa), prior to placing concrete to reduce the concrete tensile stresses under load, but the losses owing to shrinkage and plastic flow of the concrete were too high and counteracted the prestress compression force. Dill (1925) introduced unbonded tendons that were post-tensioned allowing concrete shrinkage to occur prior to stressing, thus, reducing losses while the use of hard steel or steel of high elastic limit and high ultimate strength was effective to relieve tensile stresses in the concrete when loaded. Emperger (1935) tested beams with rods having an equivalent yield point of 57 ksi (393 MPa) and wires having equivalent yield point of 170 ksi (1172 MPa) and found the wire steel performed better than rods. Abeles (1945) tested beams with high strength wire prestressing steel with an approximate ultimate stress of 262 ksi (1806 MPa) steel and rods confirming Emperger's findings. By the 1950's, prestressing was accomplished by prestressing strand or wire. Podolny (1967) published a paper describing the process of manufacturing prestressing strands or wires and their material properties. High strength wire is made from high carbon steel (0.72-0.93%) that is rolled into rods, heat treated to obtain a uniform metallurgical structure which combines high tensile strength with high ductility imparting to the rod the ability to withstand the drafting required to produce the desired wire size. Drawing the wire through tapered dies reduces the diameter and increase its tensile and yield strength by cold work done to it. The outer surface is squeezed and receives more cold working than the center portion resulting in residual stresses. In order to correct these non-

uniform residual stresses, the wire goes through a process called *stress-relieving* – the wire passes through a bath of molten lead at about 800-825 degrees Fahrenheit or heated air in a furnace. *Stress-relieving* also changed the creep (continuing elongation of the wire under constant load) characteristic of the steel; the rate of creep was no longer a logarithmic one which means less prestressing loss over time. Stress-relieved prestressing strands commonly had an ultimate stress of 250 ksi (1723 MPa) and were typically five or seven-wire strands with 3/8, 7/16, or ½-inch (10, 11, and 13 mm) diameter. In 1957, the American Society for Testing and Materials issued the first "Standard Specification for Uncoated Seven-Wire Stress-Relieved Strand for Prestressed Concrete" (ASTM A416). Stress-relieved strands in the 1970s were also available in 270 ksi (1860 MPa) and with 0.5 and 0.6-inch (13 and 15 mm) diameter. By the 1980, ASTM A416 included *low-relaxation* strand. Low-relaxation strands have significantly less loss of initial tension (Martin & Pellow, 1983). Preston (1985) indicated that the yield strength of low-relaxation strand must be at least 90 percent of the specified minimum breaking strength instead of 85 percent for stress-relieved strand and must have a stress loss that does not exceed the specified amount when loaded to the specific load, duration, and conditions (ASTM A-416, 1980). Low-relaxation strands with 270 ksi (1860 MPa) are currently used today.

Consider a simply supported rectangular beam subjected to an eccentric, initial prestressing force, P_i, shown in Figure 2-1. Using St. Venant's principle, the compressive stress on the beam cross section is uniform and has an intensity of the initial prestressing force, P_i, divided by the area of concrete being pre-compressed as indicated in Eq. 2-1.

$$f = -\frac{P_i}{A_c} \qquad \textbf{Eq. 2-1}$$

Where $A_c = bh$ is the cross-sectional area of a beam section of width b and total depth of h. A minus sign is used for compression and a plus sign is used for tension.

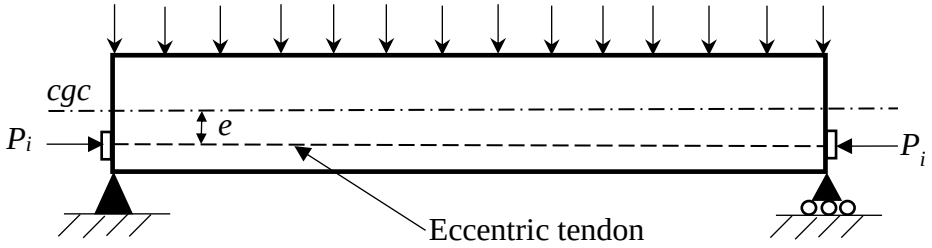

Figure 2-1: Beam eccentrically prestressed and loaded.

In addition to the uniform compressive stress, a moment, $P_i e$, is created when the tendon is placed at eccentricity e from the center of gravity of the concrete (*cgc* line). Top and bottom stresses at midspan, shown in Figure 2-2, become:

$$f_{top} = -\frac{P_i}{A_c} + \frac{P_i e}{I} - \frac{My}{I} \qquad \textbf{Eq. 2-2}$$

$$f_{bot} = -\frac{P_i}{A_c} - \frac{P_i e}{I} + \frac{My}{I} \qquad \textbf{Eq. 2-3}$$

Where:

f_{top} = stress at the top fibers

f_{bot} = stress at the bottom fibers

y = distance from the center of gravity of the section to the extreme fiber

I = moment of inertia of the section

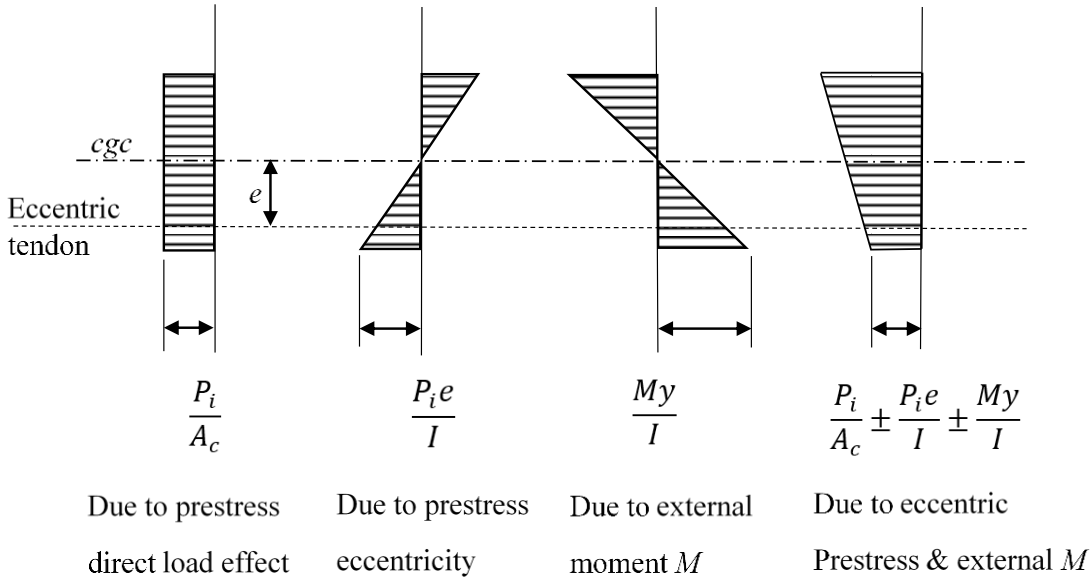

Figure 2-2: Stress distribution across an eccentric PRC section.

The initial prestressing force, P_i, is not sustained due to losses, which is explained later in this section. Therefore, an effective prestressing force, P_e, is used to describe the stresses in a member as it is loaded due to self-weight and externally applied loads. For a fully-prestressed section, one that does not crack in service, these stresses are all compressive stresses. As a fully-prestressed section, rectangular or not, is loaded past cracking or for a partially prestressed member, one that is designed to crack at service loading level, the extreme fiber stresses are tensile and compressive described in Eq. 2-4 and Eq. 2-5 and shown in Figure 2-3.

$$f_{top} = -\frac{P_e}{A_c}\left(1 - \frac{e y_t}{r^2}\right) - \frac{M}{S_t} \qquad \textbf{Eq. 2-4}$$

$$f_{bot} = -\frac{P_e}{A_c}\left(1 + \frac{e y_b}{r^2}\right) + \frac{M}{S_b} \qquad \textbf{Eq. 2-5}$$

Where:

y_t = distance from the center of gravity of the section to the extreme to top fiber

y_b = distance from the center of gravity of the section to the extreme to bottom fiber

e = distance from the center of gravity of the section to the centroid of prestressed strands (positive when below the section center of gravity, cgc)

I_g = gross moment of inertia of the section ($bh^3/12$ for a rectangular section)

r^2 = radius of gyration of the cross section squared = the gross moment of inertia divided by the area of concrete (I_g/A_c)

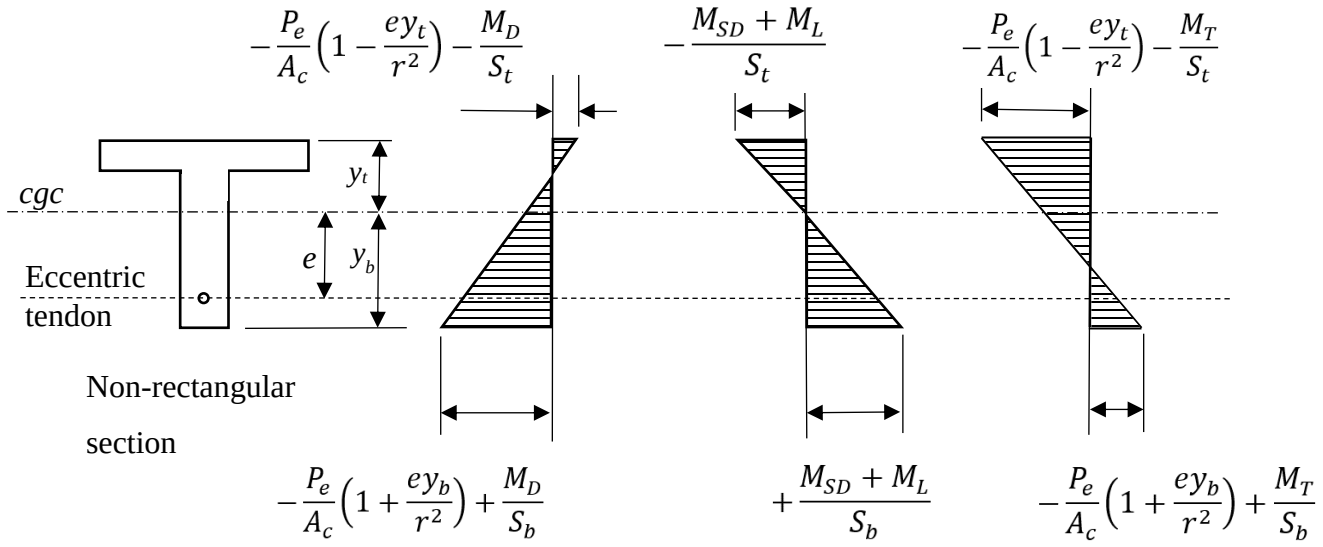

Figure 2-3: Elastic fiber stresses due to service loads at effective prestress.

Since the support section of a simply supported beam carries no moment from the external transverse load, relatively high tensile fiber stresses at the top fibers are caused by the eccentric prestressing force. To limit such stresses, the eccentricity of the prestressing tendon profile is often made less at the support section than at the midspan section or eliminated altogether. This can be achieved by harping the strands as shown in Figure 2-4 or draping the strands (Abeles, 1979).

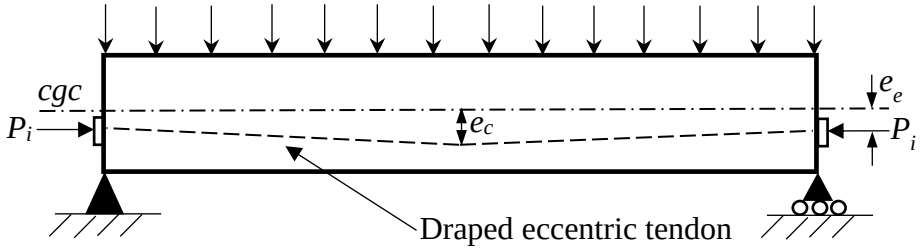

Figure 2-4: Prestressing tendon profile of a harped tendon

To avoid a large amount of prestress losses, high strength steel is needed to have effective prestressing system (Abeles, 1945). Estimating prestress loss at any given time during the life of a prestressed concrete member is a complex issue. This is due to several factors: the prestressing force applied shortens the concrete member causing a loss of tendon stress, friction and seating losses, concrete creep, concrete shrinkage concrete elastic shortening, and steel relaxation further reduce tendon stress. These losses have inherent variability due to variations of material properties and environmental and curing conditions. Over the years, different methods have been proposed and used to determine the total long-term prestress losses (Seguirant & Anderson, 1985; Kelley 2000; Tadros et al., 2003; Youakim et al., 2009; Garber et al., 2013). Without doing detailed prestressed loss calculations, Kelley (2000) indicates that for approximating prestress losses, tendons can be assumed by the designer to be stressed to eighty percent of the ultimate (maximum allowed by ACI 318) prestressing steel stress, $0.8f_{pu}$, for ASTM A416/A416M Grade 270 (1860 MPa) low-relaxation tendons. Additionally, the effective tendon stress, f_{se}, along a tendon after seating losses can be approximated as seventy percent of the ultimate prestressing steel stress, $0.7f_{pu}$. Before low-relaxation tendons were predominately used in the 1970s, stress-relieved tendons were commonly used, which resulted in higher losses due to relaxation of the prestressing tendon. Structures built prior to 1985 may contain stress-relieved tendons conforming to ASTM A886/A886M Grade 250 (1724 MPa) (Martin & Pellow,

1983). Therefore, for approximating prestress losses of stress-relieved tendons, Batal & Huang (1971) research indicates tendons are typically stressed to seventy to eighty percent of the ultimate prestressing steel stress, 0.7 to 0.8f_{pu}, with the average tendon stress along a tendon after seating losses equal to fifty-six to sixty percent of the ultimate prestressing steel stress, 0.56 to 0.60f_{pu}. PRC structures built prior to the 1960s may have cold-drawn wires instead of strands, which have more relaxation than stress-relieved and low-relaxation strands or tendons (Podolny, 1967). Knowing the type of prestressing tendon/strand/wire used in an existing structure that will be strengthened with FRP is crucial to estimate the prestressing losses which in turn affects the overall design capacity and deflection of the flexural member.

2.2.1 Moment-curvature

Developed around 1750, the Bernoulli-Euler beam theory is still an effective model for how shallow beams behave under axial forces and bending. More complex beam theory models exist, such as the Timoshenko beam theory that considers shear deformation, the change in curvature caused by shear forces. The members examined in this dissertation are not short spans with very high loads where shear deformation would need to be included. Therefore, Bernoulli-Euler beam theory is used: the moment, curvature, slope (rotation), and deflection of a beam are related. The moment may be used to determine the slope and deflection of any beam. Thus, obtaining moment-curvature relationships for experimental beams are required to develop an effective moment of inertia equation for PRC-FRP members used to determine the deflection of a member.

2.2.1.1 Moment area integration

Moment-area method is useful for determining the slope or deflection of a beam at a specific location. The integration of the bending moment is carried out indirectly, using the

geometric properties of the area under the bending moment diagram in a semi graphical method. The deformation is assumed in the elastic range resulting in small slopes and small displacements - Bernoulli-Euler beam theory is valid. Two moment area theorems are used; one that relates to the slope of the beam and one that relates to the deflection of the beam. Both theorems only provide information about one part of a beam relative to another part of the beam.

The *first moment area theorem* is that the change in the slope of a beam between two points is equal to the area under the curvature diagram between those two points. Curvature is equal to the moment divided by the flexural stiffness of the member (M/EI); the curvature diagram looks similar to the moment diagram if flexural stiffness is constant. However, when a RC or PRC member cracks, the flexural stiffness of the member (E_cI_e) changes along the length of a beam, which causes discontinuities in the curvature diagram that do not exist in the moment diagram.

The first moment area theorem is illustrated in Figure 2-5. The sample structure in the figure is a simply supported beam with an asymmetric point load; the location of maximum deflection does not coincide with that of maximum moment. This location may keep shifting as the flexural stiffness distribution keeps changing under the load. This support and loading combination results in a triangle-shaped moment diagram. To find the curvature diagram, the moment diagram is divided by *EI* at every point along the beam. If the *EI* is constant, a straight scaling of the moment diagram and the curvature diagram with a triangular shape results as shown in the Figure 2-5.

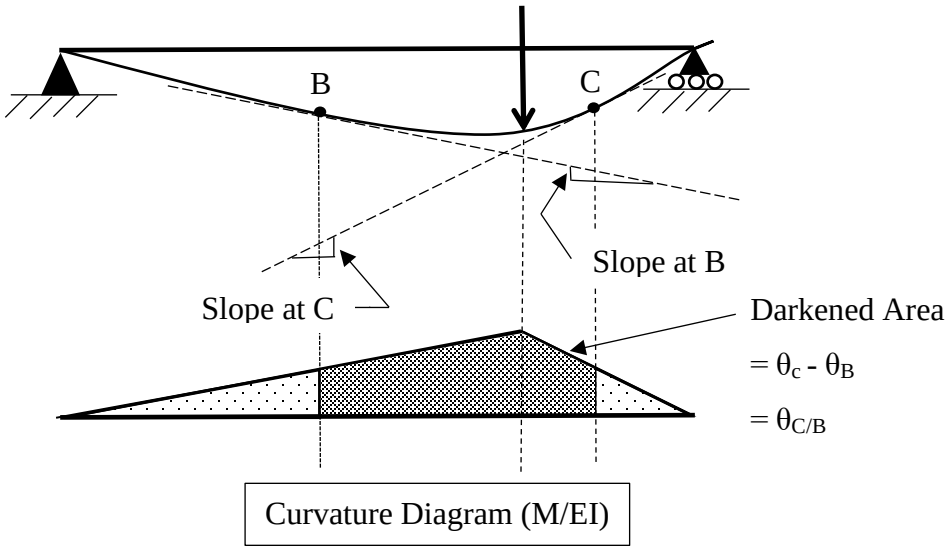

Figure 2-5: First moment area theorem

Once the curvature diagram is constructed, the first moment area theorem, relating the slope (or rotation measured in radians) at one point along a beam to the slope at another point on the beam, can be used to determine the slope at a specific point. The slopes at two points along the sample beam (points B and C) are shown in Figure 2-5. The change in slope between points B and C is equal to the area under the curvature diagram between points B and C as shown. This change in slope is referred to as $\theta_{C/B}$:

$$\theta_{C/B} = \theta_C - \theta_B \qquad \textbf{Eq. 2-6}$$

$$\theta_{C/B} = \int_B^C \frac{M(x)}{E(x)I(x)}\,dx \qquad \textbf{Eq. 2-7}$$

The second moment area theorem is used to determine deflections - the vertical distance between (a) a reference tangent line, to one point of the elastic curve of the beam, and (b) the deflected shape of the beam at another point is equal to the moment of the area under the

curvature diagram between the two points with the moments of the areas calculated relative to the point on the deflected shape (B).

The second moment area theorem is illustrated in Figure 2.6. The same sample structure used for this illustration for the first moment area theorem; therefore, it has the same curvature diagram.

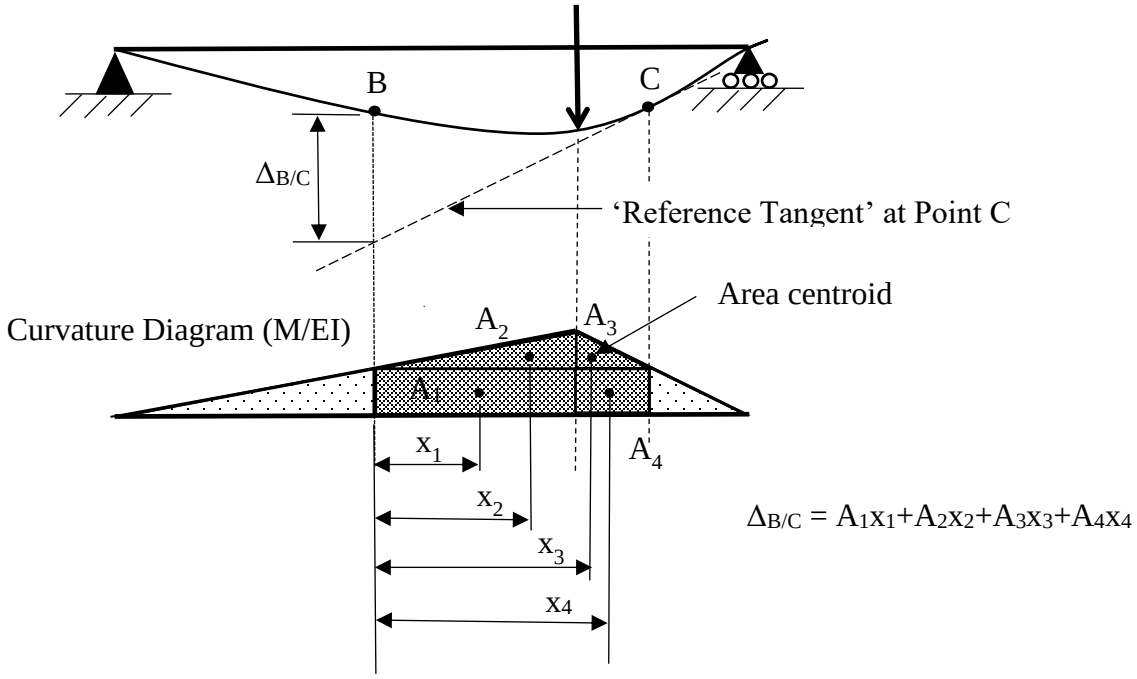

Figure 2-6: Second moment area theorem

The second moment area theorem relates the tangent line at one point on a beam to the deflection of another point of the beam, as shown in Figure 2-6. However, this gives only the distance between the reference tangent line and the deflected shape ($\Delta_{B/C}$ in the figure). The deflection of the beam relative to the initial un-deformed shape cannot be directly obtained; a multi-step process is needed to find total deflection relative to the un-deformed position using simple 2D geometry considerations.

Using the second moment area theorem itself, the relative distance (between a reference tangent at one point and the deflected shape at another point) is found by taking the moment of the area under the curvature diagram between the two points about the second point. If the area under the curvature diagram is a complex shape, splitting it into smaller areas with simple shapes (A_1 to A_4 as shown in Figure 2-6) and finding the sum of the moments of the areas for each of them is useful. A moment of an area is simply the area of the shape (A) multiplied by the distance from the point at which the deflection is measured (B) to the centroid (x). As shown in the Figure 2-6, this results in a distance between the reference tangent and the deflected shape of:

$$\Delta_{\frac{C}{B}} = A_1 x_1 + A_2 x_2 + A_3 x_3 + A_4 x_4 \qquad \textbf{Eq. 2-8}$$

$$\Delta_{\frac{C}{B}} = \int_B^C \frac{M(x)}{E(x)I(x)} x dx \qquad \textbf{Eq. 2-9}$$

Since PRC member cracks, the flexural stiffness of the member ($E_c I_e$) changes along the length of a beam, this causes discontinuities in the curvature diagram that do not exist in the moment diagram. In the present formulation, the actual stiffness distribution is accounted for by dividing the beam into three distinct regions, uncracked, post-cracked, and post-yielding. Accordingly, the position of maximum deflection is evaluated first for every load step, by

1. Determining the end rotation θ_A as shown in Figure 3-1 and Figure 2-7:

$$\theta_A = \frac{1}{L}\left[\int_0^{L_g} (L-x)\phi_{un}(x)dx + \int_{L_g}^{L_y} (L-x)\phi_{pc}(x)dx \right. \qquad \textbf{Eq. 2-10}$$

$$+ \int_{L_y}^{L_1} (L-x)\phi_{py}(x)dx + \int_{L_1}^{L-L_{yR}} (L-x)\phi_{pyR}(x)dx$$

$$\left. + \int_{L-L_{yR}}^{L-L_{gR}} (L-x)\phi_{pcR}(x)dx + \int_{L-L_{gR}}^{L} (L-x)\phi_{unR}(x)dx \right]$$

Where:

- $\phi_{un}(x)$, $\phi_{pc}(x)$, $\phi_{py}(x)$, $\phi_{unR}(x)$, $\phi_{pcR}(x)$, and $\phi_{pyR}(x)$ equal curvature expressions in the uncracked, post-cracked, and post-yielded regions on the left and right sides of the beam respectively;
- L_g and L_{gR} equal the extent of the uncracked region from left and right end, respectively; and
- L_y and L_{yR} is the extent of the post-cracked regions up to first yielding from the left and right support, respectively.

2. Equating the end rotation, θ_A, (a numerical value) with the relative rotation, $\theta_{x_{max}/A}$, to obtain the location of zero rotation or maximum deflection, x_{max}, for example:

$$\theta_{\frac{x_{max}}{A}} = \int_0^{L_g} \phi_{un}(x)dx + \int_{L_g}^{L_y} \phi_{pc}(x)dx + \int_{L_y}^{x_{max}} \phi_{py}(x)dx = \theta_A \qquad \textbf{Eq. 2-11}$$

x_{max} is within the post-yielded region. The above integrals are possible to perform analytically since $M(x)$ is given as a polynomial of x and $\phi(x)$ is linearly related to $M(x)$ within each segment of the trilinear moment-curvature (M-ϕ) function. Refer to Figure 3-2.

Eq. 2-11 yields a polynomial, one of whose roots results in x_{max}. Once x_{max} is evaluated, the maximum deflection is obtained by integrating the moment of curvature about the support point up to x_{max}, refer to Figure 3-2.

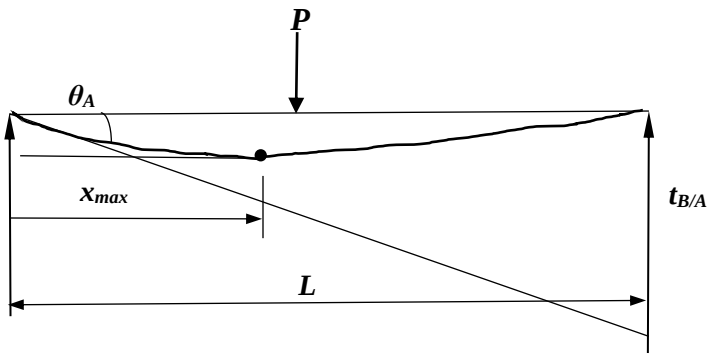

Figure 2-7: Elastic curve under asymmetric loading.

Alternatively, the double integration method may also be used to formulate the deflection at any point in the flexural member, but it does not yield closed form expression for maximum deflection. In addition, simpler analytical equations are possible to develop for symmetrical loading since the maximum deflection is always at midspan as shown in 3.3.3 Load-deflection response.

2.2.1.2 Research studies on prestressed concrete moment-curvature

In the following paragraphs, two research studies on prestressed concrete moment-curvature are presented: Burns (1964) and Warwaruk (1965). This research gives the basis of PRC members moment-curvature basis. Very little research has been conducted on PRC-FRP flexural members. Three PRC-FRP research studies are also given: Larson, Peterman, and Rasheed (2005), Cha (2001), and Reed & Peterman (2004). This research has given the moment-curvature relationship of PRC-FRP of the beams tested. Supplementary PRC-FRP research tests are given in Chapters 3, 4, and 5.

Burns (1964) presented experimental moment-curvature data for ten (seven I-section and three rectangular section) simply supported PRC beams loaded in four-point bending. Three I-

section specimens with same cross section had varying areas of prestressing steel, effective prestress, f_{se}, was 140 ksi (965 MPa) for all cases. After cracking, the PRC beams with smallest steel area went through much larger curvatures before reaching ultimate moment capacity than its companion PRC beams with more steel. Similar to the I-sections, the three rectangular specimens had the same cross section with varying amounts of effective prestressing, f_{se}, was 120 ksi (827 MPa) for all cases, ranging from under-reinforced to over-reinforced conditions, which produced significantly varying moment-curvature relationships. Burns concluded a major determining factor affecting the moment-curvature response was if the prestressing steel yielded. For example, an under-reinforced beam, prestressing steel yielded prior to concrete crushing, would undergo larger curvatures before reaching its ultimate moment capacity. In contrast, an over-reinforced beam would reach concrete crushing failure while the steel had not yielded exhibiting a brittle failure and smaller curvature. Burns also concluded that while the PRC beams remain uncracked, the stiffness would remain the same, so the initial slope of the moment-curvature relationship would be the same for all three beams. The remaining four I-section members had constant area of prestressing steel with varying levels of effective prestressing. Once the beams cracked, the moment-curvature was very different from the previous I-sections and rectangular sections. Burns determined that the higher the level of effective prestressing resulted in a higher cracking moment and greater negative curvature (camber) while the ultimate moment was practically the same over the wide range of effective prestress. In addition to the experimental test results presented by Burns, several analytical findings were presented.

Warwaruk (1965) expanded Burns (1964) research and presents experimental moment-curvature and load-deflection data for six PRC beams with rectangular cross sections. Three of

the PRC beams presented by Warwaruk are the same beams presented in Burns (1964). Warwaruk presents the experimental load-deflection data sets for the PRC beams that were not given in Burns (1964). In addition, Warwaruk clarified the beam span was nine feet with a shear span of three feet. Warwaruk concluded that the PRC beam moment-curvature and load-deflection relationships could be categorized into three stages: an uncracked beam (pre-cracking region), a cracked beam with non-yielded prestressing steel (post-cracking region), and a beam with yielded prestressing steel (post-yielding region). Warwaruk observed that the under-reinforced beams exhibited all three stages for both the moment-curvature and load-deflection relationships, while the over-reinforced PRC beam only exhibited stage 1 and stage 2. Warwaruk determined the individual behavior of the beams in stage 2 was dependent on the reinforcement ratio-to-concrete compressive strength ratio (ρ_{ps}/f'_c); beams with low ρ_{ps}/f'_c exhibited an abrupt change in the moment-curvature and load-deflection relationship.

Additionally, Warwaruk, offered that curvature could be defined as the strain gradient, the rate at which strain changes through a beam, in the compressed concrete. Thus, the relationship between moment and curvature is a function of the characteristics of the cross section and the properties of the materials - Bernoulli-Euler beam theory applies. In a cracked PRC beam, the characteristics of the cross section vary from section to section along the length of the span as shown in Figure 2-8. It is impractical, due to all the influencing factors, to derive moment-curvature relationships, which vary with distance from a crack. Instead, the actual distribution of curvature, shown as a solid line in Figure 2-8(c), can be approximated by an average curvature, shown as the dashed line in Figure 2-8(c). Furthermore, Warwaruk was able to present analytical predictions for the PRC beams.

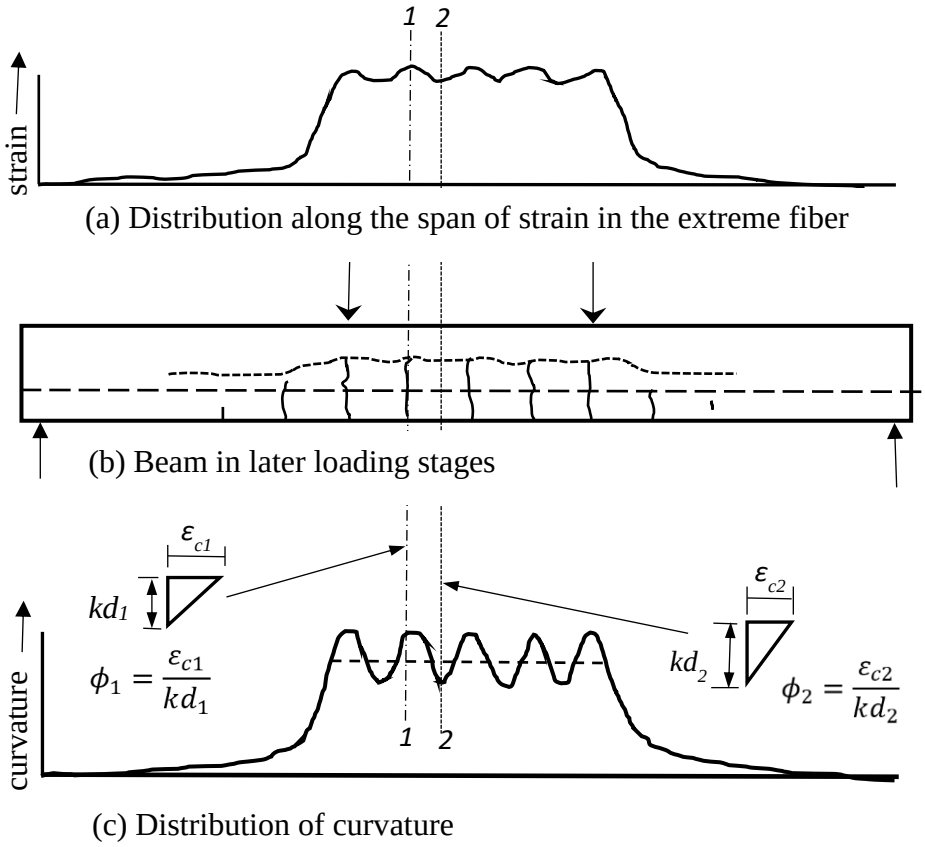

Figure 2-8: Strain and curvature distribution along span of PRC beams. (a) Distribution along the span of strain in the extreme fiber. (b) Beam in later stages of loading (c) Distribution of curvature. (Warwaruk, 1965)

Limited investigations have been conducted on PRC-FRP flexural members. Larson, Peterman, and Rasheed (2005) tested five pretensioned PRC T-girders (with straight prestressing strands) under a four-point bending loading condition. Of the five beams tested, Beam 1 was the control beam, unstrengthened. The remaining beams (Beams 2 through Beam 5) were strengthened with carbon fiber reinforced polymer (CFRP) sheets. Before strengthening the PRC girders, they were loaded past their midspan cracking moments to simulate existing members needing strengthening. The T-beams were strengthened by applying CFRP; this was accomplished by flipping the girders onto their flanges and supporting them at a minimum of

three locations along its span. Therefore, the FRP was added to the beam excluding self-weight stresses. Static tests were performed on Beam 2 and Beam 4; fatigue tests were performed on Beam 3 and Beam 5. Therefore, Beam 2 and Beam 4 are used for research presented in Chapter 3. The girders were tested in four-point bending with a clear span of 16-foot (4880 mm) and a shear span of 6-foot (1830 mm). The tests were conducted in monotonic, load control with a load rate of 500 lb/minute (2.2 kN/min). Midspan deflections were measured using two linear variable displacement transducers (LVDTs) mounted on either side of the flange. The average reading was reported. Additional information on Larson, Peterman, and Rasheed (2005) research is presented in Chapter 3.

Cha (2001) tested two sets of straight stranded PRC flexural members made with normal (approximately 5.4 ksi or 37 MPa) and high (approximately 10.2 ksi or 70 MPa) strength concrete, strengthened with CFRP sheets that were instrumented to measure deflection and strains in constituent materials, and tested to failure using four-point bending. The beams were 5.9-inch (150 mm) in width by 9.8-inch (250 mm) in depth by 9.8-foot (3 m) in span length. The prestressing tendons were conforming to ASTM A416/A416M for uncoated seven-wire stress relieved strands with a nominal diameter of 0.39-inch (10 mm) and an ultimate strength of 270 ksi (1862 MPa). The non-prestressed steel conformed to ASTM A616/A616M with a bar size of No. 3 (#10mm) and specified yield strength of 60 ksi (414 MPa). Each control set consisted of a control beam, one strengthened with 2 layers of CFRP, and one strengthened with 3 layers of CFRP. The design thickness of the CFRP sheets was 0.0043-inch (0.11 mm) with an ultimate tensile strength of 505 ksi (3,482 MPa), a modulus of elasticity of 33,425 ksi (230,458 MPa), and an ultimate strain of 0.015. The beams were tested in four-point bending. The results indicated that PRC members can be effectively strengthened using FRP with strength increases up to 86%.

Cha (2001) indicated that deflections of fully cracked sections, yield, and ultimate, failure, are much larger for PRC-FRP members compared to RC-FRP members. This implies the flexural stiffness is different between RC-FRP and PRC-FRP members. Additionally, Cha found that the addition of FRP reinforcement altered this behavior. Further information on Cha (2001) research is presented in Chapter 4.

Reed & Peterman (2004) tested three decommissioned PRC double-tee bridge members. Three of the damaged PRC double-tees were strengthened and evaluated at the Civil Infrastructure Systems Testing Laboratory at Kansas State University. Each of the 72-inch (1830 mm) wide by 23-inch (585 mm) deep members were saw cut in half longitudinally to provide six, 40-foot (12.2 m) specimens. Each specimen had four rows of prestressing tendons, each row consisting of a single 0.5-inch (13 mm) diameter strand. The strands were single-point depressed at the midspan to a height of 2-inch (50 mm) from the bottom face. In addition, two rows of mild-steel reinforcement (non-prestressed) longitudinal in the web were provided and two rows of transverse mild-steel reinforcement were in the flanges. Shear reinforcement consisted of single-legged #4 (13mm) bars positioned at the center of the web and spaced approximately 10-inch (255 mm) on center. One of the specimens (Specimen 1) was unstrengthened. Specimen 2 was strengthened for flexure and Specimen 3 was strengthened for flexure and anchorage with external CFRP. The PRC-FRP girders were tested in three-point bending with a clear span of 38-feet (11.58 m). A hydraulic actuator was used to load the specimens at midspan. A spreader beam was used to distribute the load transversely across the entire flange. Two linear variable displacement transducers (LVDTs) were positioned, one on each side of the flange, to measure midpoint deflection while monotonic loading occurred. Additional information on Reed & Peterman (2004) research is presented in Chapter 5.

2.3 Nonlinear analysis of prestressed reinforced concrete members

The criterion of adequate similarity between the real structure and its design model is a condition for properly designing structures. Nonlinear analysis allows for the defining of distributions of internal forces and displacements of the structure closer to reality (Winnicki, Cichon, & Waszczyszyn, 1990). In statically determinate systems, cross-sectional forces are not dependent on their material and geometric attributes except for the loads implicated from the self-weight. Differences in the stiffness of members caused by cracking and the nonlinear behavior of concrete influence the distribution of internal forces in the element (Czkwianianc & Kaminska, 1993) (Czkwianianc & Kaminska, 2005). Therefore, values of cross-sectional forces are a function of the physical and geometrical attributes. To account for this, analytical models and methods that can trace the structural response of buildings and bridges through their service load history and under increasing loads through their elastic, cracking, inelastic, and ultimate ranges are needed.

The three common numerical procedures for the analysis of various types of PRC structures are *Basic Method*, *C-Line Method*, and *Load-Balancing Method*. The *Basic Method* and *C-Line Method* analyze the beam as if it were a plain concrete elastic beam using the principles of statics; therefore, they do not consider nonlinearity of the system. Time-dependent effects due to load history, temperature history, creep, shrinkage and aging of the concrete, and relaxation of the prestressing steel may need to be included in the *Basic* and *C-Line* analysis methods. Any combination of non-prestressed and prestressed reinforcement may be specified so that partially and fully prestressed design cases may be analyzed. The prestressing may be provided by either pretensioned tendons, that are bonded or unbonded, and unbonded post-

tensioned tendons in which friction is considered. The advantage of a nonlinear approach is its application for defining both the ultimate limit states and serviceability limit states.

In the following section, the Lin (1958) load-balancing method is discussed.

2.3.1 Lin (1958) moment-curvature analysis method

Lin (1958) presented a numerical moment-curvature analysis method for straight tendons, fully bonded prestressed members. Load-Balancing Method T.Y. Lin design concept, otherwise known as *balanced-concept*, is based solely on deformation. An uncracked and a cracked region in which multiple points are used to define the response represent the moment-curvature response. This dissertation's proposed method and *balanced-concept* use some similar assumptions:

1. Tendons are perfectly bonded to the concrete. Changes in the strain in the steel and concrete after bonding are the same.
2. The initial strains from the effective prestressing in the tendon with no moment from applied loads, at the level of prestressing steel, are the concrete decompressive strain, ε_{ce}, and the tendon strain, ε_{se}. The tendon strain corresponds to the effective prestressing stress f_{se}, after prestressing losses.
3. Stress-strain properties for the materials are known or assumed for use in analysis.
4. Strains are distributed linearly over the depth of the beam.
5. Tension and compression forces acting on the cross section must be in equilibrium for the beam, which has only flexure without any applied axial load in addition to prestressing.
6. Ultimate moment corresponds to the usable concrete strain of 0.003 that initiates crushing or a steel strain that fractures the tendon, 0.05.

7. Flexural failure is analyzed, shear failure is prevented. Bond and anchorage of steel is adequate to prevent development length failure prior to reaching flexural strength.

These general assumptions hold true for all PRC members.

The *balanced-concept* is divided into two regions: linear-elastic region and the cracked region. The linear-elastic region is bounded by the modulus of rupture, f_r. Gross section properties and elastic behavior is used to analyze the member in the linear-elastic region. Within the linear-elastic region, three points are determined: the zero-moment point, the zero-strain in concrete at level of steel point, and the cracking point. Lin uses the first two points to establish the linear-elastic response of the moment-curvature relationship, while the third point is the boundary of the uncracked region. Lin (1958) defines the zero-moment point using the initial stress distribution due to the initial prestressing force and stresses due to eccentricity of initial prestressing force as:

$$f = -\frac{P_e}{A_c} \pm \frac{P_e e y}{I} \qquad \textbf{Eq. 2-12}$$

Stress distribution is linear in between the top and bottom fibers. Strain, ε, is determined from the stress distribution by dividing the stress by the secant modulus of concrete, E_c.

$$\varepsilon = \frac{f}{E_c} \qquad \textbf{Eq. 2-13}$$

Curvature is determined by difference in strains divided by the total height of the cross-section, h, as shown in Eq. 2-14.

$$\phi = \frac{\varepsilon_b - \varepsilon_t}{h} \qquad \textbf{Eq. 2-14}$$

Strain in the concrete at the prestressing steel level is determined using strain compatibility. Once this strain is known, the strain in the prestressing steel is calculated using the initial effective stress and the prestressing steel stress-strain relationship. In other words,

when the strain in the concrete at the prestressing steel level is zero, the corresponding stress will be zero. Eq. 2-15 indicates the total strain in the prestressing steel at zero curvature which is calculated by adding the initial strain of the concrete at prestressing steel level (the strain in the prestress strands due to initial tension after losses), ε_{se}, to initial effective prestressing strain (the strain in the strands due to initial eccentricity – decompression of the section at the level of the prestressing strands), ε_{ce}, since the strain changes the same for the concrete and the prestressing steel.

$$\varepsilon_{ps} = \varepsilon_{se} + \varepsilon_{ce} = \varepsilon_1 + \varepsilon_2 \qquad \textbf{Eq. 2-15}$$

Where:

$$\varepsilon_1 = -\frac{f_{se}}{E_{ps}} \qquad \textbf{Eq. 2-16}$$

$$\varepsilon_2 = -\frac{1}{E_c}\left[\frac{P_e}{A_c} + \frac{P_e e^2}{I_g}\right] \qquad \textbf{Eq. 2-17}$$

Prestressing steel force is determined by using internal stress distribution since the beam is uncracked, using Eq. 2-12. Stresses are distributed linearly – similar triangles are used to determine the stress in the prestressing steel. With the stress in the steel known, the moment required to counteract the stress is determined by mechanics of materials:

$$f = \frac{My_b}{I_g} \Rightarrow M = \frac{fI_g}{y_b} \qquad \textbf{Eq. 2-18}$$

Using superposition, extreme fiber stress is determined. The additional stress due to the applied load is added to the initial stress, Eq. 2-12, to determine the final stress distribution:

$$f = -\frac{P_e}{A_c} - \frac{P_e e y_b}{I_g} + \frac{My_b}{I_g} \qquad \textbf{Eq. 2-19}$$

Cracking point corresponds to where the concrete modulus of rupture is reached in the extreme fiber in tension as defined by ACI 318 (2019). Cracking point is calculated by determining the additional moment required from the point of zero concrete stress at prestressing steel level, to achieve the cracking stress since the linear-elastic response of the moment-curvature relationship has been defined by previous points. This additional stress is given in Eq. 2-20:

$$\Delta f = f_r - f \quad \textbf{Eq. 2-20}$$

Additional moment required is shown in Eq. 2-21:

$$\Delta M = \frac{\Delta f I_g}{y_b} \quad \textbf{Eq. 2-21}$$

Therefore, the cracking moment, shown in Eq. 2-22, is obtained by:

$$M_{cr} = M + \Delta M \quad \textbf{Eq. 2-22}$$

Additional stress in the prestressed strand to attain first cracking is calculated by Eq. 2-23:

$$\Delta f_{ps} = \frac{n \Delta M e}{I_g} \quad \textbf{Eq. 2-23}$$

Since the member is in the linear-elastic range, the additional strain is determined by dividing the additional stress by the secant modulus of the concrete, as shown in Eq. 2-24.

$$\Delta \varepsilon = \frac{\Delta f}{E_c} \quad \textbf{Eq. 2-24}$$

The additional curvature is given by Eq. 2-25.

$$\Delta \phi = \frac{\Delta \varepsilon}{y_b} \quad \textbf{Eq. 2-25}$$

The cracking curvature is the change in curvature because the change in curvature is taken from the zero-curvature point and is shown in Eq. 2-26.

$$\phi_{cr} = \Delta \phi \quad \textbf{Eq. 2-26}$$

The moment-curvature response in the post-cracking region is inelastic following the response of the materials. Consequently, Lin (1958) uses an iterative method to balance the compression and tension forces within the member. Once the forces are balanced, the moment and the curvature are determined from the resulting stresses and strains. Lin's procedure for determining the moment-curvature points with in the post-cracking region is given by seven steps.

Step 1 is to assume a strain at the top fiber - typically strains are checked when the top fiber strain is 0.001 in./in., 0.002 in./in., and 0.003 in./in. additional points may be checked using the method. The three points give a relatively accurate, comparable to actual tested beams, moment-curvature relationship in the post-cracking region. Additionally, the largest strain corresponds to useable concrete strain which corresponds to the concrete crushing failure; the ultimate moment is determined.

Step 2 is to assume a depth to the neutral axis and compute the internal forces – knowing the top fiber strain and the neutral axis assumed, internal compression and tension forces can be calculated. Since Lin neglects the tension contribution of the concrete, the tension force is comprised of the prestressing steel force and any tension force from the non-prestressed mild-steel reinforcement. The initial step in determining the forces due to the tension steel is to determine the strains in the steel, which is done using strain compatibility. The focus of Lin (1958) research did not include non-prestressed steel. Therefore, the strain in the prestressing strand can be found since the concrete compression strain and neutral axis are known and is shown in Eq. 2-27.

$$\varepsilon_{ps} = \varepsilon_{se} + \varepsilon_{ce} + \frac{\varepsilon_{cf}\left(d_{ps} - c\right)}{c} = \varepsilon_1 + \varepsilon_2 + \varepsilon_3 \qquad \textbf{Eq. 2-27}$$

The stress in the prestressing strand is determined from the stress-strain relationship using the Bernoulli-Euler beam theory. The final tension force in the prestressing steel is given in Eq. 2-28.

$$T = A_{ps} f_{ps} \qquad \textbf{Eq. 2-28}$$

Lin (1958) uses Hognestad's (1952) parabolic equation for the concrete compression stress-strain relationship, which was confirmed by Billet & Appleton (1954) to be valid for PRC flexural members. Figure 2-9 indicates Hognestad's concrete compression stress-strain diagram.

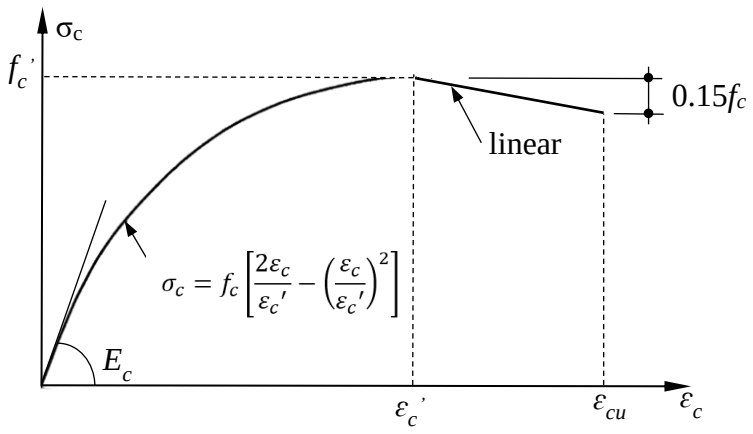

Figure 2-9: Hognestad's concrete compression stress-strain diagram for flexural members

The curvature is determined by Eq. 2-29.

$$\phi = \frac{\varepsilon_{cf}}{c} \qquad \textbf{Eq. 2-29}$$

Where the extreme fiber strain in the cross section is represented by ε_{cf}.

If Eq. 2-29 is rearranged to solve for the strain and substituted into Hognestad's (1952) equation, the compression force equation for a rectangular section is given by Eq. 2-30.

$$C = \int_0^c f_c\, b dx = b f_c' \int_0^c \left(\frac{2\phi x}{\varepsilon_c'} - \frac{\phi^2 x^2}{\varepsilon_c'^2}\right) dx = b f_c' \frac{\varepsilon_{cf}}{\varepsilon_c'} c^2 \left[1 - \frac{\varepsilon_{cf}}{3\varepsilon_c'}\right] \qquad \textbf{Eq. 2-30}$$

Additionally, the distance from the neutral axis to the line of action, the centroid of the parabolic stress block, is determined by Eq. 2-31.

$$\gamma = \left[\frac{8\varepsilon_c{}' - 3\varepsilon_{cf}}{12\varepsilon_c{}' - 4\varepsilon_{cf}}\right] \qquad \textbf{Eq. 2-31}$$

The compression force equation is adjusted to account for the variation in width of the compression block if the section is an I-shaped or T-shaped cross-section. Lin (1958) assumed the flange depth to extend to the neutral axis; this introduces a negative compression force equal to the over estimation. The final compression force is then the sum of the two forces. Lin's third step is the following:

Check to see if assumed *c* yields *C* = *T*. With the two forces determined, equilibrium is checked. The fourth step is needed to satisfy equilibrium.

Step 4 is to revise assumption for c until equilibrium is satisfied (*C* = *T*). As the initial assumption (step 2) for the depth of the neutral axis, *c*, most likely will not yield equilibrium, adjusting the neutral axis depending on previous tension and compression forces is required. If the compression force is larger than the tension force, the neutral axis should be shifted up and vice versa if the tension force is larger, the neutral axis should be shifted down to reduce the strain in the tension strand and increase the compression area.

Once the converged value of neutral axis, *c*, has occurred. Step 5 is to determine the curvature, ϕ, and the moment of the force couple, *M*, by Eq. 2-28 and summing moments about the concrete force, respectively.

Step 6 is to assume another top fiber strain in step 1and repeat steps 2 through 5 to obtain moment and curvature.

Lin's final step (Step 7) is just a summation of the steps to achieve sufficient points to define the moment-curvature response.

Lin found that the method produced ultimate moment results comparable to ACI Code calculations. Most importantly, Lin found his method gave a greater understanding of the total behavior of the member. Lastly, Lin (1958) determined that the total moment-curvature response could be used for calculating ultimate deflections.

2.3.2 Naaman (1977) stain compatibility method

Naaman (1977) proposed a non-linear analysis procedure to predict the behavior at ultimate strength of pretensioned fully bonded, prestressed and partially prestressed sections. Non-linear characteristics of the steel are accounted for, but strains and forces in the concrete are approximated by the ACI 318 (1971) and AASHTO (1973) specifications using a rectangular stress block (Mattock, Kriz & Hognestad, 1961).

Naaman (1977) *strain-compatibility* approach used the rationale that more variabilities are encountered when predicting the stress-strain properties of concrete (Popovics, 1970; Popovics 1973) than when predicting the stress-strain properties of the steel. For this strain-compatibility approach, the elastic modulus of the steel as well as the yield strength, ultimate strength, and elongation of the steel are known. Naaman used similar assumptions as Lin's load-balancing method, assumptions 1 through 7. Two additional assumptions were that the strain in the extreme fiber in compression (top fiber for a simple beam) under effective prestress alone is negligible and if non-prestressed steel is used in the tension region that it has the same center of gravity as the prestressed reinforcement.

The determination of the actual stress and strain in the prestressing steel at ultimate requires the relation between stress and strain derived from compatibility of strain and equilibrium of the section. Naaman used methods derived from Janney, Hognestad & McHenry (1956); Abeles (1966); Khachaturian & Gurfinkel (1969); Libby (1971); and Warwaruk, Sozen

& Siess (1962) to describe the stress-strain relationship of the prestressing steel. Additionally, Naaman used the equivalent rectangular stress distribution, with the average stress of $0.85f'_c$ and β_1 factor relating depth of equivalent rectangular compressive stress block to depth of neutral axis. While this does not represent the actual stress distribution in the compression zone at nominal strength, it does provide essentially the same nominal combined flexural and axial compressive strength as verified from Mattock, Kritz & Hognestad (1961).

Two aspects of the numerical technique were used: a numerical equation that adequately represents the stress-strain curve of the prestressing steel specially in its non-linear portion and the intersection of equilibrium curve and stress-strain curve are needed.

Naaman using strain compatibility determined the neutral axis location directly, unlike Lin's method, by setting the useable concrete strain equal to the strain in the prestressing steel as shown in Eq. 2-32.

$$c = \left(\frac{\varepsilon_{cu}}{\varepsilon_{ps} + \varepsilon_{cu} - \varepsilon_{se} - \varepsilon_{ce}}\right) d_{ps} \qquad \textbf{Eq. 2-32}$$

For a rectangular section at ultimate (prestressing steel yielding), the equilibrium condition leads to Eq. 2-33 to describe the internal forces.

$$A_{ps} f_{ps} + A_s f_s = 0.85 f'_c b \beta_1 c + A'_s f'_s \qquad \textbf{Eq. 2-33}$$

Naaman further presents how to modify the equilibrium condition for concretes for which the dimensional factors of the stress block are different.

Combining Eq. 2-32 and Eq. 2-33 leads to the following relationship:

$$f_{ps} = \left[\frac{0.85 f'_c b \beta_1}{A_{ps}}\right]\left[\frac{\varepsilon_{cu}}{\varepsilon_{ps} + \varepsilon_{cu} - \varepsilon_{se} - \varepsilon_{ce}}\right] d + \frac{A'_s f'_s - A_s f_s}{A_{ps}} \qquad \textbf{Eq. 2-34}$$

If the non-prestressed reinforcement in the tension region and compression region have not yielded, their stresses are a function of the strain in the prestressing steel as shown in Eq. 2-35 and Eq. 2-36.

$$f_s' = E_s\left[\varepsilon_{cu} + \frac{d'}{d}(\varepsilon_{se} + \varepsilon_{ce} - \varepsilon_{cu}) - \frac{d'}{d_{ps}}\varepsilon_{ps}\right] \leq f_y' \quad \textbf{Eq. 2-35}$$

$$f_s = E_s(\varepsilon_{ps} - \varepsilon_{se} - \varepsilon_{ce}) \leq f_y \quad \textbf{Eq. 2-36}$$

Naaman presented that the behavior in the prestressing steel at ultimate reduces to a general form shown in Eq. 2-37.

$$f_{ps} = \frac{A}{\varepsilon_{ps} + B} + C\varepsilon_{ps} + D \quad \textbf{Eq. 2-37}$$

Where A, B, C, and D are parameters depending on materials characteristic, effective prestress and geometric properties of the section. Naaman (1977) explains that the actual values of the prestressing steel stress at ultimate and the prestressing steel strain at ultimate are needed. Therefore, two equations and two unknowns can be solved for, but generally the equations are of a high order and charts were developed for their solution. Naaman also presents a computerized numerical technique instead of using the graphical technique. Several analysis models were compared including the ACI 318 recommended value of the stress in the prestressing steel given in Eq. 2-38.

$$f_{ps} = f_{pu}\left[1 - 0.5\rho_{\rho s}\frac{f_{pu}}{f_c'}\right] \quad \textbf{Eq. 2-38}$$

Naaman found that the higher the prestressing reinforcement ratio the smaller the influence of non-prestressed reinforcement was on curvature and the more accurate the curvature prediction. Additionally, using the ACI 318 code allowed the approximation of the forces in the concrete and prestressing steel at ultimate using Eq. 2-38.

2.3.3 Tri-linear moment-curvature method

Alwis (1990) presented a moment-curvature analysis for RC beams using a tri-linear representation dependent on the cracking and yielding points for rectangular cross-sections. The moment-curvature response after the yielding point was assumed to be perfectly plastic - defined by two points, the cracking point and the yielding point. However, Alwis concluded that the method was not suitable for curvatures significantly larger than the curvature at yielding point, as the member was assumed to be perfectly plastic after yielding. Alwis did find good correlation between load-deflection curves derived from the moment-curvature method and load-deflection curves using Branson's formula within the service load range. In addition, Alwis concluded that the methods would produce only minor differences in their predictions in the service load range due to their use of cracked and uncracked sectional properties in their derivations. Alwis presented several numerical and experimental comparisons to further support his conclusions.

Although Alwis did not find a good comparison from experimental results in his research, Charkas, Rasheed & Melhem (2003) presented a tri-linear moment-curvature analysis method for RC beams including the effects of FRP for strengthening the member. While non-prestressed members are outside the scope of the present method, Charkas, Rasheed & Melhem (2003) presents relevant concrete analysis and moment-area integration procedures. In particular, the derivation of the equivalent stress block factor, α as:

$$\alpha = \frac{\int_0^{\varepsilon_{cf}} \sigma_c d\varepsilon_c}{f_c' \varepsilon_{cf}} = \left[\frac{\varepsilon_{cf}}{\varepsilon_c'} - \frac{\varepsilon_{cf}^2}{3\varepsilon_c'^2}\right] \qquad \textbf{Eq. 2-39}$$

In addition, the derivation of the neutral axis multiplier, γ, as:

$$\gamma = 1 - \frac{\int_0^{\varepsilon_{cf}} \sigma_c d\varepsilon_c}{\varepsilon_{cf} \int_0^{\varepsilon_{cf}} f_c \, d\varepsilon_c} = \frac{\frac{1}{3} - \frac{\varepsilon_{cf}}{12\varepsilon_c'}}{1 - \frac{\varepsilon_{cf}}{3\varepsilon_c'}}$$ **Eq. 2-40**

Since the load-deflection response is based on the moment-curvature response, their research also provided bases for developing the moment-area procedure for determining the structural response of the member. However, as the initial curvature was assumed equal to zero, the effects of the prestressing are not accounted for.

In 2007, Peterson and Rasheed built on Charkas, Rasheed & Melham (2003) research and proposed a tri-liner moment-curvature method that predicted the short-term deflection for straight, bonded tendons in PRC members. The moment-curvature distribution was separated into three flexural stiffness regions: uncracked, post-cracking, and post-yielding. The uncracked region was bounded by the external moment required to cause a tension stress, f_r, in the bottom extreme concrete fiber while the post-cracking region was bounded by the first cracked boundary point and an external moment that causes the prestressing strand to yield, at 0.01 in./in. strain. The third region, post-yielding region, was bounded by the first yielding boundary point and the external moment required for the member to fail, by strand rupture or concrete crushing. Each of the boundary moments has a corresponding curvature. Since the moment-curvature is assumed tri-linear, points within the flexural stiffness regions are determined through interpolation using the boundary points.

This derived procedure used closed form and iterative equations to determine neutral axis locations, moments, and curvatures to define a tri-linear moment-curvature response. Peterson's procedure derives closed form deflection equations using moment-area theorem from the tri-linear moment-curvature response. In deriving the equations, internal stress analysis was used

for the linear elastic region while strain-compatibility was used for the post-cracked regions of the response along with material behaviors.

Peterson and Rasheed (2007) procedure is intended for rectangular, T-section, and I-section cross-sections including mild compression steel. Both strand rupture and concrete crushing failure modes were analyzed for each cross-section shape. The use of linear compressive stress distributions in the uncracked and post-cracking regions and parabolic compressive stress distribution, Hognestad's parabola, for the post-yielding region are discussed.

Peterson's proposed tri-linear moment-curvature method was checked against nine specimens, which included both experimental and analytical derived data. Of the nine specimens, seven had moment-curvature graphs and five had load-deflection graphs to compare. At least one specimen contained mild compression steel, was loaded uniformly, and was a T-section or an I-section. Peterson included a comparison to the PCI deflection calculations methods, bilinear moment-deflection analysis and effective moment of inertia analysis, for an analytical rectangular specimen.

Peterson and Rasheed (2007) determined that the tri-linear moment-curvature method produced accurate predictions for moment-curvature and short-term load-deflection responses. In addition, the proposed method was capable of capturing deflections within the post-yielding region of the load-deflection response, as opposed to current methods.

2.4 Deflection of prestressed reinforced concrete members

As the prestressed member is loaded greater than the cracking load, or in the case of partial prestressing where limited controlled cracking is allowed, or when members are

strengthened, the use of the gross moment of inertia underestimates the camber or deflection of the PRC flexural member.

Due to the complex nature of the flexural behavior of PRC beams and the desirability of having a simplified method for calculating deflections due to short-term loads, various procedures have been proposed over the years. Despite the wide use of prestressing, a simple, practical method for accurately predicting the time dependent losses and deflections of prestressed concrete members currently does not exist. This is partly due to the difficulty in predicting the coefficients related to the properties of steel and concrete and the uncertain environmental conditions in which the structure is subjected to after prestressing. The material parameters that influence concrete deflection are modulus of elasticity, modulus of rupture, creep, and shrinkage. Concrete modulus of elasticity, secant modulus, is strongly influenced by the concrete materials and proportions used; it becomes stiffer as the compressive strength of concrete increases. In addition, higher values of the modulus can be used to reduce deflections resulting in lower creep levels. Deflections are a function of the age of the concrete at the time of loading due to the long-term effects of shrinkage and creep that significantly increase with time. Creep is the time-dependent increase of strain in hardened concrete subjected to sustained stress. Factors such as the nonhomogeneous nature of concrete properties caused by the stages of construction, the histories of water content, temperature and loading on the structure and their effect on the material response are difficult to quantify even for structures that have been in service for years (ACI Committee 435, 2003). Even when these factors can be predicted precisely, an accurate analysis that accounts for the interdependence of the effects of shrinkage, creep, and relaxation of steel is too complicated to be widely used in practice.

Currently, the American Concrete Institute (ACI) and Prestressed Concrete Institute (PCI) procedures for instantaneous deflection of prestressed members are based on the bilinear-moment deflection relationship or the effective moment of inertia method. Both procedures provide accurate instantaneous deflections for prestressed members in the working load range. However, at higher loads the current prediction methods become inaccurate and later within the dissertation a trilinear moment-curvature response is used for the proposed deflection analysis for PRC-FRP members.

ACI 318 *Building Code Requirements for Structural Concrete* (ACI 318) separates the behavior of PRC flexural members into three classes: Class U, Class C, and Class T (ACI Committee 318, 2019). These designations correspond to the level of tensile stress in the extreme fiber of the section under service loading. Class U members are uncracked with a tensile stress less than $7.5\sqrt{f_c'}$ (psi) and Class C members are cracked members with a tensile stress above $12\sqrt{f_c'}$ (psi). While, Class T members are assumed to be in transition between uncracked and cracked members. These classes apply both to bonded and unbonded prestressed flexural members. Partially prestressed members are cracked under service loads and need to be checked for deflection and crack control. Immediate deflection calculations of Class T and Class C flexural members are based on cracked transformed section analysis, and the designer is permitted to use the bilinear moment deflection relationship or an effective moment of inertia relationship.

PCI Design Handbook (2017) method for immediate deflection calculation is divided into two categories: elastic deflections and bilinear behavior. Elastic deflections are used for Class U prestressed members where calculation of instantaneous deflections of both RC and PRC members caused by superimposed service loads follows classical methods of mechanics.

The uncracked moment of inertia, I_g, is used for calculating deflections for these members. *PCI Design Handbook* (2017) defines the extent of the elastic deflection region by the modulus of rupture of concrete: f_r. ACI 318 defines the modulus of rupture for normal weight concrete as indicated by Eq. 2-41.

$$f_r = 7.5\sqrt{f_c'}\ (psi)\ \&\ f_r = 0.623\sqrt{f_c'}\ (MPa) \quad \textbf{Eq. 2-41}$$

If the tensile stress at the bottom of the member is greater than the modulus of rupture of concrete, f_r, (Class T and Class C), the deflection calculations according to *PCI Design Handbook* and ACI 318 are based on a transformed cracked section analysis. Once the cracked section analysis is completed, the ACI 318 and *PCI Design Handbook* allow for the use of bilinear or effective moment of inertia deflection calculations (ACI Committee 318, 2019 & PCI, 2017).

2.4.1 Bilinear behavior method

Bilinear behavior method also known as the bilinear computation method is used to determine the flexural stiffness of a cracked member, Class T or Class C. The deflection before the component has cracked is calculated using the gross, uncracked moment of inertia, I_g, and the additional deflection after cracking is calculated using the inertia of the cracked section, I_{cr}. Therefore, the total deflection is given by Eq. 2-43.

$$\Delta_t = \Delta_g + \Delta_{cr} \quad \textbf{Eq. 2-42}$$

Where Δ_t is the total deflection, Δ_g is the deflection before the member has cracked caused by self-weight and externally applied loads up to the cracking moment, and Δ_{cr} is the deflection caused by the additional loads after cracking is reached.

A bilinear moment-deflection function in the elastic uncracked and cracked stages is shown in Figure 2-10 without prestress effects included in the illustration. The elastic stage

extends to the onset of the first flexural crack. The second stage follows until the ultimate flexural capacity. Additionally, the *PCI Design Handbook* (2017) allows for an alternative to the bilinear behavior method, the effective moment of inertia method as given in ACI 318.

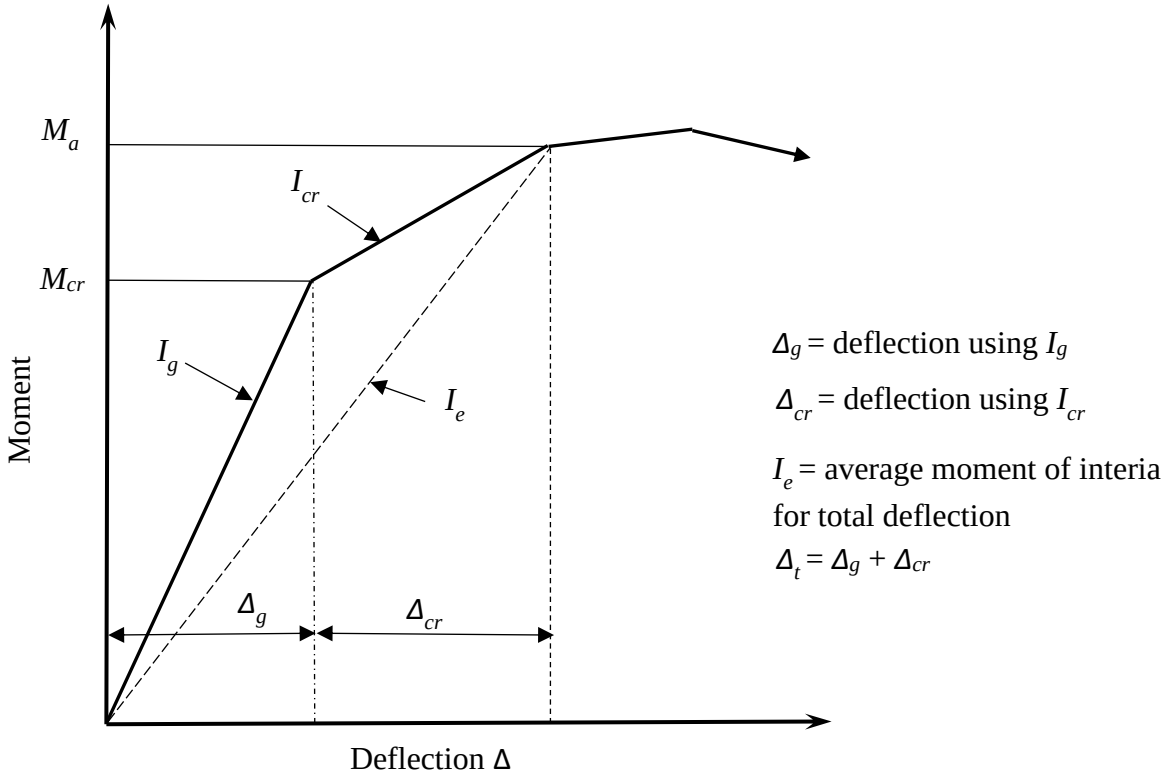

Figure 2-10: Bilinear moment-deflection and effective moment of inertia comparison adapted from PCI (2017)

In graphical form, the bilinear moment-deflection relationship follows uncracked and cracked stages. The ACI code requires that computation of deflection in the cracked zone in the bonded tendon beams be based on the transformed section whenever the tensile stress, f_t, in the concrete exceeds $6\sqrt{f_c'}$ (psi). Therefore, the cracked moment of inertia is evaluated using the transformed I_{cr} utilizing the contribution of the reinforcement in the bilinear method of deflection computation. The cracked moment of inertia can be calculated by PCI approach for fully prestressed members as in Eq. 2-43.

$$I_{cr} = n_p A_{ps} d_p^2 \left(1 - 1.6\sqrt{n_p \rho_p}\right) \quad \textbf{Eq. 2-43}$$

Where $n_p = E_{ps}/E_c$

For partial prestressing (with mild reinforcement carrying some of the tensile force), the cracked moment of inertia becomes:

$$I_{cr} = \left(n_p A_{ps} d_p^2 + n_s A_s d^2\right)\left(1 - 1.6\sqrt{n_p \rho_p + n_s \rho_s}\right) \quad \textbf{Eq. 2-44}$$

Where $n_s = E_s/E_c$

While Eq. 2-43 and Eq. 2-44 are useful and easy to use, the cracked moment of inertia can be calculated more accurately from the moment-curvature relationship along the beam span and from the stress and consequently strain distribution across the depth of the critical sections.

2.4.2 Effective moment of inertia method

The American Concrete Institute (ACI) currently uses an effective moment of inertia method. The first version of the method was proposed by Branson (1963) to determine short-term (instantaneous) deflections for RC concrete members. This was verified by Branson & Kripanarayanan (1971) and Nawy & Huang (1977) for pretensioned prestressed beams while Branson & Trost (1982) validated this method for partially prestressed members. Branson proposed a semi-empirical approximation to define the transition between the moment of inertia of the loaded member between its uncracked and cracked condition known as the *effective moment of inertia method* (Branson, 1963). When examining the slope-deflection, the slope of line for uncracked section is approximately equal to the concrete modulus of elasticity times the gross moment of inertia including the reinforcing steel, $E_c I_{gt}$. The slope of post-cracking section near yielding of tension steel is approximately equal to the modulus of elasticity of concrete times the fully cracked moment of inertia including the reinforcing steel, $E_c I_{cr}$. At points

between cracking and yielding of the steel, intermediate values of flexural stiffness, *EI*, exist. Branson derived the effective moment of inertia equation that was observed in experimental data and is shown in Eq. 2-45:

$$I_e = \left(\frac{M_{cr}}{M_a}\right)^m I_{gt} + \left[1 - \left(\frac{M_{cr}}{M_a}\right)^m\right] I_{cr} = I_{cr} + \left(\frac{M_{cr}}{M_a}\right)^m \left(I_{gt} - I_{cr}\right) \leq I_{gt} \qquad \textbf{Eq. 2-45}$$

Branson tested the validity of his model by comparing it to deflection data obtained during other investigations of 58 simply supported and continuous RC beams subjected to uniform loads. These 58 beams were rectangular and flanged cross-sections with tension reinforcement ratio of approximately 1.65% and ratio of moment of inertia of the fully cracked transformed cross section and moment of inertia of the gross cross section, I_{cr} /I_{gt}, approximately equal to 0.45 at maximum applied (elastic) moment equal to 2.5M_{cr}. The model, given by Eq. 2-38, is in the form of applied load and inherently bounded by I_{cr} and by a logical upper bound of I_{gt}. The cubic exponent was empirically determined by applying the model to rectangular and flanged cross-sectioned beams subjected to uniform loading. Branson suggested that the tension stiffening and the variation in flexural stiffness, *EI*, along the length of the member could be accounted for by using a constant value of *m* equal to 3. This exponent allowed the model to inherently account for the permanent deflection sustained by a RC member due to the inelastic effects of tensile cracking, tension-stiffening action. In 1968, Beeby found that for 133 experimental RC beams that the effective moment of inertia procedure had the highest degree of accuracy to predict deflections over the four commonly accepted methods at that time, namely, 1, 2, 3, and 4. In 1971, ACI 318 *Building Code Requirements for Structural Concrete* adopted Branson's equation with an exponent of three and for simplicity used the moment of inertia of the gross concrete section, I_g, ignoring the small increase in the moment of inertia due to the reinforcement as shown in Eq. 2-46:

$$I_e = \left(\frac{M_{cr}}{M_a}\right)^3 I_g + \left[1 - \left(\frac{M_{cr}}{M_a}\right)^3\right] I_{cr} \leq I_g \qquad \textbf{Eq. 2-46}$$

Eq. 2-46 is currently used in the ACI 318 for PRC members.

The effective moment of inertia procedure to determine the flexural stiffness of PRC members has been validated by numerous researchers. In 1970, Shaikh & Branson found that for 12 rectangular pretensioned concrete beams the effective moment of inertia procedure predicated deflections up to 80 percent of the ultimate load within 19 percent of the measured values. Nawy & Potyondy (1970, 1971) found that for 22, I- and T-shaped, pretensioned PRC beams Eq. 2-34 gave excellent results for evaluating the effective moment of inertia of the section for short-term loading. Branson & Kripanarayanan (1971) examined the deflection of uncracked and cracked PRC members with bonded prestressing and with and without non-prestressed steel using the ACI 318 effective moment of inertia method (Eq. 2-46). They found that this effective moment of inertia method applied well to the 12 PRC beams loaded into the cracking range in the study. During this study, the measured modulus of rupture equaled approximately $11\sqrt{f_c'}$ while ACI 318 currently uses $7.5\sqrt{f_c'}$ for normal weight concrete. Deflections under superimposed loads were computed by using the secant rigidity, $E_c I_e$, for the flexural stiffness (Branson, 1972). Furthermore, Bennet & Veerasubramanina (1972) found that for 34 rectangular, I-, T-, and composite T- pretensioned PRC beams the effective moment of inertia method was accurate for I-section beams but conservative for monolithic and composite T-section beams. Moreover, Nawy & Huang (1977) found for 19 I- and T-pretensioned PRC beams the generally accepted effective moment of inertia procedure provided results within acceptable ranges.

Branson & Trost (1982) further defined the use of the effective moment of inertia method in deflection calculations for PRC members to account for initial prestress force and defines the cracking moment for zero curvature in a prestressing member as:

$$M_{cr} = \frac{f_r I_{gt}}{y_{bot}} + \frac{P_e I_{gt}}{A_{gt} y_{bot}} \qquad \textbf{Eq. 2-47}$$

Figure 2-11 indicates the basic stress distribution for uncracked, partially cracked, and fully cracked sections. Additionally, Figure 2-12 provides the diagram indicating the strains and curvatures for a member loaded into the cracking range.

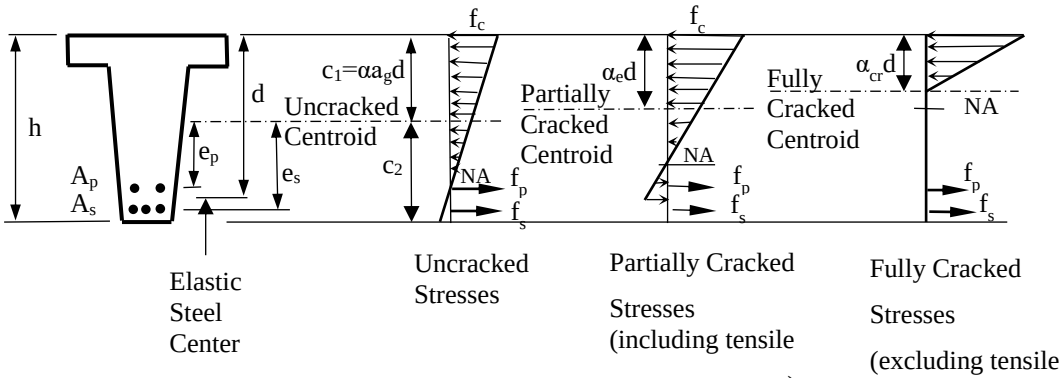

Figure 2-11: Basic stress distribution diagrams for uncracked, partially cracked, and fully cracked sections (Branson & Trost, 1982)

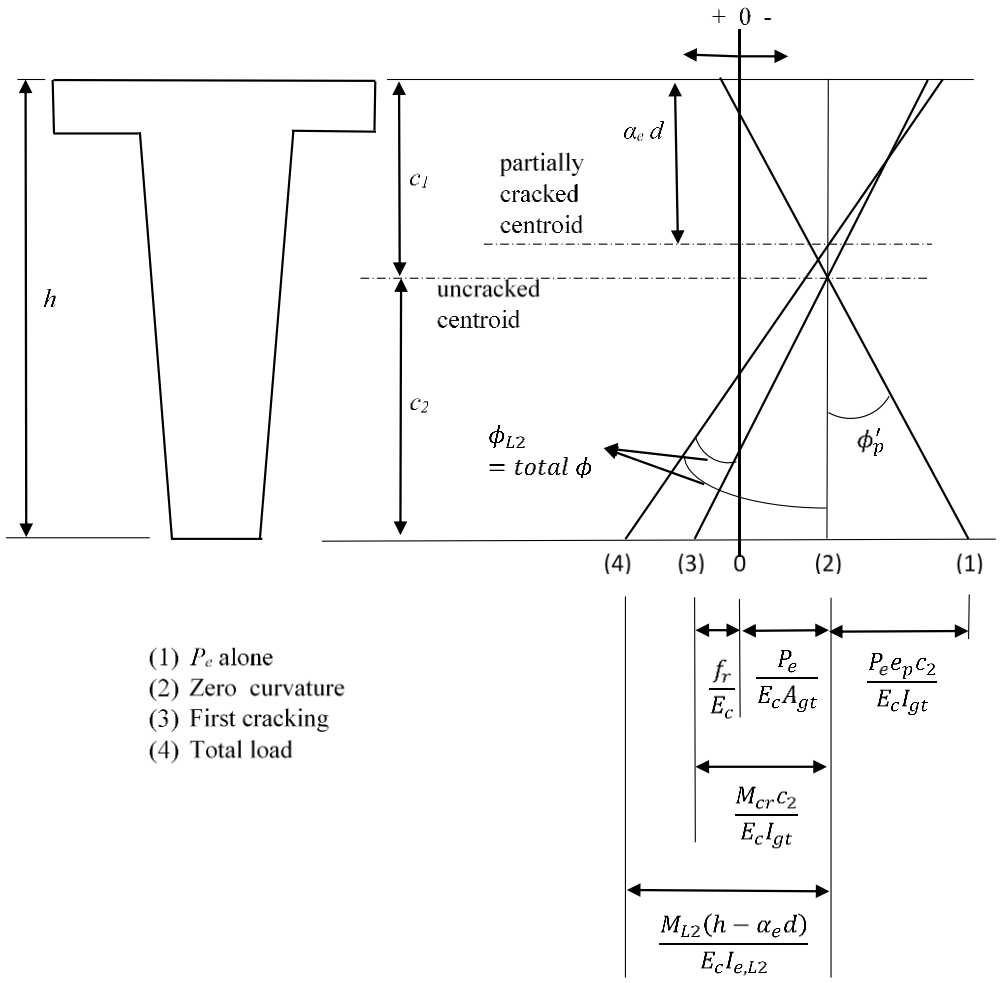

Figure 2-12: Strains and curvatures for the general case of a member loaded into the cracking range (modified from Branson & Trost 1982)

Their research concluded the effective moment of inertia method for predicting short-term deflections produced satisfactory results up to a high moment levels, above normal working load ranges. Within this study the effective moment of inertia approaches the cracked moment of inertia which gives good predictions. However, Branson and Trost determined that the moment-deflection response flattens at higher moments due to the compressive stress-strain behavior of the concrete. This attribute is not predicted by the effective moment of inertia method; as the stress-strain behavior is a material property, not a cross-section property.

Branson & Trost (1982) effective moment of inertia method provides generally accurate instantaneous deflections for unstrengthened PRC members in the working load range. Branson & Trost (1982) method becomes inaccurate at higher loads, past yielding; a more accurate method at higher loads is a tri-linear moment-curvature response behavior approach proposed for the short-term deflection analysis of unstrengthened PRC beams by Charkas, Rasheed, and Melhem (2003).

PCI adopted the ACI method (Eq. 2-46) with modifications proposed by Branson and Trost (1982) for prestressed members to determine short-term deflections. The cracking moment to applied moment ratio is equal to one minus the applied live load stress minus the modulus of rupture divided by the stress due to the applied live load as shown in Eq. 2-48.

$$\frac{M_{cr}}{M_a} = 1 - \left(\frac{f_{tl} - f_r}{f_l}\right) \qquad \textbf{Eq. 2-48}$$

Where:

- f_{lt} = stress caused by total load
- f_l = stress caused by live (transient) load

Further discussion will be presented on deflection of PRC-FRP members in Chapters 3, 4, and 5.

2.5 Response of fiber reinforced polymer materials

Strengthening of existing RC and PRC flexural members is well studied with accepted design procedures. In 1991, the first applications of externally bonded FRP systems to increase the flexural strength of RC bridges occurred in Switzerland (Meier, 1987). FRP systems have high tensile strength and are non-corroding, lightweight reinforcements created by combining carbon or glass fibers with a polymer resin to create the composite laminate used to bond it to the concrete substrate. The physical and mechanical properties of FRP materials presented explain

the behavior and properties affecting their use in concrete structures. The effects of factors, such as loading history and durations, temperature, and moisture on the properties of FPR are discussed within this section.

FRP strengthening systems are available in a variety of forms (wet layup, pre-impregnated, and precured). Fiber volume, type of fiber, type of resin, fiber orientation, dimensional effects, and quality control during manufacturing establish the characteristic of FRP material. Wet layup systems consist of dry multidirectional or unidirectional fiber sheets or fabrics impregnated with a saturating resin on site. The saturating resin bonds the FRP sheets to the concrete surface. Wet layup systems are cured in place. Pre-impregnated systems consist of partially cured unidirectional or multi-directional fiber sheets or fabrics that are pre-impregnated with a saturating resin in the manufacturer's facility, typically stored under freezing temperature. Depending on the surface requirements of the existing concrete structure, pre-impregnated systems are bonded to the concrete surface with or without an additional resin application. Similar to wet layup systems, pre-impregnated systems cure on site but require additional heating to cure. The third type, precured systems, consist of a wide variety of composite shapes manufactured off site. Typically, an adhesive is used to bond the precured shapes to the concrete surface (Rasheed, 2015).

2.5.1 Characteristics of composite materials

A composite material consists of reinforcement in a matrix, polymers, with the interface acting as the bond between them. The matrix of a composite serves to bind reinforcements together to form a composite structure and protect the reinforcements from physical damage and chemical attack, while the fibers (reinforcements) provide strength and stiffness. Therefore, the

combination of fiber and polymer materials provides a synergistic effect on the overall mechanical properties.

The performance specific design of composite materials suggests that a wide range of factors influence the properties of a composite. The following list provides possible factors that can alter composite properties and influence performance (Estrada & Lee, 2014):

1. Properties of composite constituent materials
2. Distribution of constituent materials
3. Interaction (bonding) among constituents
4. Geometry of the reinforcement, specifically its shape, size, and size distribution
5. Reinforcement concentration or volume
6. Homogeneity or uniformity of the composite system
7. Orientation of fibers

While the seven abovementioned factors affect the performance specific design of composite materials, the physical and mechanical properties of FRP materials are presented in detail in Section 2.5.3.

2.5.2 Constituent materials

The properties of FRP repair systems developed for the strengthening of structural concrete members are based on materials and structural testing. These FRP composite materials have two major components: fibers and polymer matrix. Fibers control the stiffness and strength of composite materials, while the polymer matrix transfers load and provides protection against environmental exposure. Additionally, fillers are sometimes used to circumvent cracks and the roughness of the surface. Additives and modifiers may be used to enhance the overall properties of FRP. Subsequent is a short introduction to reinforcing fibers and resin matrix.

Manufacturers use different types of fibers that offer varying properties. Fibers provide the strength and stiffness of FRP systems. Fibers are used in continuous and unidirectional form, aligned with the structural axis of loading in the strengthened application, as fibers provide ultimate performance when they are in a single direction. In structural strengthening applications, carbon and glass are two of the most commonly used fibers. The selection of fibers depends on a number of factors, for example budget constraints, availability, and required performance.

Glass fibers are relatively cost-effective and therefore, often used in composite applications. Silicon dioxide with some modifying agents are the primary constituents of the glass fibers (Gibson, 1994). Electrical glass (E-glass) and structural glass (S-glass) are the common forms used in FRP. E-glass is often used for external strengthening due to its low cost; even though, its mechanical properties are lower than S-glass (Rasheed, 2015).

Even though carbon fibers are more expensive than glass fibers, carbon or graphite fibers are most often used for structural strengthening due to their high stiffness and strength. Carbon fibers are defines as containing less than 95% carbon and graphite fibers contain at least 99% carbon (Schwartz, 1984). A comparison of glass and carbon fibers are given in Table 2-1. The ultimate tensile strength (f_{fu}) is given in column two, while the design tensile modulus of elasticity (E_f) is given in column three of Table 2-1.

Table 2-1: Comparison of fiber properties

Material	**Tensile strength, 10^3 psi (MPa)**	**Tensile Modulus, 10^6 psi (GPa)**	**Density, lb/in^3 (g/cm^3)**
E-glass fibers	500 (3450)	10.5 (72)	0.092 (2.54)
S-glass fibers	650 (4482)	12.5 (86)	0.090 (2.49)
Carbon fibers (PAN precursor)			
AS-4 (Hercules)	580 (4000)	33.0 (228)	0.065 (1.80)
IM-7 (Hercules)	785(5413)	40.0 (276)	0.064 (1.77)
T-300 (Amoco)	530 (3654)	33.5 (231)	0.064 (1.77)
Carbon fibers (pitch precursor)			
P-55 (Amoco)	250 (1724)	55.0 (379)	0.072 (1.99)
P-100 (Amoco)	325 (2241)	100.0 (690)	0.078 (2.16)
Modified from Gibson (1994).			

Commercial material commonly has glass or carbon fibers in matrices based on thermosetting polymers, such as epoxy or polyester resins. Matrix plays a significant role in binding fiber reinforcement materials. The primary role of the matrix is to bind and protect fibers from the environment. Matrix has to be thermally and chemically compatible with fibers. The main type of polymeric matrices used for FRP strengthening systems used in civil structures is thermoset. Thermosets are cross-linked polymers that have undergone an irreversible chemical reaction to permanently connect all molecular chains with covalent bonds (Estrada & Lee, 2014). A polymer resin and catalyst (curing agent) are mixed together to create an exothermic reaction which gels into a cross-linked material. Thermosetting resins are categorized into three types: polyester resin, vinylester resin, and epoxy resin. These materials offer chemical resistance and thermal stability. Vinylesters, for instance, are resistant to alkalis and strong chemicals. As compared with polyesters, vinylesters are more effective against

moisture absorption and shrinkage (Estrada & Lee, 2014). The most common type used when strengthening concrete structures is epoxy resin due to its superior mechanical properties and compatibility with most fibers.

2.5.3 Mechanical properties of FRP

Flexural strength is increased by bonding FRP reinforcement with fibers oriented along the length of the member to the tension face of the PRC members (Cha, 2001) (Reed, Peterman, & Rasheed, 2005) (Rosenboom, Hassan, & Rizkalla, 2006). FRP composites provide stiffness and strength along the fiber direction in tension. Strength properties are discussed first in this section then stiffness properties. When increasing the flexural capacity of a PRC member with FRP, the tensile capacity and behavior of the unidirectional composite material is critical to the design.

2.5.3.1 Strength properties

Tensile behavior – when loaded in direct tension, unidirectional FRP materials do not exhibit any plastic behavior (yielding) before rupture. The tensile behavior of FRP materials consisting of a single type of fiber material is characterized by a linear elastic stress-strain relationship until failure (sudden and brittle) as shown in Figure 2-1 (ACI 440.2R-17).

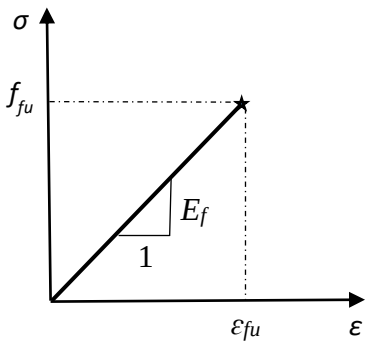

Figure 2-13: FRP design stress-strain curve along the fiber direction.

The tensile strength ($f_{fu} A_f$) and axial stiffness ($A_f E_f$) of an FRP material is dependent on several factors. The fibers in the FRP material resist the majority of the load. Therefore, the orientation of fibers, type of fiber, the quantity of fibers, and method and conditions that the composite is made affects the tensile properties of the FRP material. The load-carrying strength and the axial stiffness of the composite are based on the laminate composite area (including resin) not the bare fibers (net-fiber area). The tensile strength is given by the FRP manufacturer or determined by using the appropriate test method detailed in ASTM D3039/D3039M, D7205/D7205M, or D7585/D7565M. Table 2-2 has been modified from a table provided by ACI 440R-07 (2007) and includes some commercially available systems. The carbon fiber type systems which were used in the experimental and parametric study of this research are presented in addition to other carbon and glass fiber systems.

Table 2-2: Manufacturer mechanical properties of some commercially available systems

FRP System	Fiber Type	Weight lb/ft^2 (g/m$^{2)}$	Design thickness in. (mm)	Tensile strength ksi (MPa)	Tensile Elastic Modulus ksi (GPa)	ACI 440.3R Test Reporting Method
Fyfe Co. LLC (2005)						
Tyfo SEH51 sheet	Glass	0.19 (915)	0.052 (1.3)	83.4 (575)	3,785 (26.1)	Method 1
Tyfo SCH41 sheet	Carbon	0.14 (644)	0.040 (1.0)	143 (985)	13,900 (95.8)	Method 1
Sika Corp. (2007)						
SikaWrap Hex 100G sheet	Glass	0.19 (913)	0.040 (1.0)	77 (531)	3,430 (23.6)	Method 1
SikaWrap HEX 103C sheet	Carbon	0.13 (618)	0.040 (1.0)	104 (717)	9,450 (65.1)	Method 1
BASF (2006)						
MBrace EF 900 sheets	Glass	0.19 (900)	0.015 (0.37)	220 (1517)	10,500 (72.4)	Method 1
MBrace CF 130	Carbon	0.062 (300)	0.007 (0.17)	550 (3800)	33,000 (227)	Method 2
Modified from ACI Committee 440, 2007						

Externally bonded FRP systems are successfully used in applications where the fibers are in tension and have not been satisfactorily tested to determine their compressive strength (Rasheed, 2015). Therefore, they should not be used as compressive reinforcement. Of the longitudinal compression tests conducted on FRP laminates, the compressive behavior included transverse tensile failure, fiber micro buckling, or shear failure depending on the type of fiber, the fiber-volume fraction, and the type of resin (Ruan F. , Xu, Hou, Li, & Chu, 2018).

2.5.3.2 Time dependent behavior

Two types of time-dependent behavior are discussed in this section: creep rupture and fatigue behavior. After a period of sustained load, known as endurance time, FRP materials can fail suddenly - known as creep rupture. Endurance time decreases as the ratio of the sustained tensile stress to short-term strength of FRP laminate increases. Adverse environmental conditions, such as high temperatures, ultraviolet-radiation exposure, high alkalinity, wet and dry cycles, or freezing-and-thawing cycles, also decreases the endurance time. Carbon fibers generally are the least susceptible to creep rupture and glass fibers are most susceptible (Yamaguchi et al., 1997).

While the National Research Council of Canada has a substantial amount of data for fatigue behavior and life prediction of FRP materials in the aerospace industry, some general observations on the fatigue behavior of FRP materials can be made. For unidirectional material with approximately 60 percent fiber-volume fraction and subjected to tension-tension sinusoidal cyclic loading at a frequency low enough to not cause self-heating, a stress ratio of 0.1, and a direction parallel to the principal fiber alignment, FRP materials typically worsen the ambient environmental fatigue behavior when the ambient temperature and moisture content are raised during testing. Carbon FRP are least prone to fatigue failure with an endurance limit of 60 to 70

percent of the initial static ultimate strength (ACI 440.2R, 2017). Glass FRP fatigue behavior is more susceptible to environmental influences, moisture, alkaline or acidic solutions, than CFRP.

2.5.3.3 Flexural stiffness

Axial stiffness ($A_f E_f$) of the FRP, is a standard for measuring deformability that is based on the elastic modulus (stress per unit strain), a function of the composite material, and the moment of inertia, I, is a function of geometry of the beam. Understanding the complexities of the modulus of elasticity for the unidirectional FRP gives important insight to the deflection behavior of PRC-FRP flexural members.

Unidirectional composite is orthotropic having distinct properties along the fiber, transverse, and through-the-thickness directions. Isotropic materials have two independent engineering constants – Young's modulus of elasticity, E, and Poisson's ratio, v. While, orthotropic materials have three principal materials moduli of elasticity (E_1, E_2, E_3), three independent Poisson's ratios (v_{12}, v_{13}, v_{23}), and three shear moduli (G_{12}, G_{13}, G_{23}). An orthotropic formulation of Hooke's law, which generalizes the idea of Young's modulus, the shear moduli, and Poisson's ratio can be written in terms of a compliance matrix as follows (Rasheed, 2015):

$$\begin{Bmatrix} \varepsilon_{11} \\ \varepsilon_{22} \\ \varepsilon_{33} \\ \gamma_{12} \\ \gamma_{13} \\ \gamma_{23} \end{Bmatrix} = \begin{bmatrix} \frac{1}{E_1} & -\frac{v_{21}}{E_2} & -\frac{v_{31}}{E_3} & 0 & 0 & 0 \\ -\frac{v_{12}}{E_1} & \frac{1}{E_2} & -\frac{v_{32}}{E_3} & 0 & 0 & 0 \\ -\frac{v_{13}}{E_1} & -\frac{v_{23}}{E_2} & \frac{1}{E_3} & 0 & 0 & 0 \\ 0 & 0 & 0 & \frac{1}{G_{12}} & 0 & 0 \\ 0 & 0 & 0 & 0 & \frac{1}{G_{13}} & 0 \\ 0 & 0 & 0 & 0 & 0 & \frac{1}{G_{23}} \end{bmatrix} \begin{Bmatrix} \sigma_{11} \\ \sigma_{22} \\ \sigma_{33} \\ \tau_{12} \\ \tau_{13} \\ \tau_{23} \end{Bmatrix} \quad \textbf{Eq. 2-49}$$

Where:

$$\frac{v_{ij}}{E_i} = \frac{v_{ji}}{E_j} \qquad \textbf{Eq. 2-50}$$

The stiffness matrix is obtained by inverting the compliance matrix in Eq. 2-49 (Rasheed, 2015).

$$\begin{Bmatrix} \sigma_{11} \\ \sigma_{22} \\ \sigma_{33} \\ \tau_{12} \\ \tau_{13} \\ \tau_{23} \end{Bmatrix} = \begin{bmatrix} \frac{1 - v_{23}v_{32}}{\Delta} E_1 & \frac{v_{21} + v_{31}v_{23}}{\Delta} E_2 & \frac{v_{31} + v_{21}v_{32}}{\Delta} E_3 & 0 & 0 & 0 \\ \frac{v_{21} + v_{31}v_{23}}{\Delta} E_1 & \frac{1 - v_{13}v_{31}}{\Delta} E_2 & \frac{v_{32} + v_{12}v_{31}}{\Delta} E_3 & 0 & 0 & 0 \\ \frac{v_{31} + v_{21}v_{32}}{\Delta} E_1 & \frac{v_{32} + v_{12}v_{31}}{\Delta} E_2 & \frac{1 - v_{21}v_{12}}{\Delta} E_3 & 0 & 0 & 0 \\ 0 & 0 & 0 & G_{12} & 0 & 0 \\ 0 & 0 & 0 & 0 & G_{13} & 0 \\ 0 & 0 & 0 & 0 & 0 & G_{23} \end{bmatrix} \begin{Bmatrix} \varepsilon_{11} \\ \varepsilon_{22} \\ \varepsilon_{33} \\ \gamma_{12} \\ \gamma_{13} \\ \gamma_{23} \end{Bmatrix}$$

Eq. 2-51

Where:

$$\Delta = 1 - v_{12}v_{21} - v_{23}v_{32} - v_{13}v_{31} - 2v_{21}v_{32}v_{13} \qquad \textbf{Eq. 2-52}$$

If the compliance matrix in Eq. 2-51 is reduced to 2-D behavior, sheet analysis, the stress components σ_{33}, τ_{13}, $\tau_{23} = 0$. The third, fifth, and sixth rows and columns are removed, yielding:

$$\begin{Bmatrix} \varepsilon_{11} \\ \varepsilon_{22} \\ \gamma_{12} \end{Bmatrix} = \begin{bmatrix} \frac{1}{E_1} & -\frac{v_{21}}{E_2} & 0 \\ -\frac{v_{12}}{E_1} & \frac{1}{E_2} & 0 \\ 0 & 0 & \frac{1}{G_{12}} \end{bmatrix} \begin{Bmatrix} \sigma_{11} \\ \sigma_{22} \\ \tau_{12} \end{Bmatrix} \qquad \textbf{Eq. 2-53}$$

The 2-D compliance matrix in Equation 3 may be inverted in yield the 2-D stiffness matrix (Jones, 1975).

$$\begin{Bmatrix}\sigma_{11}\\ \sigma_{22}\\ \tau_{12}\end{Bmatrix} = \begin{bmatrix} \frac{E_1}{1-v_{12}v_{21}} & -\frac{v_{12}E_2}{1-v_{12}v_{21}} & 0 \\ -\frac{v_{21}E_1}{1-v_{12}v_{21}} & \frac{E_2}{1-v_{12}v_{21}} & 0 \\ 0 & 0 & \frac{1}{G_{12}} \end{bmatrix} \begin{Bmatrix}\varepsilon_{11}\\ \varepsilon_{22}\\ \gamma_{12}\end{Bmatrix} \quad \textbf{Eq. 2-54}$$

Jones (1976) showed that 'the first modulus along the fiber direction may be found by the rule of mixtures that results from the assumption of having the fiber and the matrix deform in equal amounts along the fiber direction. This assumption is very accurate when compared to test results (Rasheed, 2015). This leads to an accurate estimation of the Young's modulus E_1.

$$E_1 = E_f V_f + E_m V_m \quad \textbf{Eq. 2-55}$$

Where E_f is the fiber modulus, V_f is the fiber volume fraction, E_m is the matrix modulus, and V_m = 1- V_f.

Assuming the same stress, σ_2, in the fiber and matrix simplifies how to determine the second modulus, along the transverse direction to a classical mechanics-of-materials expression that leads to a lower bound value of the Young's modulus in the transverse direction, E_2 (Rasheed, 2015).

$$E_2 = \frac{E_f E_m}{V_m E_f + V_f E_m} \quad or \quad \frac{1}{E_2} = \frac{V_m}{E_m} + \frac{V_f}{E_f} \quad \textbf{Eq. 2-56}$$

Jones (1976) indicated that it can be assumed that the fiber and matrix deform in equal amounts along the fiber direction resulting in the transverse stress equal to zero. This allows for the determination of the major Poisson's ratio, v_{12}.

$$v_{12} = v_f V_f + v_m V_m \quad \textbf{Eq. 2-57}$$

In order to simplify calculations, the nonlinear shear stress-strain relationship is linearized at the onset of deformation. Due to the deformation compatibility, the shearing strain

of the fiber and matrix are identical allowing the sheet in-plane shear modulus, G_{12}, to be calculated using mechanics-of-materials approach (Rasheed, 2015).

$$G_{12} = \frac{G_f G_m}{V_m G_f + V_f G_m} \quad or \quad \frac{1}{G_{12}} = \frac{V_m}{G_m} + \frac{V_f}{G_f} \qquad \textbf{Eq. 2-58}$$

Where:

$$G_f = \frac{E_f}{2(1 + v_f)} \qquad \textbf{Eq. 2-59}$$

$$G_m = \frac{E_m}{2(1 + v_m)} \qquad \textbf{Eq. 2-60}$$

The minor Poisson's ratio, v_{21}, is calculated directly using Eq. 2-62.

$$\frac{v_{12}}{E_1} = \frac{v_{21}}{E_2} \Rightarrow v_{21} = \frac{v_{12}}{E_1} E_2 \qquad \textbf{Eq. 2-61}$$

The first modulus along the fiber direction, E_1, is also known as the *tensile elastic modulus* typically given by the manufacturer of some commercially available systems of plates or sheets as shown in Table 2-2. Depending on the FRP strengthening system selected and/or tested, calculating the engineering constants of a unidirectional composite may be required. Fibers and composites are available in various forms. Four commonly used forms for external strengthening of structural systems are uniaxial fiber sheets, 2-D fabrics, prefabricated plates, and pultruded FRP bars and tapes. Unidirectional sheets and prefabricated plates are typically used in research and strengthening existing structures.

2.5.4 Flexural failure modes

ACI 318 (2019) and ACI 440.2R (2017) use strain compatibility as well as force and moment equilibrium for the governing mechanics principles. A limit-state design philosophy that sets acceptable levels of safety for both serviceability limit states and ultimate limit states is

adopted by ACI 440.2R with different failure modes. Five flexural failure modes (ultimate state) control the strength of an FRP-strengthened concrete section (GangaRao & Vijay, 1998):

1. Crushing of the concrete in compression prior to yielding of reinforcing steel
2. Yielding of reinforcing steel in tension followed by rupture of the FRP laminate
3. Yielding of the reinforcing steel in tension followed by concrete crushing
4. Shear/tension delamination of the concrete cover (cover delamination)
5. Debonding of the FRP from the concrete substrate.

Concrete crushing is assumed to occur when the compressive strain in the concrete reaches its maximum usable strain ($\varepsilon_c = \varepsilon_{cu} = 0.003$). Typically, yielding of reinforcing steel in tension occurs when the prestressed reinforcing steel reaches a strain of $\varepsilon_{ps} = 0.01$. Rupture of the externally bonded FRP is assume to occur if the strain in the FRP reaches its design rupture strain ($\varepsilon_f = \varepsilon_{fu}$) before the concrete reaches its maximum usable strain. This design rupture strain will vary depending on the manufacturer and is defined as the tensile yield strength divided by the tensile elastic modulus. For example, SikaWrap HEX 103C sheet has a design rupture strain of 0.011, 104 ksi/9450 ksi, and MBrace CF 130 has a rupture strain of 0.0167.

Cover delamination or FRP debonding can occur if the force in the FRP cannot be sustained by the substrate. For this study, it is assumed that where the externally bonded FRP terminates debonding failure is prevented by U-wraps or proper anchorage (Khalifa, Alkhrdaji, Nanni, & Lansburg, 1999) (Grelle & Sneed, 2013). Away from the termination point of the externally bonded FRP, the effective strain in the FRP reinforcement is limited to the strain in which debonding may occur, ε_{fd}, as defined in Eq. 2-62.

$$\varepsilon_{fd} = 0.083\sqrt{\frac{f_c'}{n_f E_f t_f}} \leq 0.9\varepsilon_{fu}\ (in.-lb)\ or\ \ \varepsilon_{fd} = 0.41\sqrt{\frac{f_c'}{n_f E_f t_f}} \leq 0.9\varepsilon_{fu}\ (SI) \qquad \textbf{Eq. 2-62}$$

Chapter 3 - Analytical load-deflection behavior of prestressed concrete members strengthened with FRP

Currently, the American Concrete Institute (ACI) and Prestressed Concrete Institute (PCI) procedures for instantaneous deflection of PRC members are based on the bilinear-moment relationship or the effective moment of inertia method. Both procedures provide accurate instantaneous deflections for prestressed members in the working load range. However, at higher loads the current prediction methods become inaccurate. Additionally, the accuracy of these methods when applied to PRC-FRP members has not be well investigated. In this chapter, tri-linear moment-curvature response is used to obtain closed form analytical deflection expressions for simply supported, pretensioned, partially prestressed girders with straight strands strengthened with FRP subjected to different loading conditions. These expressions predict instantaneous deflections at higher loads, up to failure, more accurately than current methods.

3.1 Overview

The development of the effective moment of inertia equation used in ACI 318 is present in Chapter 2 for non-strengthened PRC members. Section 3.2 presents previous research conducted on the deflection behavior of RC and PRC members strengthened with FRP. Moreover, current ACI 440.2R-17 requirements for deflection calculations are presented for PRC-FRP flexural members. Section 3.3 offers a short-term deflection analysis procedure for straight strand, bonded PRC beams strengthened with FRP. To verify the accuracy of the analytical formulation, a numerical formulation is performed using the incremental deformation

approach and presented in Section 3.4. Results are given in Chapter 4 while conclusions are drawn in Chapter 6.

3.2 Effective moment of inertia background

The development of the effective moment of inertia equation used in ACI 318 is present in Chapter 2 for non-strengthened PRC members. This section presents previous research conducted on RC and PRC members strengthened with FRP. Additionally, current ACI 440.2R-17 requirements for deflection calculations are presented for PRC-FRP flexural members.

3.2.1 RC flexural members strengthened with FRP - effective moment of inertia

The most critical criterion to be considered in the design of CFRP flexural strengthened RC and PRC beams is the induced stress ratio on the reinforcing steel at the increased service load (Barnes & Mays, 1999; Heffernan & Erki, 2005). Brena et al (2005) studied RC-FRP flexural members and determined that the stress ratio in the composite system was the critical component and suggested a lower limit be included in the ACI 440.2R-17. Currently, ACI 440.2R-17 serviceability requirements state, “The serviceability of a member (deflections and crack widths) under service loads should satisfy applicable provisions of ACI 318. The effect of the FRP external reinforcement on the serviceability can be addressed using the transformed-section analysis.” (ACI 440.2R, 2017). Therefore, the ACI 440.2 recommends using effective moment of inertia method, Eq. 2-39, with consideration of the stiffness effects of the FRP in the cracked section. It also recommends avoiding inelastic deformations of RC- FRP flexural members by preventing the steel from yielding at service load levels. This is achieved by limiting the stress in the steel to 80 percent of the its yield strength and by limiting the compressive concrete stress to 60 percent of the compressive strength of the concrete.

Several research studies have examined the flexural stiffness of RC-FRP strengthened beams. El-Mihimy & Tedesco (2000) proposed a procedure to calculate deflection of RC beams strengthened with FRP plates. Two stages of deformation were considered based on the development of cracks in the beam: uncracked stage where the gross moment of inertia is used and post-cracking stage where a modified effective moment of inertia equation based on the assumption the beam degrades to a fully cracked section upon first yield is used.

$$I_e = I_{cr}\left(1 + 1 - \left(\frac{M_a}{M_y}\right)^3\right) \qquad \textbf{Eq. 3-1}$$

And

$$M_y = E_c I_{cr}\phi_y = \frac{f_y I_{cr}}{n(d-c)}, since\ \phi_y = \frac{\varepsilon_y}{d-c} \qquad \textbf{Eq. 3-2}$$

Using a rigorous procedure developed by Charkas, Rasheed & Melhem (2003), which examined 226 effective moment of inertia solutions used for statistical correlation, Rasheed & Charkas (2009) studied the complete load-deflection response of five RC-FRP strengthened beams from previous experimental beam responses. They found El-Mihimy & Tedesco (2000) proposed equations did not converge to the gross moment of inertia at first cracking, which may lead to unrealistic deflections right after cracking. Rasheed & Charkas (2009) proposed a modified Branson's effective moment of inertia formula, Eq. 3-3 and Eq. 3-4, for deflection of RC-FRP strengthened beams since Branson's cubic moment of inertia equation did not produce conservative results for RC-FRP strengthened beams in their study. Experimental verification of the parametric study was included in their research. Rasheed & Charkas (2009) post-cracking deflection equation is given by Eq. 3-3.

$$I_e = \left(\frac{M_{cr}}{M_a}\right)^3 I_g + \left[1 - \left(\frac{M_{cr}}{M_a}\right)^3\right] I_{ey} \leq I_g \quad \textbf{Eq. 3-3}$$

Where the effective beam moment of inertia at first yield, including bond-slip effects, is given by Eq. 3-4.

$$I_{ey} = 0.7323 I_{cr} + 0.025 I_g \quad \textbf{Eq. 3-4}$$

3.2.2 RC flexural members reinforced with FRP bars - effective moment of inertia

The third research study presented in this chapter examines flexural stiffness of RC members reinforced with steel and FRP bars by Bischoff & Darabi (2012). A generalized design approach using an effective moment of inertia approach to compute deflection of steel and FRP reinforced concrete slabs unstrengthened, an expansion of Bischoff & Gross (2011) research, is given. The tension stiffening factor forms the basis of the proposed model. In order to refine their model more closely to others test results, Bischoff & Darabi used several factors to define the behavior of the flexural stiffness along the length of a member after it has cracked. An example of Bischoff and Darabi proposed effective moment of inertia equation, for simply supported flexural members, used to estimate short-term deflection is shown in Eq. 3-5.

$$I_e = \frac{I_{cr}}{1 - \gamma\beta\sqrt{\chi}\eta\left(\frac{M_{cr}}{M_a}\right)} = \frac{I_{cr}}{1 - \gamma\chi\eta\left(\frac{M_{cr}}{M_a}\right)^2} \leq I_g \quad \textbf{Eq. 3-5}$$

The tension stiffening factor, β, is defined as the ratio of the cracking moment to the applied moment. This expression for beta was originally proposed by Rao (1966) for steel reinforced concrete. Gamma, γ, is the integration factor for loading and support conditions, which accounts for the change in stiffness along the length of the member. For example, for a four-point bending of a simply supported member, gamma would equal Eq. 3-6.

$$\gamma = 1.7 - 0.7\left(\sqrt{\chi}\frac{M_{cr}}{M_a}\right) \quad \textbf{Eq. 3-6}$$

Within Eq. 3-5 and Eq. 3-6, chi, χ, is the shrinkage restraint factor. For steel reinforced concrete, chi equals 0.45 and for FRP reinforced concrete chi equals 0.65. Eta, η, is a function of the ratio of the fully cracked section to the gross section moments of inertia, as shown in Eq. 3-7.

$$\eta = 1 - \frac{I_{cr}}{I_g} \quad \textbf{Eq. 3-7}$$

3.2.3 PRC flexural members strengthened with FRP - effective moment of inertia

Several published reports address the behavior of PRC-FRP flexural members (Takacs & Kanstad, 2002; Reed & Peterman, 2004; Hassan, 2002; Hassan & Rizkalla, 2002). Currently, ACI 440.2R-17 in its serviceability requirements states, "The serviceability of a member (deflections and crack widths) under service loads should satisfy applicable provisions of ACI 318. The effect of the FRP external reinforcement on the serviceability can be addressed using the transformed-section analysis." (ACI 440.2R, 2017). Similar to RC-FRP members, the ACI 440.2 recommends using effective moment of inertia method, Eq. 2-39, with consideration of the stiffness effects of the FRP in the cracked section. It also recommends avoiding inelastic deformations of PRC- FRP flexural members by preventing the prestressing steel from yielding at service load levels. This is achieved by limiting the stress at service levels in the prestressing steel to 82 percent of the its yield strength and 74 percent of its ultimate strength. Additionally, ACI 440.2R recommends the compressive stress be limited to 45 percent of the compressive strength of the concrete. These limits have been verified by Rosenboom & Rizkalla (2006) experimental research for PRC members with harped and straight strands strengthened externally bonded FRP. Rosenboom & Rizkalla (2006) examined 15 decommissioned 30-foot (9.14m)

PRC girders strengthened with various CFRP systems including NSM bars and strips and externally bonded sheets and strips. Eight PRC-FRP girders were statically loaded to failure. They found that the flexural capacity could be increased up to 72 percent without sacrificing the ductility of the original member. However, very limited work has been reported, if any, in the literature to predict accurate deflections of PRC beams strengthened with FRP up to failure.

The tri-linear moment-curvature response proposed by Charkas, Rasheed, & Melhem (2003) for RC beams strengthened with FRP, which was applied by Peterson and Rasheed (2007) for PRC beams without FRP is modified here and used for PRC members strengthened with external FRP. In this chapter, nonlinear sectional analysis, simplified by implementing a tri-linear moment-curvature response, is used to obtain closed form analytical deflection expressions for simply supported PRC rectangular and T-beams with bonded straight prestressing tendons strengthened with external FRP subjected to four-point bending, three-point bending and uniform loading conditions. Comparisons with experimental results as well as numerical results establish the accuracy of the presented analytical approach. The current deflection procedure offers a framework to examine the applicability of the state-of-the-art deflection expressions for use in the FRP strengthening applications. As such, this method shows high promise for establishing short-term deflection expressions that can be universally used in a variety of applications.

3.3 Analytical formulation

The nominal moment capacity of the strengthened partially PRC beam can be estimated using the non-linear behavior of constituent materials: concrete, non-prestressed steel, prestressed steel, and composite sheet/plate. In this model, the depth of neutral axis is computed

using the force equilibrium and strain compatibility. The iterative procedure provides the maximum moment that can be generated before the failure of one of the constituent materials. Compared to other methods, the full non-linear method has certain advantages. For example, the moment capacity of the strengthened beams can be obtained at various stages, such as when the non-prestressing steel yields. Neither the service load method nor the ultimate moment method is suitable to obtain this value because when the non-prestressed steel yields, the concrete is not generally in the linear elastic range and has not yet reached the ultimate usable strain of 0.003 to consider an ultimate condition.

The non-linear method is based on the assumptions of linear strain distribution, force equilibrium, and strain compatibility with actual stress-strain curves of concrete and reinforcements. The method allows for the prediction of the behavior through the entire range of loading including at cracking, yielding of prestressing steel, and ultimate. The corresponding curvatures and deflections at each load stage can also be computed.

A short-term deflection analysis procedure for straight tendons, bonded PRC-FRP beams is proposed herein. The derived procedure uses closed form and iterative equations to determine neutral axis locations, moments, and curvatures to define a tri-linear moment-curvature response. From the trilinear moment-curvature response, this procedure derives closed form deflection equations using the moment-area theorem. In deriving the equations, closed form analytical expressions are obtained for the pre-cracking, post-cracking, and post-yielding regions, shown in Figure 3-1.

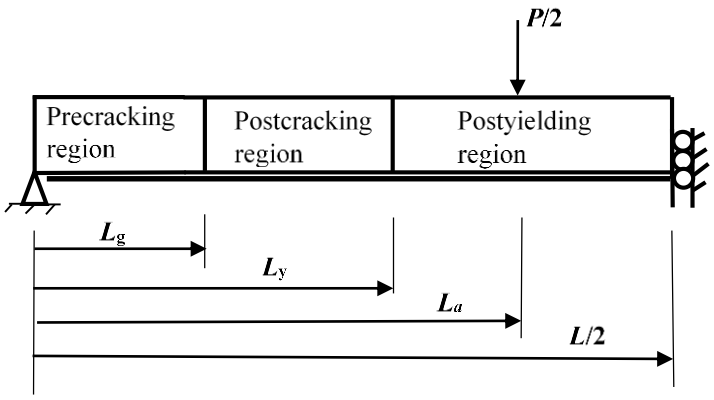

Figure 3-1: Profile of the half beam by symmetry showing the three distinct regions.

3.3.1 Assumptions

The following assumptions are made within the framework of the presented formulation:

1. Concrete in compression behaves linearly up to an extreme fiber stress of $0.7f_c$' then Hognestad's parabolic equation is used (Park and Pauley, 1975).
2. The equivalent rectangular stress block is used to replace the parabolic stress distribution at any stage of nonlinear analysis (Park and Pauley, 1975).
3. Reinforcing steel has the classical linear elastic-perfectly plastic response.
4. Unidirectional FRP laminates are used with fibers along the beam axis, which behave linearly up to brittle failure.
5. The section moment of inertia before cracking is the transformed gross value (I_g).
6. The section moment of inertia reduces to the fully cracked value (I_{cr}) upon steel yielding when the concrete response in compression is still linear (Ross et al, 1999). When the concrete response is non-linear, the section effective moment of inertia (I_e) reduces further and it is calculated from nonlinear analysis. This assumption is confirmed to be accurate by comparisons with experimental results.

7. The effective section moment of inertia at ultimate level is determined by $I_n = M_n / E_c\phi_n$ (Figure 3-2).
8. The section moment-curvature response is tri-linear (Figure 3-2). This model considers some tension stiffening effects – the effective section rigidity E_cI_e after cracking is gradually reduced from E_cI_g to E_cI_y where $I_y = M_y / E_c\phi_y$ (or E_cI_{cr} when linear analysis is applicable).
9. The curvature distribution along the beam span is obtained from the moment diagram and the moment-curvature relationship.
10. The external FRP plate/sheet extends along the entire clear span and stops just before the supports, when developing the closed form solutions. The small-unstrengthened region close to the supports is expected to add a negligible additional deflection.
11. The FRP plate/sheet is perfectly bonded to the beam that is expected to be accurate with proper transverse anchorages or thin laminates.
12. The prestressed strand yielding occurs at a strain of 0.010 and prestressing stand rupture occurs at a strain of 0.050 per *PCI Design Handbook* Section 11.2.5 (2017). The rupture strain is considered a conservative practical lower limit for strand rupture.
13. The prestressing reinforcement is straight since a single or double depressed reinforcement layout would alter the cross-sectional strand location along the member, which would require a tri-linear moment-curvature diagrams for each of the cross-sectional layouts along the member. This is studied in Chapter 5.
14. The prestressing reinforcement is fully bonded to the concrete.

15. The load-deflection response is determined up to the ultimate flexural strength. Strength equations developed by others can be used to predict premature failure loads and utilize the present load-deflection curve up to these premature failure load levels.

3.3.2 Moment-curvature relationship (sectional analysis)

An alternative to the effective moment of inertia approach of calculating RC member deflections is the integration of curvatures method (Ghali, 1993). Integration of curvatures involves calculating the curvature due to a given load at various points along a member and integrating the curvatures over the member's length to obtain the deflection at a desired location (Kassimali, 1995). The moment-curvature response is idealized as tri-linear with pre-cracking, post-cracking, and post-yielding regions as shown in Figure 3-2. The first region, pre-cracking, extends to the onset of flexural cracking. The second region, post-cracking, extends to first yield of the tension reinforcement (prestressing or mild reinforcement depending on location of reinforcement). The third region, post-yielding, extends until the limit of the useable concrete strain (0.003 in/in), FRP debonding according to the equations of ACI 440.2R-17, or the FRP rupture, depending on the flexural failure mode involved. Four key feature points completely define the moment-curvature response of the PRC-FRP flexural members: initial point ($M_a = 0$, ϕ_{in}), cracking point (M_{cr}, ϕ_{cr}), yielding point (M_y, ϕ_y), and ultimate point (M_n, ϕ_n).

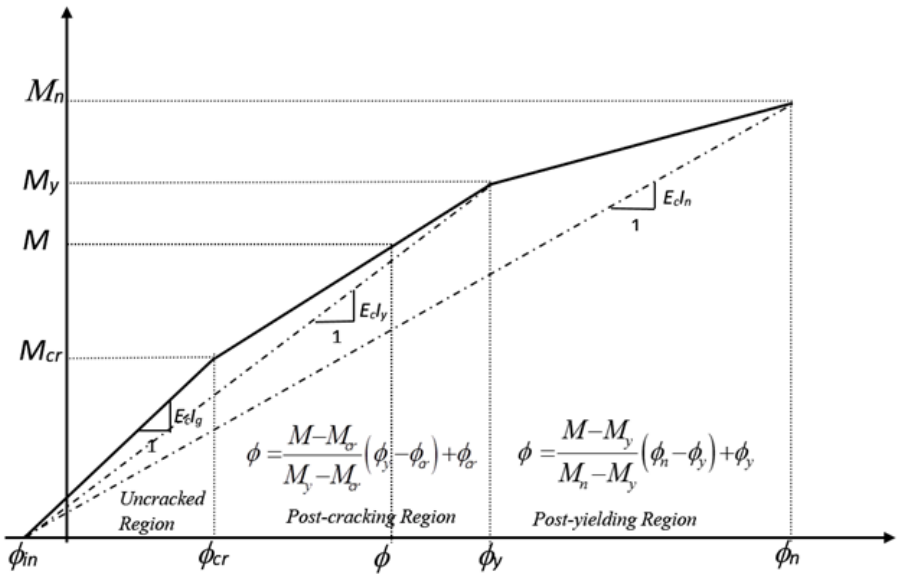

Figure 3-2: Trilinear moment-curvature behavior of PRC beams strengthened with FRP.

3.3.2.1 Initial point

The initial moment-curvature point ($M_a = 0$, ϕ_{in}) is a theoretical point in which the total externally applied moment is zero and the initial curvature is due to the prestressing after losses and neglecting self-weight defined as:

$$M_a = 0 \qquad \textbf{Eq. 3-8}$$

And

$$\phi_{in} = -\frac{P_e e}{E_c I_{gt}} \qquad \textbf{Eq. 3-9}$$

Negative sign indicates an upward deflection, camber.

3.3.2.2 Cracking point

The second point is the end of the linear-elastic response for the member; also, called the cracking moment-curvature point (M_{cr}, ϕ_{cr}) and is defined as:

$$M_{cr} = \frac{\left(f_r A_{gt} + P_e\right)\left(\frac{I_{gt}}{A_{gt}}\right)}{y_{bot}} + P_e e \qquad \textbf{Eq. 3-10}$$

and

$$\phi_{cr} = \frac{(M_{cr} - P_e e)}{E_c I_{gt}} \qquad \textbf{Eq. 3-11}$$

3.3.2.3 Yielding point

The third point, yielding point (M_y, ϕ_y), occurs as the prestressing steel reaches the yielding strain at one percent elongation with the neutral axis assumed within the concrete flange, which is accurate for almost all practical T-section dimensions. The yielding point is estimated first by assuming $I_y = I_{cr}$ with $\phi_y = \varepsilon_3 /(d_{ps} - c_y)$, where c_y is the depth of the section neutral axis at first yielding, and I_y is the effective section moment of inertia at yielding (Figure 3-3).

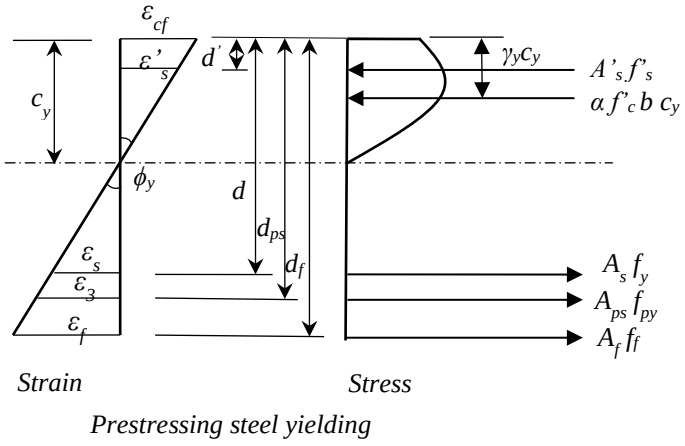

Figure 3-3: Section strain-compatibility relationships at prestressing steel yielding.

The yielding moment is equal to the modulus of elasticity of concrete times the cracked moment of inertia times the yielding curvature as shown.

$$M_y = E_c I_{cr} \phi_y, \qquad \varepsilon_{cf} = \phi_y c_y, \qquad \sigma_{cf} = E_c \varepsilon_{cf} \leq 0.7 f'_c \qquad \textbf{Eq. 3-12}$$

where: ε_{cf} is the compression strain of the extreme concrete fiber; and σ_{cf} is the corresponding stress within the linear limits based on assumption 1 in Section 3.3.1.

Using Eq. 3-12 produces very accurate estimates of the actual yielding point when the concrete behaves linearly. When the concrete response in compression is non-linear, Hognestad's classical parabolic stress-strain curve up to a concrete useable strain, ε_{cu}, equals 0.003 produces accurate estimates (Park and Paulay, 1975).

$$\sigma_c = f_c' \left[2\frac{\varepsilon_c}{\varepsilon_c'} - \left(\frac{\varepsilon_c}{\varepsilon_c'}\right)^2 \right] \quad \textbf{Eq. 3-13}$$

As shown in Figure 3-3, the concrete compressive force is expressed in terms of the parameter α that is used to convert the nonlinear stress-strain relationship into an equivalent rectangular distribution defined as:

$$\alpha = \frac{\int_0^{\varepsilon_{cf}} \sigma_c d\varepsilon_c}{f_c' \varepsilon_{cf}} = \frac{\varepsilon_{cf}}{\varepsilon_c'} - \frac{1}{3}\left(\frac{\varepsilon_{cf}}{\varepsilon_c'}\right)^2 \quad \textbf{Eq. 3-14}$$

Accordingly, the force equilibrium and strain compatibility of the section produces:

$$\sum F_x = 0 \Longrightarrow \alpha f_c' \, b c_y + A_s' f_s' = A_s f_y + A_{ps} f_{py} + A_f f_f \quad \textbf{Eq. 3-15}$$

where the stress in the compression steel is:

$$f_s' = E'_s \varepsilon_3 \left(\frac{c_y - d'}{d_{ps} - c_y} \right) \quad \textbf{Eq. 3-16}$$

with the strain in the prestressing strands due to additional loading equaling, ε_3, assuming prestressing strand yielding at 0.01 elongation:

$$\varepsilon_3 = 0.01 - \varepsilon_1 - \varepsilon_2 = 0.01 - \frac{f_{se}}{E_{ps}} - \frac{1}{E_c}\left[\frac{P_e}{A_{gt}} + \frac{P_e e^2}{I_{gt}}\right] \quad \textbf{Eq. 3-17}$$

and the stress in the FRP, considering the effect of initial deformations due to service loads during beam strengthening, is:

$$f_f = E_f\left[\varepsilon_3\left(\frac{d_f - c_y}{d_{ps} - c_y}\right) - \varepsilon_{bi}\right] \quad \textbf{Eq. 3-18}$$

In addition, as given in *PCI Design Handbook* (2017), the effective prestressing stress, f_{ps}, for 270 ksi (1862 MPa) strand is approximated by the following equation:

$$f_{ps} = 270 - \frac{0.04}{\left(\varepsilon_{ps} - 0.007\right)}(ksi) \; or \; f_{ps} = 1860 - \frac{0.276}{\left(\varepsilon_{ps} - 0.007\right)}\;(MPa) \quad \textbf{Eq. 3-19}$$

On the other hand, 250 ksi (1724 MPa) prestressing strands are more common in prestressed concrete structures built prior to 1970's, which have an effective prestressing stress, f_{ps}, approximated by the following equations:

$$f_{ps} = 250 - \frac{0.04}{\left(\varepsilon_{ps} - 0.0064\right)}(ksi) \; or \;\; f_{ps} = 1720 - \frac{0.276}{\left(\varepsilon_{ps} - 0.0064\right)}\;(MPa) \quad \textbf{Eq. 3-20}$$

The yielding stress varies with the strength of the prestressing used.

$$f_{py} = E_{ps}[\varepsilon_3 - \varepsilon_{bi}] \quad \textbf{Eq. 3-21}$$

Substituting Equations 3-16 through 3-18 and 3-21 into Equation 3-15 yields:

$$f_c' b c_y^2\left[1 - \frac{c_y \varepsilon_3}{3\left(d_{ps} - c_y\right)}\right]\frac{\varepsilon_3}{\varepsilon_c'} + A_s' E_s \varepsilon_3\left(c_y - d'\right) \quad \textbf{Eq. 3-22}$$

$$= A_s f_y\left(d_{ps} - c_y\right)$$

$$+ A_{ps} f_{py}\left(d_{ps} - c_y\right) + \; A_f E_f\left[\varepsilon_3\left(d_f - c_y\right) - \varepsilon_{bi}\left(d_{ps} - c_y\right)\right]$$

Equation 3-22 is solved directly for the neutral axis location at yield, c_y, which is adjusted based on nonlinear analysis.

The point of action of the concrete compressive force measured from the extreme compression fiber of concrete is written as a fraction of the neutral axis depth, $\gamma_y c_y$. The parameter γ_y is obtained from the following expression (Park and Pauley, 1975):

$$\gamma_y = 1 - \frac{\int_0^{\varepsilon_{cf}} \varepsilon_c \sigma_c d\varepsilon_c}{\varepsilon_{cf} \int_0^{\varepsilon_{cf}} f_c d\varepsilon_c} = \frac{\frac{1}{3} - \frac{\varepsilon_{cf}}{12\varepsilon_c'}}{1 - \frac{\varepsilon_{cf}}{3\varepsilon_c'}}$$ **Eq. 3-23**

The yielding point, (M_y, ϕ_y), is determined by summing the moments about the point of concrete compression resultant force as shown in Equations 3-24 and 3-25.

$$M_y = A_s f_y\left(d - \gamma_y c_y\right) + A_f E_f \left[\frac{\varepsilon_3\left(d_f - c_y\right)}{\left(d_{ps} - c_y\right)} - \varepsilon_{bi}\right]\left(d_f - \gamma_y c_y\right)$$ **Eq. 3-24**

$$+ A_{ps} f_{py}\left(d_{ps} - \gamma_y c_y\right) + A_s' E_s \left[\frac{\varepsilon_3\left(c_y - d'\right)}{\left(d_{ps} - c_y\right)}\right]\left(\gamma_y c_y - d'\right)$$

and

$$\phi_y = \frac{\varepsilon_3}{d_{ps} - c_y}$$ **Eq. 3-25**

Where $\gamma_y c_y$ is the depth of the resultant force of concrete in compression at first yielding measured from the extreme compression fiber.

3.3.2.4 Ultimate point

The fourth point, ultimate moment-curvature point, (M_n, ϕ_n) is determined based on the mode of failure (crushing of concrete or FRP rupture/FRP debonding). Refer to Figure 3-4 for the section stain-compatibility/force equilibrium relationships.

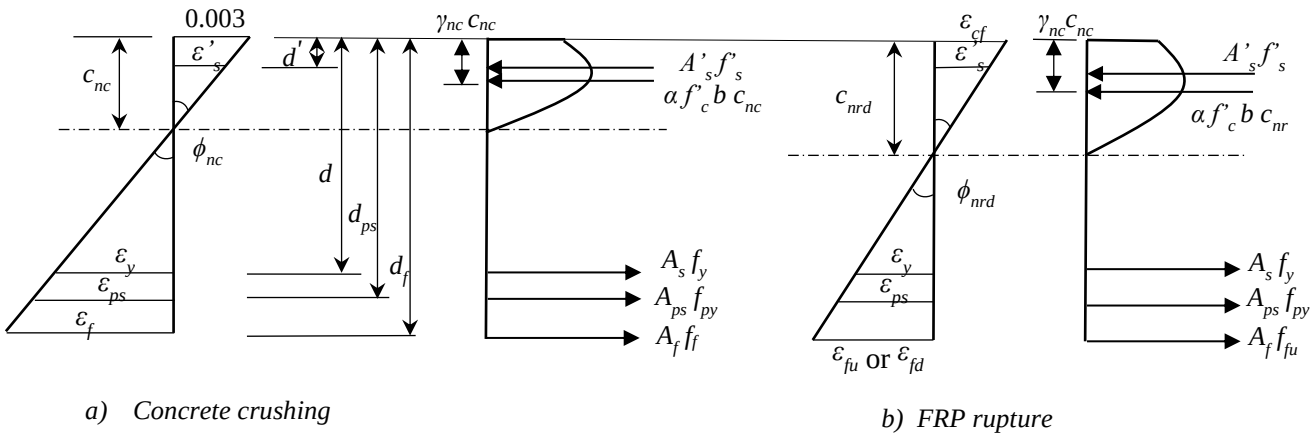

a) Concrete crushing *b) FRP rupture*

Figure 3-4: Section strain-compatibility relationships. a) Concrete crushing and b) FRP rupture/debonding

Applying the force equilibrium equation:

$$\sum F_x = 0 \Longrightarrow \alpha f_c' \, b c_n + A_s' f_s' = A_s f_y + A_{ps} f_{py} + A_f f_{fe} \qquad \textbf{Eq. 3-26}$$

In the case of crushing of the concrete, 0.003 is considered the ultimate concrete useful strain (Triantafillou & Plevris, 1991) (El-Mihilmy & Tedesco, 2000). Accordingly, the concrete compression block depth, c_{nc}, is iteratively obtained from the force equilibrium, Eq. 3-26, after substituting strain compatibility equations, Eq. 3-27 through Eq. 3-30, into it:

$$\varepsilon_{fe} = \left[\frac{0.003}{c_{nc}}\left(d_f - c_{nc}\right) - \varepsilon_{bi}\right] \qquad \textbf{Eq. 3-27}$$

$$\varepsilon_s' = \frac{0.003}{c_{nc}}\left(c_{nc} - d'\right) \qquad \textbf{Eq. 3-28}$$

$$\varepsilon_{ps} = \varepsilon_1 + \varepsilon_2 + \frac{0.003}{c_{nc}}\left(d_{ps} - c_{nc}\right) \qquad \textbf{Eq. 3-29}$$

$$f_{fe} = E_f \varepsilon_f, \quad f_s' = E_s \varepsilon_s' \leq f_y \qquad \textbf{Eq. 3-30}$$

Once the depth of the neutral axis, c_{nc}, is evaluated, M_n and ϕ_n are directly obtained with $\gamma_{cn} c_{nc}$ as the depth of the resultant of concrete in compression from the extreme compression fiber

at concrete crushing; and ψ_f is the external FRP strengthening reduction factor equal to 0.85. This factor is based on the reliability analysis of the experimentally calibrated statistical values that accounts for the less predictable failure mode of debonding of FRP reinforcement, for nominal flexure strength when designing (ACI 440.2R, 2017) (Okeil, Bingol & Alkhrdaji, 2007). When comparing the derived equation to the experimental results, ψ_f equals 1.0.

$$M_n = A_s f_y(d - \gamma_{nc} c_{nc}) + A_{ps} f_{py}\left(d_{ps} - \gamma_{nc} c_{nc}\right) + \psi_f A_f f_f\left(d_f - \gamma_{nc} c_{nc}\right) + A'_s f'_s(\gamma_{nc} c_{nc} - d') \quad \textbf{Eq. 3-31}$$

and

$$\phi_n = \phi_{nc} = \frac{0.003}{c_{nc}} \quad \textbf{Eq. 3-32}$$

If the failure mode is FRP rupture/debonding, the neutral axis depth is defined as c_{nrd} and the steel (mild and prestressing) and concrete stains are related to the FRP limit strain by using strain compatibility as:

$$\varepsilon_{cf} = \varepsilon_{fu}\left(\frac{c_{nrd}}{d_f - c_{nrd}}\right) \; or \; \varepsilon_{fd}\left(\frac{c_{nrd}}{d_f - c_{nrd}}\right) \quad \textbf{Eq. 3-33}$$

$$\varepsilon'_s = \varepsilon_{fu}\left(\frac{c_{nrd} - d'}{d_f - c_{nrd}}\right) \; or \; \varepsilon_{fd}\left(\frac{c_{nrd} - d'}{d_f - c_{nrd}}\right) \quad \textbf{Eq. 3-34}$$

$$\varepsilon_{ps} = \varepsilon_1 + \varepsilon_2 + \left[\left(\varepsilon_{fu} + \varepsilon_{bi}\right)\frac{\left(d_{ps} - c_{nrd}\right)}{\left(d_f - c_{nrd}\right)} \; or \left(\varepsilon_{fd} + \varepsilon_{bi}\right)\frac{\left(d_{ps} - c_{nrd}\right)}{\left(d_f - c_{nrd}\right)}\right] \quad \textbf{Eq. 3-35}$$

Once c_{nrd} is evaluated, M_n and ϕ_n are directly obtained.

$$M_n = A_s f_y(d - \gamma_{nrd} c_{nrd}) + A_{ps} f_{ps}\left(d_{ps} - \gamma_{nrd} c_{nrd}\right) + \psi_f A_f\left(f_{fu} \; or \; f_{fd}\right)\left(d_f - \gamma_{nrd} c_{nr}\right) + A'_s f'_s(\gamma_{nrd} c_{nrd} - d') \quad \textbf{Eq. 3-36}$$

and

$$\phi_n = \phi_{nrd} = \frac{\varepsilon_{fu} \ or \ \varepsilon_{fd}}{d_{fu} - c_{nrd}} \quad \textbf{Eq. 3-37}$$

3.3.3 Load-deflection response

The effective flexural rigidity of the section reduces with increased moment. The actual stiffness distribution is accounted for by dividing the beam into three distinct regions: pre-cracking, post-cracking, and post-yielding as shown in Figure 3-1 for four-point bending. The response is determined using the second moment-area theorem. The rigidity of the flexural member will vary along its length depending on its moment diagram. This presented formulation furnishes closed form expressions for midspan deflection of simple span beams under four-point bending, three-point bending or uniform loading.

The general solution can be obtained by adding the deflection contribution of the three regions.

$$\Delta_{mid} = \delta_1 + \delta_2 + \delta_3 = \int_0^{L_g} x\phi_{un}(x)\,dx + \int_{L_g}^{L_y} x\phi_{pc}(x)dx + \int_{L_y}^{\frac{L}{2}} x\phi_{py}(x)dx \quad \textbf{Eq. 3-38}$$

3.3.3.1 Four-point bending

3.3.3.1.1 Pre-cracking region – As shown in Figure 3-5a, the curvature distribution curve is the solid line connecting the initial curvature, ϕ_{in}, to the curvature, ϕ_a, corresponding to the moment M_a, and extends as a constant to the center of the beam. To simplify the deflection equations, a curvature triangle with a height of ($\phi_a - \phi_{in}$) and a base of L_a is added to the negative rectangle with a height of (ϕ_{in}) and a base of L_a. The curvature $\phi_{(x)}$ is assumed to extend across the beam. Thus, a single deflection equation that encompasses the entire uncracked scenario is provided. Additionally, the necessity to determine the zero-curvature moment and location from

the beam end is eliminated by distributing the curvature in this manner. Once the curvatures are found, the first region yields the classical uncracked (prismatic) beam problem, the midspan deflection equation is determined, in terms of curvatures, by:

$$\Delta_{mid} = \int_0^{\frac{L}{2}} x\phi_x dx = \int_0^{L_a} x\phi_x dx + \int_{L_a}^{\frac{L}{2}} x\phi_a dx \qquad \textbf{Eq. 3-39}$$

where

$$\phi_x = \phi_{in} + \frac{M(x)}{M_a}(\phi_a - \phi_{in}) \qquad \textbf{Eq. 3-40}$$

Substituting Eq. 3-40 into Eq. 3-39:

$$\Delta_{mid} = \int_0^{L_a} \phi_{in} x dx + \int_0^{L_a} x\frac{M(x)}{M_a}(\phi_a - \phi_{in})dx + \int_{L_a}^{\frac{L}{2}} x(\phi_a)dx \qquad \textbf{Eq. 3-41}$$

The deflection Eq. 3-41 is valid if $M_a \leq M_{cr}$ and the curvature corresponding to the maximum moment, ϕ_a, is equal to $(PL_a / 2E_cI_{gt}) + \phi_{in}$). If the beam is unloaded, $\phi_a = \phi_{in}$, the maximum initial camber is obtained as shown in Eq. 3-9.

The moment along the length of the shear span varies according to the relationship of the location in question and applied maximum moment. This relationship is shown in Eq. 3-42 Eq. 3-42 for four-point bending.

$$\frac{M(x)}{x} = \frac{M_a}{L_a} \Rightarrow M(x) = \frac{M_a}{L_a}x \qquad \textbf{Eq. 3-42}$$

In addition, for four-point bending with a total applied load equal to P, the applied load for half span, as shown in Figure 3-1, equals $P/2$. The ratio of the applied maximum moment, M_a, to location of applied load, L_a, equals the total load divided by 2 as shown in Eq. 3-43. Additionally, from the tri-linear moment curvature relationship of the ratio of the cracking moment to the cracking curvature minus the initial curvature due to prestressing that equals the flexural stiffness of the member as indicated in Eq. 3-44.

$$M_a = \frac{P}{2} L_a \Rightarrow \frac{P}{2} = \frac{M_a}{L_a} \quad \textbf{Eq. 3-43}$$

$$\frac{M_{cr}}{\phi_{cr} - \phi_{in}} = \frac{E_c I_{gt}}{1} \Longrightarrow M_{cr} = E_c I_{gt}(\phi_{cr} - \phi_{in}) \quad \textbf{Eq. 3-44}$$

Similarly, as shown in Figure 3-2 and from the tri-linear moment curvature relationship, the applied maximum moment to curvature relationship in the uncracked section is specified in Eq. 3-45.

$$\frac{M_a}{\phi_a - \phi_{in}} = \frac{E_c I_{gt}}{1} \Longrightarrow M_a = E_c I_{gt}(\phi_a - \phi_{in}) \quad \textbf{Eq. 3-45}$$

Substituting Eq. 3-42 into Eq. 3-41 and simplifying, pre-cracking deflection at midspan relationship, Eq. 3-46, is derived.

$$\Delta_{mid} = \int_0^{L_a} \phi_{in} x dx + \int_0^{L_a} \frac{x^2}{L_a}(\phi_a - \phi_{in})\, dx + \int_{L_a}^{L/2} x\,(\phi_a) dx \quad \textbf{Eq. 3-46}$$

$$= \phi_{in} \frac{x^2}{2}\Big|_0^{L_a} + \frac{x^3}{3L_a}(\phi_a - \phi_{in})\Big|_0^{L_a} + (\phi_a)\frac{x^2}{2}\Big|_{L_a}^{L/2}$$

$$= \phi_{in} \frac{L_a^2}{2} + \frac{L_a^2}{3}\,(\phi_a - \phi_{in}) + (\phi_a)\left(\frac{L^2}{8} - \frac{L_a^2}{2}\right)$$

For four-point bending and when load equals *P/2*, the first stage yields the classical uncracked prismatic, beam problem including the initial camber with midspan deflection of:

$$\Delta_{mid} = \frac{(\phi_a - \phi_{in})}{24}\left(3L^2 - 4{L_a}^2\right) + \frac{\phi_{in} L^2}{8} \quad \textbf{Eq. 3-47}$$

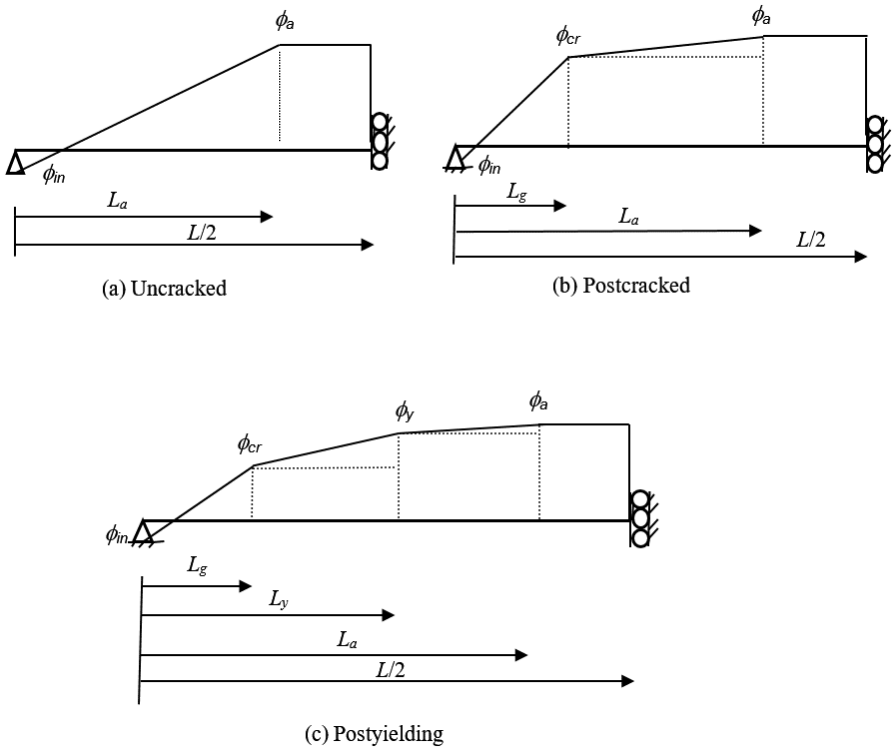

Figure 3-5: Curvature distribution for the (a) uncracked scenario, (b) post-cracked scenario, and (c) post-yielding scenario for four-point loading case.

3.3.3.1.2 Post-cracking region - Three curvature points, initial curvature, cracking curvature and yielding curvature, define the moment-curvature response along the post-cracking scenario for the member. As the curvature corresponding to the applied maximum moment, M_a, emerges into the post-cracking flexural stiffness region, Eq. 3-53 is used to determine ϕ_a. Consequently, M_y and ϕ_y, must be determined according to equations in Section 3.3.2.3 Additionally, in this stage of loading, L_g identifies the extent of the uncracked region (Eq. 3-48) as shown in Figure 3-5b and L_y identifies the extent of the unyielded region (Eq. 3-49).

$$L_g = \frac{2M_{cr}}{P} \qquad \textbf{Eq. 3-48}$$

$$L_y = \frac{2M_y}{P} \qquad \textbf{Eq. 3-49}$$

The solid line in Figure 3-5b represents the curvature distribution with the area under the curve divided into rectangles and triangles for moment area calculations. Furthermore, the curvature triangle with a height of (ϕ_{cr} - ϕ_{in}) and a base of L_g is added to the negative rectangle with a height of (ϕ_{in}) and a base of L_g, determined by Eq. 3-48. Integration of the remainder of the post-cracking region is directly applied. The moment-area theorem is used to obtain the midspan deflection by analytical integration of the moment of curvature distribution along half the span about the pinned location.

$$\Delta_{mid} = \int_0^{\frac{L}{2}} x\phi(x)dx = \int_0^{L_g} x\phi_{un}(x)dx + \int_{L_g}^{L_a} x\phi_{pc}(x)dx + \int_{L_a}^{L/2} x\phi_a(x)dx \qquad \textbf{Eq. 3-50}$$

Where the uncracked curvature, ϕ_{un}, is defined in Eq. 3-51 and the post-cracked to yield curvature, ϕ_{pc}, is defined in Eq. 3-52.

$$\phi_{un}(x) = \phi_{in} + \frac{M(x)}{M_{cr}}(\phi_{cr} - \phi_{in}) \qquad \textbf{Eq. 3-51}$$

$$\phi_{pc}(x) = \phi_{cr} + \frac{M(x) - M_{cr}}{M_y - M_{cr}}(\phi_y - \phi_{cr}) \qquad \textbf{Eq. 3-52}$$

And ϕ_a is calculated by linear interpolation between the cracking curvature and the yielding curvature shown in Figure 3-5b and Eq. 3-53.

$$\phi_a = \frac{(\phi_y - \phi_{cr})(M_a - M_{cr})}{(M_y - M_{cr})} + \phi_{cr} \qquad \textbf{Eq. 3-53}$$

Substituting the uncracked curvature and the post-cracked to yield curvature relationships into the midspan deflection equation,

Eq. 3-54 is determined.

$$\Delta_{mid} = \int_0^{L_g} x\left[\phi_{in} + \frac{M(x)}{M_{cr}}(\phi_{cr} - \phi_{in})\right]dx + \int_{L_g}^{L_a} x\left[\phi_{cr} + \frac{M(x) - M_{cr}}{M_y - M_{cr}}\left(\phi_y - \phi_{cr}\right)\right]dx + \int_{L_a}^{L/2} x\phi_a dx \qquad \textbf{Eq. 3-54}$$

Replacing the values for the moment, $M(x)$, applied maximum moment, M_a, and cracking moment, M_{cr}, relationships (Eq. 3-42, Eq. 3-43, and Eq. 3-48) into

Eq. 3-54 and simplifying,

Eq. 3-55 is originated.

$$\Delta_{mid} = \int_0^{L_g} x\phi_{in}dx + \int_0^{L_g} \frac{x^2}{L_g}(\phi_{cr} - \phi_{in})\,dx + \int_{L_g}^{L_a} x\phi_{cr}dx + \int_{L_g}^{L_a} \frac{x^2}{(L_y - L_g)}\left(\phi_y - \phi_{cr}\right)dx - \int_{L_g}^{L_a} x\frac{L_g}{L_y - L_g}\left(\phi_y - \phi_{cr}\right)dx + \int_{L_a}^{L/2} x\phi_a dx \qquad \textbf{Eq. 3-55}$$

Performing analytical integration of the moment of curvature distribution along half the span about the pinned location (

Eq. 3-55) and simplifying obtains

Eq. 3-56.

$$\Delta_{mid} = \phi_{in}\frac{x^2}{2}\Big]_0^{L_g} + (\phi_{cr} - \phi_{in})\frac{x^3}{3L_g}\Big]_0^{L_g} + \phi_{cr}\frac{x^2}{2}\Big]_{L_g}^{L_a}$$
$$+ (\phi_y - \phi_{cr})\frac{x^3}{3(L_y - L_g)}\Big]_{L_g}^{L_a} - (\phi_y - \phi_{cr})\frac{L_g}{L_y - L_g}\frac{x^2}{2}\Big]_{L_g}^{L_a}$$
$$+ \phi_a\frac{x^2}{2}\Big]_{L_a}^{L/2} \qquad \textbf{Eq. 3-56}$$

$$\Delta_{mid} = \phi_{in}\frac{{L_g}^2}{2} + (\phi_{cr} - \phi_{in})\frac{{L_g}^2}{3} + \phi_{cr}\left(\frac{{L_a}^2 - {L_g}^2}{2}\right)$$
$$+ (\phi_y - \phi_{cr})\frac{({L_a}^3 - {L_g}^3)}{3(L_y - L_g)}$$
$$- (\phi_y - \phi_{cr})\frac{L_g}{(L_y - L_g)}\frac{({L_a}^2 - {L_g}^2)}{2} + \phi_a\left(\frac{L^2}{8} - \frac{{L_a}^2}{2}\right) \qquad \textbf{Eq. 3-57}$$

Manipulating the applied curvature equation (Eq. 3-53) in the post-cracked region and exchanging the values of moments to load and length relationships (Eq. 3-43, Eq. 3-48, and Eq. 3-49), Eq. 3-58 is obtained.

$$(\phi_a - \phi_{cr}) = \frac{(L_a - L_g)}{(L_y - L_g)}(\phi_y - \phi_{cr}) \qquad \textbf{Eq. 3-58}$$

Plugging Eq. 3-58 into

Eq. 3-57 and manipulating, the midspan deflection for the post-cracked member is given by

Eq. 3-59.

$$\Delta_{mid} = \phi_{in}\frac{{L_g}^2}{2} + (\phi_{cr} - \phi_{in})\frac{{L_g}^2}{3} + \phi_{cr}\frac{{L_a}^2 - {L_g}^2}{2} + (\phi_a - \phi_{cr})\frac{\left(2{L_a}^2 - L_a L_g - {L_g}^2\right)}{6} + \phi_a\left(\frac{L^2}{8} - \frac{{L_a}^2}{2}\right) \quad \textbf{Eq. 3-59}$$

Grouping of terms in post-cracked midspan deflection

Eq. 3-59 and simplifying gives Eq. 3-60. As previously described, this is solved by finding the moment of the area under the curvature diagram in closed form using the triangular and rectangular areas shown in Figure 3-5b, resulting:

$$\Delta_{mid} = \frac{\phi_a}{24}(3L^2 - 4L_a^2) + \left(\frac{L_a + L_g}{6}\right)\left(\phi_{cr}L_a - \phi_a L_g\right) + \frac{L_g^2}{6}\phi_{in} \quad \textbf{Eq. 3-60}$$

This is valid when the applied moment, M_a, is less than or equal to the yield moment, M_y.

3.3.3.1.3 Post-yielding region

Figure 3-5c shows the post-yielding moment-curvature scenario applied to a member in four-point bending. Upon yielding of the tensile steel, sections in the post-yielding stage are assumed to be fully cracked. This assumption is verified to be accurate since the effective moment of inertia, I_e, of the section beyond yielding from nonlinear analysis considering tension stiffening is comparable to or less than that of I_{cr}. The midspan deflection at any load level after yielding is analytically formulated by determining the moment of the area under the curvature distribution. As with the post-cracked scenario, the curvature triangle with a height of ($\phi_{cr} - \phi_{in}$)

and a base of L_g is added to the negative rectangle with a height of (ϕ_{in}) and a base of L_g. In the post-yielding scenario, four curvatures (initial, cracking, yielding, and maximum) define the moment curvature response. In addition, the locations of the cracking moment and yielding moment need to be defined.

Putting the deflection at mid-span in terms of the curvatures and their locations, yields

Eq. 3-61.

$$\Delta_{mid} = \int_0^{\frac{L}{2}} x\phi(x)dx$$

$$= \int_0^{L_g} x\phi_{un}(x)dx + \int_{L_g}^{L_y} x\phi_{pc}(x)dx + \int_{L_y}^{L_a} x\phi_{py}(x)dx$$

$$+ \int_{L_a}^{L/2} x\phi_a(x)dx \qquad \textbf{Eq. 3-61}$$

Where the uncracked curvature, ϕ_{un}, is defined Eq. 3-51, the post-cracked-to-yield curvature, ϕ_{pc}, is defined in Eq. 3-52, and the post-yielded-to-nominal (ultimate) curvature, ϕ_{py}, is defined in Eq. 3-62.

$$\phi_{py} = \phi_y + \frac{M(x) - M_y}{M_n - M_y}(\phi_n - \phi_y) \qquad \textbf{Eq. 3-62}$$

And ϕ_a is calculated by linear interpolation between the yielding curvature and the ultimate curvature shown in Figure 3-5c and

Eq. 3-107.

$$\phi_a = \frac{(M_a - M_y)(\phi_n - \phi_y)}{(M_n - M_y)} + \phi_y$$ **Eq. 3-63**

Substituting the uncracked curvature, the post-cracked-to-yield curvature and the post-yield-to-ultimate curvature relationships into the midspan deflection equation,

Eq. 3-64 is determined.

$$\Delta_{mid} = \int_0^{L_g} x\left[\phi_{in} + \frac{M(x)}{M_{cr}}(\phi_{cr} - \phi_{in})\right]dx + \int_{L_g}^{L_y} x\left[\phi_{cr} + \frac{M(x) - M_{cr}}{M_y - M_{cr}}(\phi_y - \phi_{cr})\right]dx + \int_{L_y}^{L_a} x\left[\phi_y + \frac{M(x) - M_y}{M_n - M_y}(\phi_n - \phi_y)\right]dx + \int_{L_a}^{L/2} x[\phi_a]\,dx$$ **Eq. 3-64**

Substituting the moment equation (Eq. 3-42) and the applied curvature equation for post-yielding region (Eq. 3-63) into the post-yielding midspan deflection formula (

Eq. 3-64), then performing integration,

Eq. 3-65 is obtained for the midspan deflection.

$$\Delta_{mid} = \phi_{in}\frac{x^2}{2}\Big]_0^{L_g} + (\phi_{cr} - \phi_{in})\frac{x^3}{3L_g}\Big]_0^{L_g} + \phi_{cr}\frac{x^2}{2}\Big]_{L_g}^{L_y}$$

$$+ (\phi_y - \phi_{cr})\frac{x^3}{3(L_y - L_g)}\Big]_{L_g}^{L_y} - (\phi_y - \phi_{cr})\frac{x^2 L_g}{2(L_y - L_g)}\Big]_{L_g}^{L_y}$$

$$+ \phi_y\frac{x^2}{2}\Big]_{L_y}^{L_a} + (\phi_a - \phi_y)\frac{x^3}{3(L_a - L_y)}\Big]_{L_y}^{L_a}$$

$$- (\phi_a - \phi_y)\frac{x^2 L_y}{2(L_a - L_y)}\Big]_{L_y}^{L_a} + \phi_a\frac{x^2}{2}\Big]_{L_a}^{L/2} \qquad \textbf{Eq. 3-65}$$

Substituting the limits of integration and re-arranging the terms, the post-yielding midspan deflection equation becomes

Eq. 3-66.

$$\Delta_{mid} = \phi_{in}\frac{{L_g}^2}{2} + (\phi_{cr} - \phi_{in})\frac{{L_g}^2}{3} + \phi_{cr}\left(\frac{{L_y}^2 - {L_g}^2}{2}\right)$$
$$+ (\phi_y - \phi_{cr})\left(\frac{{L_y}^3 - {L_g}^3}{3(L_y - L_g)}\right) - (\phi_y - \phi_{cr})\left(\frac{{L_y}^2 - {L_g}^2}{2(L_y - L_g)}\right)L_g$$
$$+ \phi_y\left(\frac{{L_a}^2 - {L_y}^2}{2}\right) + (\phi_a - \phi_y)\left(\frac{{L_a}^3 - {L_y}^3}{3(L_a - L_y)}\right)$$
$$- (\phi_a - \phi_y)\left(\frac{{L_a}^2 - {L_y}^2}{2(L_a - L_y)}\right)L_y + \phi_a\left(\frac{\left({}^{L}/_{2}\right)^2 - {L_a}^2}{2}\right) \quad \textbf{Eq. 3-66}$$

Additional elimination of terms finds

Eq. 3-67 for the post-yielding midspan deflection.

$$\Delta_{mid} = \phi_{in}\frac{{L_g}^2}{6} + \phi_{cr}\frac{{L_g}^2}{3} + \phi_{cr}\left(\frac{{L_y}^2 - {L_g}^2}{2}\right)$$
$$+ \left(\phi_y - \phi_{cr}\right)\left(\frac{{L_y}^2 + L_y L_g + {L_g}^2}{3}\right)$$
$$- \left(\phi_y - \phi_{cr}\right)\left(\frac{L_y + L_g}{2}\right)L_g + \phi_y\left(\frac{{L_a}^2 - {L_y}^2}{2}\right)$$
$$+ \left(\phi_a - \phi_y\right)\left(\frac{{L_a}^2 + L_a L_y + {L_y}^2}{3}\right) - \left(\phi_a - \phi_y\right)\left(\frac{L_a + L_y}{2}\right)L_y$$
$$+ \phi_a\left(\frac{L^2}{8} - \frac{{L_a}^2}{2}\right) \qquad \textbf{Eq. 3-67}$$

Abridging and merging terms gives the final midspan post-yielding deflection equation,

Eq. 3-68.

$$\Delta_{mid} = \frac{\phi_a}{24}\left(3L^2 - 4{L_a}^2\right) + \frac{\phi_{cr}L_y - \phi_y L_g}{6}\left(L_y + L_g\right)$$
$$+ \frac{\phi_y L_a - \phi_a L_y}{6}\left(L_a + L_y\right) + \frac{\phi_{in}{L_g}^2}{6} \qquad \textbf{Eq. 3-68}$$

3.3.3.2 Uniform loading

While the four-point bending condition provides a simple loading case to do a deflection analysis, the use of four-point bending is typically limited to laboratory tests. A more common loading case is a uniform loading case, which is also a symmetric loading case. The uniform loading case is characterized by a load, *w*, distributed evenly across the member. Moment-area theorem may be used to determine the deflection at mid-span. Since the load is distributed across the entire beam evenly, the moment distribution is not linear. Therefore, when the tri-linear moment-curvature relationship is applied to a member, the curvature distribution is not

linear in each region. Figure 3-6 shows the curvature distribution for a uniform loading condition.

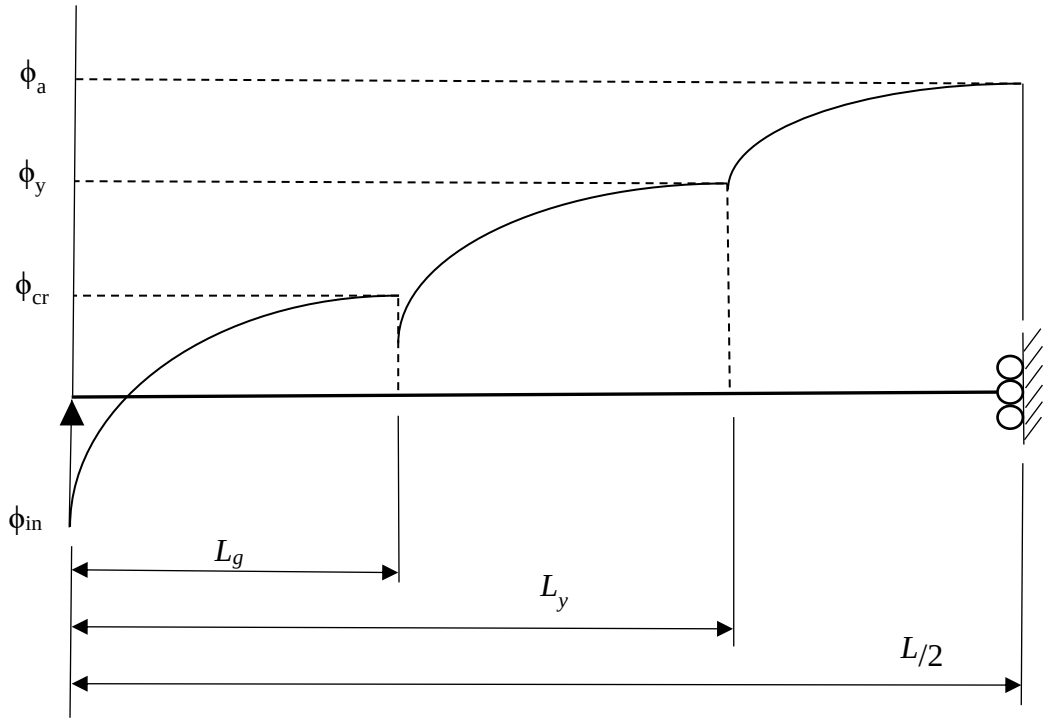

Figure 3-6: Curvature distribution for uniform loading condition.

As the curvature distribution is nonlinear in the regions, the summation of the moment of areas under the curve with respect to the support of the member requires integration. Since the curvature distributions vary from region-to-region it is necessary to integrate each region individually, shown by Equation 3-38 and repeated here.

$$\Delta_{mid} = \delta_1 + \delta_2 + \delta_3 = \int_0^{L_g} x\phi_{un}(x)dx + \int_{L_g}^{L_y} x\phi_{pc}(x)dx + \int_{L_y}^{L/2} x\phi_{py}(x)dx \qquad \textbf{Eq.} \text{ 3-38}$$

The moment along the beam is:

$$M = \frac{wL}{2}x - \frac{wx^2}{2} \qquad \textbf{Eq. 3-69}$$

From Eq. 3-69, the locations of the cracking moment, and yielding moment are determined.

3.3.3.2.1 Contribution of pre-cracking region

If M_{cr} and L_g are substituted into Eq. 3-69 Eq. 3-81for M and x respectively, and L_g is solved for, it yields Eq. 3-72:

$$M_{cr} = \frac{wL}{2}L_g - \frac{wL_g^2}{2} \quad \textbf{Eq. 3-70}$$

$$L_g^2 - LL_g + \frac{2M_{cr}}{w} = 0 \quad \textbf{Eq. 3-71}$$

$$L_g = \frac{L - \sqrt{L^2 - 4(1)\left(\frac{2M_{cr}}{w}\right)}}{2(1)} = \frac{L}{2} - \frac{L}{2}\sqrt{1 - \frac{8M_{cr}}{wL^2}} \quad \textbf{Eq. 3-72}$$

With the location of the cracking moment determined, deflection contribution of the uncracked region is determined. If Eq. 3-72 and Eq. 3-69 are substituted into the first term of

Eq. 3-38 and analytically integrated; Eq. 3-73 is derived.

$$\delta_1 = \int_0^{L_g} x\phi_{un}(x)dx = \int_0^{L_g} x\left(\frac{M(\phi_{cr} - \phi_{in})}{M_{cr}} + \phi_{in}\right)dx \quad \textbf{Eq. 3-73}$$

Plugging the moment along the beam equation, Eq. 3-69, and simplifying,

Eq. 3-74 is found.

$$\delta_1 = \int_0^{L_g} x\left(\left(\frac{wLx}{2M_{cr}} - \frac{wx^2}{2M_{cr}}\right)(\phi_{cr} - \phi_{in}) + \phi_{in}\right)dx$$

$$\delta_1 = \int_0^{L_g} \left(\left(\frac{wLx^2}{2M_{cr}} - \frac{wx^3}{2M_{cr}}\right)(\phi_{cr} - \phi_{in}) + \phi_{in}x\right)dx \quad \textbf{Eq. 3-74}$$

Performing integration and combining terms, the uncracked midspan deflection contribution for a uniformly loaded member is obtained,

Eq. 3-75.

$$\delta_1 = \left(\frac{wLx^3(\phi_{cr} - \phi_{in})}{6M_{cr}} - \frac{wx^4(\phi_{cr} - \phi_{in})}{8M_{cr}}\right) + \frac{\phi_{in}x^2}{2}\Bigg|_0^{L_g}$$

$$= \frac{wLL_g^3(\phi_{cr} - \phi_{in})}{6M_{cr}} - \frac{wL_g^4(\phi_{cr} - \phi_{in})}{8M_{cr}} + \frac{\phi_{in}L_g^2}{2}$$

$$\delta_1 = \frac{wL_g^3(\phi_{cr} - \phi_{in})}{2M_{cr}}\left(\frac{L}{3} - \frac{L_g}{4}\right) + \frac{\phi_{in}L_g^2}{2} \qquad \textbf{Eq. 3-75}$$

If the member has not cracked, *L*/2 may be substituted for L_g in

Eq. 3-75 to determine the deflection due to the cracking moment that occurs when *L*/2 equals L_g. This simplifies to

Eq. 3-76 and camber is indicated as negative.

$$\delta_1 = \frac{w\left(L/2\right)^3(\phi_{cr} - \phi_{in})}{2M_{cr}}\left(\frac{L}{3} - \frac{L/2}{4}\right) + \frac{\phi_{in}\left(L/2\right)^2}{2}$$

$$= \frac{5wL^4(\phi_{cr} - \phi_{in})}{384M_{cr}} + \frac{\phi_{in}L^2}{8}$$

Eq. 3-76

$$\delta_1 = \frac{5wL^4}{384E_cI_{gt}} - \frac{P_e e L^2}{8E_cI_{gt}}$$

3.3.3.2.2 Post-cracking region

As with the cracking point, the yielding moment location is determined from Eq. 3-77. If the terms M_y and L_y are inserted for M and x respectively into Eq. 3-69, the location where the first yield occurs along the length of the member, L_y, is determined by

Eq. 3-78.

$$M_y = \frac{wL}{2} L_y - \frac{wL_y^2}{2} \qquad \textbf{Eq. 3-77}$$

$$L_y = \frac{L}{2} - \frac{L}{2}\sqrt{1 - \frac{8M_y}{wL^2}} \qquad \textbf{Eq. 3-78}$$

In addition to determining the location of the first yielding point, the post-cracking flexural stiffness region in the curvature distribution is determined using Eq. 3-53. The deflection contribution for the post-cracked flexural stiffness region represented by

Eq. 3-79 is derived by substituting Eq. 3-69 and Eq. 3-53 into the second term of

Eq. 3-38 and simplifying.

$$\delta_2 = \int_{L_g}^{L_y} x\,\phi_{pc}(x)dx = \int_{L_g}^{L_y} x\left(\frac{(M - M_{cr})(\phi_y - \phi_{cr})}{(M_y - M_{cr})} + \phi_{cr}\right)dx$$

$$= \int_{L_g}^{L_y} x\left(\frac{(\phi_y - \phi_{cr})}{(M_y - M_{cr})}\left(\frac{wL}{2}x - \frac{wx^2}{2} - M_{cr}\right) + \phi_{cr}\right)dx$$

Eq. 3-79

$$\delta_2 = \int_{L_g}^{L_y} \left(\frac{(\phi_y - \phi_{cr})}{(M_y - M_{cr})} \left(\frac{wLx^2}{2} - \frac{wx^3}{2} - M_{cr}x \right) + \phi_{cr}x \right) dx$$

Performing integration and combining terms gives

Eq. 3-80 for the midspan deflection contribution of the post-cracked region of the beam loaded uniformly.

$$\delta_2 = \frac{(\phi_y - \phi_{cr})}{(M_y - M_{cr})} \left(\frac{wLx^3}{6} - \frac{wx^4}{8} - \frac{M_{cr}x^2}{2} \right) + \frac{\phi_{cr}x^2}{2} \Bigg|_{L_g}^{L_y}$$

$$= \frac{(\phi_y - \phi_{cr})}{(M_y - M_{cr})} \left(\frac{wL}{6}(L_y^3 - L_g^3) - \frac{w}{8}(L_y^4 - L_g^4) - \frac{M_{cr}}{2}(L_y^2 - L_g^2) \right)$$

$$+ \frac{\phi_{cr}}{2}(L_y^2 - L_g^2)$$

$$= \frac{(\phi_y - \phi_{cr})}{(M_y - M_{cr})} \left(\frac{wL}{6}(L_y^3 - L_g^3) - \frac{w}{8}(L_y^4 - L_g^4) - \frac{M_{cr}}{2}(L_y^2 - L_g^2) \right)$$

$$+ \frac{\phi_{cr}}{2}(L_y^2 - L_g^2) \qquad \textbf{Eq. 3-80}$$

Replace M_y and M_{cr} for Eq. 3-70 and Eq. 3-77, respectively and combining terms yields:

$$\delta_2 = \frac{(\phi_y - \phi_{cr})}{12} \frac{(L_g - L_y)\left(2L(L_g + 2L_y) - 3(L_g + L_y)^2\right)}{(L_g + L_y - L)} + \frac{\phi_{cr}}{2}(L_y^2 - L_g^2) \qquad \textbf{Eq. 3-81}$$

For the post-yielding flexural stiffness region, the curvature distribution is determined by Eq. 3-63. The location of the M_u occurs at $L/2$ due to the symmetric loading condition and simply supported end condition. Hence, if the member has not reached the post-yielding flexural stiffness region the contribution of the post-cracked flexural stiffness region is determined by substituting $L/2$ for L_y in

Eq. 3-81 to yield:

$$\delta_2 = \frac{(\phi_y - \phi_{cr})}{(M_y - M_{cr})}\left(\frac{5wL^3}{384} + \frac{M_{cr}}{2}\left(L_g^2 - \frac{L^2}{4}\right) - \frac{wL_g^3}{2}\left(\frac{L}{3} - \frac{L_g}{4}\right)\right)$$

$$+ \frac{\phi_{cr}}{2}\left(\frac{L^2}{4} - L_g^2\right) \qquad \textbf{Eq. 3-82}$$

Combining

Eq. 3-75 and

Eq. 3-82 gives the total midspan deflection in the post-cracked region for a uniformly loaded beam.

$$\Delta_{mid} = \frac{wL_g^3(\phi_{cr} - \phi_{in})}{2M_{cr}}\left(\frac{L}{3} - \frac{L_g}{4}\right) + \frac{\phi_{in}L_g^2}{2}$$

$$+ \frac{(\phi_y - \phi_{cr})}{(M_y - M_{cr})}\left(\frac{5wL^3}{384} + \frac{M_{cr}}{2}\left(L_g^2 - \frac{L^2}{4}\right) - \frac{wL_g^3}{2}\left(\frac{L}{3} - \frac{L_g}{4}\right)\right)$$

$$+ \frac{\phi_{cr}}{2}\left(\frac{L^2}{4} - L_g^2\right) \qquad \textbf{Eq. 3-83}$$

3.3.3.2.3 Post-yielding region

For the post-yielding flexural stiffness region, the curvature distribution is determined by Eq. 3-104. The location of the M_a is at $L/2$ due to the symmetric loading condition and simply supported end condition. When the post-yielding region is involved, the member has three flexural stiffness zones to consider when determining the total deflection: uncracked, post-cracking, and post-yielding represented by δ_1, δ_2, and δ_3 respectively.

Eq. 3-38 gives the total deflection of a member that has yielded. To determine the contribution of the post-yielded flexural stiffness region, Eq. 3-69 and Eq. 3-62 are substituted into the third term of Equation 3-38 resulting in

Eq. 3-84.

$$\delta_3 = \int_{L_y}^{L/2} x\,\phi_{py}(x)dx$$

$$= \int_{L_g}^{L_y} \left(\frac{(\phi_n - \phi_y)}{(M_n - M_y)} \left(\frac{wLx^2}{2} - \frac{wx^3}{2} - M_y x \right) + \phi_y x \right) dx \qquad \textbf{Eq. 3-84}$$

Integrating and combining terms results in

Eq. 3-85 for the deflection corresponding to the post-yielding region.

$$\delta_3 = \frac{(\phi_n - \phi_y)}{(M_n - M_y)}\left(\frac{wLx^3}{6} - \frac{wx^4}{8} - \frac{M_y x^2}{2}\right) + \frac{\phi_y x^2}{2}\Bigg|_{L_y}^{L/2}$$

$$= \frac{(\phi_n - \phi_y)}{(M_n - M_y)}\left(\frac{wL}{6}\left(\left(L/2\right)^3 - L_y^3\right) - \frac{w}{8}\left(\left(L/2\right)^4 - L_y^4\right)\right.$$

$$\left. - \frac{M_y}{2}\left(\left(L/2\right)^2 - L_y^2\right)\right) + \frac{\phi_y}{2}\left(\left(L/2\right)^2 - L_y^2\right)$$

$$= \frac{(\phi_n - \phi_y)}{(M_n - M_y)}\left(\frac{wL^4}{48} - \frac{wLL_y^3}{6} - \frac{wL^4}{128} + \frac{wL_y^4}{8} - \frac{M_y L^2}{8} + \frac{M_y L_y^2}{2}\right)$$

$$+ \frac{\phi_y}{2}\left(\frac{L^2}{4} - L_y^2\right)$$

$$\delta_3 = \frac{(\phi_n - \phi_y)}{(M_n - M_y)}\left(\frac{5wL^4}{384} + \frac{M_y}{2}\left(L_y^2 - \frac{L^2}{4}\right) - \frac{wL_y^3}{2}\left(\frac{L}{3} - \frac{L_y}{4}\right)\right)$$

$$+ \frac{\phi_y}{2}\left(\frac{L^2}{4} - L_y^2\right) \qquad \textbf{Eq. 3-85}$$

The deflection at mid-span of a beam having a post-yielding region is determined by inserting

Eq. 3-76,

Eq. 3-81, and

Eq. 3-85 into

Eq. 3-38 for the first thru third terms, respectively.

3.3.3.3 Three-point bending

The three-point bending case is another common loading case. Similar to the other loading conditions, the effective flexural rigidity of the section reduces with increased moment. The actual stiffness distribution is accounted for by dividing the beam into three distinct regions: pre-cracking, post-cracking, and post-yielding as shown in Figure 3-7 for three-point bending. The response is determined using the second moment-area theorems. The rigidity of the flexural member will vary along its length depending on its moment diagram. This presented formulation furnishes closed form expressions for midspan deflection of simple span beams under three-point bending.

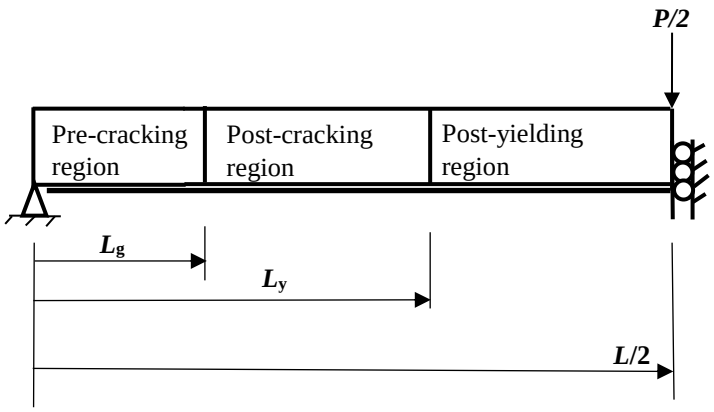

Figure 3-7: Profile of the half beam by symmetry showing the three distinct regions loaded in three-point bending.

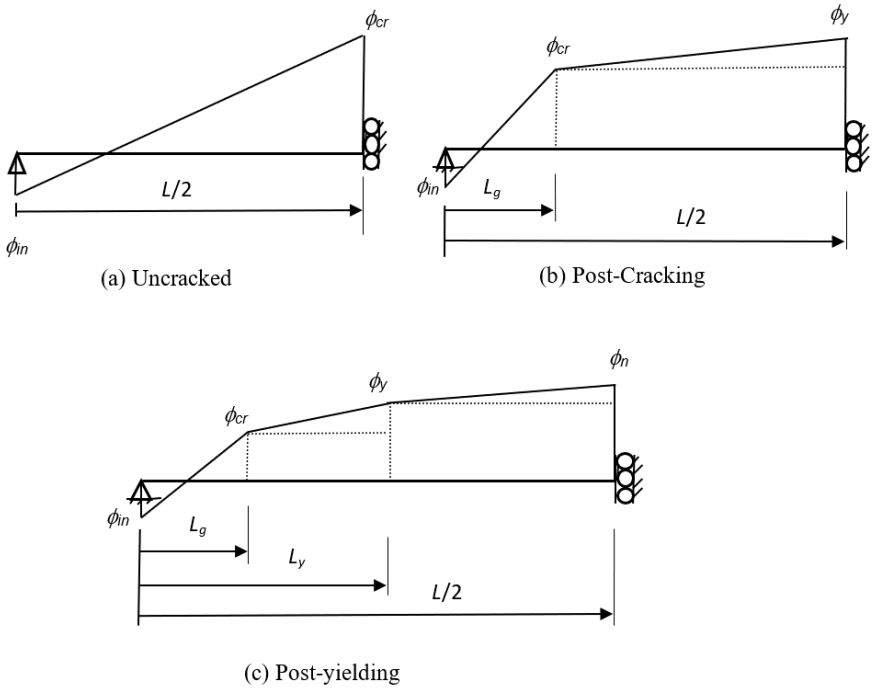

Figure 3-8: Curvature distribution for the (a) uncracked scenario, (b) post-cracked scenario, and (c) post-yielding scenario for three-point bending case.

3.3.3.1.1 Pre-cracking region – As shown in Figures 3-2 and 3-8a, the curvature distribution curve is the solid line connecting the initial curvature, ϕ_{in}, to the curvature, ϕ_{un}, corresponding to the moment *M*, and extends to the center of the beam. Similar to the previous

loading condition derivations, to simplify the deflection equations, a triangular curvature distribution with a base of $L/2$ and a height of $(\phi_{in} - \phi_{un})$ is assumed. The curvature ϕ_{un} is a variable extending across the beam. Thus, a single deflection equation that encompasses the entire uncracked scenario is provided.

$$\Delta_{mid} = \delta_1 = \int_0^{\frac{L}{2}} x\phi_x dx = \int_0^{\frac{L}{2}} x\phi_{un}(x)dx \qquad \textbf{Eq. 3-86}$$

Where

$$\phi_{un} = \phi_{in} + \frac{M(x)}{M_{cr}}(\phi_{cr} - \phi_{in}) \qquad \textbf{Eq. 3-87}$$

Substituting the uncracked curvature equation, Eq. 3-87, into the midspan deflection equation, Eq. 3-86, Eq. 3-88 is obtained.

$$\Delta_{mid} = \int_0^{\frac{L}{2}} \phi_{in} x dx + \int_0^{\frac{L}{2}} x \frac{M(x)}{M_{cr}}(\phi_{cr} - \phi_{in})\, dx \qquad \textbf{Eq. 3-88}$$

In addition, for the three-point bending, the total applied load is equal to P applied at the span midpoint, which is twice that shown in Figure 3-7 due to symmetry. The moment along the beam is equal to half the total load times the distance from the support to the designated section, as indicated in Eq. 3-89.

$$M(x) = \frac{P}{2}x \qquad \textbf{Eq. 3-89}$$

Replacing the moment, $M(x)$, in Eq. 3-88 with the load relationship shown in Eq. 3-89, Eq. 3-90 gives the midspan deflection equation of the uncracked beam.

$$\Delta_{mid} = \int_0^{\frac{L}{2}} \phi_{in} x dx + \int_0^{\frac{L}{2}} \frac{Px^2}{2M_{cr}}(\phi_{cr} - \phi_{in})\, dx \qquad \textbf{Eq. 3-90}$$

Integrating and simplifying gives

Eq. 3-91.

$$\Delta_{mid} = \frac{x^2}{2}\,\phi_{in} + \frac{Px^3}{6M_{cr}}(\phi_{cr} - \phi_{in})\Big]_0^{\frac{L}{2}} = \frac{L^2}{8}\,\phi_{in} + \frac{PL^3}{48M_{cr}}(\phi_{cr} - \phi_{in}) \qquad \textbf{Eq. 3-91}$$

Using the tri-linear moment curvature relationship of the ratio of the cracking moment to the cracking curvature minus the initial curvature contribution due to prestressing that equals the flexural stiffness of the member as indicated in Eq. 3-44, the uncracked deflection equation for three-point bending is equal to:

$$\Delta_{mid} = \frac{PL^3}{48E_cI_{gt}} + \frac{L^2}{8}\phi_{in} \qquad \textbf{Eq. 3-92}$$

If the cracking moment occurs within the shear span at L_g, then the uncracked section deflection, δ_1, is equal to

Eq. 3-93.

$$\delta_1 = \frac{PL_g{}^3}{48E_cI_{gt}} + \frac{L_g{}^2}{8}\phi_{in} \qquad \textbf{Eq. 3-93}$$

3.3.3.3.2 Post-cracking region – Three curvature points, ϕ_{in}, ϕ_{cr}, and ϕ_a, define the moment-curvature response along the post-cracking scenario for the member. Refer to Figure 3-2 and Figure 3-8b. As the curvature corresponding to the applied moment, $M(x)$, emerges into the post-cracking flexural stiffness region, Eq. 3-51and Eq. 3-52 are used to determine ϕ_{un} and ϕ_{pc}, respectively. Consequently, M_y and ϕ_y, must be determined according to equations in Section 3.3.2.3. Additionally, in this stage of loading, L_g identifies the extent of the uncracked region (Eq. 3-48).

The solid line in Figure 3-8b represents the curvature distribution with the area under the curve divided into triangles and rectangles. Furthermore, the curvature is assumed to have a height of (ϕ_{cr} - ϕ_{in}) with the base of the triangle equal to L_g. Similar to the previous derivations, a rectangular negative curvature area is added with a height of ϕ_{in} and a base of L_g. A positive curvature area is added in the post-cracked region – where the curvature ϕ_{cr} extends across the

length of that region and a triangular positive area is added between L_g and $L/2$; refer to Figure 3-8b. The moment-area theorem is used to obtain the midspan deflection by analytical integration of the moment of curvature distribution along half the span about the pinned location.

$$\Delta_{mid} = \int_0^{\frac{L}{2}} x\phi(x)dx = \delta_1 + \delta_2 = \int_0^{L_g} x\phi_{un}(x)dx + \int_{L_g}^{L/2} x\phi_{pc}(x)dx \qquad \textbf{Eq. 3-94}$$

Solving for the pre-cracking and post-cracking terms by substituting uncracked curvature, ϕ_{un}, relationship (Eq. 3-53) and the post-cracking-to-yielding curvature, ϕ_{pc}, relationship (Eq. 3-52) into the midspan deflection equation,

Eq. 3-94,

Eq. 3-95is determined.

$$\Delta_{mid} = \int_0^{L_g} \phi_{in} x dx + \int_0^{L_g} x \frac{M(x)}{M_{cr}} (\phi_{cr} - \phi_{in})\, dx$$

$$+ \int_{L_g}^{\frac{L}{2}} x \left[\phi_{cr} + \frac{M(x) - M_{cr}}{M_y - M_{cr}} (\phi_y - \phi_{cr}) \right] dx \qquad \textbf{Eq. 3-95}$$

Replacing the values for the moment, $M(x)$, applied maximum moment, M_a, and cracking moment, M_{cr}, relationships (Eq. 3-89, Eq. 3-48 and Eq. 3-49) in

Eq. 3-95 and simplifying,

Eq. 3-96 is originated.

$$\Delta_{mid} = \int_0^{L_g} \phi_{in} x dx + \int_0^{L_g} \frac{x^2}{L_g} (\phi_{cr} - \phi_{in})\, dx + \int_{L_g}^{\frac{L}{2}} x \left[\phi_{cr} + \frac{x - L_g}{L_y - L_g} (\phi_y - \phi_{cr}) \right] dx \quad \textbf{Eq. 3-96}$$

Performing analytical integration of the moment of curvature distribution along half the span of about the hinge location (

Eq. 3-96) and simplifying obtains

Eq. 3-97.

$$\Delta_{mid} = \phi_{in} \frac{x^2}{2}\Big]_0^{L_g} + (\phi_{cr} - \phi_{in}) \frac{x^3}{3L_g}\Big]_0^{L_g} + \phi_{cr} \frac{x^2}{2}\Big]_{L_g}^{\frac{L}{2}} + (\phi_y - \phi_{cr}) \frac{x^3}{3(L_y - L_g)}\Big]_{L_g}^{\frac{L}{2}} - (\phi_y - \phi_{cr}) \left(\frac{L_g}{L_y - L_g} \right) \frac{x^2}{2}\Big]_{L_g}^{\frac{L}{2}} \quad \textbf{Eq. 3-97}$$

$$\Delta_{mid} = \phi_{in}\frac{{L_g}^2}{2} + (\phi_{cr} - \phi_{in})\frac{{L_g}^2}{3} + \phi_{cr}\left(\frac{L^2}{8} - \frac{{L_g}^2}{2}\right)$$

$$+ (\phi_y - \phi_{cr})\frac{\left(\left(\frac{L}{2}\right)^3 - L_g^3\right)}{3(L_y - L_g)}$$

$$- (\phi_y - \phi_{cr})\frac{L_g}{(L_y - L_g)}\frac{\left(\left(\frac{L}{2}\right)^2 - L_g^2\right)}{2} \qquad \textbf{Eq. 3-98}$$

Manipulating the applied curvature equation (Eq. 3-53) in the post-cracked region and exchanging the values of moments to load and length relationships (Eq. 3-43, Eq. 3-48, and Eq. 3-49), Eq. 3-99 is obtained.

$$(\phi_a - \phi_{cr}) = \frac{(L/2 - L_g)}{(L_y - L_g)}(\phi_y - \phi_{cr}) \qquad \textbf{Eq. 3-99}$$

Plugging Eq. 3-99 into

Eq. 3-98 and manipulating, the midspan deflection for the post-cracked member is given by

Eq. 3-100.

$$\Delta_{mid} = \phi_{in}\frac{{L_g}^2}{2} + (\phi_{cr} - \phi_{in})\frac{{L_g}^2}{3} + \phi_{cr}\frac{(\frac{L}{2})^2 - {L_g}^2}{2}$$

$$+ (\phi_a - \phi_{cr})\frac{\left(2(\frac{L}{2})^2 - L/2L_g - {L_g}^2\right)}{6} \qquad \textbf{Eq. 3-100}$$

Grouping of terms in post-cracked midspan deflection

Eq. 3-100 and simplifying gives

Eq. 3-101. As previously described, this is solved by finding the moment of the area under the curvature diagram in closed form using the triangular and rectangular areas shown in Figure 3-8b, resulting:

$$\Delta_{mid} = \frac{\phi_{cr} L^2}{12} + \left(\frac{\frac{L}{2} + L_g}{6}\right)\left(\phi_{cr}\frac{L}{2} - \phi_a L_g\right) + \phi_{in}\frac{{L_g}^2}{6} \qquad \textbf{Eq. 3-101}$$

This is valid when the applied moment, M_a, is less than or equal to the yield moment, M_y.

3.3.3.3.3 Post-yielding region

Figure 3-8c shows the post-yielding moment-curvature scenario applied to a member in three-point bending. Upon yielding of the tensile steel, sections in the post-yielding stage are assumed to be fully cracked. This assumption is verified to be accurate since the effective moment of inertia, I_e, of the section beyond yielding from nonlinear analysis considering tension stiffening is comparable to or less than that of I_{cr}. The midspan deflection at any load level after yielding is analytically formulated by determining the moment of the area under the curvature distribution. As with the post-cracked scenario, the curvature is assumed to have a height of ($\phi_{cr} - \phi_{in}$) and the base of a triangle of L_g. In the uncracked region, this triangular area is added to the negative rectangular area of ϕ_{in} as height and L_g as a base. In the post-yielding scenario, four curvatures (initial, cracking, yielding, and ultimate) define the moment curvature response. In addition, the locations of the cracking moment and yielding moment need to be defined.

Putting the deflection at mid-span in terms of the curvatures and their locations, yields

Eq. 3-102.

$$\Delta_{mid} = \int_0^{\frac{L}{2}} x\phi(x)dx = \delta_1 + \delta_2 + \delta_3$$

$$= \int_0^{L_g} x\phi_{un}(x)dx + \int_{L_g}^{L_y} x\phi_{pc}(x)dx + \int_{L_y}^{\frac{L}{2}} x\phi_{py}(x)dx \qquad \textbf{Eq. 3-102}$$

Where the uncracked curvature, ϕ_{un}, is equal to Eq. 3-51, the post-cracked to yield curvature, ϕ_{pc}, is equal to Eq. 3-52, and the post-yielded to nominal (ultimate) curvature, ϕ_{py}, is equal to Eq. 3-62. Substituting the uncracked curvature, the post-cracked to yield curvature and the post-yield to ultimate curvature relationships into the midspan deflection equation,

Eq. 3-103 is determined.

$$\Delta_{mid} = \int_0^{L_g} x\left[\phi_{in} + \frac{M(x)}{M_{cr}}(\phi_{cr} - \phi_{in})\right]dx$$

$$+ \int_{L_g}^{L_y} x\left[\phi_{cr} + \frac{M(x) - M_{cr}}{M_y - M_{cr}}(\phi_y - \phi_{cr})\right]dx$$

$$+ \int_{L_y}^{\frac{L}{2}} x\left[\phi_y + \frac{M(x) - M_y}{M_n - M_y}(\phi_n - \phi_y)\right]dx \qquad \textbf{Eq. 3-103}$$

Substituting the moment equation (Eq. 3-42) and the applied curvature equation for post-yielding region (Eq. 3-63) into the post-yielding midspan deflection formula (

Eq. 3-103), then performing integration,

Eq. 3-104 is obtained for the midspan deflection.

$$\Delta_{mid} = \phi_{in}\frac{x^2}{2}\Big]_0^{L_g} + (\phi_{cr} - \phi_{in})\frac{x^3}{3L_g}\Big]_0^{L_g} + \phi_{cr}\frac{x^2}{2}\Big]_{L_g}^{L_y}$$
$$+ (\phi_y - \phi_{cr})\frac{x^3}{3(L_y - L_g)}\Big]_{L_g}^{L_y} - (\phi_y - \phi_{cr})\frac{x^2 L_g}{2(L_y - L_g)}\Big]_{L_g}^{L_y}$$
$$+ \phi_y\frac{x^2}{2}\Big]_{L_y}^{\frac{L}{2}} + (\phi_n - \phi_y)\frac{x^3}{3(L/2 - L_y)}\Big]_{L_y}^{\frac{L}{2}}$$
$$- (\phi_n - \phi_y)\frac{x^2 L_y}{2(L/2 - L_y)}\Big]_{L_y}^{\frac{L}{2}} \qquad \textbf{Eq. 3-104}$$

Simplifying and grouping terms gives

Eq. 3-106 for the midspan deflection for a three-point bending load case for post-yielding.

$$\Delta_{mid} = \phi_{in}\frac{{L_g}^2}{6} + \phi_{cr}\left(\frac{{L_y}^2}{2} - \frac{{L_g}^2}{6}\right) + \frac{1}{3}\left({L_g}^2 + L_g L_y + {L_y}^2\right)\left(\phi_y - \phi_{cr}\right)$$
$$+ \left(-\frac{{L_g}^2}{2} - \frac{L_g L_y}{2}\right)\left(\phi_y - \phi_{cr}\right) + \phi_y\left(\frac{L^2}{8} - \frac{{L_y}^2}{2}\right)$$
$$+ \frac{1}{3}\left({L_y}^2 + 4L_y\frac{L}{2} + \left(\frac{L}{2}\right)^2\right)\left(\phi_a - \phi_y\right)$$
$$+ \frac{1}{2}\left(-\frac{L_y L}{2}\right)\left(\phi_a - \phi_y\right) \qquad \textbf{Eq. 3-105}$$

$$\Delta_{mid} = \frac{L^2}{12}\phi_n + \left(\frac{\frac{L}{2} + L_y}{6}\right)\left(\phi_y\frac{L}{2} - \phi_a L_y\right) + \left(\frac{L_y + L_g}{6}\right)\left(\phi_{cr}L_y - \phi_y L_g\right)$$
$$+ \phi_{in}\frac{{L_g}^2}{6} \qquad \textbf{Eq. 3-106}$$

3.4 Numerical formulation

The numerical analysis is performed using the incremental deformation approach. Moment-curvature is defined by increasing the extreme compression fiber of concrete from zero to the ultimate value (e.g. 0.003inch/inch in case of concrete crushing failure). For every strain value, a neutral axis depth is assumed, which completely defines the strain, stress and force profile. An iterative loop is made to converge at the neutral axis depth that satisfies the force equilibrium equation using Goal Seek function in Excel. Once the correct neutral axis depth is found, the corresponding moment and curvature are computed for that extreme strain step. This is repeated until all the moment-curvature response is specified.

Since the present analysis is applicable to PRC girders with straight strand, the moment curvature response is the same for all sections along the span. For the sake of performing the load-deflection analysis, the shear span is divided into a large number of segments (e.g. 50-100)

while the constant moment region is represented by a single segment. The moment at the end of each segment (M_i) is evaluated first then the corresponding curvature value is extracted from the moment curvature curve (ϕ_i) obtained previously. By substituting the curvatures into the deflection expression from moment-area theorem, the mid-span deflection is numerically evaluated:

$$\Delta = \int_0^{L/2} x\phi(x)dx = \sum_{i=1}^{n} \left(\frac{\phi_i + \phi_{i+1}}{2}\right)(x_{i+1} - x_i)\left(\frac{x_i + x_{i+1}}{2}\right) \qquad \textbf{Eq. 3-107}$$

Limited studies are available to address the deflection analysis of PRC beams strengthened with FRP. Therefore, the four-point bending equations derived in this chapter are validated by analyzing static experiment results of beams tested by Larson, Peterman, and Rasheed (2005) and Cha (2001). This validation of the derived equations occurs in subsequent Chapter 4 Parametric Study on Prestressed Reinforced Concrete Members with Straight Strands Strengthened with FRP to Calibrate an Improved "Branson" Effective Moment of Interia Equation.

Chapter 4 - Parametric study on prestressed reinforced concrete members with straight strands strengthened with FRP to calibrating an improved “Branson” effective moment of inertia equation

The work presented in this chapter is intended to verify a practical procedure for calculating instantaneous deflections of PRC-FRP based on a modified Branson effective moment of inertia equation. ACI 440.2-17 serviceability requirements for PRC-FRP members is “under service loads the strengthened member should avoid inelastic deformations of the strengthen member by limiting the prestressing steel from yielding at service load levels.” ACI 440.2-17 relies on the ACI 318 (2019), which uses an effective moment inertia method or the bi-linear method, to determine the flexural stiffness of a PRC member and using this methodology to determine the flexural stiffness of a PRC-FRP member.

In the previous chapter, Rasheed & Charkas (2009) proposed a modified Branson’s effective moment of inertia formula, Eq. 3-3 and Eq. 3-4, for deflection of RC-FRP strengthened beams. Therefore, this chapter examines, through a parametric study, contributing factors affecting the flexural stiffness of PRC-FRP members. A similar approach using a trilinear moment-curvature response is used to apply the closed form analytical deflection expressions, derived in Chapter 3, for simply supported, pretensioned, PRC- FRP subjected to four-point bending conditions that predict instantaneous deflections at higher loads more accurately than current code methods.

4.1 Overview

The rigorous procedure developed in Chapter 3 is used to calculate the overall beam effective moment of inertia after cracking and to the point where the pretensioned prestressed steel starts to yield. Section 4.2 presents a simplified analytical model. A large number of variables in strengthened prestressed members exist. To verify if the proposed modified Branson effective moment of inertia equation is valid, a parametric study is presented in Section 4.3. Application of the proposed method is given in Section 4.4.

4.2 Simplified analytical model

Similar to RC beams strengthened with FRP, the stiffness distribution is accounted for by using the integration of curvatures method (Ghali, 1993) and dividing the beam into three distinct regions: pre-cracked, post-cracking, and post-yielding regions as shown in Figure 3-1. The PRC-FRP beams have an initial curvature generated by the pretensioned prestressing reinforcement. The first region, precracking, extends to the onset of flexural cracking. The second region, post-cracking, extends to first yield of the tension reinforcement (prestressing or mild reinforcement depending on location of reinforcement and stresses involved). The third region, post-yielding, extends until the limit of concrete useful strain (0.003 in/in), the FRP rupture, or the FRP debonding, depending on the flexural failure mode involved. The focus of this chapter is on the post-cracking region as a serviceability assessment of PRC-FRP beams. Three key feature points completely define the moment-curvature response of the PRC-FRP girders up to yielding: initial point ($M_a = 0$, ϕ_{in}), cracking point (M_{cr}, ϕ_{cr}) and yielding point (M_y, ϕ_y). For the initial moment-curvature point, equations Eq. 3-8 and Eq. 3-9 are used for the applied moment and initial curvature, respectively. It is well-established that Branson's equation

evaluates the effective moment of inertia (I_e) based on the gross and cracked moments of inertia but the actual cracked moment of inertia may be different from the cracked moment of inertia typically used due to the nonlinearity of concrete in compression and of prestressing steel after the proportionality limit. Therefore, the effective yield beam moment of inertia is suggested to replace the cracked moment of inertia in Branson's equation (Eq. 2-46 with Eq. 3-10 defined as the cracking moment, M_{cr}). The curvature at cracking is given in Eq. 3-11.

The yielding point is determined by considering nonlinear concrete response in compression using Hognestad's parabola (Park & Paulay, 1975) and occurs as the prestressing steel reaches the yielding strain at one percent elongation within the nonlinear range as well. The yielding point is estimated first by assuming the yielding curvature, $\phi_y = \varepsilon_3 / (d_{ps} - c_y)$, where c_y is the depth of the section neutral axis at first yielding, and ε_3 is the remaining strain in prestressing after deducting the initial prestressing and decompression strains at yielding ($\varepsilon_3 =$ 0.01- ε_1- ε_2, Figure 3-3 and Eq. 3-17). For this parametric study, mild reinforcement (non-prestressed) is neglected for the range of members examined. The yielding moment, removing the non-prestressed reinforcement, becomes:

$$M_y = A_{ps} f_{py}\left(d_{ps} - \gamma_y c_y\right) + A_f f_f\left(d_f - \gamma_y c_y\right) \qquad \textbf{Eq. 4-1}$$

Using Eq. 3-12 produces very accurate estimates of the actual yielding point when the concrete behaves linearly. When the concrete response in compression is non-linear, Hognestad's classical parabolic stress-strain curve up to a useful concrete strain, ε_{cu}**,** equals 0.003 produces accurate estimates (Park & Paulay, 1975). Accordingly, the force equilibrium and strain compatibility of the section produces Eq. 4-2. Refer to Section 3.3.2.3 for more detailed information. The neutral axis at yield, c_y, is determined by solving numerically in Excel using

goal-seek for the experimental beams. For the parametric study, the neutral axis at yield, c_y, is defined and the area of FRP, A_f, is determined from equilibrium.

$$\sum F_x = 0 \Longrightarrow \int_0^c \sigma_c(y)dy = A_{ps}f_{py} + A_f f_f \Longrightarrow bf_c' c_y^2 \phi_y \left[\frac{1}{\varepsilon_c'} - \frac{c_y\phi_y}{3\varepsilon'^2_c}\right] = A_{ps}f_{ps} + A_f f_f \quad \textbf{Eq. 4-2}$$

Where the stress in the concrete, σ_c, is given by Eq. 3-13 (repeated in the first part of Eq. 4-3) and the strain in the concrete, ε_c, is represented in Eq. 4-3.

$$\sigma_c = f_c'\left[2\frac{\varepsilon_c}{\varepsilon_c'} - \left(\frac{\varepsilon_c}{\varepsilon_c'}\right)^2\right], \qquad \varepsilon_c = \phi_y c_y \quad \textbf{Eq. 4-3}$$

The stress in the FRP, f_f, represented by Eq. 3-18, along with considering the effect of initial deformations due to service loads during beam strengthening, can be written in terms of the neutral axis depth and the yielding stain using the section strain compatibility is:

$$f_f = E_f\left[\varepsilon_3\left(\frac{d_f - c_y}{d_{ps} - c_y}\right) - \varepsilon_{bi}\right] \quad \textbf{Eq. 4-4}$$

The strain in the prestressing strands due to additional loading equals ε_3. The strain in the prestressing steel due to initial tension after losses is represented by strain 1, ε_1, and the strain in the prestressing steel due to initial eccentricity, otherwise known as the decompression of the section at the level of the prestressing strands is given by strain 2, ε_2. Assuming prestressing strand yields at 0.01 elongation, the strain in the prestressing strands due to the additional loading is equal to Eq. 3-17 and is repeated here for clarity.

$$\varepsilon_3 = 0.01 - \varepsilon_1 - \varepsilon_2 = 0.01 - \frac{f_{se}}{E_{ps}} - \frac{1}{E_c}\left[\frac{P_e}{A_{gt}} + \frac{P_e e^2}{I_{gt}}\right] \quad \textbf{Eq. 3-17}$$

The yield stress in the prestressing steel varies with the strength of the prestressing used. The effective prestressing stress at yield, f_{py}, for 270 ksi strand is approximated by Eq. 3-19.

$$f_{py} = 270 - \frac{0.04}{(\varepsilon_{ps} - 0.007)} = 256.67\ ksi\ \ or$$

$$f_{ps} = 1860 - \frac{0.276}{(\varepsilon_{ps} - 0.007)} = 1768\ MPa \qquad \textbf{Eq. 3-19}$$

The yielding point, (M_y, ϕ_y), shown in Eq. 3-24 and Eq. 3-25 with non-prestressed steel, is determined by summing the moments about the point of concrete compression resultant force. Eq. 4-5 is the yielding moment equation without non-prestressed steel considered. The curvature at yield equation is the same with or without non-prestressed steel considered, as shown in Eq. 3-25.

$$M_y = A_f f_f (d_f - \gamma_y c_y) + A_{ps} f_{ps} (d_{ps} - \gamma_y c_y) \qquad \textbf{Eq. 4-5}$$

and

$$\phi_y = \frac{\varepsilon_3}{d_{ps} - c_y} \qquad \textbf{Eq. 3-25}$$

Where $\gamma_y c_y$ is the depth of the resultant force of concrete in compression at first yielding measured from the top extreme fiber in compression. Refer to Chapter 3 for additional information.

4.2.1 PRC-FRP four-point bending deflection equations

The load-deflection response is expressed in terms of the effective flexural rigidity of the section that reduces with increased moment. As shown by Kramer and Rasheed 2018 study, the actual stiffness distribution is accounted for by dividing the beam into three distinct regions: precracking, post-cracking, and post-yielding (Kramer & Rasheed, 2018). The response is determined using the second moment-area theorem. The rigidity of the beam will vary along its

length depending on its moment diagram. This presented formulation furnishes closed form expressions for midspan deflection of simple span beams under four-point bending.

The general solution can be obtained by adding the deflection contribution of the three regions, as shown in Section 3.3.3:

$$\Delta_{mid} = \delta_1 + \delta_2 + \delta_3 = \int_0^{L_g} x\phi_{un}(x)\,dx + \int_{L_g}^{L_y} x\phi_{pc}(x)dx + \int_{L_y}^{\frac{L}{2}} x\phi_{py}(x)dx \qquad \textbf{Eq. 4-6}$$

Precracking region: When the load equals *P/2*, then $M_a = PL_a/2$ and $P/2 = M_a/L_a$, as shown in Section 3.3.3.1.1, the uncracked stage yields the classical uncracked prismatic, beam problem with midspan deflection of:

$$\Delta_{mid} = \frac{(\phi_a - \phi_{in})}{24}\left(3L^2 - 4{L_a}^2\right) + \frac{\phi_{in}L^2}{8} \qquad \textbf{Eq. 4-7}$$

Post-cracking region**:** In this stage of loading, L_g identifies the extent of the uncracked region and is equal to two times the cracking moment divided by the applied total load, *P*. When the applied moment, $M_a = PL_a/2$, equal to the yield moment, M_y, the deflection expression at the yielding point is shown in Eq. 3-60 and is used to obtain the beam effective moment of inertia at first yielding. The derivation is shown in Section 3.3.3.1.2.

$$\Delta_{mid} = \frac{\phi_a}{24}(3L^2 - 4L_a^2) + \left(\frac{L_a + L_g}{6}\right)\left(\phi_{cr}L_a - \phi_a L_g\right) + \frac{L_g^2}{6}\phi_{in} \qquad \textbf{Eq. 4-8}$$

Where $\phi_a = \phi_y$

4.3 Parametric study

Numerous beams were analyzed and studied with the objective of generating simple relationships to evaluate the effective moment of inertia of PRC-FRP beams at yielding moment based on the entire beam properties using the analytical solution developed in Chapter 3. Wide

ranges of geometric and material properties are examined. Geometric properties varied by examining six different rectangular PRC beam sizes with beam widths (b_w) of 150 mm (5.9 inches) and 300 mm (11.8 inches), and beam width to overall depth (h) of unstrengthened beam ratio of 0.15, 0.30, and 0.45. Beam sizes varied from 150 mm by 333 mm (5.9 inches by 13.1 inches) to 300 mm by 2000 mm (11.8 inches by 78.7 inches). Table 4-1indicates the six beam sizes studied.

Table 4-1: Beam sizes for parametric study

Parametric study beam sizes	
Web width (b_w) mm (inches)	Beam depth (h) mm (inches)
150 (5.9)	1000 (39.4)
150 (5.9)	500 (19.7)
150 (5.9)	333 (13.1)
300 (11.8)	2000 (78.7)
300 (11.8)	1000 (39.4)
300 (11.8)	667 (26.3)

Further geometric properties scrutinized are the span, L, and shear-span-to-span ratio, L_a/L. Three span (L) to depth (h) ratios are considered: 10, 15, and 20 – spans vary from 3,330 mm to 40,000 mm (130 inches to 1575 inches). Three shear-span-to-span ratios (L_a/L) are examined: 0.31, 0.375, and 0.44.

In addition to geometric properties, material properties are varied. The specified minimum concrete compressive strength at time of strengthening and after 28-days of concrete placement (f_c') is 30 MPa (4.35 ksi), 40 MPa (5.80 ksi), and 50 MPa (7.25 ksi), which are common for PRC beams. The PRC beams have fully bonded, straight pretensioned prestressing strands with the centroid of the strands taken in one location ($h - d_{ps}$), 75 mm (3-inches) from the

bottom of the unstrengthened PRC beam. Low-relaxation prestressing strands with an ultimate strength of 1860 MPa (270 ksi) and a yield strength at 1% elongation of 1768 MPa (256 ksi) are used. Mild reinforcement is neglected from the parametric study since the PRC flexural members being strengthened may or may not have mild reinforcement. If the actual strengthened members have mild reinforcement, they will have a slightly greater stiffness than members without non-prestressed reinforcement (mild reinforcement).

Prestressing reinforcement ratio is determined by area of prestress (A_{ps}) divided by width of the beam web multiplied by the depth of prestress from extreme fiber in compression ($A_{ps}/b_w d_{ps}$). For this parametric study, the prestressing reinforcement ratio (ρ_{ps}) varies between its minimum and maximum values specified in ACI 318-19 and AASHTO LRFD (ACI Committee 318, 2019) (AASHTO, 2017). The first design requirements for prestressed concrete bridges was published in 1954 and the design of prestressed concrete ACI-ASCE Committee 323 report was first published in 1958; both without the requirements for minimum reinforcement requirements for prestressed concrete (Bureau of Public Roads, 1954) (ACI-ASCE Committee 323, 1958). In 1963, prestressed concrete was incorporated within the scope of ACI 318. Within the separate prestressed concrete design chapter of ACI 318-63, the minimum reinforcement requirement for prestressed concrete was introduced: the provided area of steel was required to be adequate to develop an ultimate load capacity greater than 1.2 times the cracking load based on a modulus of rupture of $0.62\sqrt{f_c'}$ MPa ($7.5\sqrt{f_c'}$ psi) (ACI Committee 318, 1963). Both ACI 318-19 and AASHTO LRFD currently use this minimum requirement ($1.2M_{cr}$), but use a different modulus of rupture to calculate the cracking moment. The modulus of rupture, $f_{r,}$ used depends on the limit state being checked and the specified concrete strength. Typically, the cited modulus of rupture values range between $0.62\sqrt{f_c'}$ MPa ($7.5\sqrt{f_c'}$ psi) and $0.97\sqrt{f_c'}$ MPa ($11.7\sqrt{f_c'}$

psi) (ACI Committee 318, 2019) (Walker & Bloem, 1960) (Khan, Cook, & Mitchell, 1996). For determining minimum steel requirements using the AASHTO LRFD provisions, the cracking moment is calculated using an estimated modulus of rupture equal to $0.97\sqrt{f_c'}$ MPa ($11.7\sqrt{f_c'}$ psi). The AASHTO LRFD rationale for using a higher modulus of rupture value for minimum steel requirements is that the use of the upper bound value is justified since it is a strength limit state. The flexural members examined in this parametric study are strengthened with FRP. Therefore, the minimum area of prestressed steel strands, conforming to ASTM A416, is determined by ACI 318-19 requirements for beams with bonded prestressed reinforcement, where the area of prestressing, A_{ps}, needs to be adequate to develop a factored load at least 1.2 times the cracking load calculated on the basis of a modulus of rupture, f_r, equal to $0.62\sqrt{f'_c}$ MPa ($7.5\sqrt{f'_c}$ psi). Some PRC strengthened members may have originally been designed to be fully prestressed, not to crack. Since these members are being strengthened, it is assumed that they will crack under new loading conditions. Therefore, the lower bound for the modulus of rupture is justified.

In the next few pages, the minimum prestressing steel per ACI 318-19 is derived for a rectangular compression stress block within the flange by setting the nominal moment capacity equal to the 120% of the cracking moment, M_{cr}, as shown in Eq. 4-9. Since the T-section assumes a rectangular compression stress block within the flange, the minimum prestressing steel equation derived is also applicable for rectangular flexural members.

$$\rho_{ps,min} \Rightarrow M_n = 1.2M_{cr} \qquad \textbf{Eq. 4-9}$$

Where the cracking moment (Eq. 4-10) is equal to the modulus of rupture times the section modulus plus the moment caused by the compressive stress in the concrete due to the effective prestress forces after allowance for all prestress losses and initial prestressing moment including losses.

$$M_{cr} = f_r S_{bt} + P_e \left(e + \frac{\frac{I_{gt}}{A_{gt}}}{c_b} \right)$$ **Eq. 4-10**

Where:

A_{gt} = gross transformed area of the section including reinforcing steel and FRP

c_b = distance from the center of gravity of the section to the extreme bottom fiber of the concrete

e = distance from the center of gravity of the section to the centroid of prestressed strands (positive when below the section center of gravity, cgc)

I_{gt} = gross transformed moment of inertia of the section including reinforcing steel and FRP

P_e = equivalent prestressed force

S_{bt} = gross transformed section bottom modulus of the section including reinforcing steel and FRP.

Setting the nominal moment equal to 120 percent of the cracking moment, Eq. 4-11 is derived.

$$M_n = A_{ps} f_{ps} \left(d_{ps} - \frac{\beta_1 c_n}{2} \right) = 1.2 \left(f_r S_{bt} + P_e \left(e + \frac{\frac{I_{gt}}{A_{gt}}}{c_b} \right) \right)$$ **Eq. 4-11**

Where:

A_{ps} = area of prestressing steel

d_{ps} = depth of centroid of prestressing steel from extreme compression fiber

β_1 = factor relating depth of equivalent rectangular compressive stress block to depth of neutral axis.

A rectangular compression block, width equal to b_w, with the centroid located at $\frac{\beta_1 c_n}{2}$, is used. Equating the internal compression and tension forces by assuming concrete crushing failure mode, Eq. 4-12 is obtained.

$$\sum F_x = 0 \Longrightarrow 0.85 f_c' b_w \beta_1 c_n = A_{ps} f_{ps} \quad \textbf{Eq. 4-12}$$

With the prestressing stress, f_{ps}, based on strain compatibility and nonlinear strand stress-strain curve is equal to:

$$f_{ps} = f_{pu} - \frac{0.04}{\varepsilon_1 + \varepsilon_2 + \frac{0.003\left(d_{ps} - c_n\right)}{c_n} - 0.007} \quad \textbf{Eq. 4-13}$$

Where:

f_{pu} = ultimate tensile strength of prestressing steel

ε_1 = strain in the prestress strands due to initial tension after losses

ε_2 = strain in the strands due to initial eccentricity (decompression strain).

With β_1, the factor relating depth of equivalent rectangular compressive stress block to depth of neutral axis equal to the value specified by ACI 318-19. Manipulating Eq. 4-12, the neutral axis, c_n, can be defined as:

$$c_n = \frac{A_{ps} f_{ps}}{0.85 f_c' b_w \beta_1} \quad \textbf{Eq. 4-14}$$

Plugging Eq. 4-14 into Eq. 4-11, the nominal moment equal to 120 percent of the cracking moment equation can be written as:

$$M_n = A_{ps} f_{ps} \left(d_{ps} - \left(\frac{\beta_1}{2}\right) \frac{A_{ps} f_{ps}}{0.85 f_c' b_w \beta_1} \right) = 1.2 \left(f_r S_b + P_e \left(e + \frac{\frac{I_{gt}}{A_{gt}}}{c_b} \right) \right) \quad \textbf{Eq. 4-15}$$

Eq. 4-16 is obtained by simplifying

Eq. 4-15.

$$A_{ps}f_{ps}d_{ps} - 0.59\frac{A_{ps}^2 f_{ps}^2}{f_c' b_w} = 1.2\left(f_r S_b + P_e\left(e + \frac{\frac{I_{gt}}{A_{gt}}}{c_b}\right)\right) \qquad \textbf{Eq. 4-16}$$

Rearranging

Eq. 4-16 into a standard quadratic equation format,

Eq. 4-17 is obtained.

$$0.59\frac{A_{ps}^2}{b_w^2 d_{ps}^2}\frac{f_{ps}^2}{f_c' b_f} b_w^2 d_{ps}^2 - \frac{A_{ps}}{b_w d_{ps}} f_{ps} d_{ps}^2 b_w + 1.2\left(f_r S_b + P_e\left(e + \frac{\frac{I_{gt}}{A_{gt}}}{c_b}\right)\right) = 0 \qquad \textbf{Eq. 4-17}$$

Where the prestressing reinforcing ratio squared is presented by Eq. 4-18 and the prestressing reinforcing ratio is offered as Eq. 4-19.

$$\rho_{ps}^2 = \frac{A_{ps}^2}{b_w^2 d_{ps}^2} \qquad \textbf{Eq. 4-18}$$

$$\rho_{ps} = \frac{A_{ps}}{b_w d_{ps}} \qquad \textbf{Eq. 4-19}$$

Divide

Eq. 4-17 by $1/f'_c\, d^2_{ps} b_w$ to obtain

Eq. 4-20.

$$0.59\rho_{ps}^2\frac{f_{ps}^2}{f_c'^2}-\rho_{ps}\frac{f_{ps}}{f_c'}+1.2\left(f_rS_b+P_e\left(e+\frac{\frac{I_{gt}}{A_{gt}}}{c_b}\right)\right)\left(\frac{1}{f_c'd_{ps}^2b_w}\right)=0 \qquad \textbf{Eq. 4-20}$$

Eq. 4-20 may be rewritten as:

$$0.59\omega^2-\omega+1.2R=0 \qquad \textbf{Eq. 4-21}$$

Where

$$\omega=\rho_{ps}\frac{f_{ps}}{f_c'},R=\left(f_rS_b+P_e\left(e+\frac{\frac{I_{gt}}{A_{gt}}}{c_b}\right)\right)\left(\frac{1}{f_c'd_{ps}^2b_w}\right) \qquad \textbf{Eq. 4-22}$$

Using the quadratic formula, the generalized minimum prestressing steel reinforcement ratio (ω) can be solved as shown in

Eq. 4-23.

$$\omega=\frac{1-\sqrt{1-4(0.59)1.2R}}{2(0.59)}=\frac{1-\sqrt{1-2.83R}}{1.18}$$

$$\rho_{ps,min}=\omega\frac{f_c'}{f_{ps}} \qquad \textbf{Eq. 4-23}$$

For this parametric study, the strain ε_3 in the prestress strands due to strain compatibility is estimated to equal 0.027 by assuming $c_n \approx 0.1d_{ps}$, as given in Eq. 4-24.

$$\varepsilon_3=\frac{0.003\left(d_{ps}-c_n\right)}{c_n}=0.027 \qquad \textbf{Eq. 4-24}$$

It is widely acceptable that $\varepsilon_1 + \varepsilon_2 \approx 0.005 - 0.006$, making the total strain $\approx 0.032 - 0.003$. This strain results in $f_{ps} = 268.4 - 268.46$ ksi ≈ 270 ksi (1860 MPa), which will be used in

Eq. 4-23.

ACI 318 (2019) defines tension-controlled members as elements having a minimum extreme fiber in tension equal to yield strain of the steel plus the usable strain of the concrete, ε_{ty} + 0.003. ACI 318 (2014) defined tension-controlled members as elements having a minimum extreme fiber in tension equal to 0.005. ACI 318 (2019) was modified to incorporate higher strength non-pretensioned steel (billeted steel). Using a similar philosophy, a value of 0.005 for the extreme fiber in tension is used to determine the maximum prestressing steel. By means of strain compatibility with the useable concrete-strain equal to 0.003 and the net tensile strain in prestressing strands equal to 0.005, the maximum prestressing steel reinforcement ratio can be determined. As shown in Figure 4-2, using similar triangles of the strains above and below the neutral axis, an expression is derived to calculate the depth of the neutral axis, c.

$$\frac{c}{d_{ps} - c} = \frac{0.003}{\varepsilon_t} \implies c\varepsilon_t - 0.003\left(d_{ps} - c\right) = 0 \qquad \textbf{Eq. 4-25}$$

$$c = \frac{0.003}{0.003 + \varepsilon_{ty}} d_{ps} = \frac{0.003}{0.003 + 0.005} d_{ps} = \frac{3}{8} d_{ps} \qquad \textbf{Eq. 4-26}$$

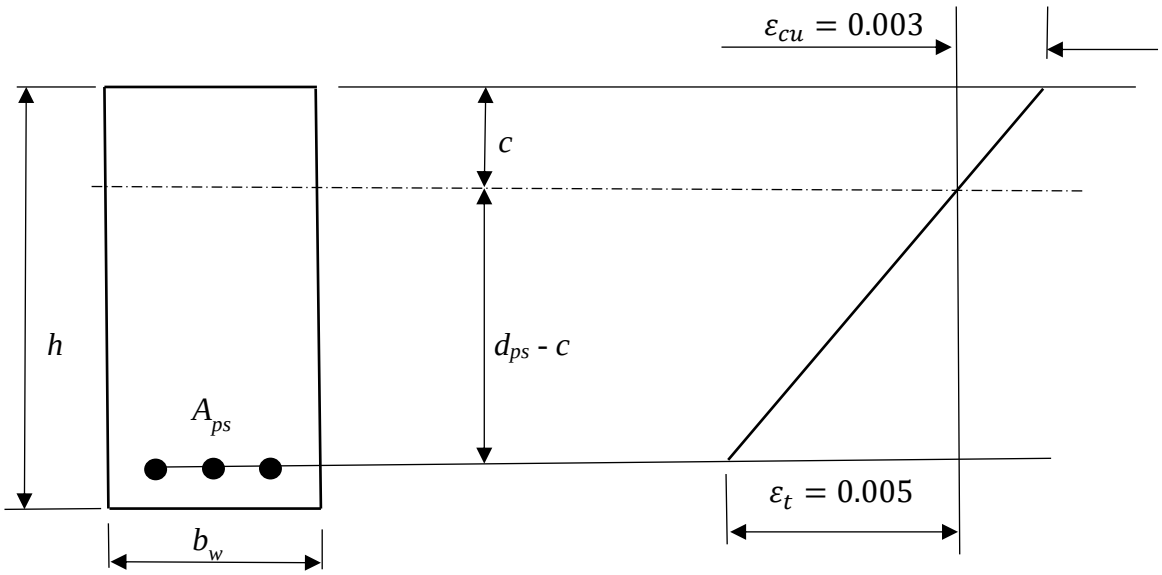

Figure 4-1: Location of the neutral axis, c, with the tensile stress in steel ($A_{ps,max}$).

The ratio of c/d_{ps} given in Eq. 4-27 is frequently used to check if a section is tension-controlled. When ε_{ty} plus 0.003 equals 0.005, the lowest location of the neutral axis depth for a tension-controlled section is c/d_{ps} = 3/8. The corresponding depth of the equivalent stress block is given in Eq. 4-27.

$$a_{max} = \frac{A_{ps,max} f_{ps}}{0.85 f_c' b_w} = \frac{3}{8}\beta_1 d_{ps} \qquad \textbf{Eq. 4-27}$$

Where $A_{ps,max}$ is the amount of prestressing steel necessary to have an extreme fiber in tension strain equal to 0.005.

Substituting $\rho_{ps,max} b_w d_{ps}$ for $A_{ps,max}$ in Eq. 4-27, then rearranging, the largest reinforcement ratio value is obtained by Eq. 4-29. Since all the prestressing steel is taken at one depth, 75 mm (3-inches) from the bottom of the unstrengthened PRC beam, for this parametric study, the depth of prestressing steel to the extreme fiber in tension ratio equals 1 when using one layer of prestressing or lumping all prestressing in one location for the maximum prestressing derivation.

$$\frac{\rho_{ps,max} b_w d_{ps} f_{ps}}{0.85 f_c' b_w} = \frac{3}{8}\beta_1 d_{ps}$$ **Eq. 4-28**

$$\rho_{ps,max} = \frac{3}{8}(0.85)\beta_1 \frac{f_c'}{f_{ps}} = 0.319\beta_1 \frac{f_c'}{f_{ps}}$$ **Eq. 4-29**

Using the derived minimum and maximum steel reinforcement ratios,

Eq. 4-23 and Eq. 4-29, respectively, the prestressing reinforcement ratio is varied in this parametric study from the specified ACI 318-19 minimum ($\rho_{ps,\,min}$) and maximum ($\rho_{ps,\,max}$). This is achieved by adding a percentage of the difference between the minimum and maximum reinforcement ratio to the minimum reinforcement ratio in one quarter increments: $\rho_{ps,\,min}$, $0.25(\rho_{ps,\,max} - \rho_{ps,\,min}) + \rho_{ps,\,min}$, $0.50(\rho_{ps,\,max} - \rho_{ps,\,min}) + \rho_{ps,\,min}$, $0.75(\rho_{ps,\,max} - \rho_{ps,\,min}) + \rho_{ps,\,min}$, and $\rho_{ps,\,max}$. Refer to Table 4-2.

Table 4-2: Prestressing reinforcement ratio range for the parametric study

Prestressing reinforcement ratio range					
Prestressing reinforcement ratio	symbol	minimum	maximum	FRP min. ratio*	FRP max. ratio*
$\rho_{ps,\,min}$	$\rho_{ps,min}$	0.000739	0.001405	0.000077	0.002582
$0.250(\rho_{ps,\,max} - \rho_{ps,\,min}) + \rho_{ps,\,min}$	$0.250\rho_{ps,min}$	0.001748	0.002756	0.000147	0.002564
$0.500(\rho_{ps,\,max} - \rho_{ps,\,min}) + \rho_{ps,\,min}$	$0.500\rho_{ps,min}$	0.002708	0.004106	0.000057	0.002730
$0.750(\rho_{ps,\,max} - \rho_{ps,\,min}) + \rho_{ps,\,min}$	$0.750\rho_{ps,min}$	0.003667	0.005457	0.000079	0.002695
$\rho_{ps,\,max}$	$\rho_{ps,max}$	0.004629	0.006807	0.000062	0.002741
*Range for the three shear-span-to-span ratios and two types of FRP.					

As shown in Table 4-2, the FRP reinforcement ratio, ρ_f, is also varied for the study. The area of FRP is determined by equilibrium of the section with predetermined neutral axis locations that varied in increments of one hundredth the height (depth) of the unstrengthened

beam; for example, 0.26h to 0.33h. The layers of CFRP for the PRC-FRP strengthened members is limited for this study - one to five layers of CFRP. A maximum of five layers was used for constructability and economics. A minimum width of 50 mm (2 inches) and one layer of FRP is used. This is due to the fact that such a small FRP plate area is expected to add an insignificant contribution to flexure. Two approaches of applying the layers of FRP are examined: (1) FRP placed only on the bottom of the beam with a maximum width of the beam and (2) FRP placed on the bottom of the web of the beam with a maximum wrap up the sides of 0.167*h*, where *h* is the total height of the unstrengthened PRC member. This wrap height varied from 56 mm (2.2 inches) to 334 mm (13.1 inches) depending on the beam height examined. As the length of the wrap increases, it becomes less effective in resisting moment, strengthening the flexural member; hence, the use of 0.167h. Full size layers were used for all layers except the last one and only what was required for equilibrium was used, as long as its width was at least 50 mm. For example, if the beam width was 150 mm (5.9 inches) and the FRP was only being applied to the bottom of the beam and three layers are required, two layers, 150 mm (5.9 inches) wide, and one layer, 85 mm (3.3 inches) in width (outer layer) are used.

Formerly mentioned, the area of FRP is calculated by equilibrium of the section at first yield, which is controlled by yielding of prestressing steel in tension, intermediate crack-induced debonding or rupture of the FRP, or concrete crushing in compression prior to yielding of prestressing steel failure modes. Cover delamination near the section where externally bonded FRP terminates is assumed to be prevented by U-wraps or other anchorage methods. Full beam width layers or full wrapped width layers, depending on approach of strengthening, are used except for the outer layer required in which the width varied based on equilibrium requirements.

Additional considerations when calculating equilibrium of the section are the yield strain of the prestressing steel, ε_{ps}, and the initial substrate strain, ε_{bi}. Because the stress-strain curve for prestressing steel does not have a distinct yield point, the strain in the prestressing steel is taken as 0.01 that signifies the relatively turning portion of the stress-strain curve, based on the specification of the PCI Design Handbook. When determining the effective strain in the FRP reinforcement at the yield state, ε_{fe}, the initial substrate strain used in the parametric study was estimated to be 0.0006. This value is known to be conservative when considering prestressed concrete girders that are strengthened under dead load plus some sustained live load. Since FRP materials are linear elastic until failure, the strain in the FRP will dictate the stress developed in the FRP. The strain developed in the FRP at yield is governed by either the point at which the FRP ruptures or the point at which the FRP debonds from the substrate. In the case of high prestressing reinforcement ratios, ρ_{max}, concrete crushing occurred prior to FRP rupture or FRP debonding.

Table 4-3: Range of neutral axis locations for various prestressing steel reinforcement ratios

Range of neutral axis locations for various prestressing steel reinforcement ratios					
ρ_{ps}	$\rho_{ps,min}$	$0.25\rho_{ps,min}$	$0.50\rho_{ps,min}$	$0.75\rho_{ps,min}$	$\rho_{ps,max}$
c_y **	0.15h - 0.24h	0.22h - 0.32h	0.27h - 0.36h	0.31h - 0.40h	0.35h - 0.46h
**Average for the three shear-span-to-span ratios and two types of FRP.					

Two types of carbon FRP commonly used in strengthening or rehabilitation of structural elements are studied – SikaWrap Hex 103C sheet (CFRP1) and M-Brace CF130 (CFRP2). SikaWrap Hex 103C sheet has a thickness of 1 mm (0.04 inches), tensile elastic modulus, E_f, equal to 65.1 GPa (9,442 ksi), tensile strength, f_{fu}, equal to 717 MPa (104 ksi). M-Brace CF130 has a thickness of 0.17 mm (0.007 inches), E_f equal to 227 GPa (32,924 ksi), f_{fu} equal to 3800

MPa (551 ksi) based on the fiber net area. Glass FRP is not studied due to creep rupture and is not a common material for strengthening existing prestressed structural elements.

Four-point bending is examined with a shear span-to-span ratio, L_a/L, of 0.31, 0.375, and 0.44. Four-point bending is selected to compare the experimental beams with the parametric study. This parameter variation generated 6,325 load-deflection solutions used in a statistical correlation. Figure 4-3 shows the range of the parameters.

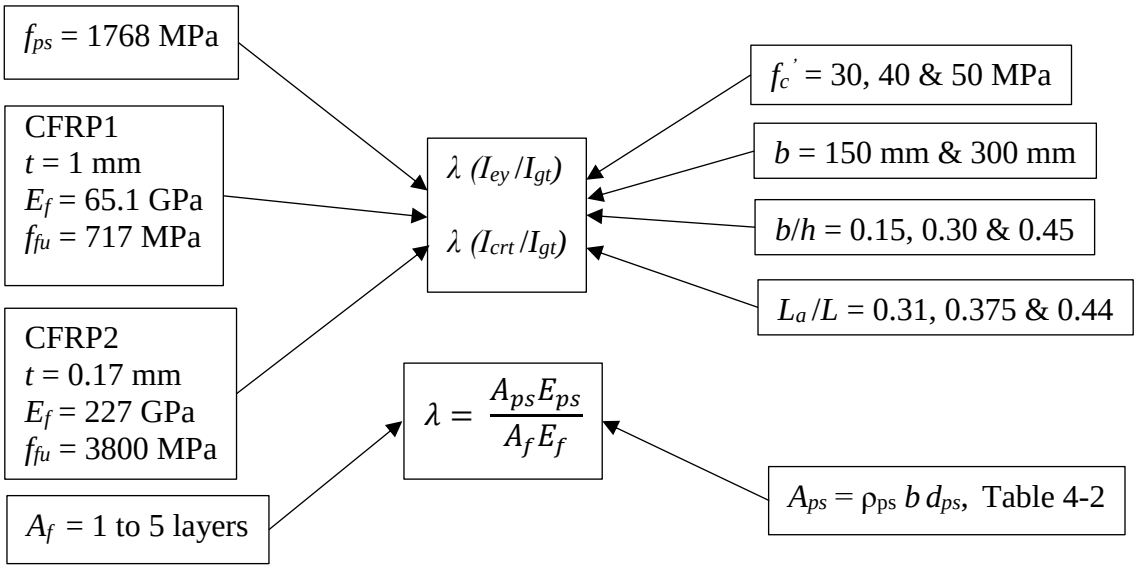

Figure 4-2: Variation of design variables in the parametric study for PRC beams strengthened with CFRP.

As presented in Section 3.2.1, Rasheed & Charkas (2009) proposed a modified Branson's effective moment of inertia formula, Eq. 3-3 and Eq. 3-4, for deflection of RC-FRP strengthened beams since Branson's cubic moment of inertia equation did not produce conservative results for RC-FRP strengthened beams. Their study included an experimental verification of their parametric study. From this, Rasheed & Charkas (2009) proposed a post-cracking deflection equation for RC-FRP strengthened flexural members, shown in Eq. 3-3 and given here for ease of reading.

$$I_e = \left(\frac{M_{cr}}{M_a}\right)^3 I_g + \left[1 - \left(\frac{M_{cr}}{M_a}\right)^3\right] I_{ey} \leq I_g \qquad \textbf{Eq. 3-3}$$

ACI 440 subcommittee F (2013) further studied the effective beam moment of inertia at first yield including bond-slip, and recommended:

$$I_{ey} = 0.73 I_{cr} + 0.05 I_g \qquad ACI\ 440\ subcommittee\ F \qquad \textbf{Eq. 4-30}$$

A similar approach is used for this study. The first parameter examined to normalize the beam effective moment of inertia at first yield, I_{ey}, is the gross transformed moment of inertia. Using the equations from Sections 3.2.1 and 4.2.2, data was generated for this parametric study. Figure 4-3 indicates I_{ey} versus I_{cr} normalized by I_{gt} for rectangular PRC-FRP sections strengthened with M-Brace CF130 CFRP for L_a/L equal to 0.44. Figure 4-4 indicates I_{ey} versus I_{cr} normalized by I_{gt} for rectangular PRC-FRP sections strengthened with M-Brace CF130 CFRP for L_a/L equal to 0.31. Various reinforcement ratios are indicated: $\rho_{ps,\,min}$ = orange square, 0.25 $\rho_{ps,\,min}$ = grey circle, 0.50 $\rho_{ps,\,min}$ = purple triangle, 0.75 $\rho_{ps,\,min}$ = blue diamond, and $\rho_{ps,\,max}$ = green dash. Figure 4-5 is for the same type of CFRP and parameters except the shear-span-to-span ratio is equal to 0.31, 0.375, and 0.44 combined with both types of CFRP applied. When examining Figure 4-3 and Figure 4-4, the beam effective moment of inertia at first yielding, I_{ey}, does not correlate well for all PRC-FRP flexural members when normalized, by dividing by the gross transformed moment of inertia, I_{gt}. For PRC-FRP strengthened members with minimum prestressing reinforcement ratio, this normalization parameter may work well, but as the prestressing reinforcement ratio increases, the scatter is magnified. Additionally, the shear-span-to-span ratio impacts the scatter, as shown when comparing Figure 4-3 and Figure 4-4. Figure 4-5 indicates both types of carbon fiber polymers, M-Brace CF130 (CFRP2) & SikaWrap Hex 103C (CFRP1), used in the study. A linear correlation of $R^2 = 0.8182$ occurs, as shown in Figure 4-5, for dividing by the gross transformed moment of inertia. Eq. 4-31 and Eq. 4-32 indicate the

effective beam moment of inertia at first yield including bond-slip if this parameter is used for the first yield effective moment of inertia.

$$\frac{I_{ey}}{I_{gt}} = 1.1009\left(\frac{I_{cr}}{I_{gt}}\right) + 0.0987 \qquad \textbf{Eq. 4-31}$$

$$I_{ey} = 1.1009 I_{cr} + 0.0987 I_{gt} \qquad \textbf{Eq. 4-32}$$

Since the scatter is large and the linear correlation is approximately 80 percent, other normalization parameters are examined.

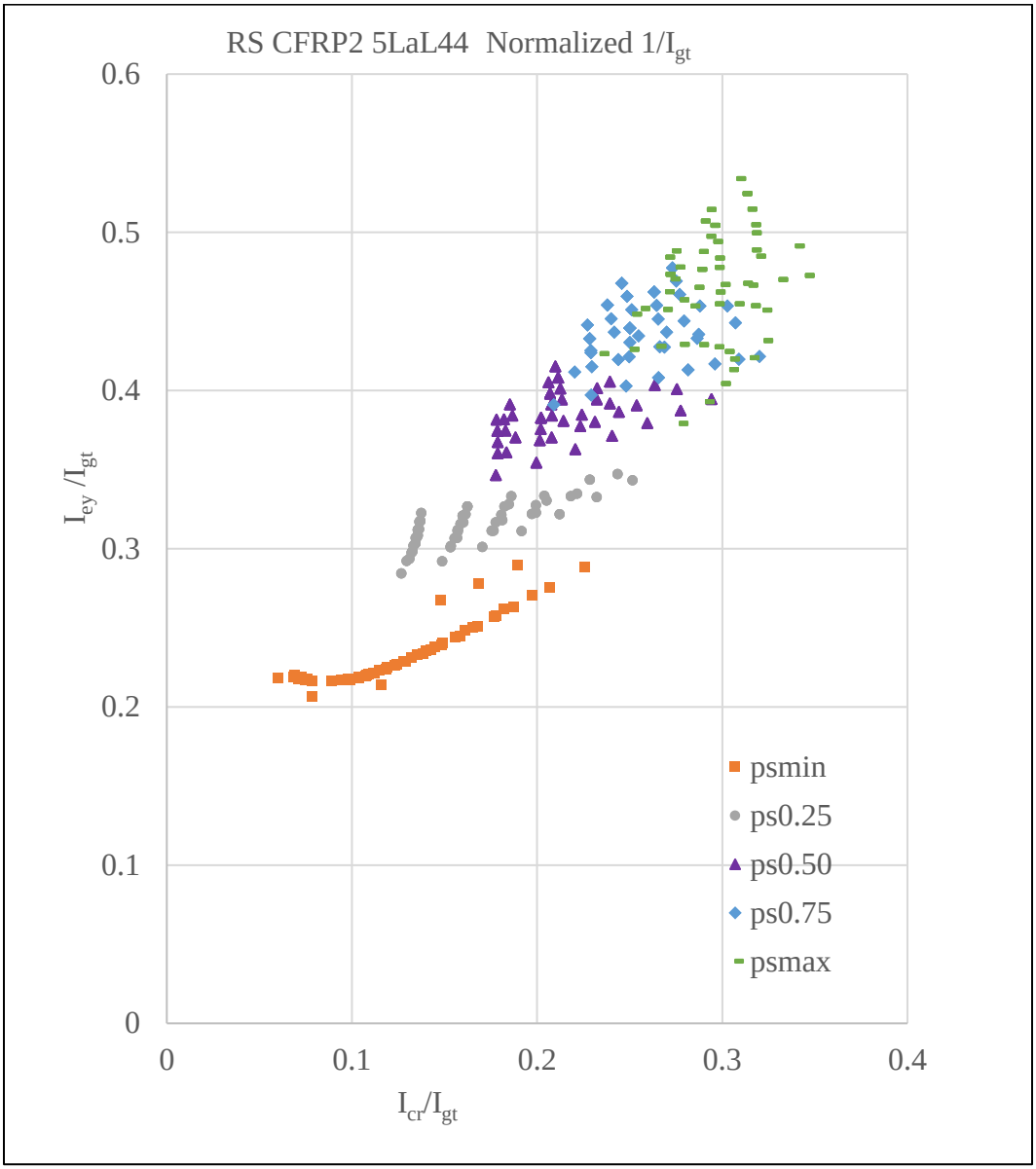

Figure 4-3: Normalized by divided by gross moment of inertia I_{ey} versus I_{cr} relationship for M-Brace CF130 and L_a/L = 0.44.

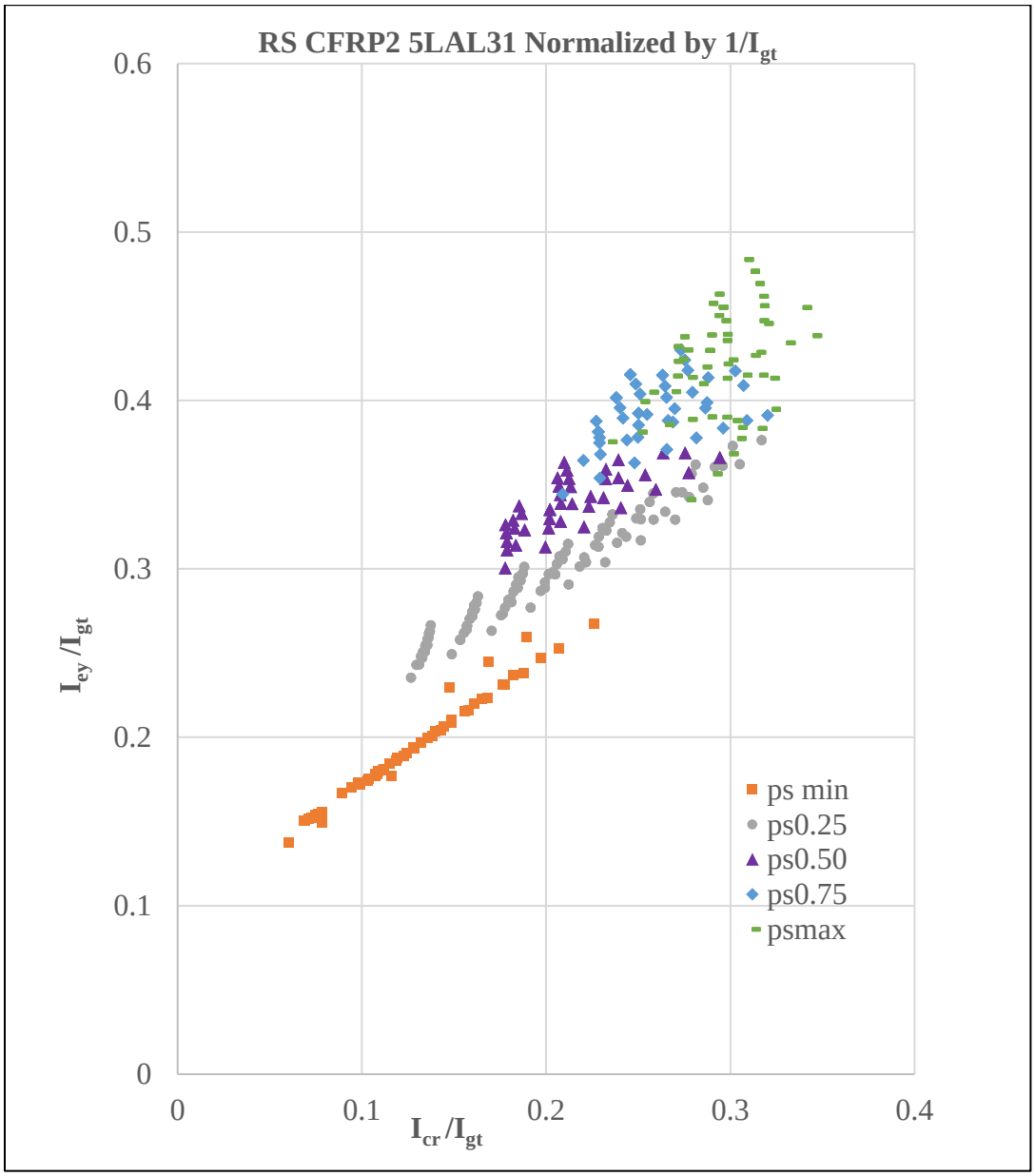

Figure 4-4: Normalized by divided by gross moment of inertia I_{ey} versus I_{cr} relationship for M-Brace CF130 and L_a/L = 0.31.

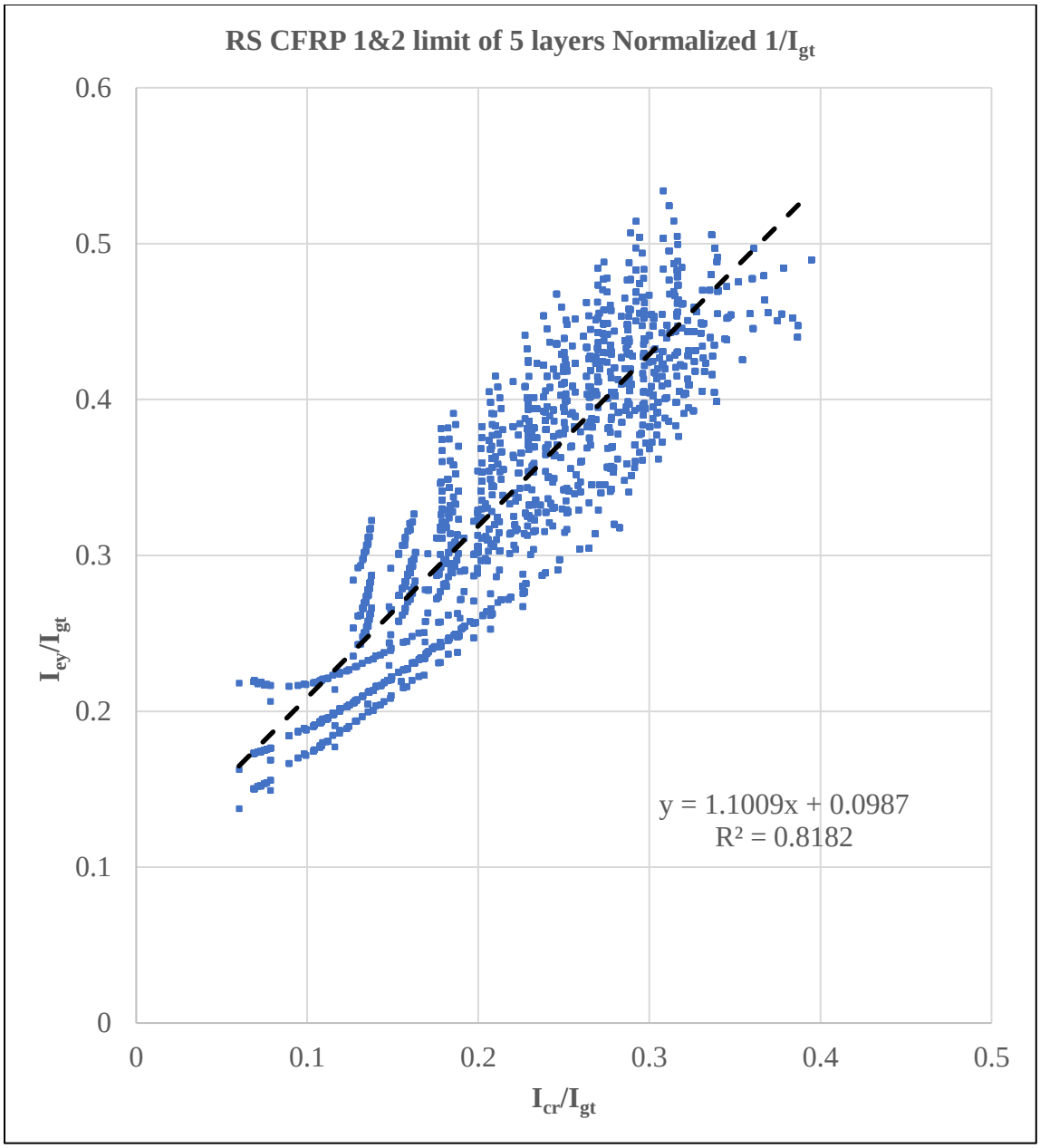

Figure 4-5: Normalized/divided by gross moment of inertia I_{ey} versus I_{cr} relationship for M-Brace CF130 & SikaWrap Hex 103C for L_a/L = 0.31, 0.375, and 0.44.

As indicated in Figure 4-3 and Figure 4-4, the prestressing reinforcement ratio, shown in different colors and shapes, appears to have a crucial role in the effective beam moment of inertia. The members studied are strengthened with the required amount of FRP to cause internal couple equilibrium at a given neutral axis. Therefore, the members with the least amount of

prestressing have larger FRP ratios than the members with higher prestressing reinforcement ratios. Both the prestressing reinforcement ratio and the FRP reinforcement ratio are examined with the FRP reinforcement ratio giving a higher degree of correlation for normalization. Therefore, the second parameter presented to normalize the yielding moment of inertia and cracking moment of inertia is dividing the yielding moment of inertia and cracking moment of inertia by the FRP reinforcement ratio, Eq. 4-33, and by the gross moment of inertia transformed times 0.001, as shown in Eq. 4-34. This produces a linear correlation of $R^2 = 0.9802$ as shown in Figure 4-6 indicating all the beams examined in this study. Eq. 4-34 and Eq. 4-35 indicate the effective beam moment of inertia at first yield including bond-slip for this normalization parameter.

$$\rho_f = \frac{A_f}{bd_{ps}} \qquad \textbf{Eq. 4-33}$$

Where:

A_f = equivalent area of fiber in composite, FRP plate area

Therefore,

$$\frac{I_{ey}}{I_{gt}\rho_f}(0.001) = 1.8292\left(\frac{I_{cr}}{I_{gt}\rho_f}(0.001)\right) - 0.0146 \qquad \textbf{Eq. 4-34}$$

$$I_{ey} = 1.8292I_{cr} - 14.6I_{gt}\rho_f \qquad \textbf{Eq. 4-35}$$

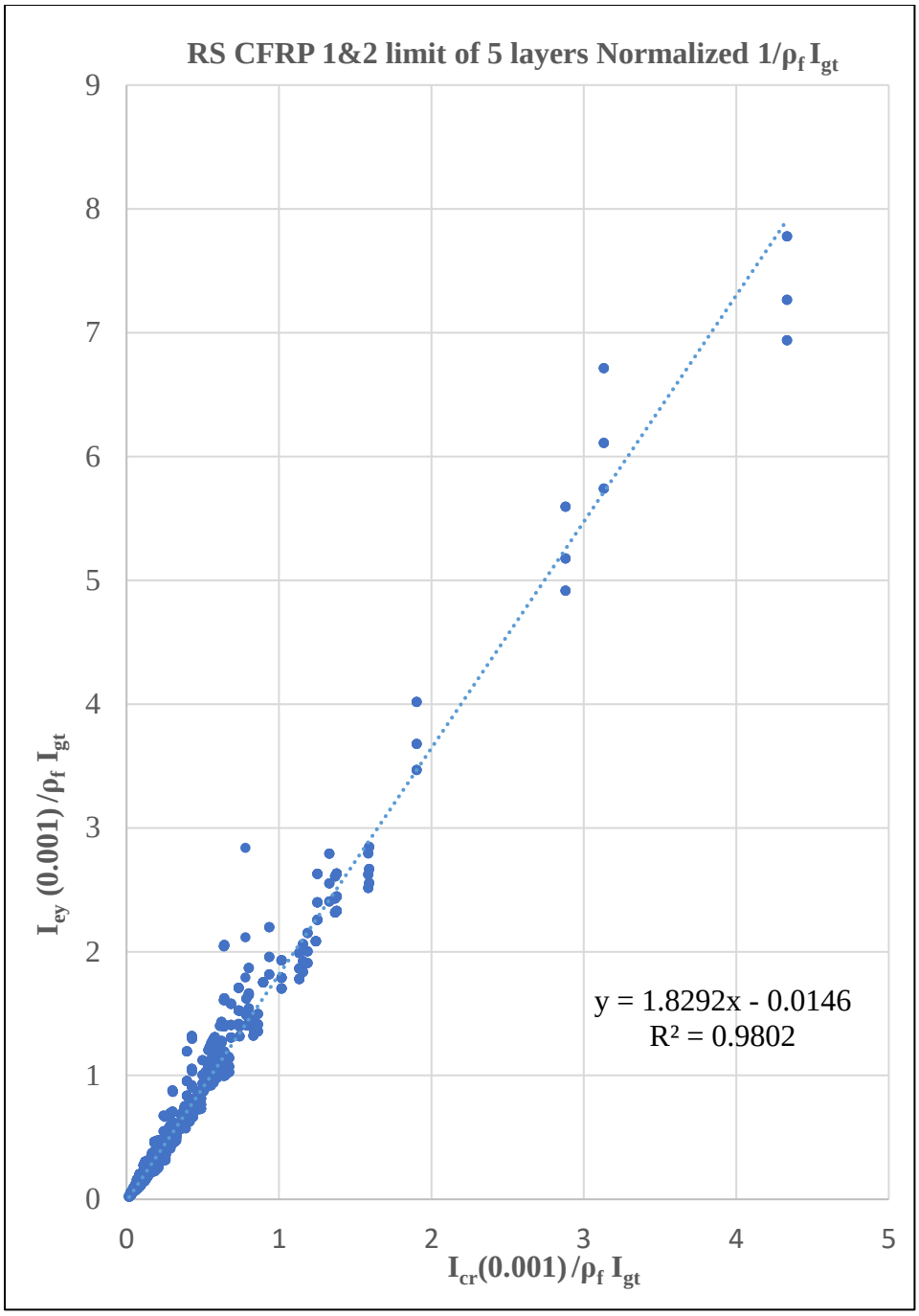

Figure 4-6: Rectangular section normalized by prestressing ratio divided by gross moment of inertia I_{ey} versus I_{cr} relationship for M-Brace CF130 & SikaWrap Hex 103C for L_a/L = 0.31, 0.375, and 0.44

Figure 4-7 indicates the parametric results for a rectangular PRC-FRP member strengthened with a maximum of 5 layers of CFRP Type 2 and a shear-span-to-span ratio of 0.44. Different colors and shapes are used to indicate the prestressing steel reinforcement ratio; for example, purple triangles for $\rho_{ps0.50}$ and green dashes for ρ_{psmax}. Series 1 in Figure 4-7 is all reinforcement ratios and is needed to show the linear series equation. The data points in Figure 4-7 indicate the lower prestressing reinforcement ratios have a higher linearized slope while higher prestressing reinforcement ratios produce a lower linearized slope on the graph. The other L_d/L and CFRP types indicated similar results.

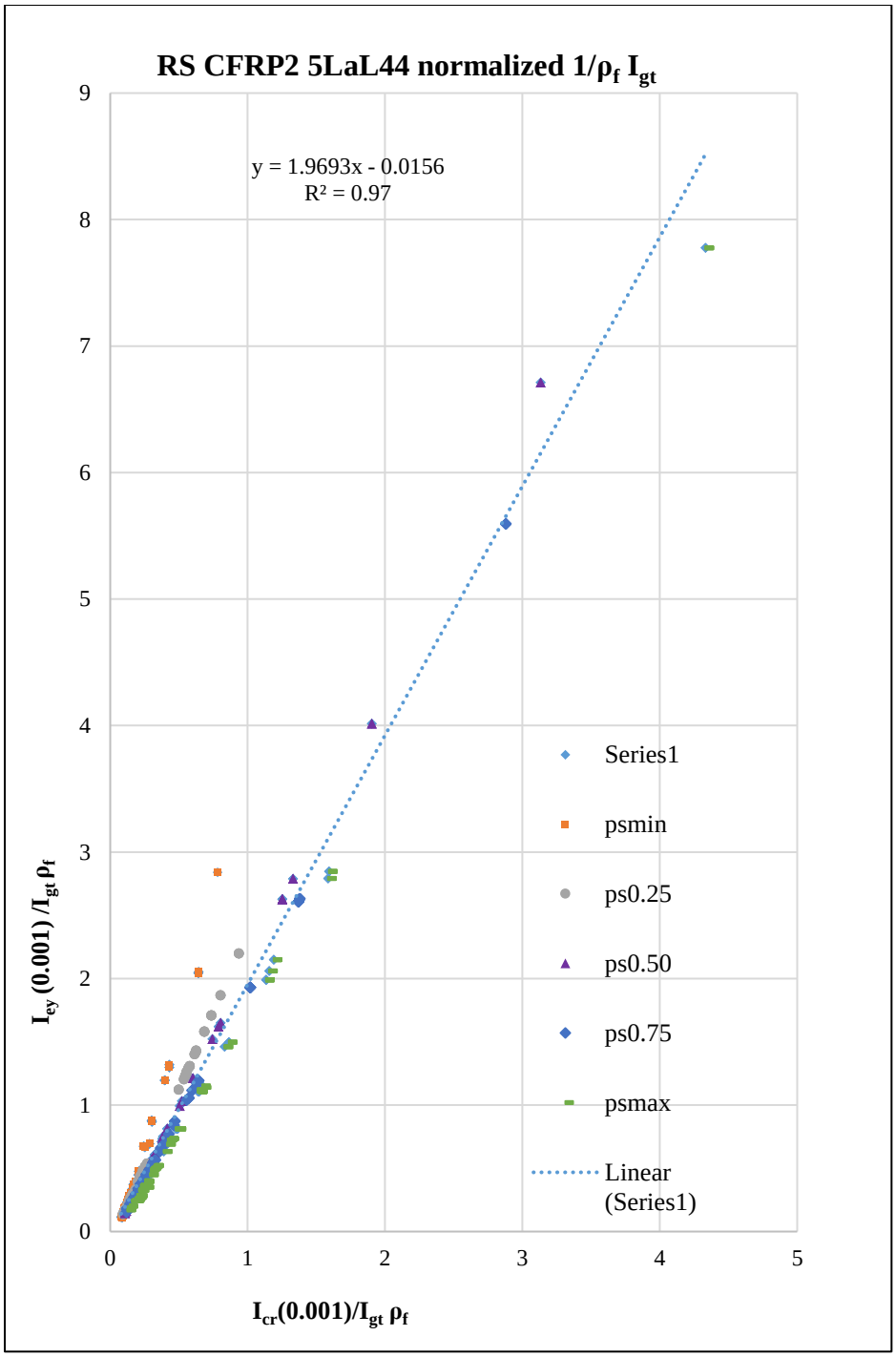

Figure 4-7: Rectangular section normalized by FRP ratio and gross moment of inertia, I_{ey} versus I_{cr} relationship for M-Brace CF130 and L_a/L = 0.44

While this linear correlation generates very good results, scatter still occurs as shown in Figure 4-6 and Figure 4-7. Therefore, a third parameter is used to normalize the yielding moment of inertia and cracking moment of inertia as given in Eq. 4-38. This parameter is the ratio of the axial stiffness of the FRP to the axial stiffness of the prestressing steel, λ, (Eq. 4-36) divided by the gross transformed moment of inertia, which resulted in an excellent linear correlation of $R^2 = 0.9886$ as shown in Figure 4-8.

$$\lambda = \frac{A_{ps}E_{ps}}{A_f E_f} \quad \textbf{Eq. 4-36}$$

$$\frac{I_{ey}}{I_{gt}\lambda} = 1.21\left(\frac{I_{cr}}{I_{gt}\lambda}\right) + 0.0287 \quad \textbf{Eq. 4-37}$$

$$I_{ey} = 1.209I_{cr} + 0.0287I_{gt}\lambda \quad \textbf{Eq. 4-38}$$

Similar to the second parameter, Figure 4-9 indicates the parametric results for a rectangular PRC-FRP member strengthened with a maximum of 5 layers of CFRP Type 2 and a shear-span-to-span ratio of 0.44. Different colors are used to indicated the prestressing steel reinforcement ratio. For example, orange square for ρ_{psmin} and blue diamond for $\rho_{ps0.75}$, etc. The data points in Figure 4-9 indicate that lower prestressing reinforcement ratios have a higher linearized slope while higher prestressing reinforcement ratios produce shallower linearized slope on the graph, as observed in Figure 4-7. The other L_a/L ratios and CFRP type indicates similar results.

Comparison of the effective moment of inertia compared to experimental results is given in proceeding section.

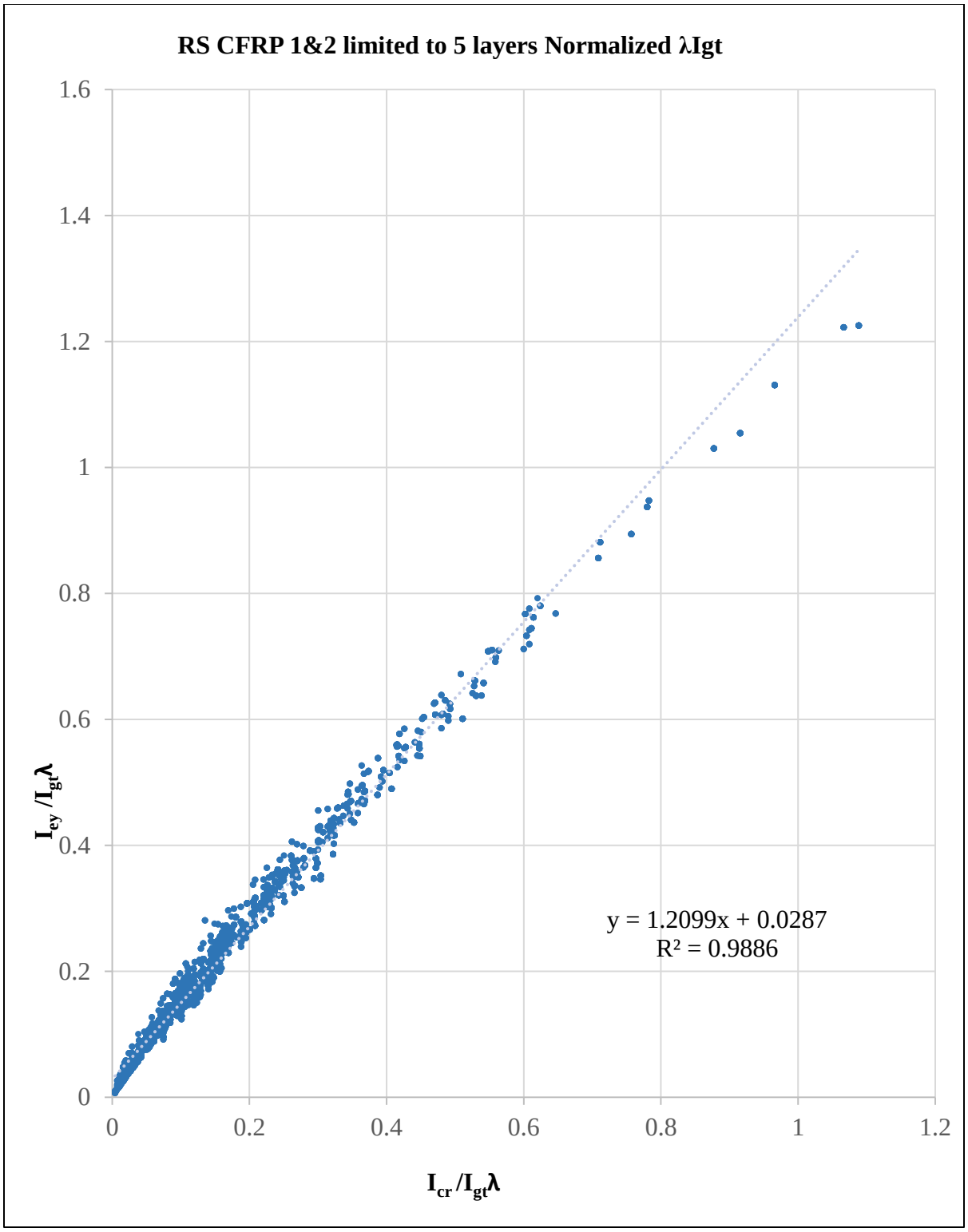

Figure 4-8: Rectangular beams I_{ey} versus I_{cr} relationship normalized by the ratio of the axial stiffness of the prestressing steel to the axial stiffness of the FRP, λ, divided by the gross moment of interia for M-Brace CF130 & SikaWrap Hex 103C for L_a/L = 0.31, 0.375, and 0.44

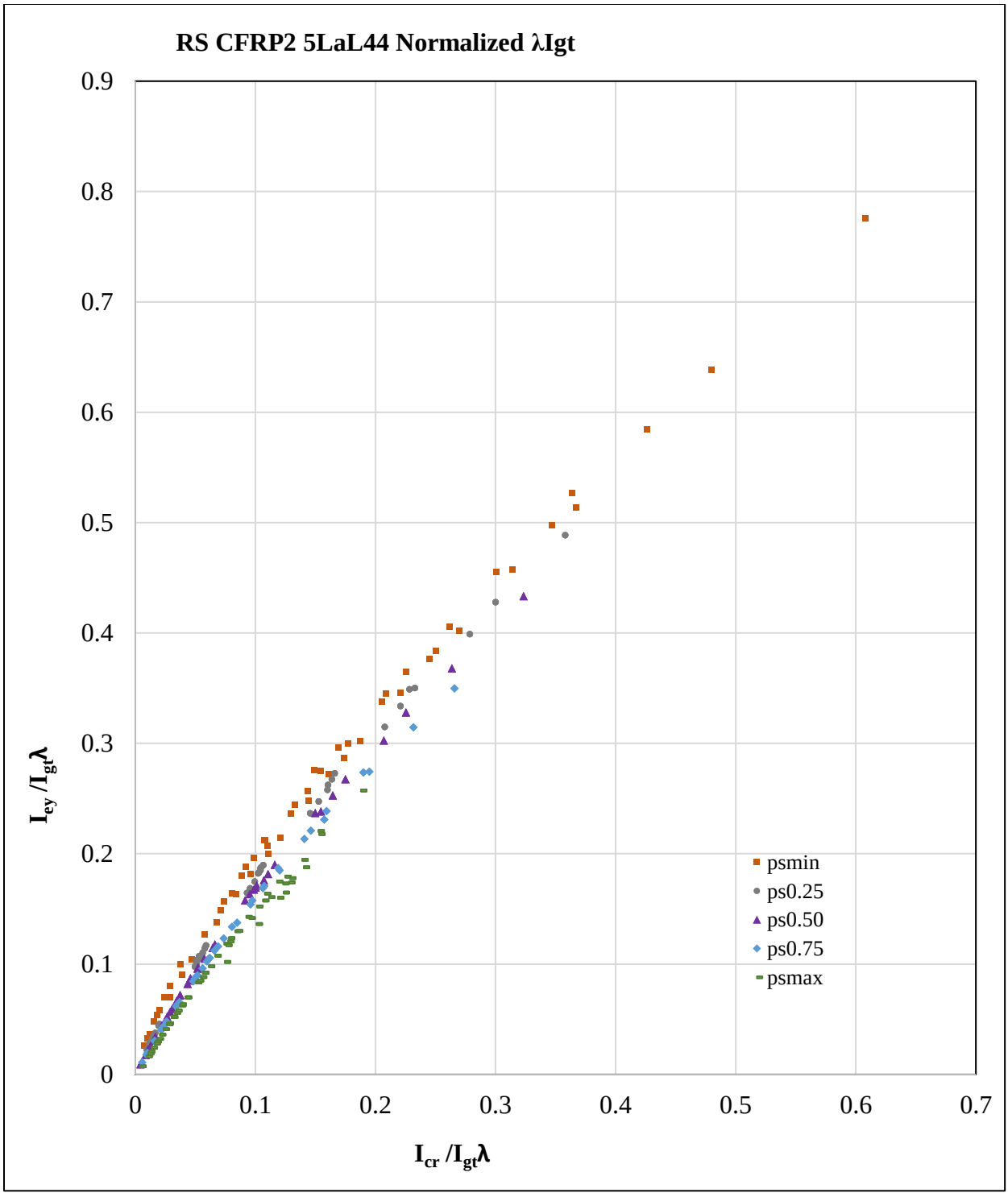

Figure 4-9: Rectangular beams I_{ey} versus I_{cr} relationship normalized by the ratio of the axial stiffness of the prestressing steel to the axial stiffness of the FRP, λ, divided by the gross moment of interia for M-Brace CF130 for L_a/L = 0.44

4.4 Applications

Studies addressing the deflection analysis of PRC beams strengthened with FRP are limited. Nonlinear sectional analysis, simplified by implementing a quad-linear (uncracked, post-cracked to mild steel yielding, mild steel yielding to prestress steel yielding, post yielding) moment-curvature response, is used to obtain closed form analytical deflection expressions for simply supported beams subjected to 4-point loading conditions. The experimental database used to evaluate the proposed equations is compiled from experiment results published in literature as shown in Table 4-4. The database consisted of six beams, four were from a PhD dissertation by Jun Y. Cha and two beams from a journal paper by Larson, Peterman, and Rasheed 2005 (Cha, 2001) (Larson, Peterman, & Rasheed, 2005). Cha beams are rectangular and Larson beams are T-beams.

Table 4-4: PRC-FRP beam database collected from literature.

Beam ID	h	h_f	b_w	b_f	A_{ps}	A_f	d_{ps}	d_f	f'_c	E_c	f_{ps}	E_{ps}	f_f	E_f	L	L_a
	mm	*mm*	*mm*	*mm*	*mm²*	*mm²*	*mm*	*mm*	*MPa*	*MPa*	*MPa*	*MPa*	*MPa*	*MPa*	*mm*	*mm*
Cha B2	250	-	150	-	54.8	30.8	190	250.1	35	28000	1862	192300	4093	259000	3000	1000
Cha B3	250	-	150	-	54.8	46.2	190	250.2	35	28000	1862	192300	4093	259000	3000	1000
Cha B5	250	-	150	-	54.8	30.8	190	250.1	70	39600	1862	192300	4093	259000	3000	1000
Cha B6	250	-	150	-	54.8	46.2	190	250.2	70	39600	1862	192300	4093	259000	3000	1000
Larson B2	356	102	102	457	110	29.3	381	457.1	49	33000	1862	195100	3868	227500	4800	1830
Larson B4	356	102	102	457	110	35.6	381	457.2	49	33000	1862	195100	3868	227500	4800	1830

***non-prestressed reinforcement (compression or tension) is not shown.**

4.4.1 Cha (2001) beams

To verify the parametric study response, a fully nonlinear analysis of the same rectangular-beam strengthened with CFRP is performed using testing results from beams tested by Cha (2001) in which they examined six, pretensioned, straight-strand, bonded PRC rectangular beams (Cha, 2001). Of the six beams tested, beams B1 and B4 were the control beams, unstrengthened; while the remaining beams (B2, B3, B5, and B6) were strengthened with one type of CFRP sheets. Therefore, Cha B2, Cha B3, Cha B5, and Cha B6 are used for this study. The beams were tested in four-point bending with a clear span of 3000 mm (118 inches) and a shear span of 1000 mm (39 inches). The Forney testing machine was used with load applied in increments of 4.45 kN (1 kip) prior to cracking and 2.22 kN (0.5 kips) after cracking load was reached. Deflections were measured by mechanical dial gauges with 76mm (3 inch) travel and 0.0254 mm (0.001) reading accuracy mounted at the longitudinal centerline of the beam and located at midspan and at each loading point. The beams were strengthened by applying CFRP to the flipped beams' surface and curing for two weeks minimum.

Cha B1 and Cha B4, the control beams, were 150 mm (5.9 inch) wide by 250 mm (9.8 inch) high with a concrete strength at 28 days from standard cylinder testing of 37.0 MPa (5,366 psi) and 69.54 MPa (10,086 psi), respectively. The beams were reinforced with bonded prestressing strands conforming to ASTM A416 and non-prestressed reinforcement conforming to ASTM A616. The prestressing steel was seven-wire strand with a nominal diameter of 10 mm (3/8 inch) and an ultimate strength of 1862 MPa (270 ksi). One prestressing tendon, located 190 mm (7.48 inch) from the top surface, was used and prestressing was applied by a single wire hydraulic Freyssinet jack operated by a hand pump. The two, non-prestressed steel bars had a 10

mm (3/8 inch) diameter with a specified yield strength of 414 MPa (60 ksi). The two No. 3 (10 mm) bars were placed 215 mm (8.46 inch) from the extreme fiber in compression.

Cha B2 and Cha B3, beams with concrete compressive strength of 35 MPa (5,076 psi), were strengthened with two layers and three layers, respectively, of 0.11 mm (0.004 inch) thickness by 140 mm (5.5 inches) wide CFRP. Cha B5 and Cha B6, beams with concrete compressive strength of 70 MPa (10,153 psi), were strengthened with two layers and three layers, respectively, of 0.11 mm (0.004 inch) thickness by 140 mm (5.5 inches) wide CFRP. The effective prestress force for Cha B2, Cha B3, Cha B5, and Cha B6 beams were given as: 55.6 kN (12.5 kip), 59.7 kN (13.4 kip), 60.6 kN (13.6 kip), and 62.2 kN (14.0 kip), respectively. Load, midspan deflection, and strains were recorded while loading the beams to failure. Cha B2, Cha B3, Cha B5, and Cha B6 failure modes are debonding of carbon composite, crushing of concrete, rupture of CFRP plate, and debonding of CFRP plate, respectively.

Cha (2001) presented graphs with experimental moment versus experimental strains for the various materials within the PRC-FRP beams tested. These graphs have been digitized and this data is used to create Figure 4-10 that displays the experimental moment versus the experimental strains of the top concrete strain (extreme fiber in compression), pre-tensioned prestressing steel strain, the mild steel (non-prestressing) strain, and the FRP strain for Cha B2. This experimental data is used to compare the analytical formula presented herein of the moment versus strain of the different materials.

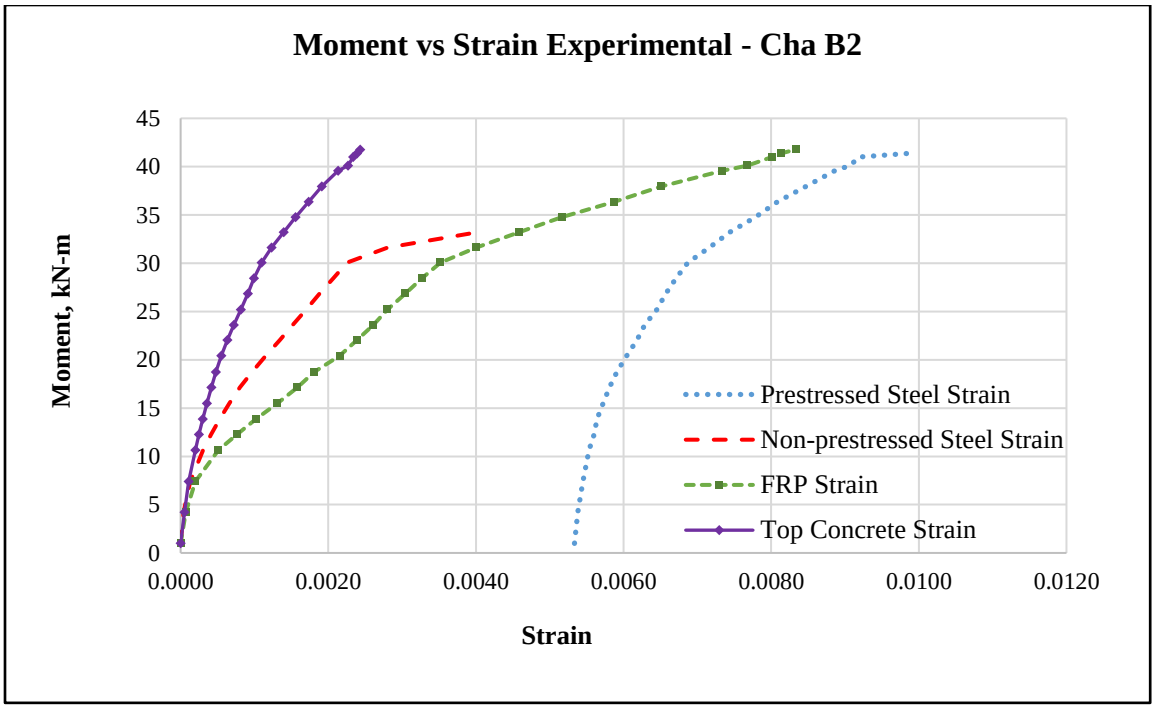

Figure 4-10: Experimental moment versus strain for Cha B2

Figure 4-11 through Figure 4-14 illustrate the moment versus strain of Cha B2 based on the strains extrapolated from Cha (2001). The total superimposed, cracking load noted for Cha B2 was 12.49 kN (2.81 k). When examining Figure 4-11, the experimental top strain (strain in the extreme fiber in compression – concrete strain, ε_c, is larger than the analysis strain at a superimposed cracking moment equal to 6.25 kN-m (4.61 k-ft). At the cracking load noted during testing, the experimental strain is given as 0.000105 and the analysis strain determined in this study is 0.000085 in addition to a negative strain of 0.000005 due to prestressing, which gives a total cracking analysis strain of 0.0001. The experimental strain does not include the strain due to the prestressing since the strain gauges were placed after prestressing was complete (initial strain equals 0). Furthermore, the strain reported Cha (2001) does not clearly indicate if the self-weight of the beam is included, but most likely the strain due to the self-weight is not included in the reported strain values. The analysis strain of the concrete in the extreme compression fiber is very close to the experimental strain at this load. The analysis predicts a

superimposed cracking moment of 13.29 kN-m (9.80 k-ft), cracking load of 6.65 kN (1.50 k). The moment-curvature analysis is displacement controlled. Therefore, it has a flat line or even a drop as the beam transitions from gross to partially cracked properties by means of displacement increase, as seen in Figure 4-11 through Figure 4-14.

The next critical load is the yield load. The non-prestressing steel yields prior to the prestressing steel for Cha B2 as shown in Figure 4-10 by the plateau, flatting of the non-prestressing steel curve (increase in strain with little increase in applied moment). The superimposed yield load given by Cha (2001) is 54.82 kN (12.32 k), 27.4 kN-m moment (20.21 k-ft). Per analysis with the first yield governed by mild steel, the superimposed yield load is 53.25 kN (11.97 k), 26.63 kN-m (19.64 k-ft). The experimental, top concrete strain, taken from the moment-strain graph, is 0.00099 which is slightly larger than the strain produced by analysis 0.00094. From analysis, prestressing steel yielding occurs at 58.0 kN-m (38.36 k-ft) or 76.90 kN (17.29 k). Examining Figure 4-11, a change in slope of the analysis moment-strain curve occurs at yielding of the mild steel and again at yielding of the prestressing steel is more pronounced than the experimental.

The experimental ultimate load is 81.68 kN (18.36 k), ultimate moment equal to 40.84 kN-m (30.12 k-ft), with experimental strain of 0.00243 and analysis strain of 0.00217, at the same load. Cha B2 failure mode was debonding of the carbon composite (CFRP) prior to concrete crushing; therefore, the top strain does not reach 0.003.

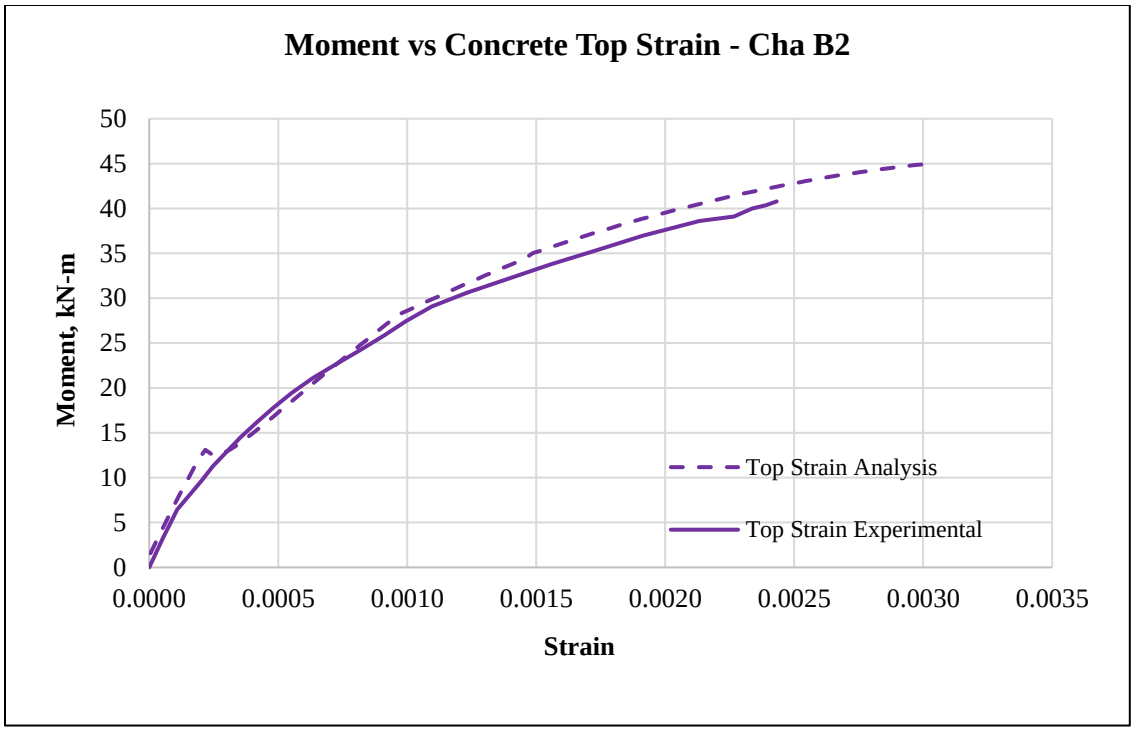

Figure 4-11: Moment versus concrete top strain for experimental and analytical curves of Cha B2 beam

Figure 4-12 indicates the moment versus prestressing steel strain for the experimental and analysis of Cha B2. The initial prestressing steel strain for experimental and analysis are 0.005335 and 0.005304, respectively. Similar to the top strain, the experimental strain (0.00545) is higher than the analysis strain (0.00534) for the prestressing steel at the superimposed cracking moment. Since the non-prestressing steel yields prior to the prestressing steel, two yield points are apparent in Figure 4-12 at approximately 27 kN-m (19.91 k-ft) and 38 kN-m (28.02 k-ft). At the experimental noted first yield, the strain in the prestressing steel was given as 0.00671, which is slightly lower than the analysis strain of 0.00702. The change in slope for the yielding of the non-prestressing steel and again for the prestressing steel is more pronounced in the Figure 4-12 than Figure 4-11. The experimental ultimate moment of 40.84 kN-m (30.12 k-ft) is extrapolated from Cha 2001 with experimental strain of 0.00995 and analysis strain of 0.01067. Cha B2

failure mode was debonding of the carbon fiber composite (CFRP). The analysis determined an ultimate moment of 45 kN-m (33 k-ft) where the experimental recorded 41 kN-m (30 k-ft).

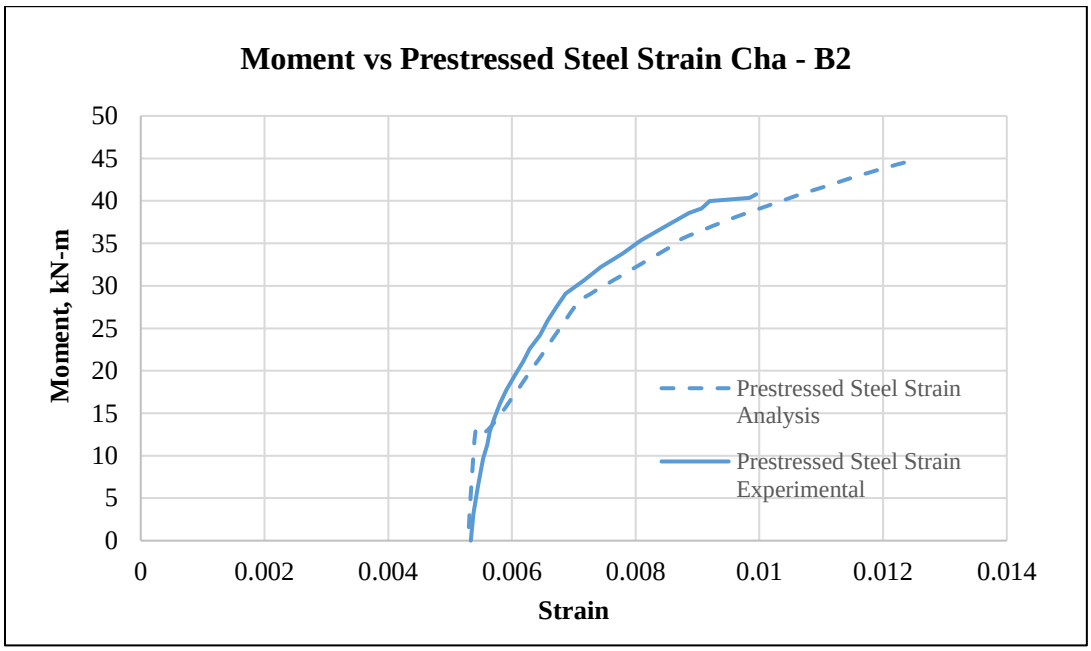

Figure 4-12: Moment versus pre-tensioned prestressing steel strain for experimental and analytical response of Cha B2 beam

Figure 4-13 indicates the moment versus non-prestressing steel strain for the experimental curve, shown as the solid line, and the analysis, shown as a dashed line. The initial experimental strain in the non-prestressing steel is given as 0.0 where the analysis produced a strain of - 0.000065, the negative strain is produced by the prestressing of the beam. At the cracking load, the experimental strain in the non-prestressing steel is 0.00013 and the analysis produced a strain of -0.00001. The analysis strain is lower than the experimental strain based on how the strain gauges are taking readings in the uncracked region. Once the section has cracked, the slope of the moment-strain lines for the experimental and analysis are very similar as shown in Figure 4-14. The yield strain of the non-prestressing steel is 0.00206 and 0.00200 for experimental response and analysis, respectively. The experimental strain stops at 0.004, prior to the prestressing steel yielding. Since most strain gauges have a limit of 0.005 and the

experimental strains were not recorded beyond 0.004, no comparison of experimental strain and analysis strain for non-prestressing steel at ultimate is performed. The behavior of the non-prestressed steel is elastic-perfectly plastic (i.e. it shows a flat plateau when its stress-strain response is plotted). However, in Figure 4-13, the graph relates the applied sectional moment versus mild steel strain. Since the applied moment continuously increases due to the stiffness of FRP and prestressing steel beyond the yielding point of mild steel and the strain in mild steel also increases after yielding of its reinforcement, the response appears to be hardening as shown by the analysis. On the other hand, the experimental curve is plotted to have a flat plateau, which is clearly erroneous trend for this type of graphs since the sectional moment applied continues to increase with increasing the steel strain.

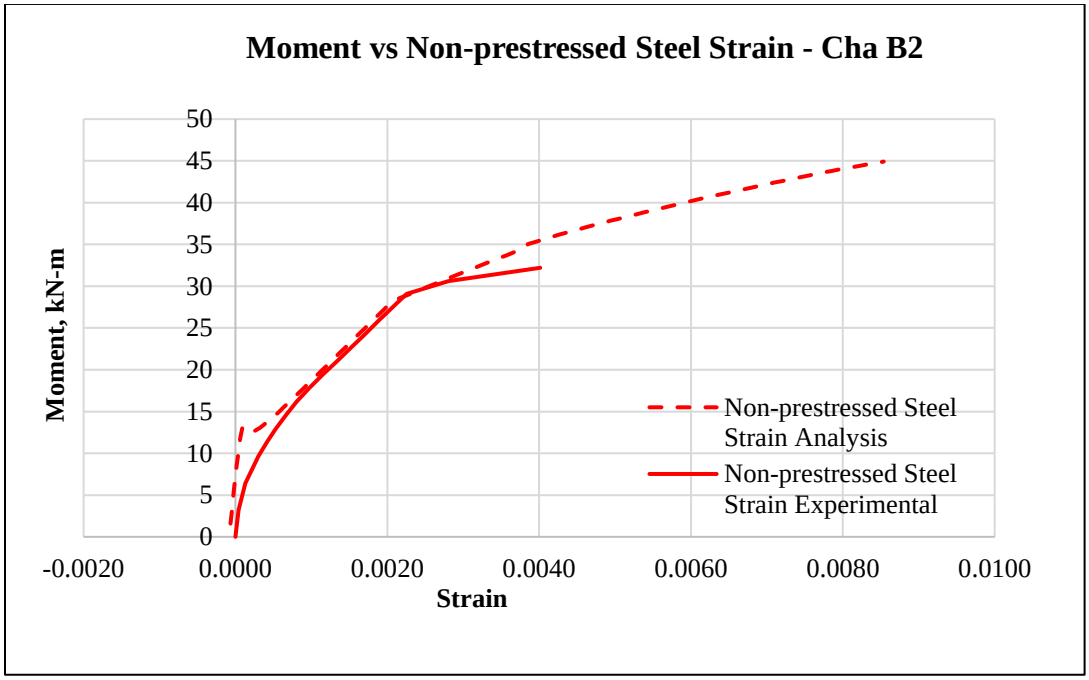

Figure 4-13: Moment versus non-prestressing steel strain for experimental and analytical response of Cha B2 beam

Figure 4-14 designates the moment versus FRP strain for Cha B2 with the analysis shown as a solid line. The initial experimental strain of the FRP is specified as 0.0; the initial analysis strain is 0.000097. The experimental strains are higher than analysis strains when compared: the cracking strain of 0.00019 experimental to 0.00017 analysis, the first yield strain of 0.00327 experimental to 0.00265 analysis, and the ultimate strain of 0.00834 experimental to 0.00784 analysis. When examining Figure 4-14, some softening of the experimental beam prior to cracking appears to have occurred, which is common with prestressed beams. Otherwise, the analysis correlates very well to the experimental response.

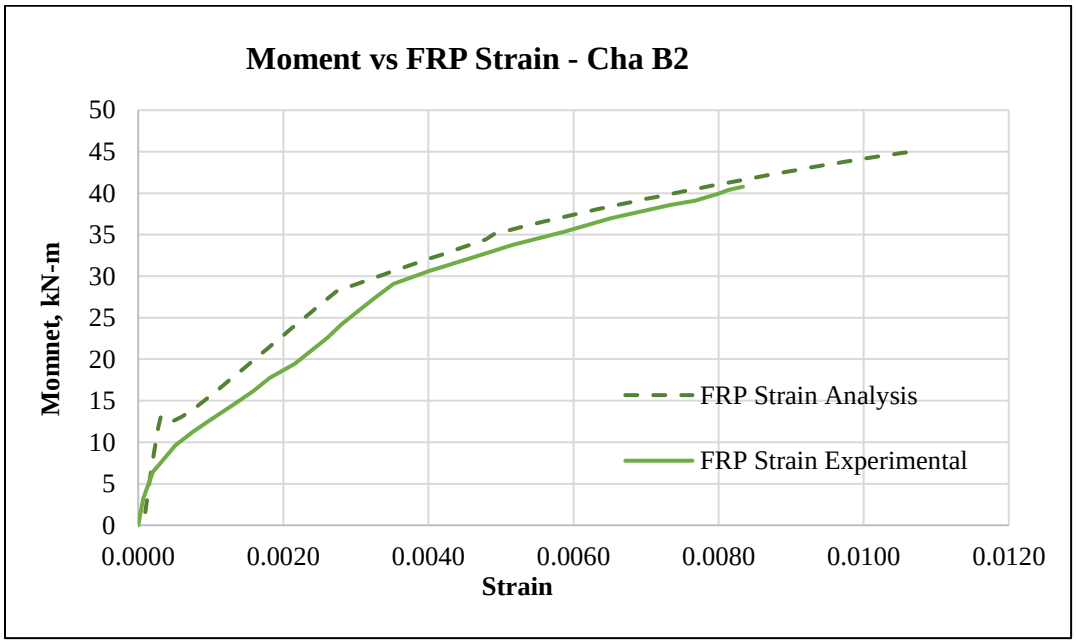

Figure 4-14: Moment versus FRP strain for experimental and analytical curves Cha B2 beam

As previously stated, the failure mode of Cha B2 is debonding of carbon fiber composite at 81.68 kN (18.36 k), with yielding load of 54.82 kN (12.32 k), cracking load equaled 12.49 kN (2.81 k).

Table 4-5 displays the experimental strains and analysis strains for these given loads.

Table 4-5: Cha B2 experimental and analysis comparison of strains

Cha B2 strain comparisons excluding tension stiffening								
strains	Initial strain P* = 0		Cracking strain P* = 12.49 kN (2.81 k)		Yield strain^{+} P* = 54.82 kN (12.32 k)		Ultimate strain P* = 81.68 kN (18.36 k)	
	Exp.	Analyt.	Exp.	Analyt.	Exp.	Analyt.	Exp.	Analyt.
ε_c	0	0.000005	0.00011	0.00009	0.00099	0.00094	0.00243	0.00217
ε_{ps}	0.005335	0.005304	0.00545	0.00534	0.00671	0.00702	0.00995	0.01067
ε_s	0	-0.000065	0.00013	-0.00001	0.00206	0.00200	NR	0.00629
ε_{frp}	0	0.000097	0.00019	0.00017	0.00327	0.00265	0.00834	0.00784
*indicates superimposed load $^{+}$indicates first yield (non-prestressing steel yielded prior to prestressing) NR – not recorded								

Figure 4-15 shows the moment curvature response of Cha B2 beam with the experimental curve as a solid line and the analysis as a dashed line. The analysis underestimates the curvature, but the slope from cracking to first yield and first yield to ultimate are almost identical. Again, the behavior prior to cracking, possibly due to microcracking, differential shrinkage, or prestress losses, is nonlinear for the experimental beam whereas for analysis it is assumed that the beam has linear behavior.

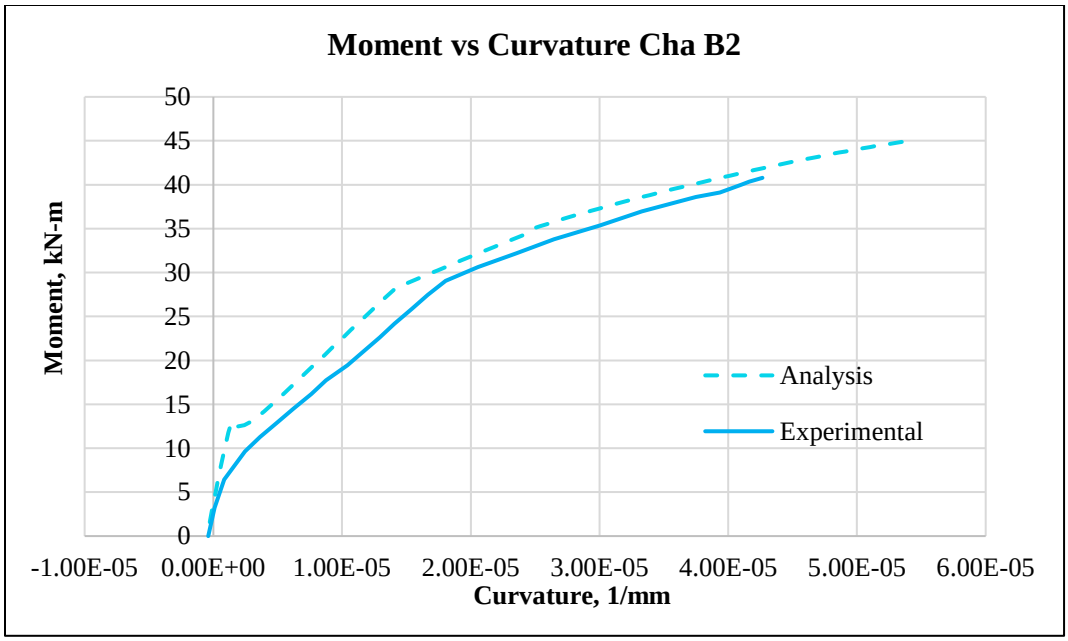

Figure 4-15: Moment versus curvature for experimental and analytical curves Cha B2 beam

Figure 4-16 illustrates the load-deflection of Cha B2 beam up to ultimate capacity, with the experimental response as a solid line and the numerical response as a short dashed line, analytical response as a long dashed line. The analysis slightly overestimates the deflection after the section has cracked; otherwise, the analysis gives an excellent correlation to the experimental curve. The analytical line takes the first yield of the non-prestressing steel into account. The behavior before cracking, possibly due to concrete shrinkage effects, is nonlinear for the experimental beam; whereas for, analysis it is assumed that the beam has linear behavior.

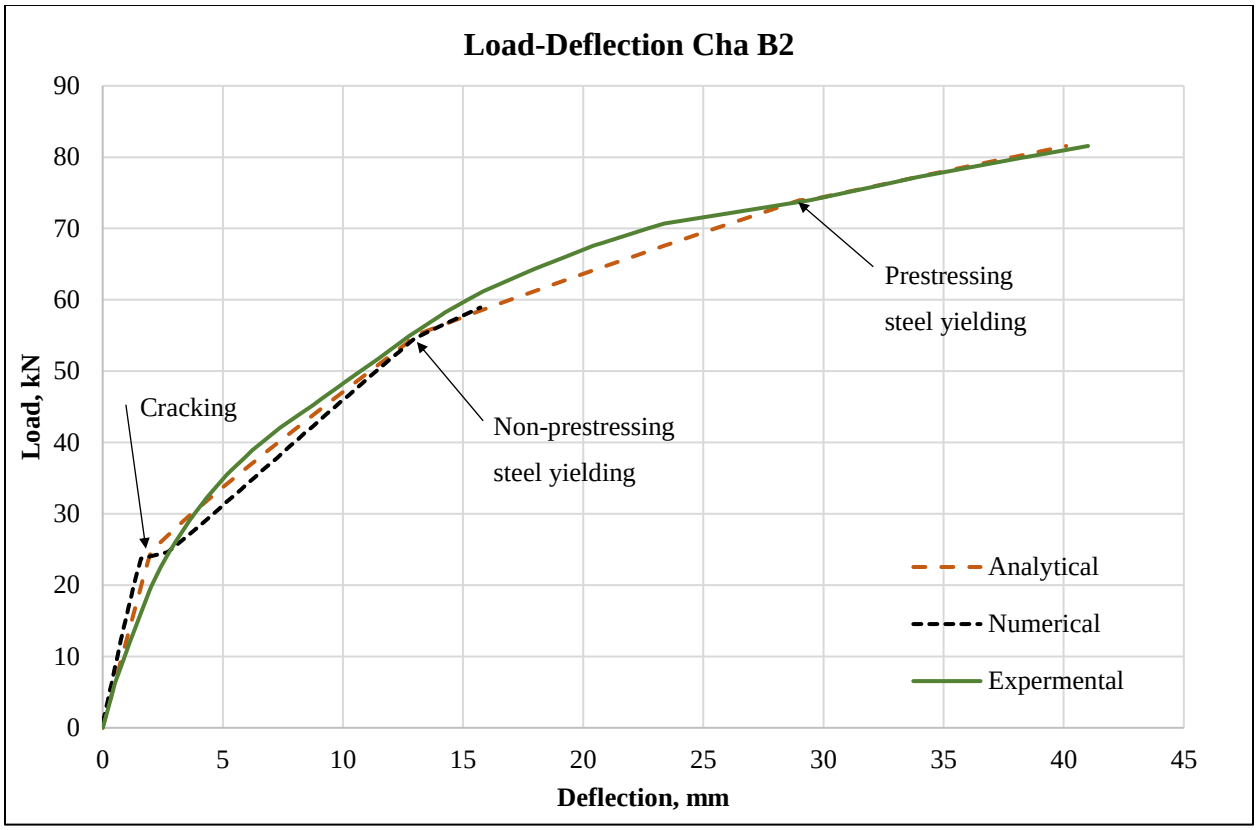

Figure 4-16: Load versus deflection for experimental and analysis curves of Cha B2 beam

The second beam studied is Cha B3. The graphs of experimental moment versus experimental strain for Cha B3 were digitized to create Figure 4-17. This experimental data is used to compare the analytical formula presented herein of the moment versus strain of the different materials. Failure mode of Cha B3 was crushing of the concrete at 108.98 kN (24.5 k), with yielding load of 63.83 kN (14.35 k) and cracking load equaled 13.45 kN (3.02 k).

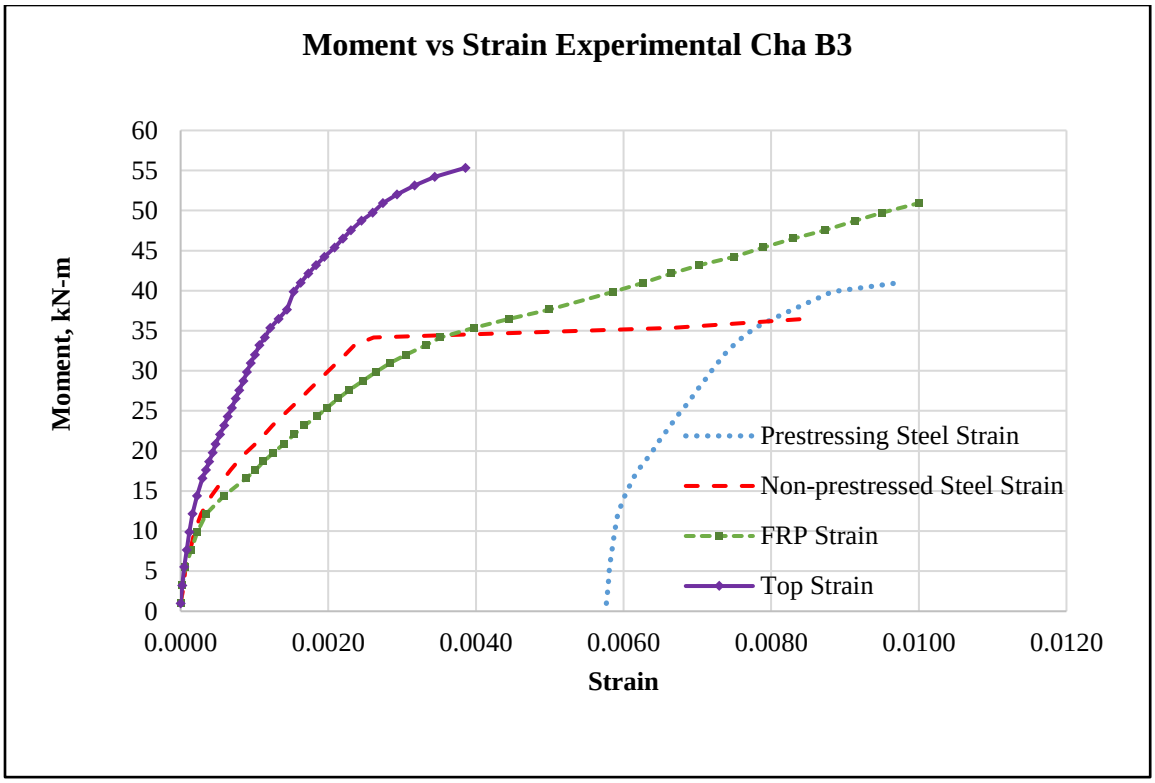

Figure 4-17: Experimental moment versus strain for Cha B3 beam

Figure 4-18 indicates the moment versus concrete top strain for the experimental and analysis, with and without tension stiffening, of Cha B3. The initial top strain for experimental and analysis is 0.0 and 0.000003, respectively. At the experimental superimposed cracking moment of 13.45 kN-m (9.92 k-ft), the experimental strain (0.00022) is lower than the analysis strain without tension stiffening (0.00034) for the concrete top fiber strain, but is very close to the top strain for the analysis including tension stiffening (0.00025). The analysis determined the section cracking at a superimposed moment of 13.39 kN-m (9.88 k-ft). Hence, the shift in the strain from going from gross moment of interia to cracked moment of interia for the analysis without tension stiffening included. Considering this shift, the top strains of the analysis matches the experimental strain very well. The analysis stops at a useable concrete strain of 0.00300 where the experimental noted a concrete strain of 0.00386. This is why the analysis curve stops while the experimental response continues. Table 4-6 indicates the strains for the various

materials. An ultimate load equal to 95.5 kN (21.47 k) or an ultimate moment of 47.75 kN-m (35.22 k-ft) is used for comparison purposes.

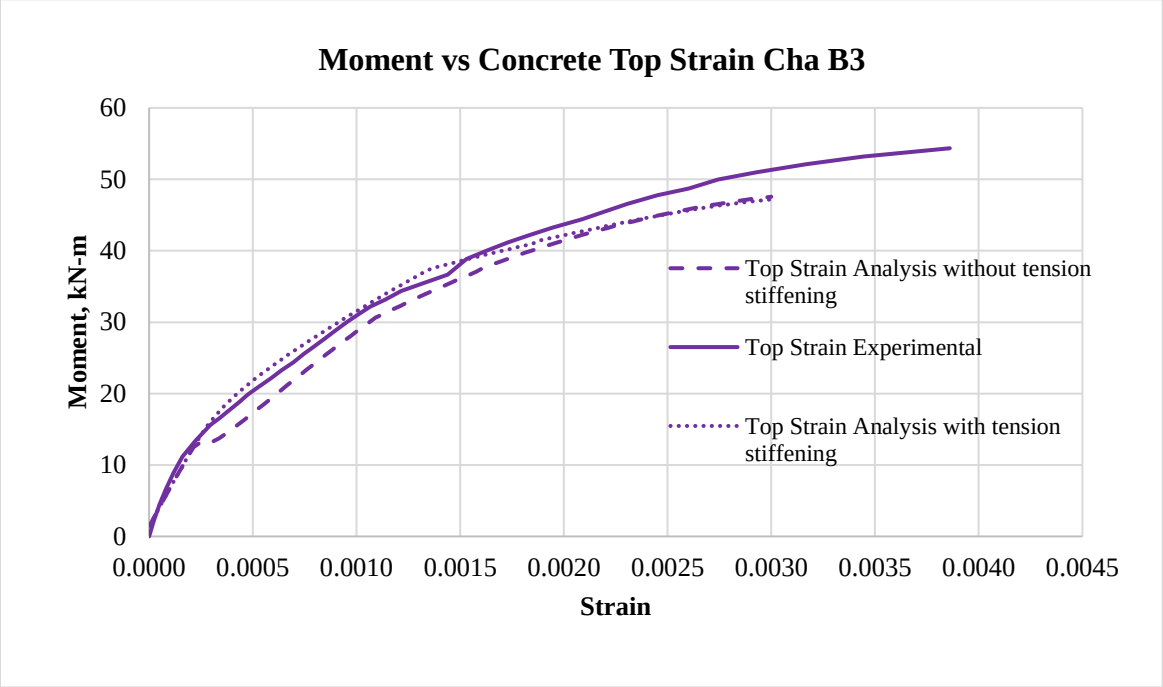

Figure 4-18: Moment versus concrete top strain for experimental and analytical curves of Cha B3 beam

Figure 4-19 indicates the moment versus prestressing steel strain for the experimental and analysis, with and without tension stiffening included, of Cha B3 beam. The initial prestressing steel strain for experimental and analysis are 0.005768 and 0.005626, respectively. The experimental strain (0.00602) is higher than the analysis strain without tension stiffening included (0.00593) for the prestressing steel at the superimposed cracking moment. Since the non-prestressing steel yields prior to the prestressing steel, two yield points are apparent in Figure 4-20 at approximately 30 kN-m (22.1 k-ft) and 43 kN-m (31.7 k-ft). At the experimental response noted first yield, the strain in the prestressing steel was given as 0.00746, which is slightly lower than the analysis strain, not including tension stiffening, of 0.00763. The

experimental prestressing steel strain gauges stopped recording data at a superimposed moment of 40 kN-m (29.5 k-ft). It is apparent that the prestressing steel is yielding at this moment due to the increased strain with little increase in moment. After cracking, the analysis curve not including tension stiffening follows the experimental very nicely.

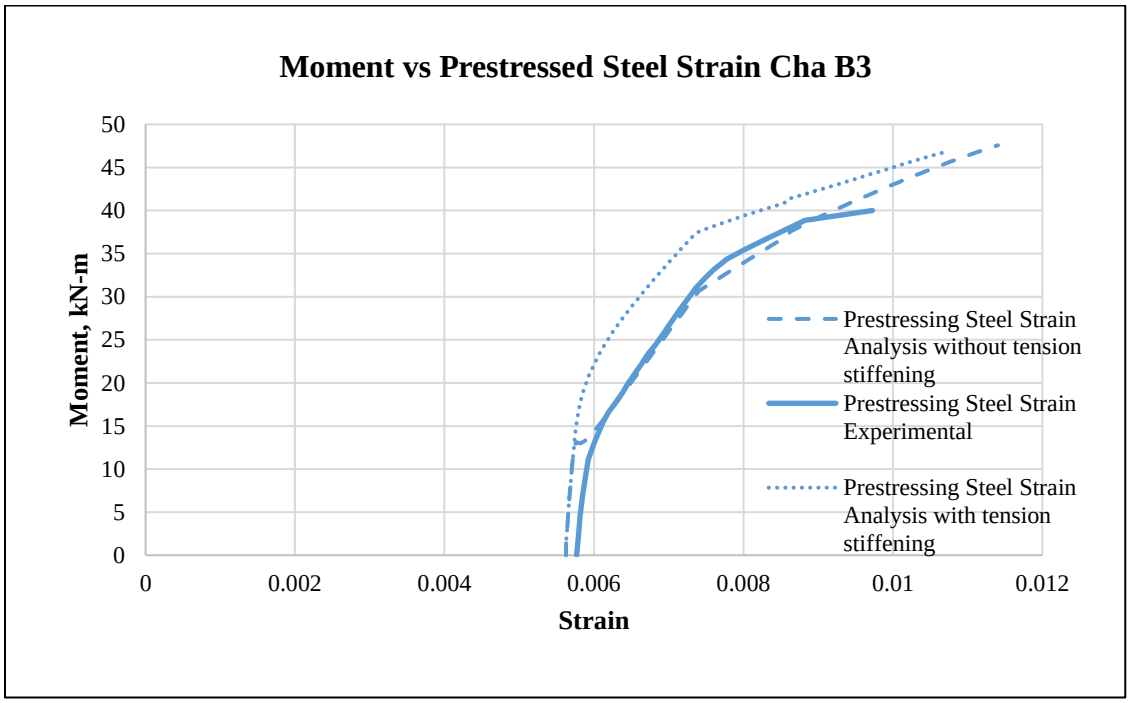

Figure 4-19: Moment versus pre-tensioned prestressing steel strain for experimental and analytical curves of Cha B3 beam

Figure 4-20 indicates the moment versus non-prestressing strain for the experimental response, and the analysis with and without tension stiffening. The initial experimental strain in the non-prestressing steel is given as 0.0 whereas the analysis produced a strain of -0.000078, the negative strain is produced by the prestressing of the beam. At the cracking load, the experimental strain in the non-prestressing steel is 0.00042 and the analysis, not including tension stiffening, produced a strain of 0.00031 that correlates to a total change of strain of 0.0004. Once the section has cracked, the slope of the moment-strain lines for the experimental

and analysis are almost identical as shown in Figure 4-20. Using the experimentally documented yield load, the yield strain of the non-prestressing steel is 0.00239 and 0.00234 for experiment and analysis without tension stiffening, respectively. The experimental strain of the non-prestressed steel stops at 0.0084. The behavior of the non-prestressed steel is elastic-perfectly plastic (i.e. it shows a flat plateau when its stress-strain response is plotted). However, in Figure 4-20, the graph relates the applied sectional moment versus mild steel strain. Since the applied moment continuously increases due to the stiffness of FRP and prestressing steel beyond the yielding point of mild steel and the strain in mild steel also increases after yielding of its reinforcement, the response appears to be hardening as shown by the analysis. On the other hand, the experimental curve is plotted to have a flat plateau, which is clearly erroneous trend for this type of graphs since the sectional moment applied continues to increase with increasing the steel strain.

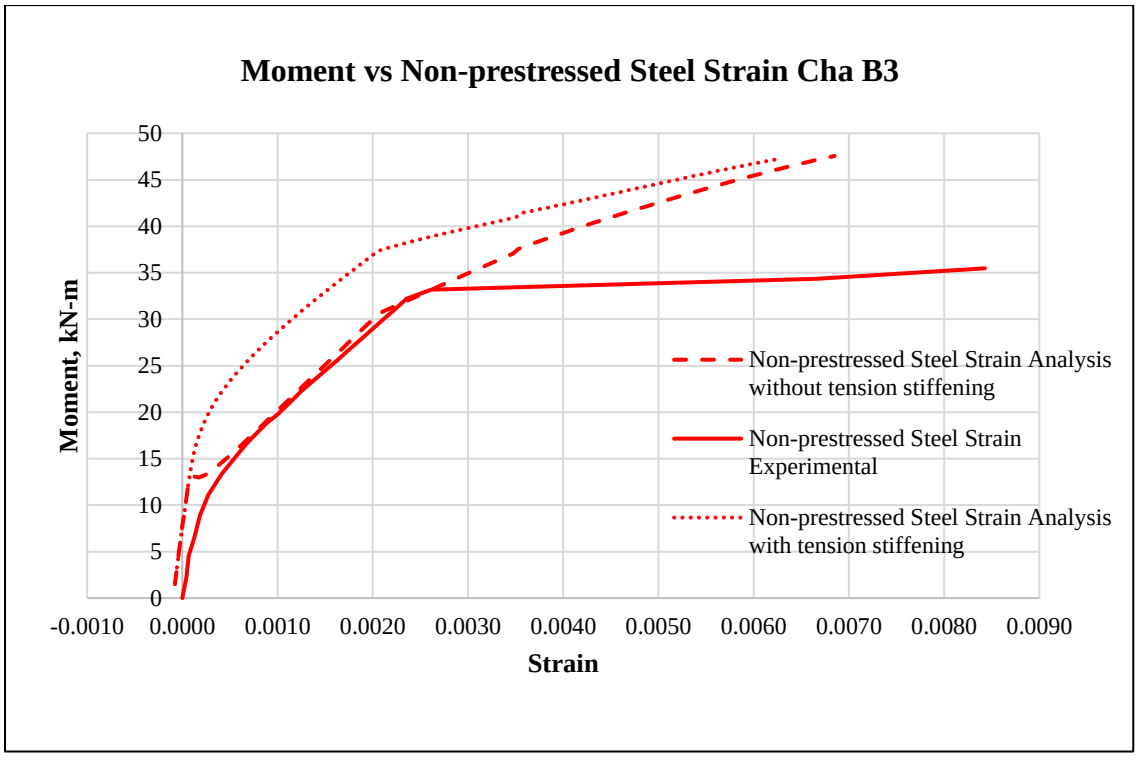

Figure 4-20: Moment versus non-prestressing steel strain for experimental and analytical curves of Cha B3 beam

Figure 4-21 designates the moment versus FRP strain for Cha B3 beam with the experimental shown as a solid line. Analytical results are shown by short-dashed line for strains including tension stiffening and long-dashed line for strains excluding tension stiffening. The initial experimental strain of the FRP is specified as 0.0; the initial analysis strain is 0.000079. The experimental cracking strain, 0.00059, is slightly higher than the analysis cracking strain, without tension stiffening, 0.00054. The experimental strains are larger than the analysis strains: the first yield strain of 0.00325 compared to 0.00268 (without tension stiffening), and the ultimate strain of 0.00914 to 0.00851 (without tension stiffening). When examining Figure 4-21, the analysis correlates very well to the experimental curve.

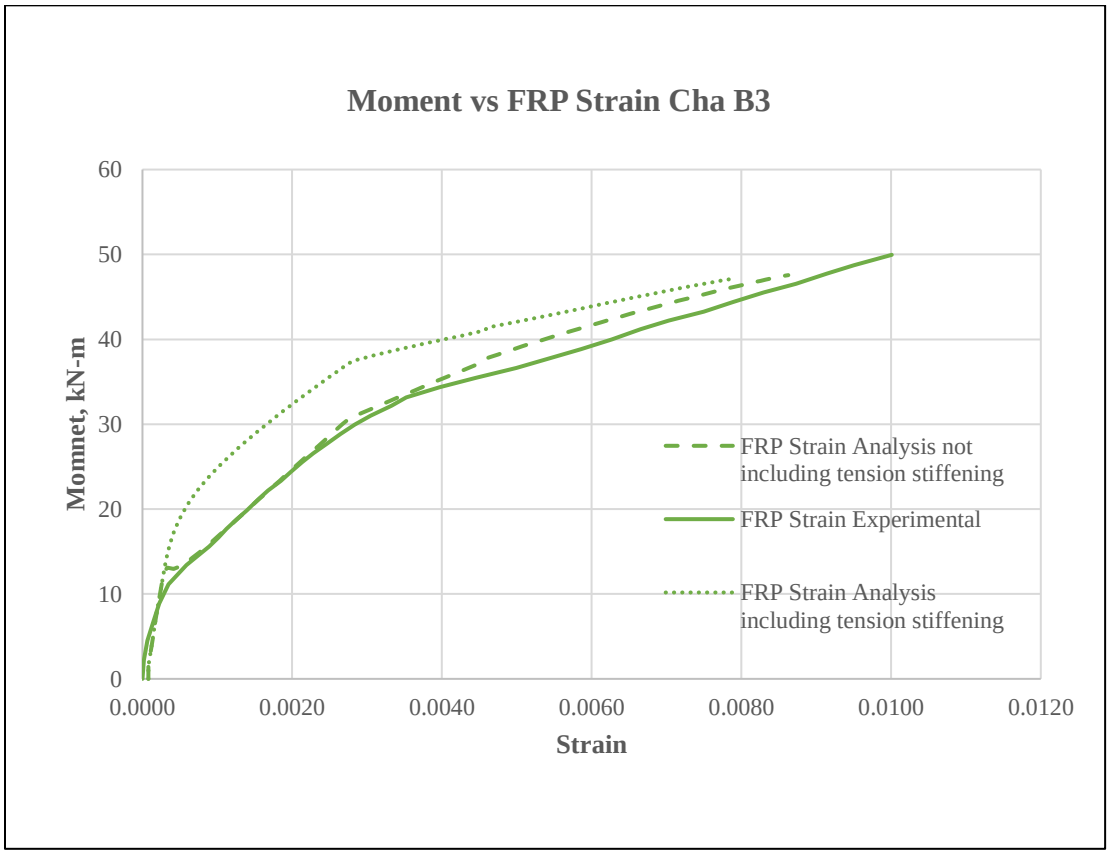

Figure 4-21: Moment versus FRP strain for experimental and analytical curves of Cha B3 beam

As previously stated, the failure mode of Cha B3 beam is concrete crushing at 108.98 kN (24.50 k), with yielding load of 63.83 kN (14.35 k), cracking load equaled 26.9 kN (6.04 k). Table 4-6 displays the experimental strains and analysis strains for these given loads.

Table 4-6: Cha B3 experimental and analysis comparison of strains

Cha B3 strain comparisons without strain hardening								
strains	Initial strain P* = 0		Cracking strain P* = 26.90 kN (6.04 k)		Yield strain^{+} P* = 63.83 kN (14.35 k)		Ultimate strain** P* = 95.50 kN (21.47 k)	
	Exp.	Analyt.	Exp.	Analyt.	Exp.	Analyt.	Exp.	Analyt.
ε_c	0	0.000003	0.00022	0.00032	0.00106	0.00118	0.00386	0.00300
ε_{ps}	0.005768	0.005626	0.00602	0.00593	0.00746	0.00763	NR	0.01133
ε_s	0	-0.000078	0.00042	0.00031	0.00239	0.00234	NR	0.00676
ε_{frp}	0	0.000079	0.00059	0.00054	0.00325	0.00309	0.00914	0.00851

*indicates superimposed load

**indicates strains based on experimental load lower than the ultimate noted in testing of 108.98 kN (24.50 k)

$^{+}$indicates first yield (non-prestressing steel yielded prior to prestressing)

NR – not recorded

Figure 4-22 illustrates the moment curvature of Cha B3 with the experimental as a solid line and the analysis including tension stiffening as a short-dashed line, and the analysis excluding tension stiffening as a long-dashed line. The analysis excluding tension stiffening estimates the curvature extremely well. Since the beams were constructed in a lab and tested shortly after construction, the magnitude of tension stiffening that occurs in members that are much older did not occur.

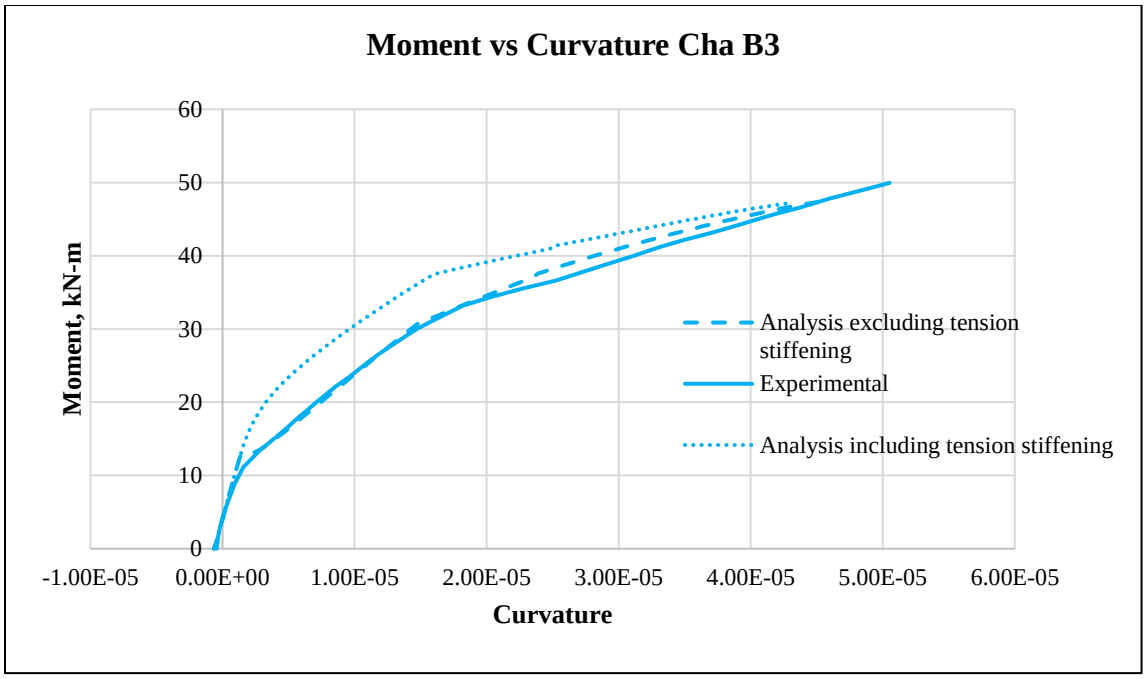

Figure 4-22: Moment versus curvature for experimental and analytical curves of Cha beam B3

Figure 4-23 presents the experimental, numerical, and analytical load-deflection curves of Cha B3 beam. The numerical analysis slightly overestimates the deflection after the section has cracked; otherwise, the analysis gives an excellent correlation to the experimental curve. The analytical line takes the first yield of the non-prestressing steel into account. The experimental line continues to a load of 108.98 kN (24.50 k), a concrete strain of 0.00386 whereas the analysis stops at 95.50 kN (21.47 k), a concrete strain of 0.0030. Cha B3 failed due to concrete crushing.

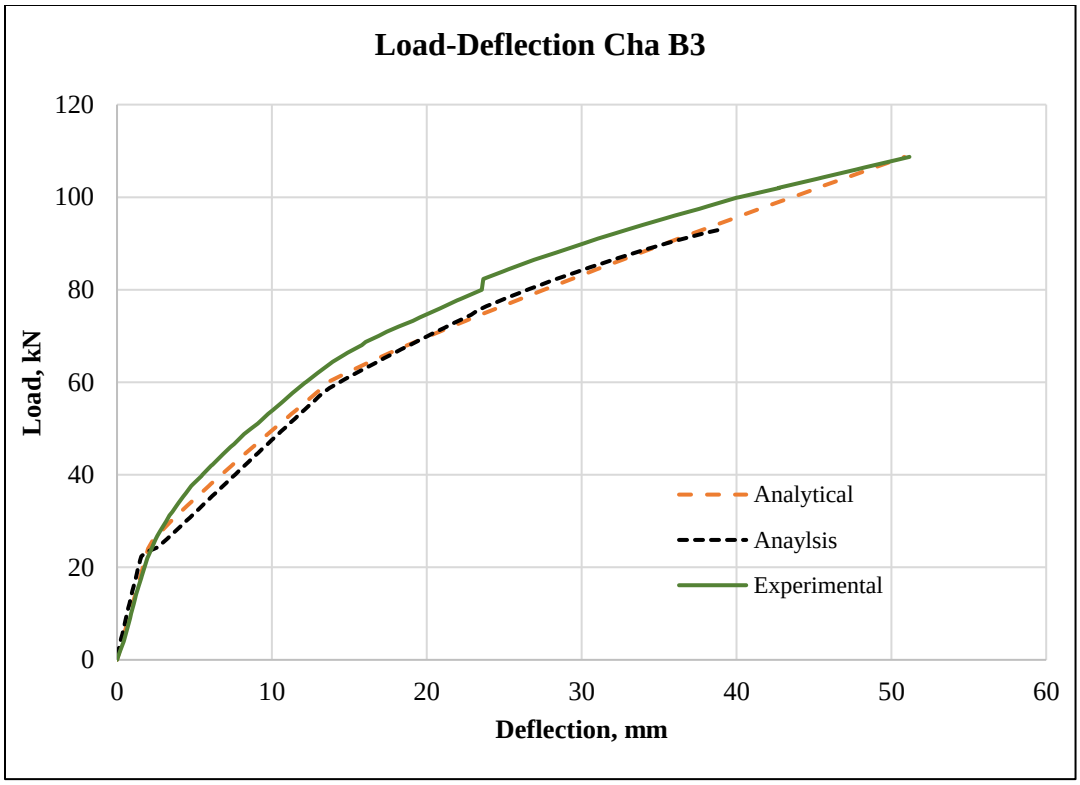

Figure 4-23: Load versus deflection for experimental and analysis of Cha B3 beam

The third beam presented is Cha B5 that failed due to rupture of the carbon fiber composite at a load of 106.75 kN (24.0 k), had a yielding load equal to 60.05 kN (13.50 k), and a cracking load equaling 31.42 kN (7.06 k). The graphs of experimental moment versus experimental strain for Cha B5 were digitized to create Figure 4-24. This experimental data is used to compare the analytical formula presented herein of the moment versus strain of the different materials.

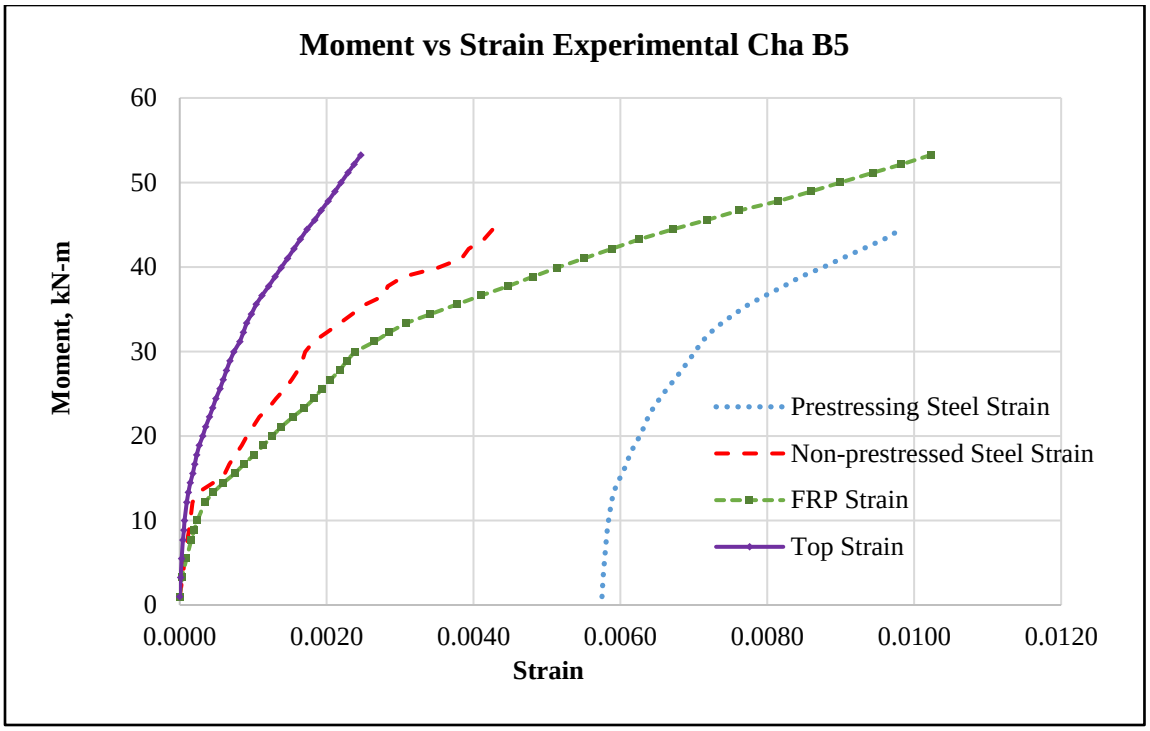

Figure 4-24: Experimental moment versus strain for Cha beam B5

Figure 4-25 indicates the moment versus concrete top strain for the experimental and analytical curves, with and without tension stiffening, of Cha B5 beam. The initial top strain for experiment and analysis, without tension stiffening is 0.0 and 0.000019, respectively. At the experimental superimposed cracking moment of 15.71 kN-m (11.59 k-ft), the experimental strain (0.00021) is less than the analysis strain, without tension stiffening, (0.00026) for the concrete top strain. The analysis determined the section cracking at a superimposed moment of 15.11 kN-m (11.14 k-ft). Hence, the shift in the strain from going from gross moment of interia to cracked moment of interia. Considering this shift, the top strains of the analysis matches the experimental strain well. The useable concrete strain of 0.003 was not achieved due to the failure mode of rupture of CFRP. The analysis determined an ultimate moment of 48.5 kN-m (35.78 k-ft) while the experiment's reported ultimate moment is 53.4 kN-m (32.00 k-ft) causing the analysis curve to stop and the experimental plot to continue. Table 4-7 indicates these strains

in tabulated form for the various materials. An ultimate load equal to 97.0 kN (21.81 k) or an ultimate moment of 48.5 kN-m (35.77 k-ft) is used for comparisons of strains.

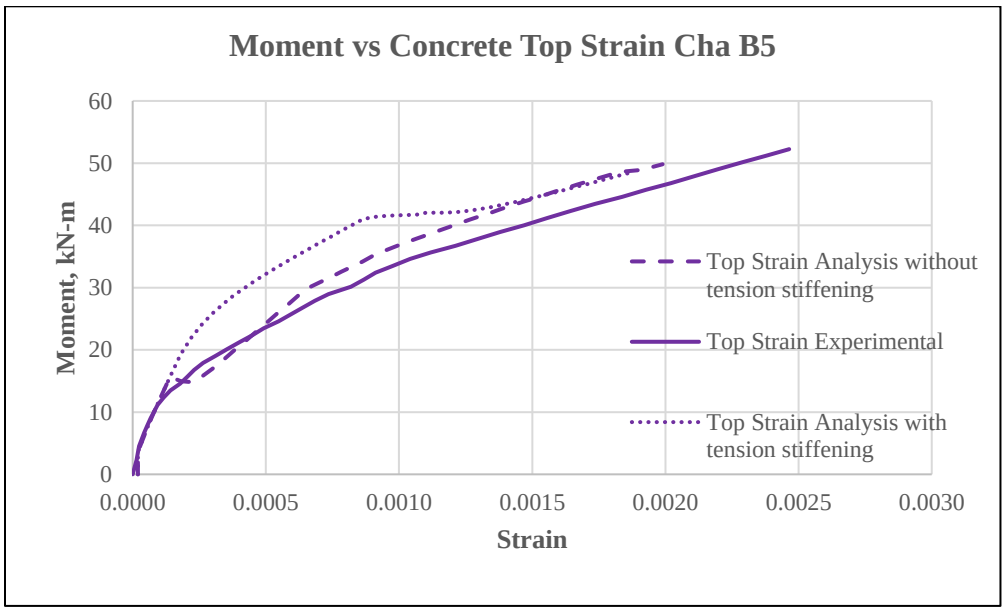

Figure 4-25: Moment versus concrete top strain for experimental and analytical curves of Cha B5 beam

Figure 4-26 designates the moment versus prestressing steel strain for the experimental and analysis, with and without tension stiffening, of Cha B5 beam. The initial prestressing steel strain for experimental and analysis are 0.005749 and 0.005741, respectively. At the superimposed cracking moment, the experimental strain (0.00608) is slightly lower than the analysis strain (0.00616) for the prestressing steel. Since the non-prestressing steel yields prior to the prestressing steel, two yield points are apparent in Figure 4-26 at approximately 29 kN-m (21.4 k-ft) and 39 kN-m (28.8 k-ft). At the experimental noted first yield, the strain in the prestressing steel was given as 0.00756, which is slightly higher than the analysis strain of 0.00740. The experimental prestressing steel strain gauges stopped recording data at a superimposed moment of 43.45 kN-m (32.04 k-ft). Prior to the mild steel yielding, the

experimental curve crosses the analysis curve; i.e, the experimental curve has a steeper slope. For the majority of this region, the analysis correlates well to the experiment.

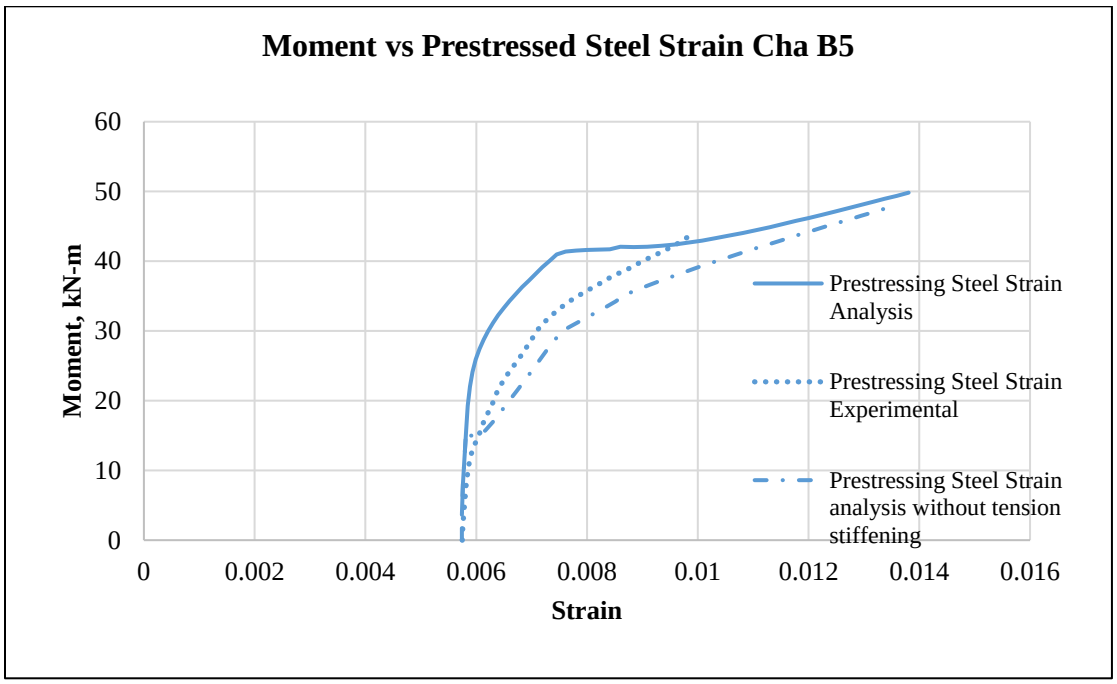

Figure 4-26: Moment versus pre-tensioned prestressing steel strain for experimental and analytical curves of Cha B5 beam

Figure 4-27 presents the moment versus non-prestressing strain for the experimental curve, and the analysis. The initial experimental strain in the non-prestressing steel is given as 0.0 where the analysis produced a strain of - 0.000025, the negative strain is produced by the prestressing of the beam. At the cracking load, the experimental strain in the non-prestressing steel is 0.00068 and the analysis without tension stiffening produced a strain of 0.00048 that correlates to a total change of strain of 0.0005. Once the section has cracked, the slopes of the moment-strain lines for the experimental and analysis are similar until yielding of the non-prestressing steel. Once this has occurred, the experimental strains are less than the analysis strains as shown in Figure 4-27. Using the experimentally documented yield load, the yield strain of the non-prestressing steel is 0.00180 and 0.00212 for experimental and analysis without

tension stiffening, respectively. The last experimental strain of the non-prestressed steel recorded was 0.0043 at a moment of 43.45 kN-m (32.04 k-ft).

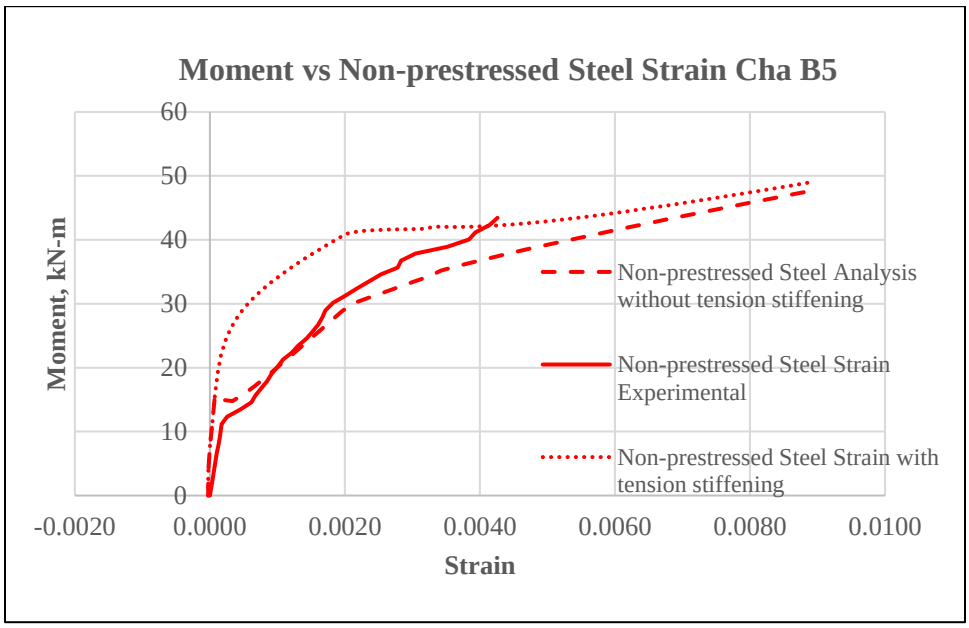

Figure 4-27: Moment versus non-prestressing steel strain for experimental and analytical curves of Cha B5 beam

Figure 4-28 designates the moment versus FRP strain for Cha B5 beam. The initial experimental strain of the FRP is specified as 0.0; the initial analysis strain, without tension stiffening, is 0.000093. The experimental cracking strain (0.00088) is slightly higher than analysis strain (0.00072). Conversely, the experimental first yield strain (0.00263) is less than the analysis first yield strain, excluding tension stiffening, (0.00269) analysis. Additionally, at a superimposed moment of 48.5 kN-m (35.76 k-ft), the ultimate experimental strain (0.00881) is less than the ultimate analysis strain, without tension stiffening, (0.01130). When examining Figure 4-28, some softening of the experimental beam prior to cracking appears to have occurred, which is common with prestressed beams. As shown in Figure 4-28, the analysis correlates very well to the experimental.

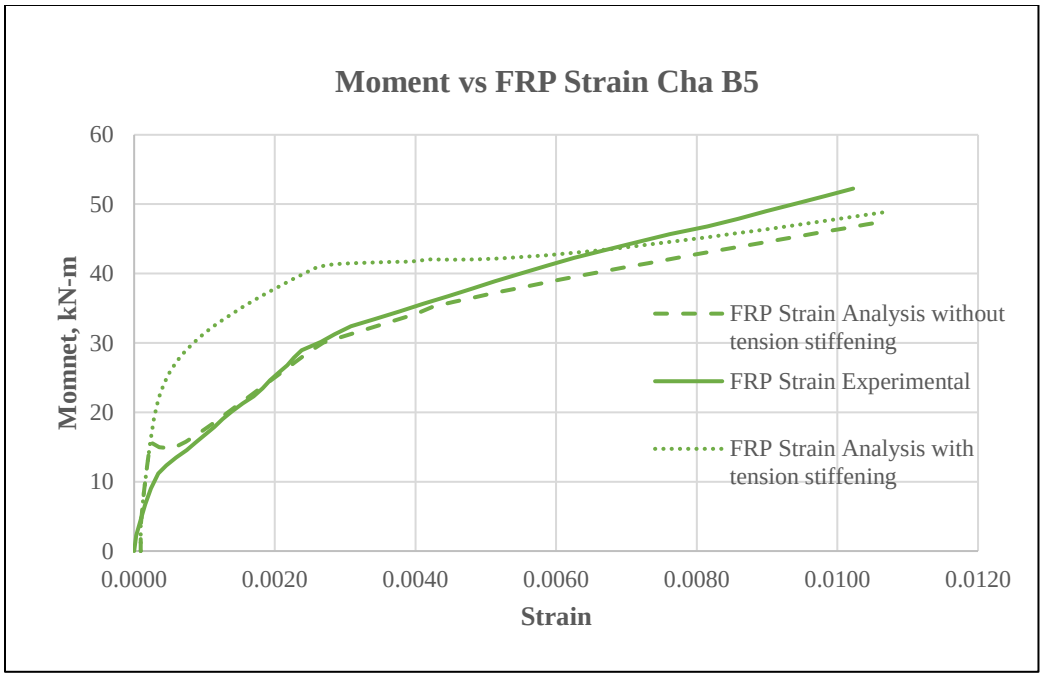

Figure 4-28: Moment versus FRP strain for experimental and analytical curves of Cha B5 beam

As previously stated, the failure mode of Cha B5 beam is rupture of the CFRP. Table 4-7 displays the experimental strains and analysis strains excluding tension stiffening.

Table 4-7: Cha B5 experimental and analysis comparison of strains

Cha B5 strain comparisons excluding tension stiffening								
strains	Initial strain P* = 0		Cracking strain P* = 31.42 kN (7.06 k)		Yield strain^{+} P* = 60.05 kN (13.50 k)		Ultimate strain** P* = 97.00 kN (21.81 k)	
	Exp.	Analyt.	Exp.	Analyt.	Exp.	Analyt.	Exp.	Analyt.
ε_c	0	0.000019	0.00021	0.00026	0.00081	0.00066	0.00216	0.00183
ε_{ps}	0.005749	0.005741	0.00608	0.00616	0.00709	0.00756	NR	0.01382
ε_s	0	-0.000025	0.00068	0.00048	0.00180	0.00212	NR	0.00935
ε_{frp}	0	0.000025	0.00088	0.00072	0.00263	0.00269	0.00881	0.01130
*indicates superimposed load **indicates strains based on experimental load lower than the ultimate noted in testing of 106.75 kN (24.00 k) $^{+}$indicates first yield (non-prestressing steel yielded prior to prestressing) NR – not recorded								

Figure 4-29 illustrates the moment curvature response of Cha B5 beam with the experimental as a dash-dotted line and the analysis as a solid line. The analysis estimates the curvature extremely well until the yielding of the prestressing steel when the analysis slightly overestimates the curvature. This may be due to the high concrete compressive strength (70 MPa, 10176 psi) and the model used for the compression block.

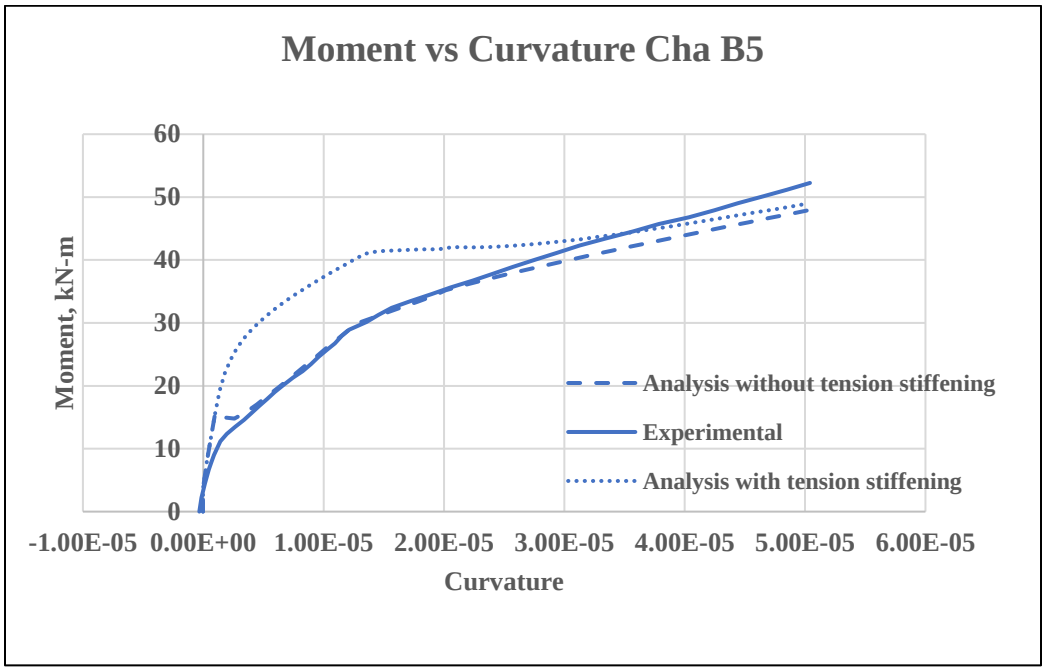

Figure 4-29: Moment versus curvature for experimental and analytical curves of Cha B5 beam

Figure 4-30 indicates the experimental and analysis load-deflection of Cha B5 beam. The analysis slightly overestimates the deflection after the section has cracked; otherwise, the analysis gives an excellent correlation to the experimental response. The analytical line takes the first yield of the non-prestressing steel into account. The experimental line continues to a load of 108.98 kN (24.50 k), a concrete strain of 0.0034 whereas the analysis stops at 95.50 kN (21.47 k), a concrete strain of 0.0031. As a reminder, the concrete compressive strength for Cha B5 beam is 70 MPa (10.173 psi) with a usable strain equal to 0.031 using $\varepsilon_c' = 1.71\left(f_c'/E_c\right)$.

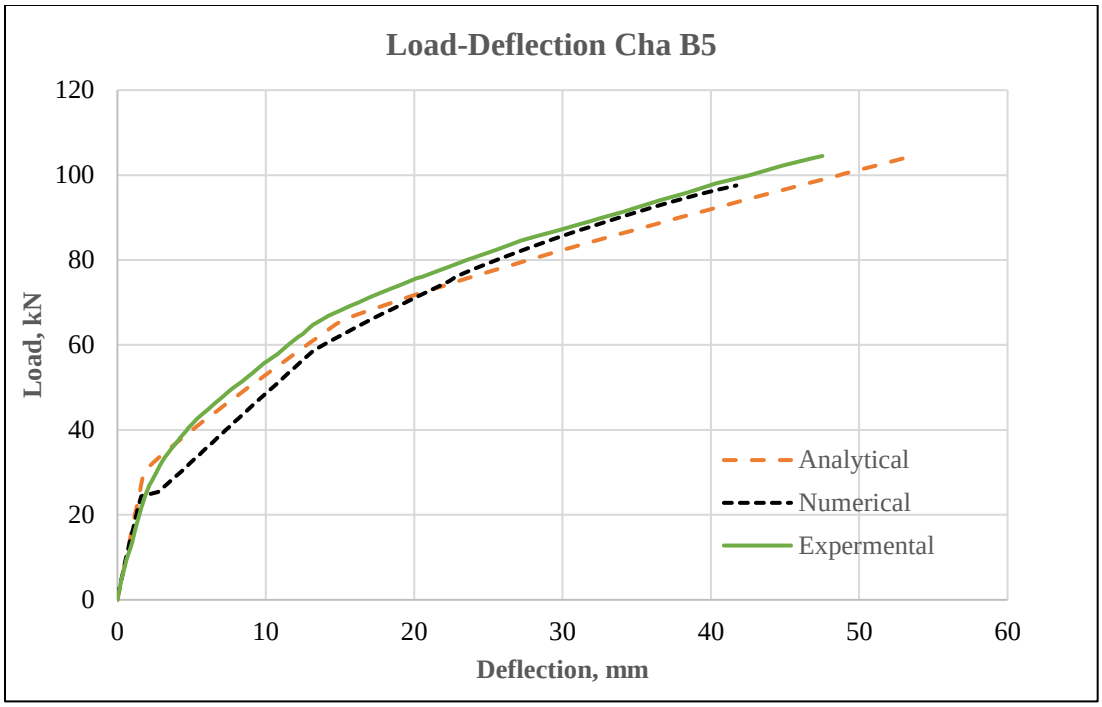

Figure 4-30: Load versus deflection for experimental and analytical curves of Cha B5 beam

Failure mode of Cha B6 beam was debonding of carbon fiber composite at a superimposed load of 125.79 kN (28.28 k) with the first yielding load at 71.17 kN (16.00 k) and a cracking load equaled 33.68 kN (7.57 k). Figure 4-31 displays the moment versus concrete top strain for the experimental curve and analysis, with and without tension stiffening, of Cha B6 beam. The initial top strain for the experiment and analysis is 0.0 and 0.000019, respectively. At the experimental superimposed cracking moment of 16.84 kN-m (12.42 k-ft), the experimental strain (0.00028) is slightly higher than the analysis strain, without tension stiffening, (0.00027) for the concrete top strain. For the most part, the top strains of the analysis match the experimental strain well. The experimental strains are higher than the analysis strain, possibly caused by the compression block model used that may not be ideal for concrete compressive strength of 72.13 MPa (10,462 psi). Table 4-7 indicates the strains for the various

materials. An ultimate load equal to 114.27 kN (25.69 k) or an ultimate moment of 57.14 kN-m (42.14 k-ft) is used for comparison purposes.

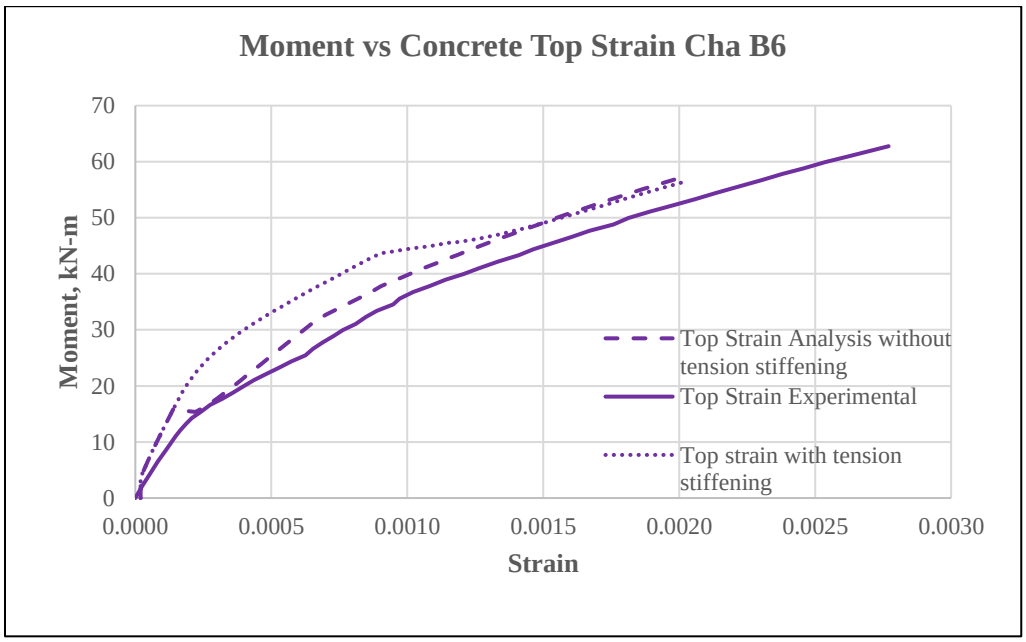

Figure 4-31: Moment versus concrete top strain for experimental and analytical curves of Cha B6 beam

Figure 4-32 designates the moment versus prestressing steel strain for the experimental and analysis, with and without tension stiffening, of Cha B6 beam. The initial prestressing steel strain for experimental and analysis are 0.005902 and 0.005893, respectively. At the superimposed cracking moment, the experimental strain (0.00618) is higher than the analysis strain, excluding tension stiffening, (0.00635) for the prestressing steel. Since the non-prestressing steel yields prior to the prestressing steel, two yield points based on analysis are 31 kN-m (22.9 k-ft) and 43 kN-m (31.7 k-ft). At the experimental noted first yield at 35.6 kN-m (26.3 k-ft), the strain in the prestressing steel was given as 0.00699, which is lower than the analysis strain of 0.00749. The experimental prestressing steel strain gauges stopped recording data at a superimposed moment of 61 kN-m (45.0 k-ft). Prior to the mild steel yielding, the experimental curve crosses the analysis curve; i.e, the experimental curve has a steeper slope.

For the majority of this region, the analysis correlates well to the experimental. After non-prestressing steel yields, the analysis predicts higher strains at a given moment.

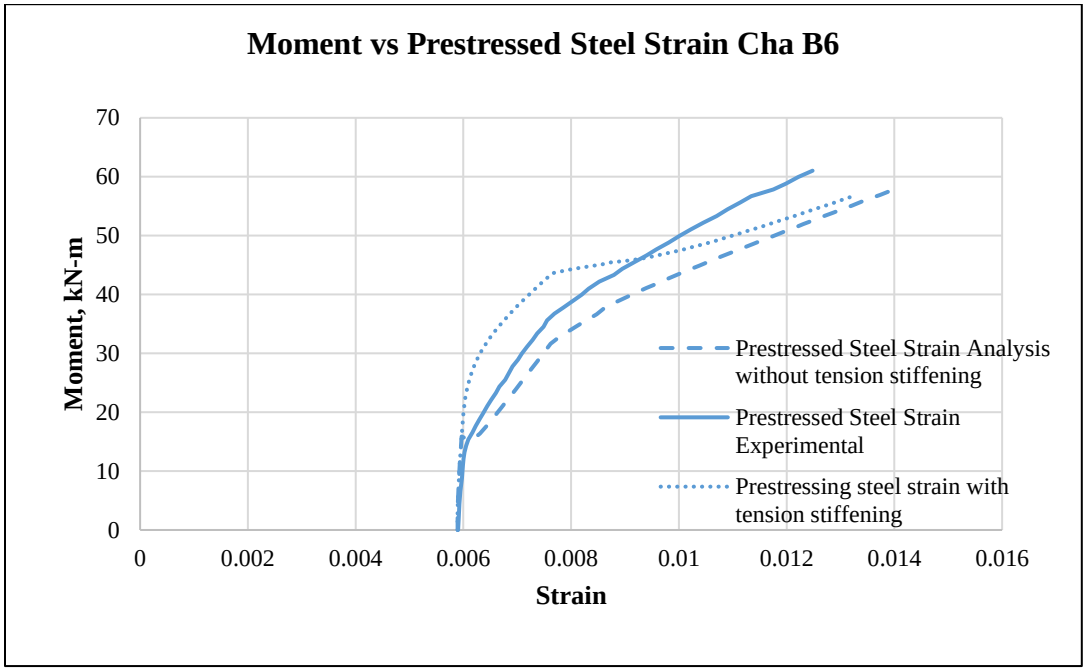

Figure 4-32: Moment versus pre-tensioned prestressing steel strain for experimental and analytical curves of Cha B6 beam

Figure 4-33 gives the moment versus non-prestressing strain for the experimental and the analysis, with and without tension stiffening. The initial experimental strain in the non-prestressing steel is given as 0.0 where the analysis produced a strain of - 0.00003. At the cracking load, the experimental and analysis strain, excluding tension stiffening, in the non-prestressing steel are 0.00063 and 0.00052, respectively. Once the section has cracked, the slopes of the moment-strain lines for the experimental and analysis are the same until yielding of the non-prestressing steel. The last experimental strain of the non-prestressed steel is 0.00685 at a moment of 39.9 kN-m (29.43 k-ft). The behavior of the non-prestressed steel is elastic-perfectly plastic (i.e. it shows a flat plateau when its stress-strain response is plotted). However, in Figure 4-33, the graph relates the applied sectional moment versus mild steel strain. Since the

applied moment continuously increases due to the stiffness of FRP and prestressing steel beyond the yielding point of mild steel and the strain in mild steel also increases after yielding of its reinforcement, the response appears to be hardening as shown by the analysis. On the other hand, the experimental curve is plotted to have a flat plateau, which is clearly erroneous trend for this type of graphs since the sectional moment applied continues to increase with increasing the steel strain.

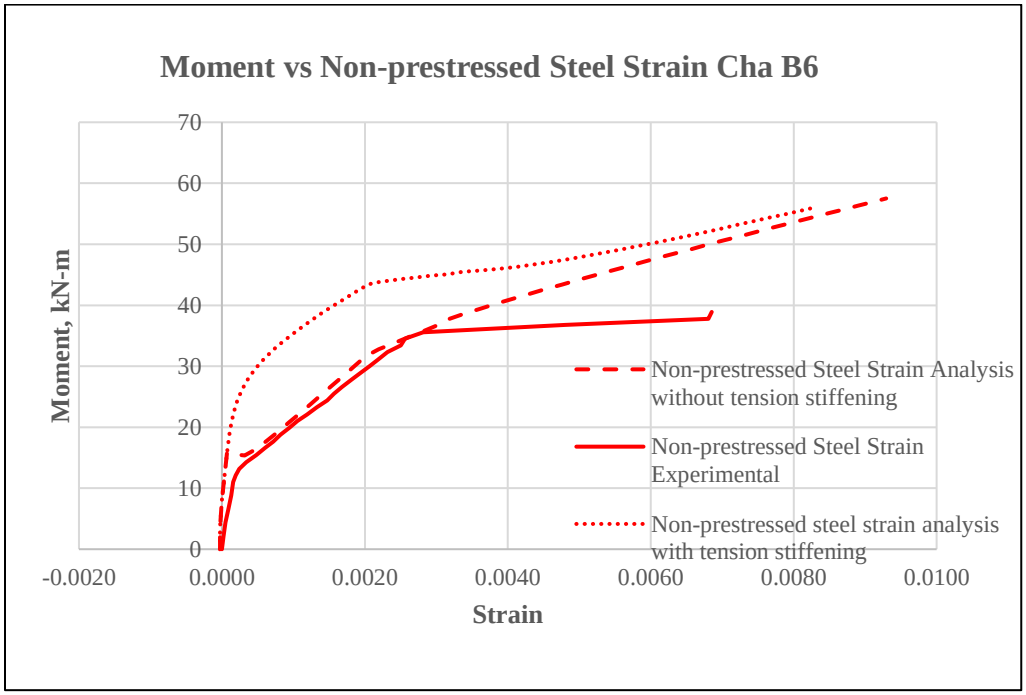

Figure 4-33: Moment versus non-prestressing steel strain for experimental and analytical curves of Cha B6 beam

Figure 4-34 designates the moment versus FRP strain for Cha B6 beam. The initial experimental strain of the FRP is specified as 0.0; the initial analysis strain, excluding tension stiffening, is 0.000088. The experimental cracking strain, first yield strain, and ultimate strain are lower than the analysis strains, excluding tension stiffening, at the same moment: 0.00049 versus 0.00077, 0.00196 versus 0.00238, and 0.00939 versus 0.01126. As shown in Figure 4-34, the analysis correlates very well to the experimental curve. This may be due to the amount of prestressing losses with the higher compressive strength of the concrete.

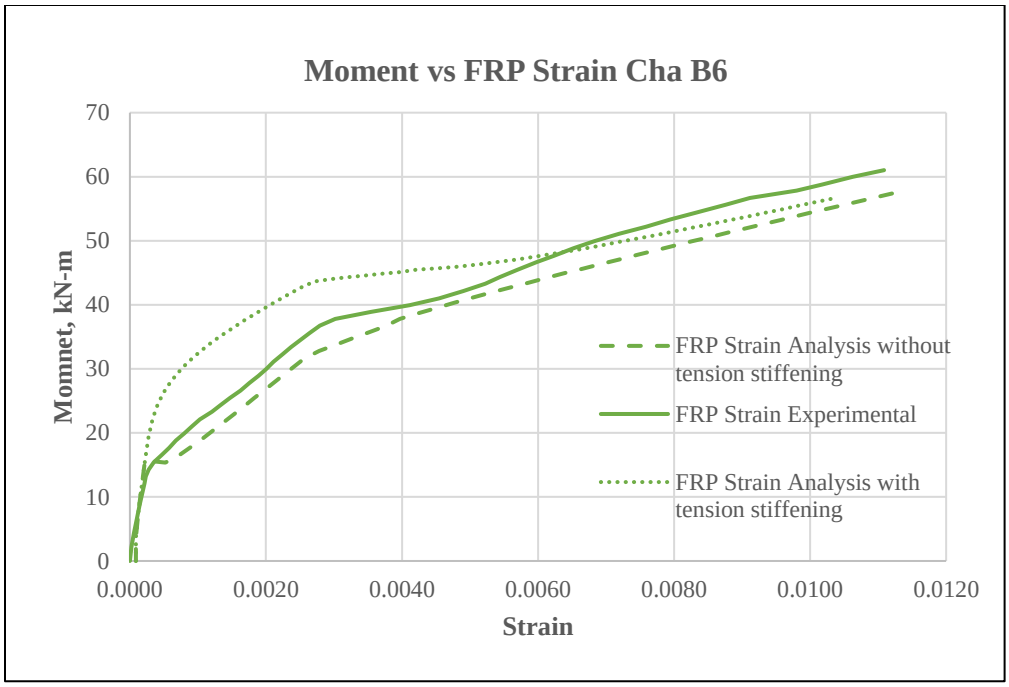

Figure 4-34: Moment versus FRP strain for experimental and analytical curves of Cha B6 beam

As previously stated, the failure mode of Cha B6 beam is debonding of the CFRP. Table 4-8 displays the experimental strains and analysis strains.

Table 4-8: Cha B6 experimental and analysis comparison of strains

Cha B6 strain comparisons without tension stiffening								
strains	Initial strain P* = 0		Cracking strain P* = 33.68 kN (7.57 k)		Yield strain+ P* = 71.17 kN (16.00 k)		Ultimate strain P* = 114.27 kN (25.69 k)	
	Exp.	Analyt.	Exp.	Analyt.	Exp.	Analyt.	Exp.	Analyt.
ε_c	0	0.000019	0.00028	0.00027	0.00085	0.00062	0.00233	0.00203
ε_{ps}	0.005902	0.005893	0.00618	0.00635	0.00720	0.00749	NR	0.01390
ε_s	0	-0.000026	0.00063	0.00052	0.00152	0.00186	NR	0.00929
ε_{frp}	0	0.000088	0.00049	0.00077	0.00196	0.00238	0.00939	0.01126
*indicates superimposed load **indicates strains based on experimental load lower than the ultimate noted in testing of 125.79 kN (28.28 k) +indicates first yield (non-prestressing steel yielded prior to prestressing) NR – not recorded								

Figure 4-35 illustrates the moment curvature of Cha B6 beam with the experimental as a solid line, the analysis including tension stiffening as a short-dashed line, and the analysis excluding tension stiffening as a long-dashed line. The analysis excluding tension stiffening estimates the curvature extremely well until the yielding of the prestressing steel when the analysis slightly overestimates the curvature. This may be due to the high concrete compressive strength and the model used for the compression block.

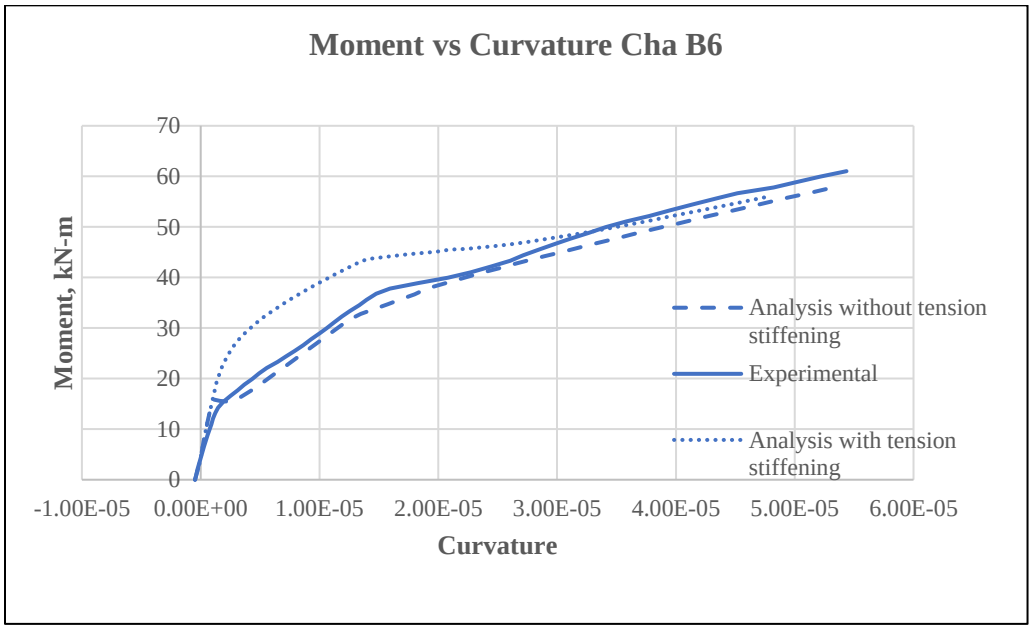

Figure 4-35: Moment versus curvature for experimental and analytical curves of Cha B6 bam

Figure 4-36 indicates the load-deflection relationship for Cha B6 beam for the experimental, the numerical, and the analytical response. The numerical and analytical correlate well with the experimental curve. The analytical shown is using the tri-linear model with the first yield (yielding of the non-prestressing steel) curvature. When using the second yield (prestressing steel) curvature, the analytical model more closely follows the numerical model.

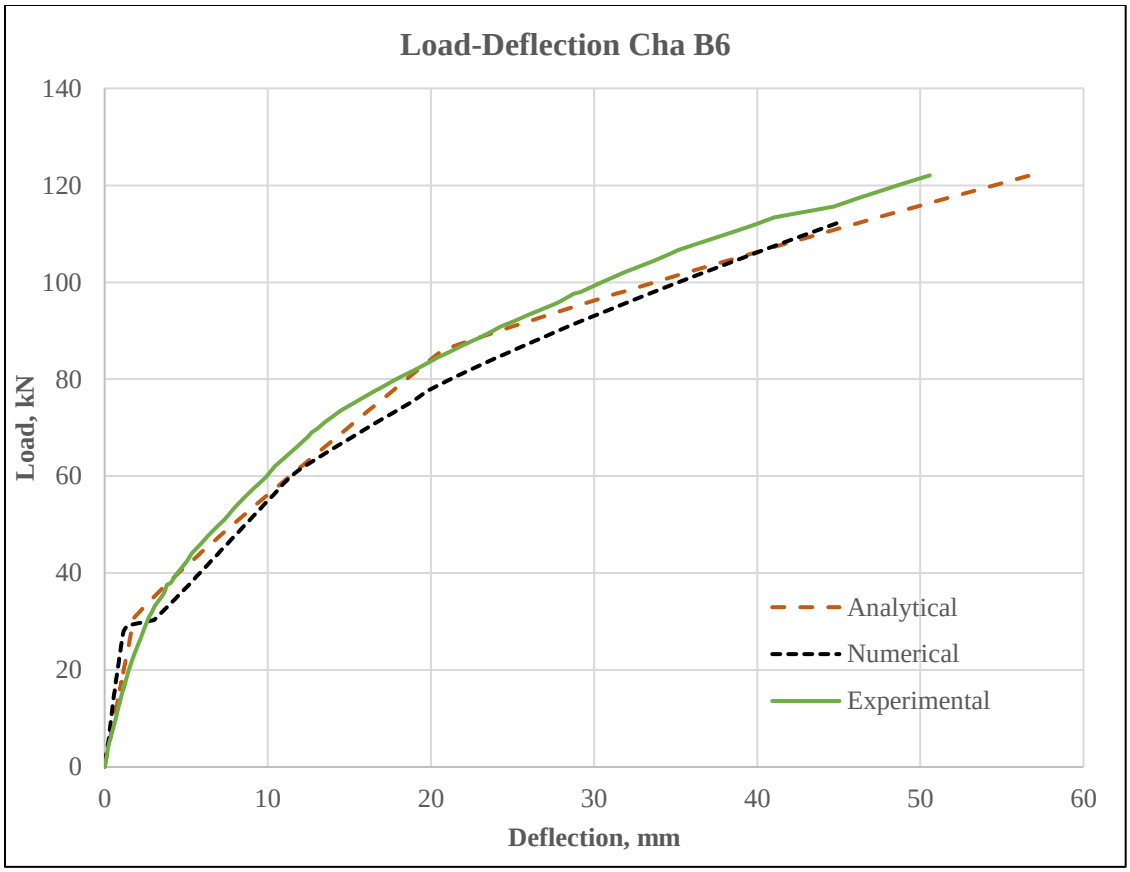

Figure 4-36: Load versus deflection for experimental and analytical curves of Cha B6

4.4.2 Larson, Peterman & Rasheed (2005) beams

To further verify the parametric study response, a fully nonlinear analysis of PRC-FRP strengthened T-beams is performed using testing results from beams tested by Larson, Peterman, and Rasheed (2005) in which five, pretensioned, bonded PRC T-girders were examined. The beams were cast at a prestressed concrete plant. Of the five beams tested, Beam 1 was the control beam, unstrengthened; the remaining beams (Beams 2-5) were strengthened with CFRP sheets. Static tests were performed on Beams 2 and 4 (Larson B2 and Larson B4 in Table 4-4); fatigue tests were performed on Beams 3 and 5. Therefore, Beam 2 (Larson B2) and Beam 4 (Larson B4) are used for this study. The girders were tested in four-point bending with a clear span of 4880 mm (192 inch) and a shear span of 1,830 mm (72 inch). The tests were conducted

in monotonic, load control with a load rate of 2.2 kN/min (500 lb/min). Midspan deflections were measured using two linear variable displacement transducers (LVDTs) mounted on either side of the flange. The average reading was reported. Before strengthening the girders, they were loaded past their midspan cracking moments. The T-beams were strengthened by applying CFRP; this was accomplished by flipping the girders onto their flanges and supporting them at a minimum of three locations along its span while the CFRP was applied and cured.

Larson B1, the control beam, consisted of a flange width of 457 mm (18 inch); flange thickness of 102.6 mm (4 inch); tapered web width starting at 152.4 mm (6 inches) at the flange junction down to a width of 102.6 mm (4 inch) at the bottom; and overall depth of 355.6 mm (14 inch). The concrete strength at 28 days from standard cylinder testing was 48.6 MPa (7043 psi). The beams were reinforced with prestressing strands and mild reinforcement. The beams were reinforced with bonded prestressing strands conforming to ASTM A416 and non-prestressed reinforcement conforming to ASTM A616. The prestressed steel was seven-wire strand with a nominal diameter of 10 mm (3/8 inch) and an ultimate strength of 1862 MPa (270 ksi). Two prestressing tendons, one located 305 mm (12 inch) and the other 254 mm (10 inch) from the top surface, were used. Four layers of mild D4 welded steel wire were used longitudinally at depth of 32, 76, 102, 178 mm (1.25, 3, 4, and 7 inch) from the top to hold the shear stirrups and flange reinforcement in place.

Larson B2, was strengthened to have a 124 MPa (18 ksi) average stand stress range under service live-load conditions. This was achieved with one layer of CFRP flexural wrapped 57 mm (2.25 inch) up the bottom of the web sides and transverse external stirrups were made of a single layer of 130 mm (5.5 inch) wide sheet at 305 mm (12 inch) spacing on center. Load, midspan deflection, and strains were recorded while loading Larson B2 beam to failure. The

load-deflection response of the beam is given and used for verification of trilinear analytical moment-curvature response. Larson B2 beam failed by CFRP rupture.

The analytical trilinear moment-curvature response for Larson B2 beam shown in Figure 4-37 matches the numerical response very well. The precracking analytical initial point and numerical cracking point are mostly identical. The numerical post-cracking response (in between first cracking and first yielding) initially slightly underestimates the analytical values closer to the cracking point while it slightly overestimates the analytical values closer to the yielding point. Overall, the analytical response accurately averages the numerical curve. From the yielding point to the ultimate point, the analytical line is slightly lower and gradually increases to where the numerical and analytical ultimate points are nearly the same.

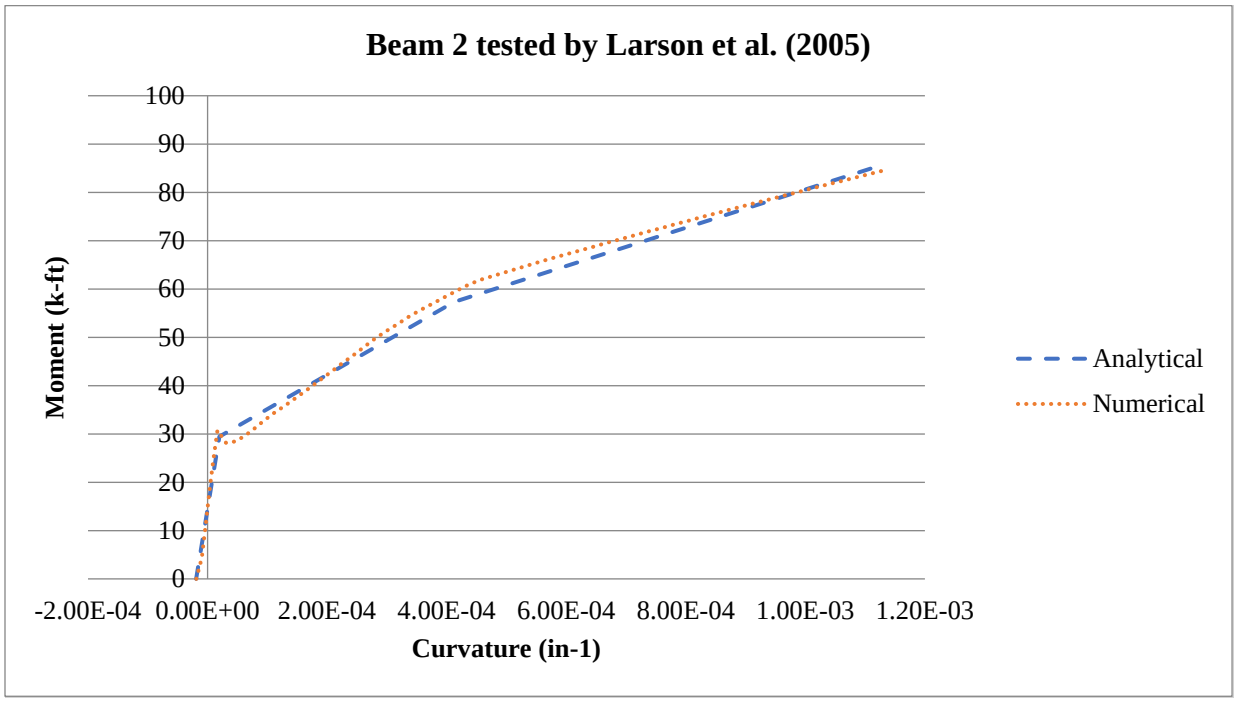

Figure 4-37: Moment-curvature response of Larson B2 beam

Figure 4-38 represents the comparison of the load-deflection response of Larson B2 beam from experimental, analytical and numerical results. The LVDTs were mounted after the beam deflected due to self-weight; therefore, the camber due to prestressing must be subtracted from the overall response. It is evident that the analytical curve closely matches the experimental response until around the yielding point. After that, the analytical curve slightly overestimated the experimental curve while maintaining the same slope. This small discrepancy might be attributed to the fact that the analytical curve ignores the effect of the self-weight on deflection. On the other hand, the numerical curve is seen to undergo cracking at a lower load level compared to the experimental curve. This is due to the fact that the numerical response ignores the tension stiffening effect of concrete. Going forward to the curve beyond the yielding point, the numerical response is seen to be closer to the experimental response than the analytical curve. This owing to the fact that the numerical analysis considers the self-weight of the girder on the deflection calculations.

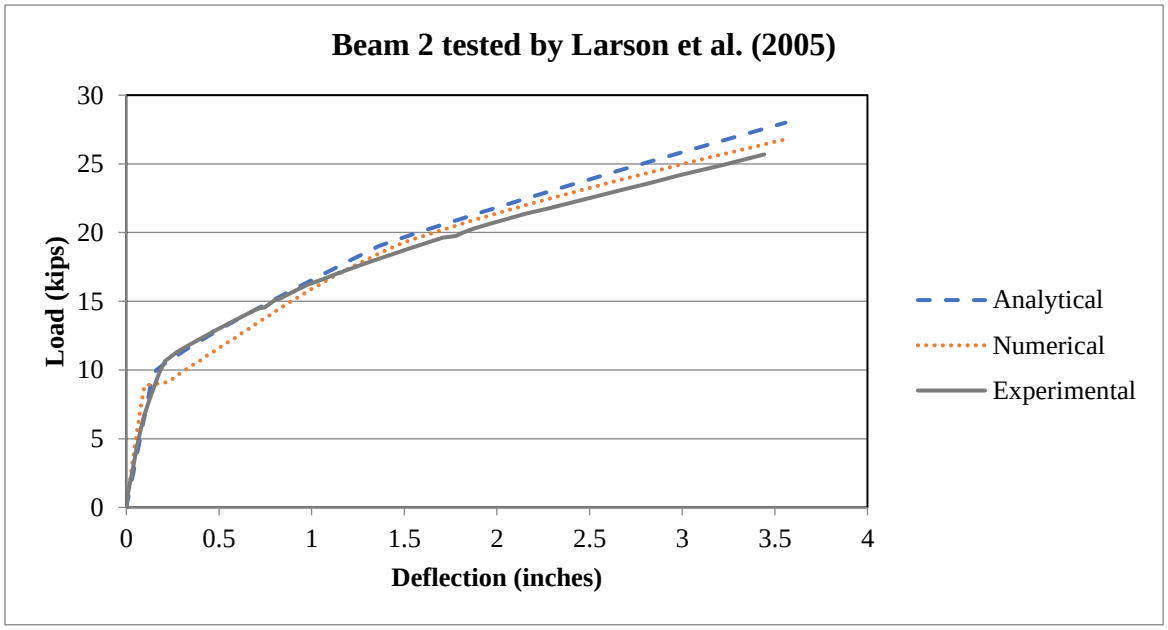

Figure 4-38: Load-deflection response of Larson B2 beam

Larson B4 beam was strengthened to have a 248 MPa (36 ksi) average stand stress range design. This was achieved with two layers of flexural CFRP bonded to the bottom of the web and wrapped 13 mm (0.5 inch) up the sides for one layer and wrapped 76 mm (3 inch) up the sides for the second layer. Transverse external stirrups made of a single layer of 130 mm (5.5 inch) wide sheet at 305 mm (12 inch) spacing on center was also used. Load, midspan deflection, and strains were recorded while loading this beam to failure. The load-deflection response of the beam is given and used for verification of trilinear analytical moment-curvature response. Larson B4 beam failed by CFRP rupture.

Figure 4-39 shows the moment-curvature response for Larson B4 beam. The numerical initial curvature point is equal to -4.836×10^{-4} /mm (-1.904×10^{-5} /inch). The numerical cracking point moment and curvature is equal to 37.87 kN-m (29.41 k-ft) and 4.920×10^{-4} / mm (1.937×10^{-5} /inch), respectively. The numerical yielding point moment and curvature is equal to 87.78 kN-m (64.74 k-ft) and 1.057×10^{-2} /mm (4.160×10^{-4}/ inch), respectively. The numerical ultimate point moment and curvature is equal to 138.31 kN-m (102.01 k-ft) and 2.908×10^{-2} /mm (1.145×10^{-3}/ inch), respectively.

The Analytical trilinear moment-curvature response for Larson B4 beam shown in Figure 4-39 matches the Numerical response very well. The precracking analytical initial point and numerical cracking point are mostly identical. The numerical post-cracking response slightly underestimates the analytical values. From the yielding point to the ultimate point, the analytical line is slightly lower due to neglecting the tension stiffening effects in the numerical analysis.

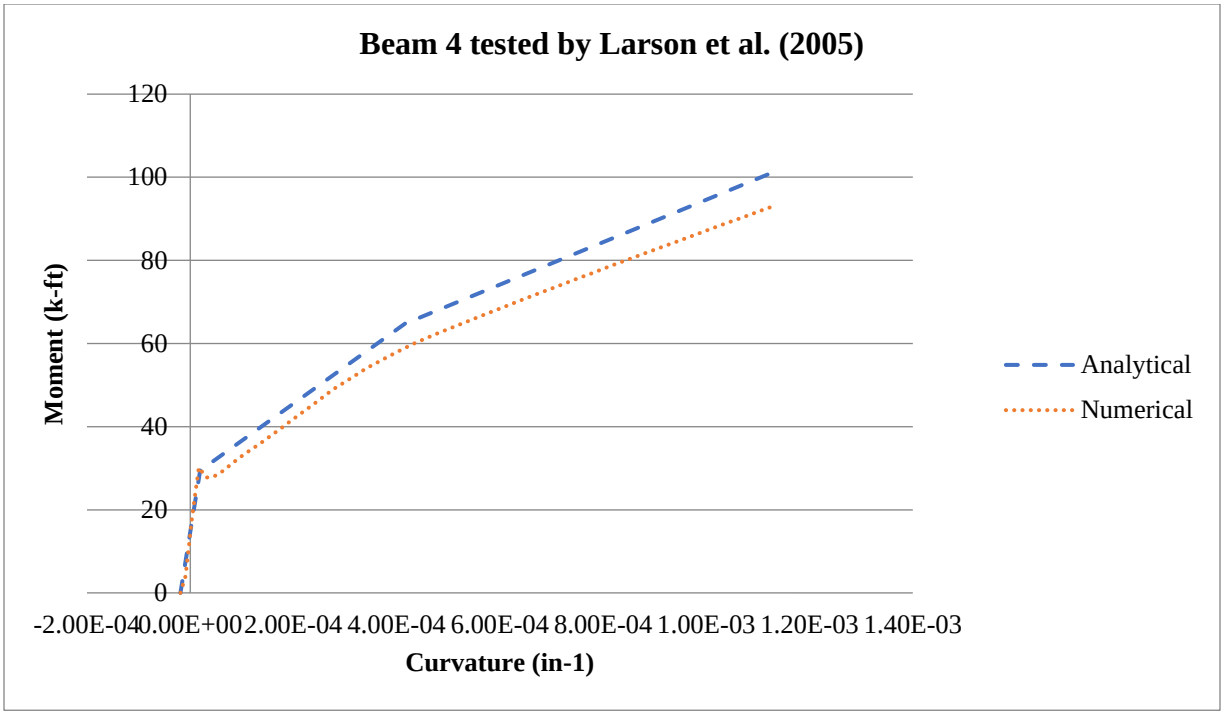

Figure 4-39: Moment-curvature for Larson B4 beam

Figure 4-40 presents the comparison of the load-deflection response of Larson B4 beam from experimental, analytical and numerical results. The LVDTs were mounted after the beam deflected due to self-weight therefore, the camber due to prestressing must be subtracted from the overall response. It is evident that the analytical curve closely matches the experiment response until around the yielding point. After that the analytical curve slightly overestimated the experimental curve while maintaining the same slope. Similar to Larson B2 beam, this small discrepancy might be attributed to the fact that the analytical curve ignores the effect of the self-weight on deflection. On the other hand, the numerical curve is seen to undergo cracking at a lower load level compared to the experimental curve. This is due to the fact that the numerical response ignores the tension stiffening effect of concrete. Going forward to the curve beyond the yielding point, the numerical response is seen to be closer to the experimental response than the

analytical curve. This owing to the fact that the numerical analysis considers the self-weight of the girder on the deflection calculations.

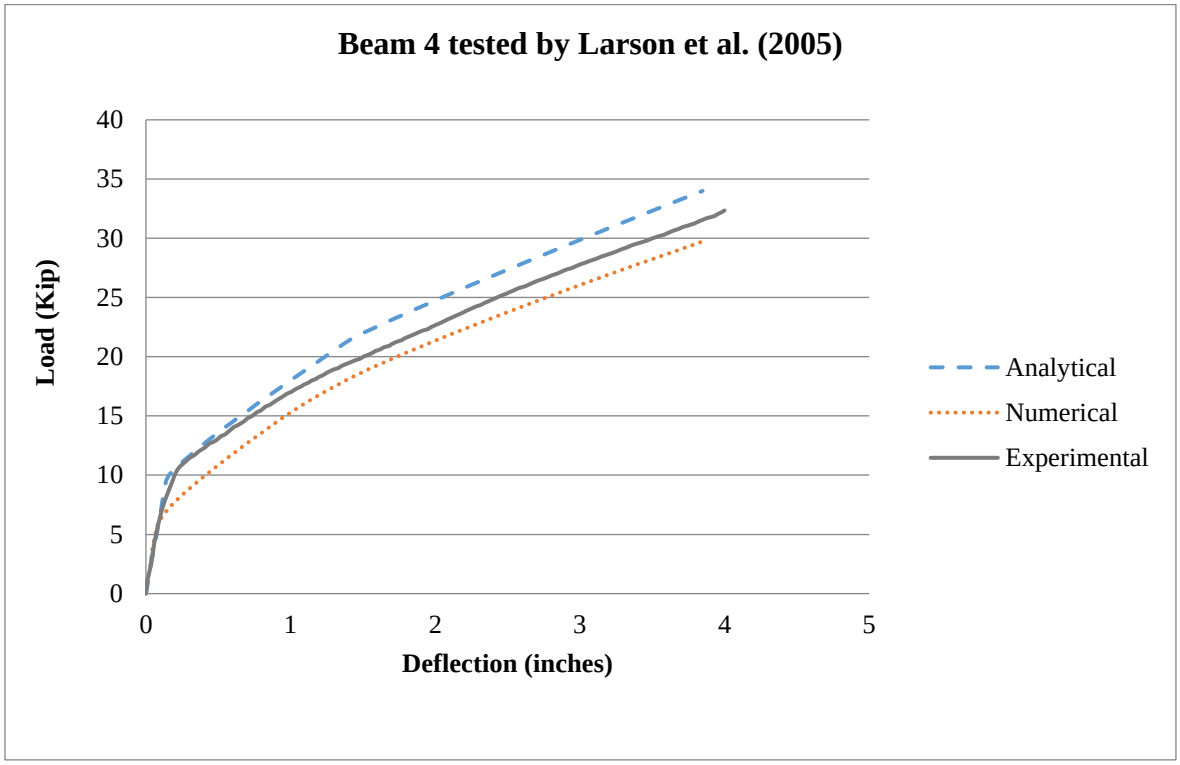

Figure 4-40: Load-deflection for Larson B4 beam

A comparison between the analytical and numerical moment-curvature response is made and presented. The comparison indicates the high accuracy of the analytically assumed moment-curvature function, which represents the foundation for establishing the short-term deflection expressions. The proposed method produced accurate predictions for moment-curvature and short-term load-deflection responses of PRC flexural members with straight strands and a T-cross section strengthened with externally bonded FRP.

4.5 Developing a design-oriented effective moment of inertia equation

A comparison with different procedures to calculate instantaneous deflections of pretensioned PRC-FRP strengthened rectangular-beams is presented. Three different sets of deflection prediction equations are examined for deflections within service limits, post-cracking to prestressing yielding. Some of the equations in this section have been previously presented but are shown here for clarity.

The first set of equations, Eq. 2-46 and Eq. 2-47, is Branson equation used by ACI 318-19 with PCI-10 modifications recommended by Branson and Trost (1982) for the prestressing and currently used by ACI 440.2R-17. This set of equations computes the beam effective moment of inertia after cracking (I_e) as follows:

$$I_e = \left(\frac{M_{cr}}{M_a}\right)^3 I_{gt} + \left[1 - \left(\frac{M_{cr}}{M_a}\right)^3\right] I_{cr} \leq I_{gt} \qquad \textbf{Eq. 2-46}$$

With the cracking moment:

$$M_{cr} = \frac{f_r I_{gt}}{y_{bot}} + \frac{P_e I_{gt}}{A_{gt} y_{bot}} \qquad \textbf{Eq. 2-47}$$

The second set of equations, Task group (Eq. 3-3 and Eq. 4-39), uses a similar approach as presented by Rasheed, Charkas, and Melhem (2004) which accounts for perfect bond of the concrete-FRP interface (Eq. 3-4) and Rasheed and Charkas (2009) which conservatively accounts for bond slip in FRP strengthened RC beams.

$$I_e = \left(\frac{M_{cr}}{M_a}\right)^3 I_{gt} + \left[1 - \left(\frac{M_{cr}}{M_a}\right)^3\right] I_{ey} \leq I_{gt} \qquad \textbf{Eq. 3-3}$$

Based on additional tested data, the deflection Task Group of ACI 440 subcommittee F on strengthening has selected a case in between that of the perfect bond and bond slip as follows (2013):

$$I_{ey} = 0.73I_{cr} + 0.05I_g \qquad ACI\ 440\ subcommittee\ F \qquad \textbf{Eq. 4-39}$$

The third set of equations, Bischoff (Eq. 4-40, Eq. 4-41, and Eq. 3-7), is developed by Bischoff and Gross (2011) for FRP reinforced beams with four-point bending and it is implemented by ACI 440.1R-15.

$$I_e = \frac{I_{cr}}{1 - \gamma\eta\left(\frac{M_{cr}}{M_a}\right)^2} \leq I_{gt} \qquad \textbf{Eq. 4-40}$$

$$\gamma = 1.72 - 0.72\left(\frac{I_{cr}}{I_{gt}}\right) \qquad \textbf{Eq. 4-41}$$

$$\eta = 1 - \frac{I_{cr}}{I_{gt}} \qquad \textbf{Eq. 3-7}$$

The two beams, Beam 2 and Beam 4, from Larson, Peterman, and Rasheed (2005) are used for comparison. The post-cracking stage of the load-deflection responses of these beams were digitized and compared to the prediction of the three sets of equations, Eq. 2-46 & Eq. 2-47; Eq. 3-3 & Eq. 4-39; and Eq. 4-40, Eq. 4-41, and Eq. 3-7, to provide a direct feedback to the ACI 440 subcommittee F task group on the applicability of these equation for deflection computations in PRC beams strengthened with external FRP. Figure 4-41 and Figure 4-42 show the load-deflection response for the three sets of equations and the analytical prediction using the method presented earlier.

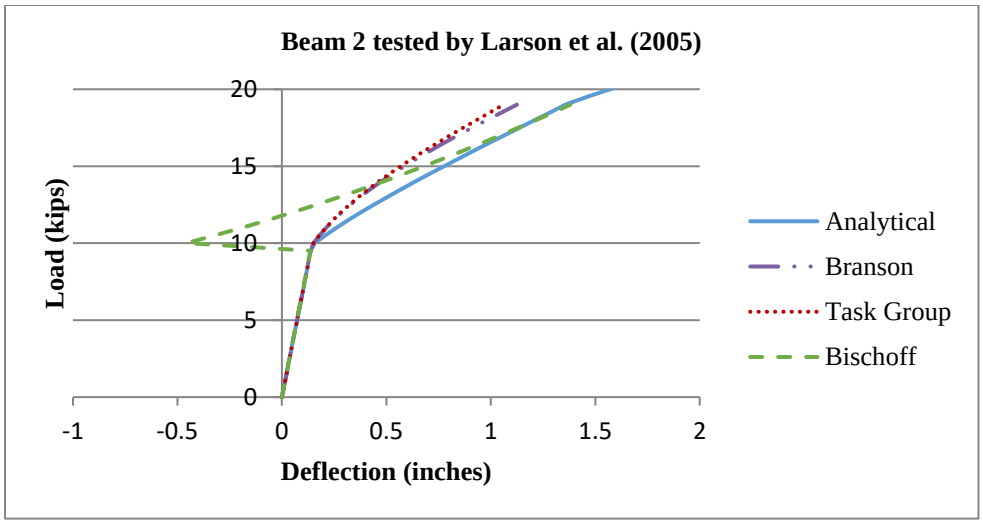

Figure 4-41: Larson el al. (2005) Beam 2 load-deflection comparison of analytical, 440 task group, Bischoff, and experimental effective moment of inertias.

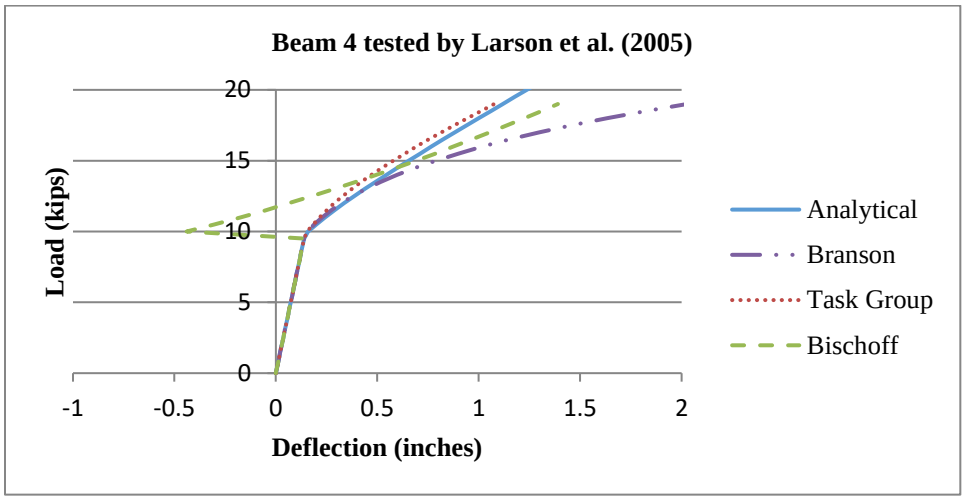

Figure 4-42: Larson et al. (2005) Beam 4 load-deflection comparison of analytical, 440 task group, Bischoff, and experimental moment of inertias.

The first set of equations, Eq. 2-46 & Eq. 2-47, overestimates the effective moment of inertia and underestimates the deflection, but follows the shape of the analytical load-deflection of the PRC FRP beams – it matches more closely to Larson Beam 4 than Larson Beam 2. The second set of equations, Eq. 3-3 & Eq. 4-39, underestimates the deflection of Larson B2, but follows the analytical curve of Larson Beam 4 very closely. The third set of equations, Eq. 4-40,

Eq. 4-41, and Eq. 3-7, is not valid directly after cracking (lightly loaded members), but follows the analytical more closely as it approaches first yield (heavily loaded members). Larson B2 beam has less FRP strengthening than Larson B4 beam.

Further refinement is needed based on the parametric study. The second set of equations is modified and used (Eq. 3-3, Eq. 4-36, and Eq. 4-42) throughout the remainder of this study.

$$I_e = \left(\frac{M_{cr}}{M_a}\right)^3 I_{gt} + \left[1 - \left(\frac{M_{cr}}{M_a}\right)^3\right] I_{ey} \leq I_{gt} \quad \textbf{Eq. 3-3}$$

$$\lambda = \frac{A_{ps}E_{ps}}{A_f E_f} \quad \textbf{Eq. 4-36}$$

$$I_{ey} = 1.21 I_{cr} + 0.029 I_{gt}\lambda \quad \textbf{Eq. 4-42}$$

The third set of equations, Bischoff (Eq. 3-5, Eq. 3-6, and Eq. 3-7), is revised from previously and is developed by Bischoff and Darbi (2012) for FRP reinforced beams with four-point bending. It is currently implemented by ACI 440.1R-15.

$$I_e = \frac{I_{cr}}{1 - \gamma \chi \eta \left(\frac{M_{cr}}{M_a}\right)^2} \leq I_{gt} \quad \textbf{Eq. 3-5}$$

With chi, $\chi = 0.45$.

$$\gamma = 1.7 - 0.7\left(\sqrt{\chi}\frac{M_{cr}}{M_a}\right) \quad \textbf{Eq. 3-6}$$

$$\eta = 1 - \frac{I_{cr}}{I_{gt}} \quad \textbf{Eq. 3-7}$$

The four beams, B2, B3, B5 and B6, from Cha (2001) were examined and are presented. When calculating the effective moment of inertia, the mild steel was neglected since mild steel was excluded from the parametric study and most prestressed members only have a small

amount of mild steel. The experimental load-deflection responses of these beams were digitized and the post-cracking behavior was compared to the prediction of the three sets of equations, Eq. Eq. 2-46 and Eq. 2-47 (Branson); Eq. 3-5, Eq. 3-6, and Eq. 3-7 (Bischoff); and Eq. 3-3, Eq. 4-36, and Eq. 4-42 (Kramer & Rasheed), to provide a direct feedback to the ACI 440 subcommittee F task group on the applicability of these equation for deflection computations in PRC beams strengthened with external FRP.

Figure 4-43 through Figure 4-46 show the load-deflection response for the three sets of equations and the analytical prediction using the methods presented in this dissertation. The experimental is shown in the solid grey line. The first set of equations, Eq. 2-46 and Eq. 2-47, are the Branson and Trost (1982) equations, indicated as the blue long-dashed and two short-dashed lines and labeled 'Branson'. The second set of equations (Eq. 3-5, Eq. 3-6, and Eq. 3-7) are the Bischoff and Gross (2011) equations shown as a medium-dashed, green line that is labeled 'Bischoff'. The third set of equations (Eq. 3-3, Eq. 4-36, and Eq. 4-42) is indicated by a long-dashed and short-dashed dark yellow line are from this study, hence labeled 'Kramer & Rasheed'. While over-estimating the deflection after cracking, the Kramer & Rasheed effective moment of inertia equation mostly closely matches the load-deflection behavior of the experimental Cha beams.

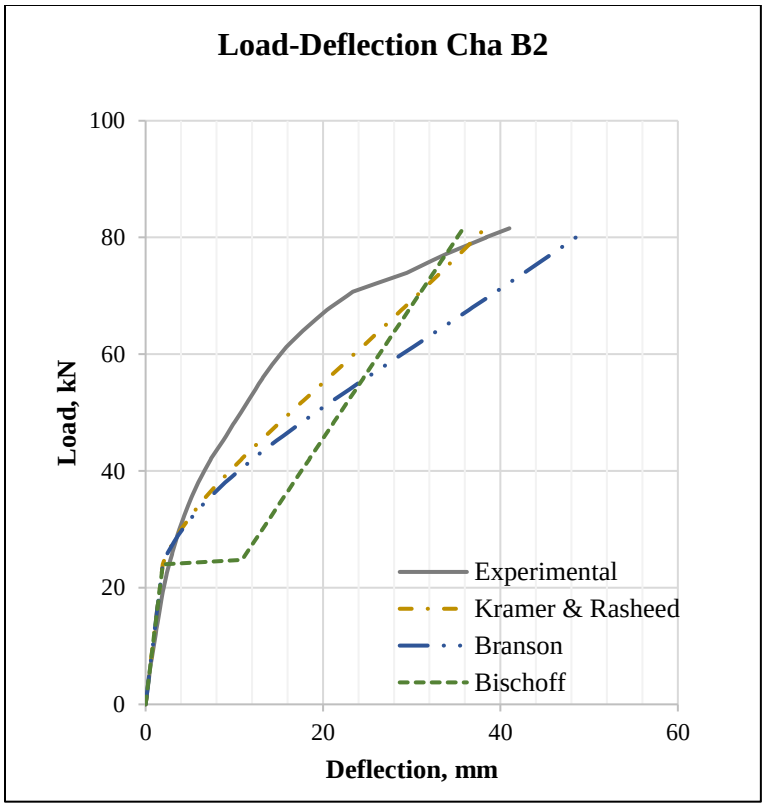

Figure 4-43: Cha B2 beam comparison of effective moment of inertia equations for PRC-FRP beams

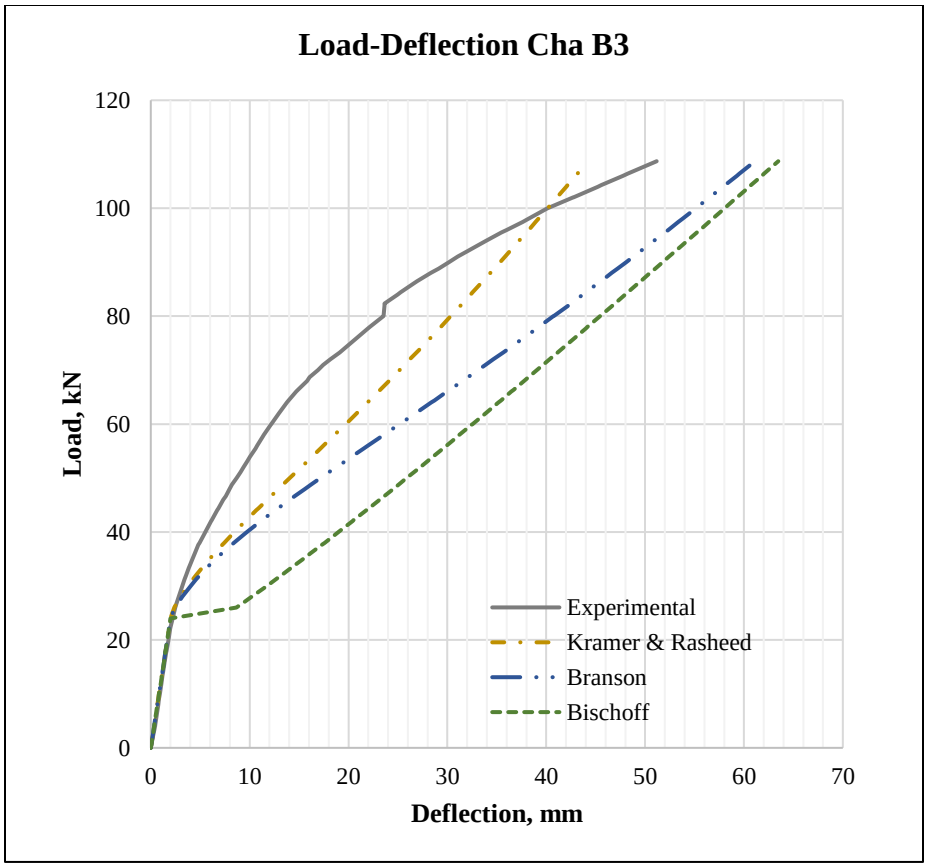

Figure 4-44: Cha B3 beam comparison of effective moment of inertia equations for PRC-FRP beams

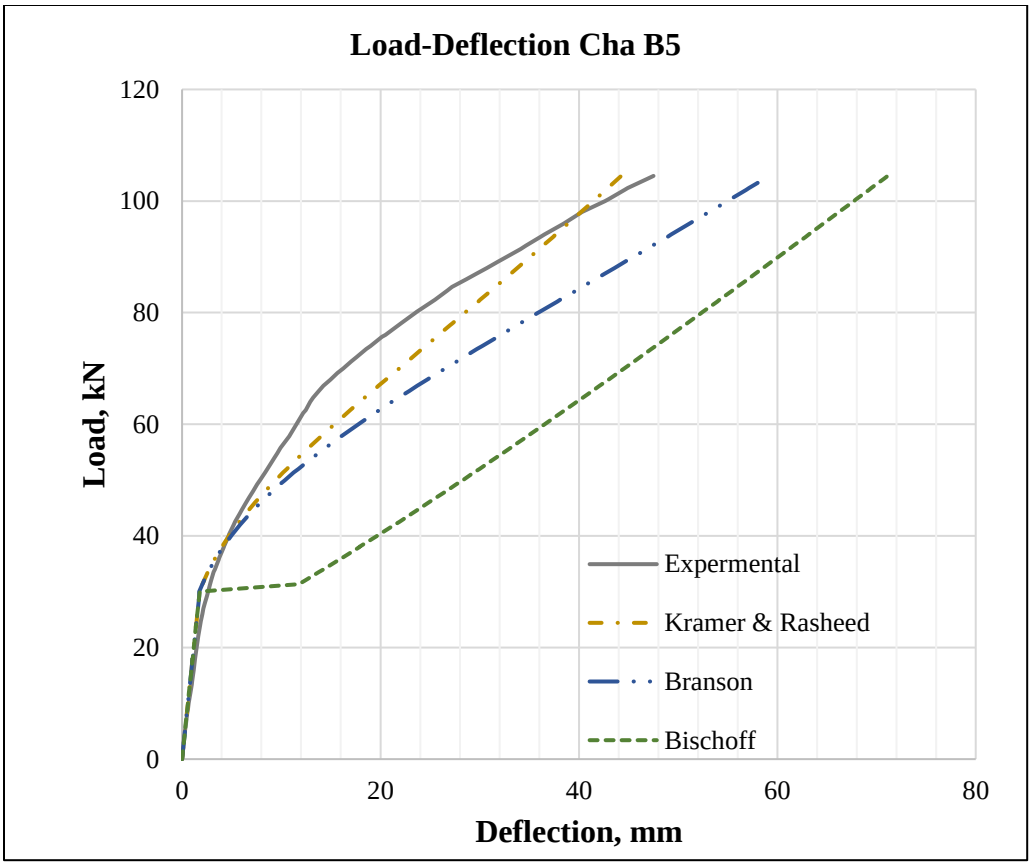

Figure 4-45: Cha B5 beam comparison of effective moment of inertia equations

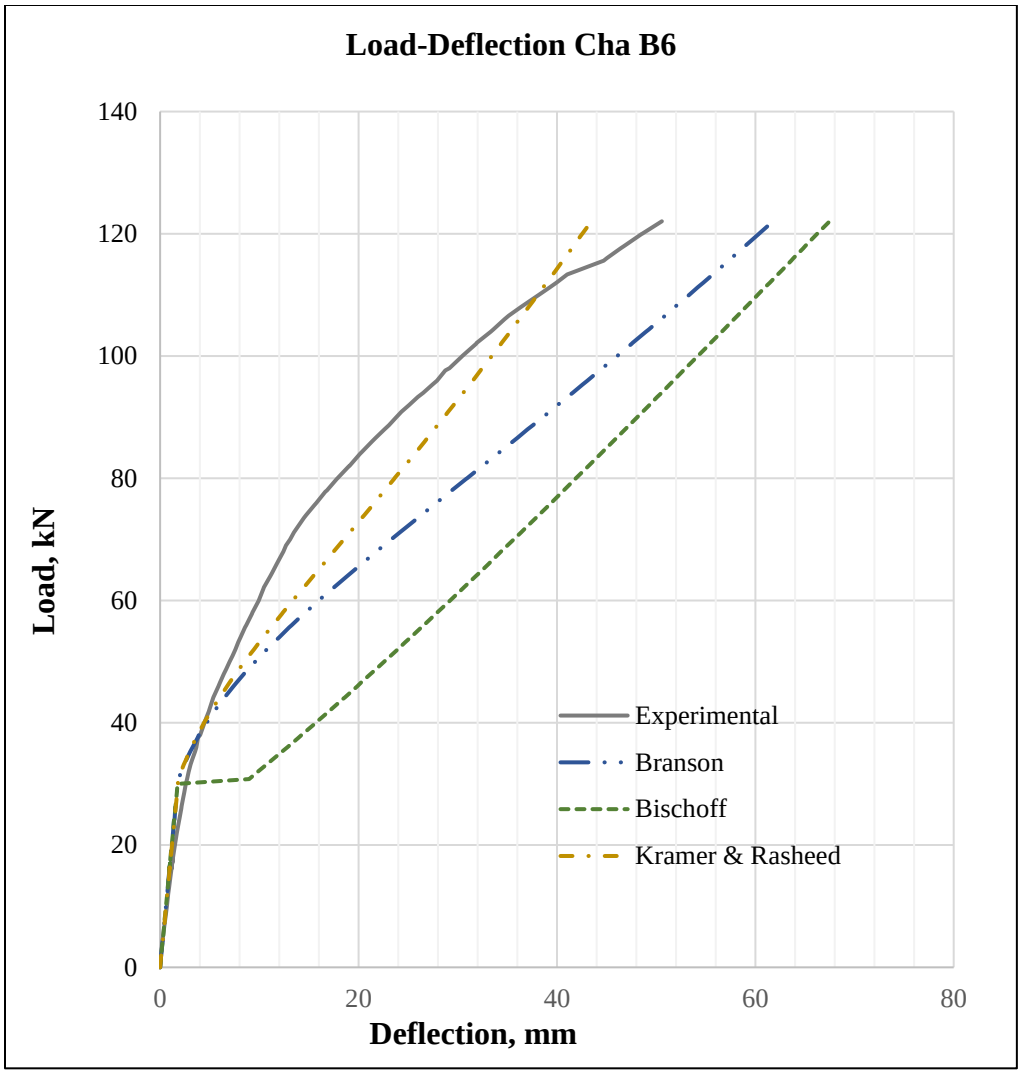

Figure 4-46: Cha B6 beam comparison of effective moment of inertia equations

Figure 4-47 and Figure 4-48 indicate the comparisons of the three sets of equations for Larson Beam 2 and Beam 4. Kramer & Rasheed and Branson methods slightly under-estimate the deflection at a given load after cracking while the Bischoff method over-estimates the deflection.

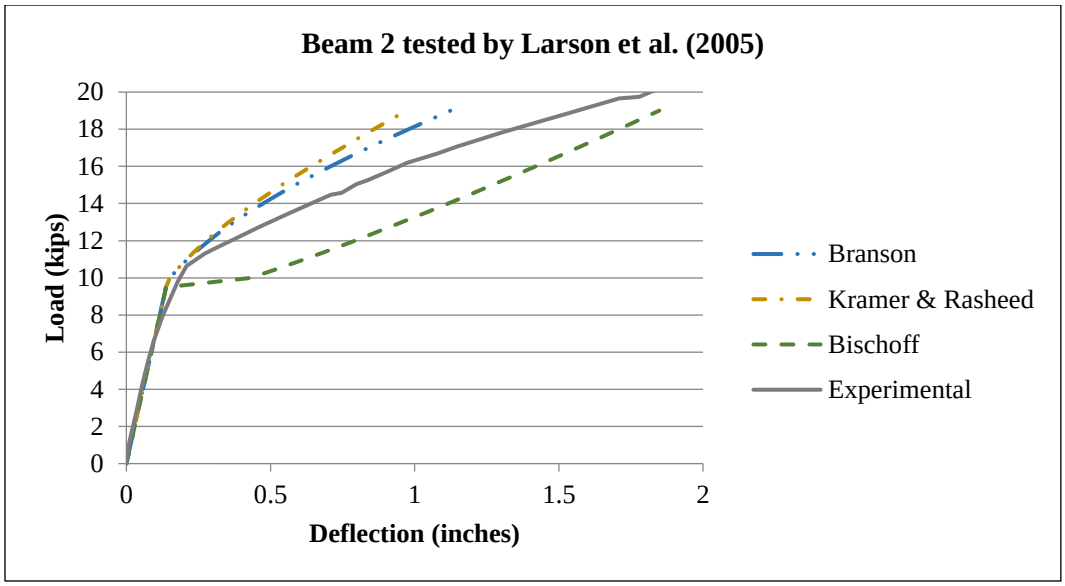

Figure 4-47: Larson B2 beam comparison of effective moment of inertia equations

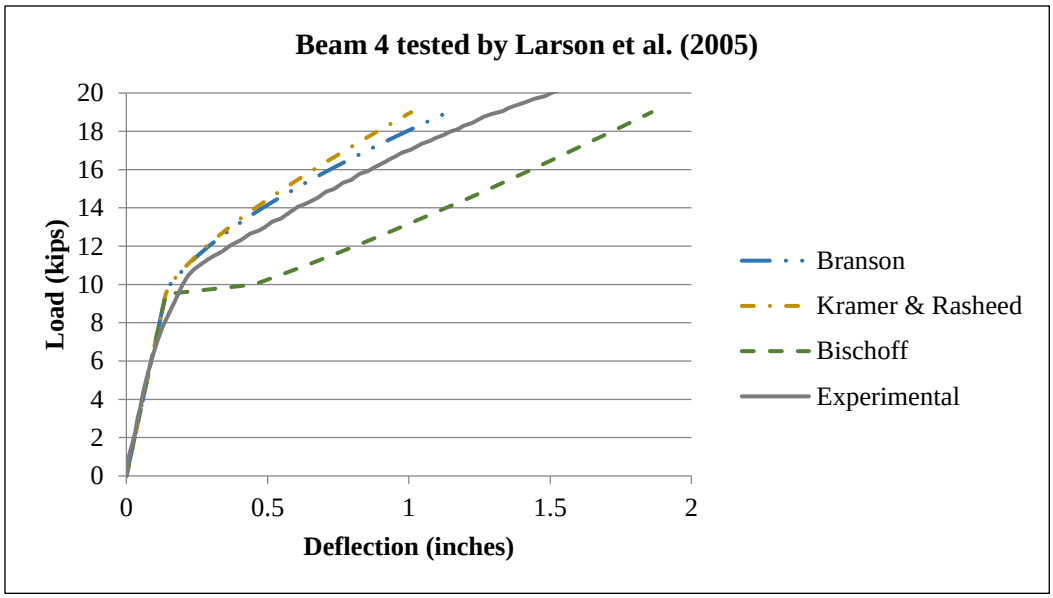

Figure 4-48: Larson B4 beam comparison of effective moment of inertia equations

Chapter 5 - Analytical load-deflection behavior of prestressed reinforced concrete members with harped strands and external FRP.

Although straight strands are generally used in precast beams of moderate span, often harped strands are used in bonded pretensioned prestressed concrete flexural members (Nawy E. G., 2009). A harped strand is an inclined tendon with discontinuity in alignment at planes of concentrated load applications, used in beams subjected primarily to concentrated transverse loading. Straight tendons in pretensioned members can cause high-tensile stresses in the concrete extreme fibers at the support section because of the absence of bending moment stresses due to self-weight and superimposed loads and the dominance of the moment due to the prestressing force alone. At the support, the tensile stress in the top fibers of concrete is eliminated by placing the harped tendon at the center of gravity of the concrete, cgc, of the section. Additionally, the required prestressing force for a harped tendon is smaller at the midspan than the prestressing force required in a straight tendon for the same loading and span. Consequently, prestressed beams can carry heavier loads when using harped strands compared to straight strands due to the balancing effect of the vertical component of the prestressing non-straight tendon. Similarly, a smaller number of strands are needed for the same load capacity of a straight strand beam. Repairs or strengthening of these members after being in-service for decades may be required. One design criterion that needs to be met is deflection.

5.1 Overview

As previously presented in Chapter 2, to determine the short-term deflection of a PRC-FRP beam, the stiffness (*EI*) is needed. After cracking, an effective moment of inertia, I_e, can be used as an average along a span of a simply supported pretensioned, bonded tendon beam. Chapter 3 shows an analytical formulation for short-term deflection analysis procedure for straight strand, bonded PRC-FRP beams. Furthermore, current ACI 440.2 requirements for deflection calculations are presented for PRC-FRP flexural members in Chapter 3. Therefore, the focus of Chapter 5 is how the information presented for straight tendons, with modifications, can be used for harped tendons. Section 5.2 Background for deflection computation of harped tendons offers effective moment of inertia background for pretensioned harped tendon flexural members. Section 5.3 Analytical formulation offers a short-term deflection analysis procedure for harped pretensioned, bonded PRC-FRP beams. To verify the accuracy of the analytical formulation, a numerical formulation is performed using the incremental deformation approach and presented in Section 5.4 Numerical formulation. Results and discussion of results is given in Section 5.5 with conclusions given in Chapter 6.

5.2 Background for deflection computation of harped tendons

As previously indicated in Chapter 2, to limit anchorage stresses, the eccentricity of the prestressing tendon profile is often made less at the support section than at the midspan section or eliminated altogether by harping the strands as shown in Figure 2-4 (Abeles, 1979). Typically for prestressed beams with harped strands, the tendons are placed at several locations along the depth of the member at the support and harped to one or more depths at or near midspan. By

varying the location of the prestressing strands along the length of the member, the sectional properties, such as, moment of interia differs along the length of the member.

In 1970, Shaikh and Branson showed that the application of the effective moment of inertia method to partially prestressed members was adequate for computing short-time deflections of cracked prestressed members even under loads well above usual service levels (Shaikh & Branson, 1970). The effective moment of inertia method for partially prestressed members, prestressed members that crack, was adopted for the 1971 *PCI Design Handbook*. This method is based on computing the live load deflection increment directly from the 'prestress camber' minus 'dead load deflection' point, as presented in Chapter 2.

Branson and Trost (1982) presented unified procedures (effective moment of inertia) for predicting the deflection and central axis location of partially cracked non-prestressed and prestressed concrete members that ACI 318 and PCI adopted.

As shown in Chapter 2, when axial prestressing force exists in a flexural member, the neutral axis which is located at the bottom of the concrete compression zone (assuming positive bending moment) does not coincide with the centroid of the transformed cracked section. Therefore, the effective moment of inertia must be determined about the centroidal axis of the cracked section and not the neutral axis. Additionally, Tadros, Ghali & Meyer (1985) presented a basic equation to determine how the influence of tendon profile on curvature variation along a simply supported member when one-point depressed tendons (harped) tendons are used. They also recommended that curvatures be computed only at key sections along the span and integrated to obtain deflection. Tadros, Ghali & Meyer (1985) recommended that a good estimate of the deflection, after cracking, for a simply supported member with one-point

depressed tendons could be found in terms of curvatures at forty percent of the span (0.4L) and midspan sections (0.5L) by using the Eq. 5-1:

$$\Delta_{mid} = \frac{5(\phi_{mid} + \phi_{0.4L})L^2}{96} \quad \textbf{Eq. 5-1}$$

With the cracking curvature equal to Eq. 5-2

$$\phi_{cr} = \frac{(M_a - Pe_{cr})}{E_c I_{cr}} \quad \textbf{Eq. 5-2}$$

Eq. 5-2 is based on the assumptions that the live load (superimposed load after cracking) curvature at the member ends is zero and that the curvature distribution is approximated as a parabola. First, curvatures due to total load plus prestressing must be obtained, and then those due to dead load (load to cause cracking) plus prestressing, using the geometric properties corresponding to each load level. The difference between the two quantities yields the live load curvatures used in Eq. 5-1.

Branson and Shaikh (1985) reexamined the effective moment of inertia method applied to partially prestressed members in 1970 and compared it computing curvatures, simplified effective moment of inertia method used by PCI and PCA at the time. When comparing to 313 experimental beams and slabs by 21 different authors over 20 years, they found that the effective moment of interia procedure considering prestressing (the current ACI method) was adequate for computing short-time deflections of cracked prestressed members even under load well above the usual service load levels. Branson and Shaikh (1985) also concluded that the curvature method that Tadros, Ghali & Meyer (1985) suggested is difficult to obtain due to needing the 0.4L curvature.

5.3 Analytical formulation

Analytical formulation for harped tendon PRC-FRP beams has not be tackled to the best of the author's knowledge. Accordingly, the equations developed in Chapter 4 is directly applied here and the accuracy of these equations are assessed. Further research is needed in this area where the author intends to extend to include a parametric study, but the parametric study is outside the scope of this dissertation.

The nominal moment capacity of the strengthened partially PRC beam can be estimated using the non-linear behavior of constituent materials: concrete, non-prestressed steel,

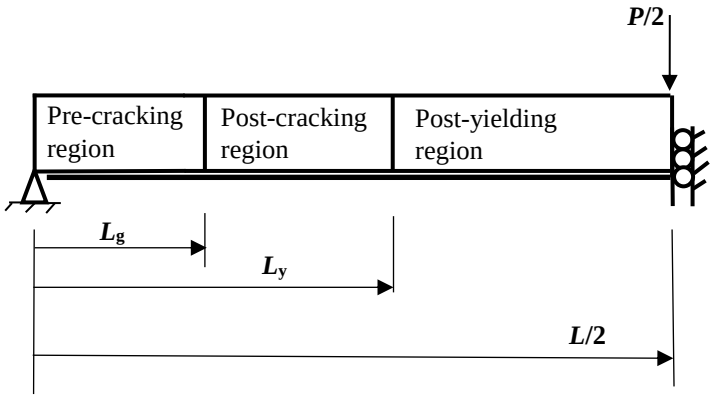

Figure 5-1: Profile of the half beam loaded at midspan, showing the three distinct regions

5.3.1 Assumptions

The following assumptions are made within the framework of the presented formulation:

1. Concrete in compression behaves linearly up to an extreme fiber stress of $0.7f_c'$ then Hognestad's parabolic equation is used (Park and Pauley, 1975).
2. The equivalent rectangular stress block is used to replace the parabolic stress distribution at any stage of nonlinear analysis (Park and Pauley, 1975).
3. Reinforcing steel has the classical linear elastic-perfectly plastic response.

4. Unidirectional FRP laminates are used with fibers along the beam axis, which behave linearly up to brittle failure.
5. The section moment of inertia before cracking is the transformed gross value (I_g).
6. The section moment of inertia reduces to the fully cracked value (I_{cr}) upon steel yielding when the concrete response in compression is still linear (Ross et al, 1999). When the concrete response is not linear, the section effective moment of inertia (I_e) reduces further and it is calculated from nonlinear analysis.
7. The effective section moment of inertia at ultimate level is determined by $I_n = M_n / E_c\phi_n$ (Figure 5-2).
8. The section moment-curvature response is tri-linear (Figure 5-2). This model considers some tension stiffening effects – the effective section rigidity E_cI_e after cracking is gradually reduced from E_cI_g to E_cI_y where $I_y = M_y / E_c\phi_y$ (or E_cI_{cr} when linear analysis is applicable).
9. The curvature distribution along the beam span is obtained from the moment diagram and the moment-curvature relationship.
10. The external FRP plate/sheet extends along the entire clear span and stops just before the supports, when developing the closed form solutions. The small-unstrengthened region close to the supports is expected to add a negligible additional deflection. Debonding of the FRP is prevented.
11. The FRP plate/sheet is perfectly bonded to the beam that is expected to be accurate with proper transverse anchorages or thin laminates.
12. The prestressed strand yielding occurs at a strain of 0.010 and prestressing stand rupture occurs at a strain of 0.050 per PCI Design Handbook Section 11.2.5

(2017). The rupture strain is considered a conservative lower limit for strand rupture.

13. The prestressing reinforcement is harped with a single depressed reinforcement layout which alters the cross-sectional strand location along the member, requiring a tri-linear moment-curvature diagrams for each of the cross-sectional layouts along the member.
14. Continuous function for curvature distribution is assumed using a cubic or quadratic polynomial to model the variations due to the profile change of the strand.
15. The prestressing reinforcement is fully bonded to the concrete.
16. The load-deflection response is determined up to the ultimate flexural strength. Strength equations developed by others can be used to predict premature failure loads and utilize the present load-deflection curve up to these premature failure load levels.

5.3.2 Harped tendon moment-curvature relationship

An alternative to the effective moment of inertia approach of calculating RC member deflections is the integration of curvatures method (Ghali, 1993). Integration of curvatures involves calculating the curvature due to a given load at various points along a member and integrating the curvatures over the member's length to obtain the deflection at a desired location (Kassimali, 1995). Since the geometric properties of the member change along the length of the member, determining the curvature at each section is difficult. Therefore, the curvature is

determined at specified sections along the length of the member and using a curvature field function.

The moment-curvature response is idealized as tri-linear with pre-cracking, post-cracking, and post-yielding regions as originally proposed by Charkas, Rasheed, and Melhem (2003) for RC beams, refer to Figure 5-2. The first region, pre-cracking, extends to the onset of flexural cracking. The second region, post-cracking, extends to first yield of the tension reinforcement (prestressing or mild reinforcement depending on location of reinforcement). The third region, post-yielding, extends until the limit of the useable concrete strain (0.003 in/in), FRP debonding according to the equations of ACI 440.2R-17, or the FRP rupture, depending on the flexural failure mode involved. Four key feature points completely define the moment-curvature response of each section of the PRC-FRP flexural members: initial point ($M_{a,i} = 0$, $\phi_{in,i}$), cracking point ($M_{cr,i}$, $\phi_{cr,i}$), yielding point ($M_{y,i}$, $\phi_{y,i}$), and ultimate point ($M_{n,i}$, $\phi_{n,i}$).

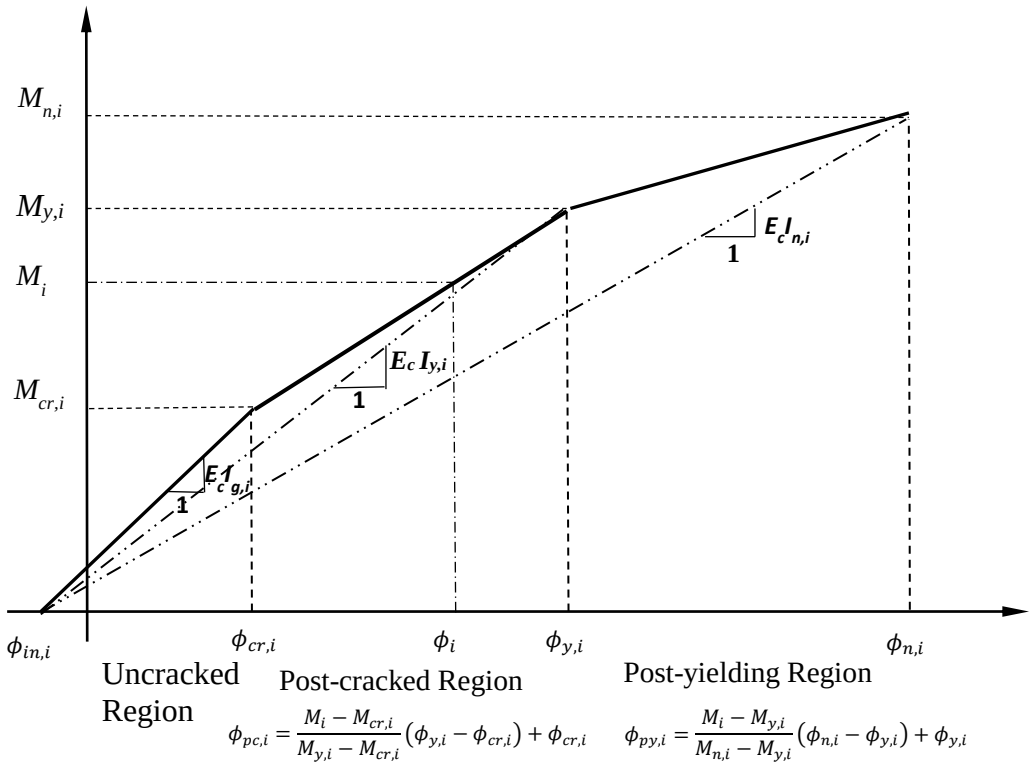

Figure 5-2: Trilinear moment-curvature behavior of harped tendon PRC-FRP at a selected section

5.3.2.1 Initial point at a selected section

Each selected section along the beam will have an initial moment-curvature point (M_a = 0, $\phi_{in,i}$) that is a theoretical point in which the total externally applied moment is zero and the initial curvature is due to the prestressing after losses and neglecting self-weight defined as:

$$M_a = 0 \qquad \textbf{Eq. 5-3}$$

and

$$\phi_{in_i} = -\frac{P_e e_i}{E_c I_{gt_i}} \qquad \textbf{Eq. 5-4}$$

Negative sign indicates an upward curvature, camber.

5.3.2.2 Cracking point at a selected section

The second critical point is the end of the linear-elastic response for the selected section along the member; also, called the cracking moment-curvature point ($M_{cr,i}$, $\phi_{cr,i}$) and is defined as:

$$M_{cr_i} = \frac{\left(f_r A_{gt} + P_{e_i}\right)\left(\frac{I_{gt_i}}{A_{gt}}\right)}{y_{bot_i}} + P_e e_i \qquad \textbf{Eq. 5-5}$$

and

$$\phi_{cr_i} = \frac{\left(M_{cr_i} - P_e e_i\right)}{E_c I_{gt_i}} \qquad \textbf{Eq. 5-6}$$

5.3.2.3 Yielding point at a selected section

The third point, yielding point ($M_{y.i}$, $\phi_{y,i}$), occurs as the prestressing steel at a specific section reaches the yielding strain at one percent elongation with the neutral axis assumed within the concrete flange, for flanged section cases. The yielding point is estimated first by assuming $I_{y,i} = I_{cr,i}$ with $\phi_{y,i} = \varepsilon_{pu,i} / d_{ps,i} - c_{y,i}$, where $c_{y,i}$ is the depth of the section neutral axis at first yielding for a selected section, and $I_{y,i}$ is the effective section moment of inertia at yielding of a selected section (Figure 5-3). . In Figure 5-3, the non-prestressing steel in the tension region and compression region and the FRP are assumed to be constant in area and depth along the length of the member.

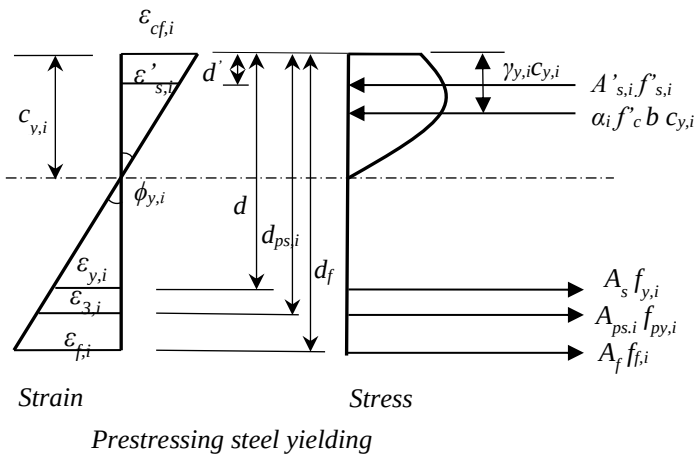

Figure 5-3: Selected section strain-compatibility relationships of harped tendon PRC-FRP at prestressing steel yielding

The yielding moment at a selected section is equal to the modulus of elasticity of concrete times the cracking moment of inertia times the yielding curvature as shown in Eq. 5-7.

$$M_{y,i} = E_c I_{cr_i} \phi_{y_i};\ \varepsilon_{cf_i} = \phi_{y_i} c_{y_i};\ \sigma_{cf_i} = E_c \varepsilon_{cf_i} \leq 0.7 f'_c \qquad \textbf{Eq. 5-7}$$

where: $\varepsilon_{cf,i}$ is the compression strain of the extreme concrete fiber; and $\sigma_{cf,i}$ is the corresponding stress within the linear limits based on assumption 1 in Section 5.3.1 Assumptions.

Using Eq. 5-7 produces very accurate estimates of the actual yielding point when the concrete behaves linearly. When the concrete response in compression is non-linear, Hognestad's classical parabolic stress-strain curve up to a concrete useable strain, ε_{cu}, equals 0.003 which produces accurate estimates (Park and Paulay, 1975).

$$\sigma_c = f'_c \left[2\frac{\varepsilon_c}{\varepsilon'_c} - \left(\frac{\varepsilon_c}{\varepsilon'_c}\right)^2 \right] \qquad \textbf{Eq. 5-8}$$

As shown in Figure 5-3, the concrete compressive force is expressed in terms of the parameter α that is used to convert the nonlinear stress-strain relationship into an equivalent rectangular distribution defined as Eq. 5-9:

$$\alpha_i = \frac{\int_0^{\varepsilon_{cf_i}} \sigma_{c_i} d\varepsilon_{c_i}}{f'_c \varepsilon_{cf_i}} = \frac{\varepsilon_{cf_i}}{\varepsilon'_c} - \frac{1}{3}\left(\frac{\varepsilon_{cf_i}}{\varepsilon'_c}\right)^2 \quad \textbf{Eq. 5-9}$$

Accordingly, assuming the non-prestressed reinforcement in the tension region of the selected section yields prior to prestressing steel yielding and all non-prestressed reinforcement in the beam has the same yield strength, the force equilibrium and strain compatibility of the selected section produces:

$$\sum F_x = 0 \Longrightarrow \alpha_i f'_c \, b c_{y_i} + A'_s f'_{s_i} = A_s f_y + A_{ps_i} f_{py} + A_f f_{f_i} \quad \textbf{Eq. 5-10}$$

If the non-prestressed reinforcement in the tension region at the selected section does not yield prior to the prestressing steel yielding at the given section, Eq. 5-10 becomes:

$$\sum F_x = 0 \Longrightarrow \alpha_i f'_c \, b c_{y_i} + A'_s f'_{s_i} = A_s f_{s_i} + A_{ps_i} f_{py} + A_f f_{f_i} \quad \textbf{Eq. 5-11}$$

where the stress in the compression steel, assuming all compression steel has the same yield strength throughout the member, is:

$$f'_{s_i} = E'_s \varepsilon_{3_i} \left(\frac{c_{y_i} - d'}{d_{ps_i} - c_{y_i}}\right) \leq f'_y \quad \textbf{Eq. 5-12}$$

and the stress in the non-prestressed tension steel prior to it yielding is:

$$f_{s_i} = E_s \varepsilon_{3_i} \left(\frac{d_i - c_{y_i}}{d_{ps_i} - c_{y_i}}\right) \leq f_y \quad \textbf{Eq. 5-13}$$

with the strain in the prestressing strands due to additional loading equaling, $\varepsilon_{3,i}$, assuming prestressing strand yielding at 0.01 elongation:

$$\varepsilon_{3_i} = 0.01 - \varepsilon_{1_i} - \varepsilon_{2_i} = 0.01 - \frac{f_{se_i}}{E_{ps}} - \frac{1}{E_c}\left[\frac{P_{e_i}}{A_{gt_i}} + \frac{P_{e_i} {e_i}^2}{I_{gt_i}}\right] \quad \textbf{Eq. 5-14}$$

and the stress in the FRP at a selected section, considering the effect of initial deformations due to service loads during beam strengthening, is:

$$f_{f_i} = E_f \left[\varepsilon_{3_i} \left(\frac{d_f - c_{y_i}}{d_{ps_i} - c_{y_i}} \right) - \varepsilon_{bi_i} \right] \quad \textbf{Eq. 5-15}$$

In addition, the stress is the prestressing steel is at a selected section:

$$f_{py_i} = E_{ps} \left[\varepsilon_{3_i} - \varepsilon_{bi_i} \right] \quad \textbf{Eq. 5-16}$$

Where the strain in the prestressing steel at a given section is:

$$\varepsilon_{ps_i} = \varepsilon_{1_i} + \varepsilon_{2_i} + \frac{0.003}{c_{nc_i}} \left(d_{ps_i} - c_{nc_i} \right) \quad \textbf{Eq. 5-17}$$

The yielding stress, $f_{py,i}$ varies with the strength of the prestressing used. As given in *PCI Design Handbook* (2017), the effective prestressing stress, $f_{ps,i}$, for 270 ksi (1862 MPa) strand is approximated by the following equations:

$$\varepsilon_{ps_i} \leq 0.0086 \text{: } f_{ps_i} = 28{,}500 \varepsilon_{ps_i} \, (ksi) \;\; or \;\; 196{,}500 \varepsilon_{ps_i} \, (Mpa)$$

$$\varepsilon_{ps_i} > 0.0086 \text{: } f_{ps_i} = 270 - \frac{0.04}{\left(\varepsilon_{ps_i} - 0.007 \right)} \, (ksi)$$

$$or \quad f_{ps_i} = 1860 - \frac{0.276}{\left(\varepsilon_{ps_i} - 0.007 \right)} \, (MPa) \quad \textbf{Eq. 5-18}$$

250 ksi (1724 MPa) prestressing strands are more common in prestressed concrete structures built prior to 1970's, which have an effective prestressing stress, $f_{ps,i}$, approximated by the following equations:

$$\varepsilon_{ps_i} \leq 0.0076 \text{: } f_{ps_i} = 28{,}500 \varepsilon_{ps_i} \, (ksi) \;\; or \;\; 196{,}500 \varepsilon_{ps_i} \, (Mpa)$$

$$\varepsilon_{ps_i} > 0.0076 \text{: } f_{ps_i} = 250 - \frac{0.04}{\left(\varepsilon_{ps_i} - 0.0064 \right)} \, (ksi)$$

$$or \quad f_{ps_i} = 1720 - \frac{0.276}{\left(\varepsilon_{ps_i} - 0.0064 \right)} \, (MPa) \quad \textbf{Eq. 5-19}$$

For the case where the non-prestressing steel in the tension region of the selected section yields, substituting Eq. 5-12, Eq. 5-14 through

Eq. 5-18 into Eq. 5-10 produces:

$$f_c' b c_{y_i}^2 \left[1 - \frac{c_{y_i}\varepsilon_{3_i}}{3\left(d_{ps_i} - c_{y_i}\right)}\right]\frac{\varepsilon_{3_i}}{\varepsilon_c'} + A_s' E_s \varepsilon_{3_i}\left(c_{y_i} - d'\right) = A_s f_y\left(d_{ps_i} - c_{y_i}\right) + A_{ps_i} f_{py}\left(d_{ps_i} - c_{y_i}\right) + A_f E_f\left[\varepsilon_{3_i}\left(d_f - c_{y_i}\right) - \varepsilon_{0_i}\left(d_{ps_i} - c_{y_i}\right)\right] \quad \textbf{Eq. 5-20}$$

As well, for the case where the non-prestressing steel in the tension region does not yield, substituting Eq. 5-12 through

Eq. 5-18 into Eq. 5-11 generates:

$$f_c' b c_{y_i}^2 \left[1 - \frac{c_{y_i}\varepsilon_{3_i}}{3\left(d_{ps_i} - c_{y_i}\right)}\right]\frac{\varepsilon_{3_i}}{\varepsilon_c'} + A_s' E_s \varepsilon_{3_i}\left(c_{y_i} - d'\right) = A_s E_s \varepsilon_{3_i}\left(\frac{d_i - c_{y_i}}{d_{ps_i} - c_{y_i}}\right) + A_{ps_i} f_{py}\left(d_{ps_i} - c_{y_i}\right) + A_f E_f\left[\varepsilon_{3_i}\left(d_f - c_{y_i}\right) - \varepsilon_{0_i}\left(d_{ps_i} - c_{y_i}\right)\right] \quad \textbf{Eq. 5-21}$$

Eq. 5-20 and

Eq. 5-21 are solved directly for the neutral axis at yield, $c_{y,i}$, which is adjusted based on nonlinear analysis.

The point of action of the concrete compressive force measured from the extreme compression fiber of concrete is written as a fraction of the neutral axis, $\gamma_{y,i}\, c_{y,i}$. The parameter $\gamma_{y,i}$ is obtained from the following expression (Park and Pauley, 1975):

$$\gamma_{y_i} = 1 - \frac{\int_0^{\varepsilon_{cf_i}} \varepsilon_{c_i}\sigma_{c_i} d\varepsilon_{c_i}}{\varepsilon_{cf_i}\int_0^{\varepsilon_{cf_i}} f_{c_i} d\varepsilon_{c_i}} = \frac{\frac{1}{3} - \frac{\varepsilon_{cf_i}}{12\varepsilon_c'}}{1 - \frac{\varepsilon_{cf_i}}{3\varepsilon_c'}} \qquad \textbf{Eq. 5-22}$$

The yielding point, ($M_{y,i}$, $\phi_{y,i}$), is determined by summing the moments about the point of concrete compression resultant force at a selected section with non-prestressed tension steel yielding is shown in

Eq. 5-23 and Eq. 5-24.

$$M_{y_i} = A_{s_i} f_y\left(d - \gamma_{y_i} c_{y_i}\right) + A_f f_f\left(d_f - \gamma_{y_i} c_{y_i}\right) + A_{ps} f_{py}\left(d_{ps_i} - \gamma_{y_i} c_{y_i}\right) + A_s' E_s\left[\frac{\varepsilon_{3_i}\left(c_{y_i} - d'\right)}{\left(d_{ps_i} - c_{y_i}\right)}\right]\left(\gamma_{y_i} c_{y_i} - d'\right) \qquad \textbf{Eq. 5-23}$$

and

$$\phi_{y_i} = \frac{\varepsilon_{3_i}}{d_{ps_i} - c_{y_i}} \qquad \textbf{Eq. 5-24}$$

where $\gamma_{y,i}\, c_{y,i}$ is the depth of the resultant force of concrete in compression at yielding of the prestressing steel.

5.3.2.4 Ultimate point

The fourth point, ultimate moment-curvature point, ($M_{n,i}$, $\phi_{n,i}$) is determined based on the mode of failure (crushing of concrete, FRP rupture or FRP debonding). Refer to Figure 5-4 for

the section stain-compatibility relationships at a selected section for harped strand PRC-FRP flexural members. In Figure 5-4, the non-prestressing steel in the tension region and compression region and the FRP are assumed to be constant in area and depth along the length of the member.

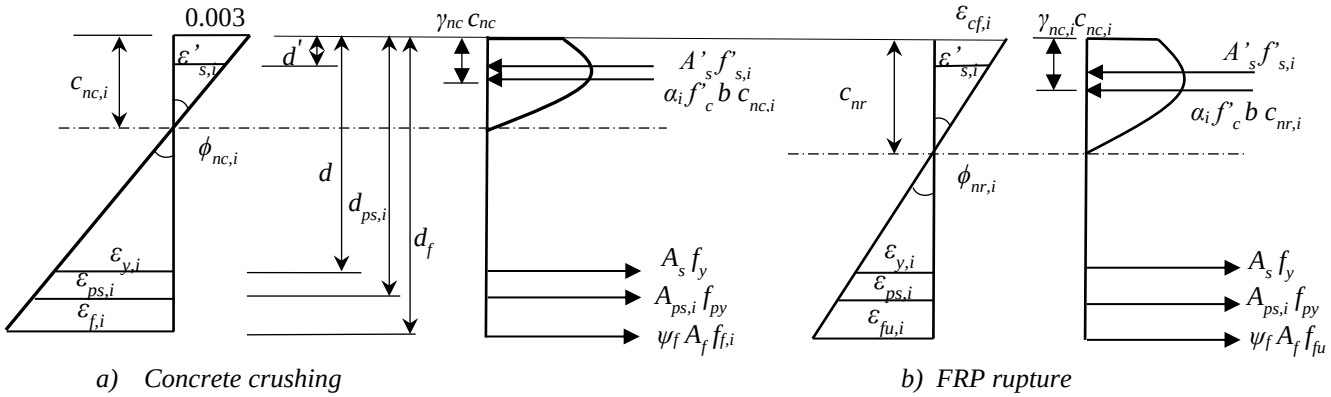

Figure 5-4: Selected section strain-compatibility relationships of harped tendon PRC-FRP. a) concrete crushing and b) FRP rupture or FRP debonding

The FRP reduction factor, ψ_f, is applied to the flexural-strength contribution of the FRP reinforcement based on the reliability analysis (Nowak & Szerszen, 2003). This reduction factor is typically 0.85 and used when designing the strengthened concrete member (ACI Committee 440, 2017). For this study, ψ_f equals one since the tested ultimate load is used. Applying the force equilibrium equation for the case of FRP rupture or FRP debonding in which the non-prestressing steel in tension and prestressing steel yielding produces:

$$\sum F_x = 0 \Longrightarrow \alpha_i f_c' \, b c_{n_i} + A_s' f_{s_i}' = A_s f_y + A_{ps_i} f_{ps} + A_f f_{fu} \qquad \textbf{Eq. 5-25}$$

In the case of crushing of the concrete, 0.003 is considered the ultimate concrete useful strain (Triantafillou & Plevris, 1991) (El-Mihilmy & Tedesco, 2000) except where the concrete compressive strength is greater than 55.2 MPa (8 ksi). In this research, a value of 0.004 is used for the ultimate concrete useful strain when the concrete compressive strength is greater than

55.2 MPa (8 ksi). At a selected section, the strain in the FRP, compression steel, non-prestressed tension steel, and prestressing steel is determined by Eq. 5-26, Eq. 5-27, and

Eq. 5-28, respectively. All are dependent on the concrete compressive strain. The stress in the FRP, compression steel, non-prestressed tension steel, and prestressing steel are determined by Eq. 5-29. Thus, the concrete compression block depth at a selected section, $c_{nc,i}$, is iteratively obtained from the force equilibrium, Eq. 5-25, after substituting strain compatibility equations, Eq. 5-26 through Eq. 5-29, into it.

$$\varepsilon_{f_i} = \left[\frac{0.003}{c_{nc_i}}\left(d_f - c_{nc_i}\right) - \varepsilon_{bi_i}\right] \quad or \quad \varepsilon_{f_i} = \left[\frac{0.004}{c_{nc_i}}\left(d_f - c_{nc_i}\right) - \varepsilon_{bi_i}\right] \qquad \textbf{Eq. 5-26}$$

$$\varepsilon'_{s_i} = \frac{0.003}{c_{nc_i}}\left(c_{nc_i} - d'\right) \quad or \quad \varepsilon'_{s_i} = \frac{0.004}{c_{nc_i}}\left(c_{nc_i} - d'\right) \qquad \textbf{Eq. 5-27}$$

$$\varepsilon_{ps_i} = \varepsilon_{1_i} + \varepsilon_{2_i} + \frac{0.003}{c_{nc_i}}\left(d_{ps_i} - c_{nc_i}\right) \quad or$$

$$\varepsilon_{ps_i} = \varepsilon_{1_i} + \varepsilon_{2_i} + \frac{0.004}{c_{nc_i}}\left(d_{ps_i} - c_{nc_i}\right) \qquad \textbf{Eq. 5-28}$$

$$f_{f_i} = E_f\varepsilon_{f_i} \;\&\; f'_{s_i} = E_s\varepsilon_{s_i} \le f_y \;\&\; f_{s_i} = E_s\varepsilon_{s_i} \le f_y \qquad \textbf{Eq. 5-29}$$

Once the depth of the selected section's neutral axis, $c_{nc,i}$, is evaluated, $M_{n,i}$ (

Eq. 5-30) and $\phi_{n,i}$ (Eq. 5-31) are directly obtained with $\gamma_{cn,i}\, c_{nc,i}$ as the depth of the resultant of concrete in compression at concrete crushing. The variable, ψ_f, is the external FRP strengthening reduction factor equal to 0.85 for design applications, which is based on the reliability analysis of the experimentally calibrated statistical values that accounts for the less

predictable failure mode of delamination of FRP reinforcement, for nominal flexure strength when designing (ACI Committee 440, 2017) (Okeil, Bingol, & Alkhrdaji, 2007). When comparing the derived equation to the experimental results, ψ_f equals 1.0.

$$M_{n_i} = A_s f_y\left(d - \gamma_{nc_i} c_{nc_i}\right) + A_{ps_i} f_{py}\left(d_{ps_i} - \gamma_{nc_i} c_{nc_i}\right) + \psi_f A_f f_f\left(d_f - \gamma_{nc_i} c_{nc_i}\right) + A'_s f'_s\left(\gamma_{nc_i} c_{nc_i} - d'\right) \quad \textbf{Eq. 5-30}$$

and depending on the compressive strength of concrete

$$\phi_{n_i} = \phi_{nc_i} = \frac{0.003}{c_{nc_i}} \quad or \quad \phi_{n_i} = \phi_{nc_i} = \frac{0.004}{c_{nc_i}} \quad \textbf{Eq. 5-31}$$

A similar procedure is used if the failure mode at a particular section is FRP rupture or FRP debonding. The neutral axis depth at a selected section is defined as $c_{nrd,i}$. The steel (mild and prestressing) and concrete stains are related to the FRP ultimate or debonding strain by using strain compatibility as shown in Eq. 5-32 through

Eq. 5-34.

$$\varepsilon_{cf_i} = \varepsilon_{fu} \frac{c_{nrd_i}}{d_f - c_{nr_i}} \quad \textbf{Eq. 5-32}$$

$$\varepsilon'_{s_i} = \varepsilon_{fu} \frac{c_{nrd_i} - d'}{d_f - c_{nrd_i}} or \ \varepsilon_{fd}\left(\frac{c_{nrd_i} - d'}{d_f - c_{nrd_i}}\right) \quad \textbf{Eq. 5-33}$$

$$\varepsilon_{ps_i} = \varepsilon_{1_i} + \varepsilon_{2_i} + \left[\left(\varepsilon_{fu} + \varepsilon_{bi_i}\right)\frac{\left(d_{ps_i} - c_{nrd_i}\right)}{\left(d_f - c_{nrd_i}\right)} \ or \ \left(\varepsilon_{fd} + \varepsilon_{bi_i}\right)\frac{\left(d_{ps_i} - c_{nrd_i}\right)}{\left(d_f - c_{nrd_i}\right)}\right] \quad \textbf{Eq. 5-34}$$

After the strains are determined, the stress in the compression steel at the given section is calculated based on Eq. 5-29; the tension steel has yielded. Once $c_{nr,i}$ is assessed, $M_{n,i}$ and $\phi_{n,i}$ are directly obtained.

$$M_{n_i} = A_s f_y\left(d - \gamma_{nr_i} c_{nrd_i}\right) + A_{ps_i} f_{py}\left(d_{ps_i} - \gamma_{nr_i} c_{nrd_i}\right) + \psi_f A_f\left(f_{fu}\ or\ f_{fd}\right)\left(d_f - \gamma_{nr_i} c_{nrd_i}\right) + A'_s f'_s\left(\gamma_{nr_i} c_{nrd_i} - d'\right) \quad \textbf{Eq. 5-35}$$

and

$$\phi_{n_i} = \phi_{nrd_i} = \frac{\varepsilon_{fu} or\ \varepsilon_{fd}}{d_{fu} - c_{nrd_i}} \quad \textbf{Eq. 5-36}$$

5.3.3 Curvature field function

The effective flexural rigidity of the member reduces with increased moment. The actual stiffness distribution is accounted for by dividing the beam into three distinct regions: pre-cracking, post-cracking, and post-yielding as shown in Figure 5-1 for three-point bending. Additionally, with harped prestressing tendons, the distinct regions vary from selected section to another. For example, due to the prestressing tendon location, a section near the support may crack at a lower moment than an adjacent section farther away from the support. Therefore, with the change of harped strand profile, an approximate distribution of curvature along the beam is determined using an approximate polynomial function.

Polynomial functions consist of one or more terms of variables with whole number exponents. The graphs of polynomial functions have predictable shapes based upon degree and the roots and signs of their first and second derivatives. Higher level derivatives do impart behavioral information into the graphs of fourth degree or higher polynomials, but these effects

are usually too subtle to notice, so would seem to have very limited usefulness. Classifying the various shapes, therefore, is thus limited, here, to the information gleaned from the first and second derivatives.

Since the prestressing tendon location varies along the length of the beam, the approach used for straight strands cannot be used. The beams are analyzed using a finite number of sections along the half span of the beam due to symmetric loading, three-point bending as shown in Figure 5-1.

The general solution can be obtained by adding the deflection contribution of the three regions.

$$\Delta_{mid} = \delta_1 + \delta_2 + \delta_3 = \int_0^{L_g} x\phi_{un}(x)\,dx + \int_{L_g}^{L_y} x\phi_{pc}(x)dx + \int_{L_y}^{\frac{L}{2}} x\phi_{py}(x)dx$$

Eq. 3-38

5.3.3.2 Parabolic curvature distribution

Three sections (two segments) is analyzed as depicted in Figure 5-5 and compared to four sections (three segments) represented in Figure 5-6.

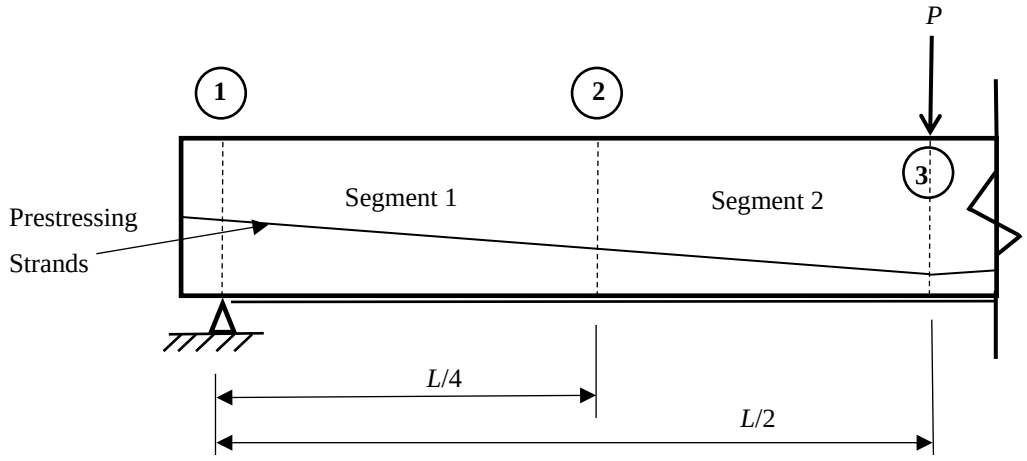

Figure 5-5: Profile of three section, half span of the FRP strengthened, harped strand pretensioned beam

Beam theory using a polynomial function to define the curvature of the beam divided into three sections:

$$\phi(x) = a_0 + a_1 x + a_2 x^2 \qquad \textbf{Eq. 5-37}$$

The first constant, a_0, is the initial curvature, $\phi_{in,1}$, at the support as shown in Eq. 5-38.

$$\phi_{in_1} = a_o = -\frac{P_{e1} e_1}{E_c I_{gt1}} \qquad \textbf{Eq. 5-38}$$

where P_{e1} is the prestressing force at Section 1. The other constants, a_1 and a_2, define the curvature at Section 2 (ϕ_2) and Section 3(ϕ_3), correspondingly. These constants, a_1 and a_2, are solve for by matrix methods. The curvature distribution in matrix form is shown in

Eq. 5-39.

$$\begin{bmatrix} \frac{L}{4} & \frac{L^2}{16} \\ \frac{L}{2} & \frac{L^2}{4} \end{bmatrix} \begin{Bmatrix} a_1 \\ a_2 \end{Bmatrix} = \begin{Bmatrix} \phi_2 - \phi_{in_1} \\ \phi_3 - \phi_{in_1} \end{Bmatrix} \qquad \textbf{Eq. 5-39}$$

To isolate the constants, the curvatures are multiplied by the inverse of the matrix of constants. In order to find the inverse, the Gauss reduction or the adjoint formula is used.

$$\begin{Bmatrix} a_1 \\ a_2 \end{Bmatrix} = \frac{1}{\frac{L^3}{16} - \frac{L^3}{32}} \begin{bmatrix} \frac{L^2}{4} & -\frac{L^2}{16} \\ -\frac{L}{2} & \frac{L}{4} \end{bmatrix} \begin{Bmatrix} \phi_2 - \phi_{in_1} \\ \phi_3 - \phi_{in_1} \end{Bmatrix} \qquad \textbf{Eq. 5-40}$$

Solving for a_1 constant from

Eq. 5-40 and simplifying gives

Eq. 5-41.

$$a_1 = \left[\frac{L^2}{4}(\phi_2 - \phi_{in_1}) - \frac{L^2}{16}(\phi_3 - \phi_{in_1})\right]\frac{32}{L^3}$$

$$= \left(8\phi_2 - 8\phi_{in_1} - 2\phi_3 + 2\phi_{in_1}\right)\frac{1}{L}$$

$$a_1 = \frac{-6\phi_{in_1} + 8\phi_2 - 2\phi_3}{L} \qquad \textbf{Eq. 5-41}$$

Similarly, solving for the a_2 constant from

Eq. 5-40 and simplifying gives

Eq. 5-42.

$$a_2 = \left[-\frac{L}{2}(\phi_2 - \phi_{in_1}) + \frac{L}{4}(\phi_3 - \phi_{in_1})\right]\frac{32}{L^3}$$

$$a_2 = \frac{8\phi_{in_1} - 16\phi_2 + 8\phi_3}{L^2} \qquad \textbf{Eq. 5-42}$$

Once the constants are found, the load-deflection behavior is examined and expressed in

Eq. 5-43.

$$\Delta_{mid} = \delta_1 = \int_{L_y}^{\frac{L}{2}} x\phi(x)dx = \int_0^{\frac{L}{2}} x[a_0 + a_1 x + a_2 x^2]dx$$

$$= \int_0^{\frac{L}{2}} (a_0 x + a_1 x^2 + a_2 x^3)dx \qquad \textbf{Eq. 5-43}$$

Integrating

Eq. 5-43 produces the following midspan deflection equation:

$$\Delta_{mid} = \left[a_0 \frac{x^2}{2} + a_1 \frac{x^3}{3} + a_2 \frac{x^4}{4} \right]_0^{\frac{L}{2}} = a_0 \frac{L^2}{8} + a_1 \frac{L^3}{24} + a_2 \frac{L^4}{64} \qquad \textbf{Eq. 5-44}$$

Substituting Eq. 5-38,

Eq. 5-41, and

Eq. 5-42 for the constants, a_0, a_1, and a_2, into

Eq. 5-44 and simplifying, the general deflection equation for a harped tendon beam with three sections is given in

Eq. 5-45.

$$\Delta_{mid} = \phi_{in_1} \frac{L^2}{8} + \left(\frac{-6\phi_{in_1} + 8\phi_2 - 2\phi_3}{L} \right) \frac{L^3}{24} + \left(\frac{8\phi_{in_1} - 16\phi_2 + 8\phi_3}{L^2} \right) \frac{L^4}{64}$$

$$= \phi_{in_1} \frac{L^2}{8} + \left(-6\phi_{in_1} + 8\phi_2 - 2\phi_3 \right) \frac{L^2}{24} + \left(8\phi_{in_1} - 16\phi_2 + 8\phi_3 \right) \frac{L^2}{64}$$

$$\Delta_{mid} = L^2 \left(\frac{\phi_2}{12} + \frac{\phi_3}{24} \right) \qquad \textbf{Eq. 5-45}$$

Where the curvature at Section 2 and Section 3 are given by Eq. 5-46 and Eq. 5-47, respectively. The gross transformed moment of inertia specific to the given section are used in the curvature equations of Section 2 and Section 3.

$$\phi_2 = \frac{M_2}{E_c I_{gt_2}} + \phi_{in_2} \quad \textbf{Eq. 5-46}$$

$$\phi_3 = \frac{M_3}{E_c I_{gt_3}} + \phi_{in_3} \quad \textbf{Eq. 5-47}$$

For the specific load condition of three-point bending, the moments at Section 2 and Section 3 are defined by Eq. 5-48 and Eq. 5-49, separately.

$$M_2 = \frac{PL}{8} \quad \textbf{Eq. 5-48}$$

$$M_3 = \frac{PL}{4} \quad \textbf{Eq. 5-49}$$

Replacing the curvatures in

Eq. 5-45 with Eq. 5-46 through Eq. 5-49 creates the deflection equation,

Eq. 5-50, specific to 3-point bending.

$$\Delta_{mid_{3pt}} = L^2 \left(\frac{\frac{PL}{8}}{\frac{E_c I_{gt}}{12}} + \phi_{in_2} + \frac{\frac{PL}{4}}{\frac{E_c I_{gt}}{24}} + \phi_{in_3} \right) = L^2 \left(\frac{PL}{2E_c I_{gt}} + \phi_{in_2} + \phi_{in_3} \right) \quad \textbf{Eq. 5-50}$$

The curvatures are dependent on the whether the section is in the pre-cracking, post-cracking, and post-yielding regions. Eq. 5-51 and Eq. 5-54 are the curvatures for the pre-cracking region;

Eq. 5-52 and Eq. 5-55 are the curvatures for the post-cracking region; and Eq. 5-53 and Eq. 5-56 are curvatures for the post-yielding region at Section 2 and Section 3, respectively. The moment of interia at a specific section after the section has cracked and prior to yielding is I_{tpci} and the moment of interia at a specific section after yielding is I_{tpyi}.

$$\phi_2 = \frac{M_2}{E_c I_{gt}} + \phi_{in_2} \qquad (uncracked) \qquad \textbf{Eq. 5-51}$$

$$\phi_2 = \frac{M_2 - M_{cr_2}}{E_c I_{t_{pc2}}} + \phi_{in_2} \quad (postcracking) \qquad \textbf{Eq. 5-52}$$

$$\phi_2 = \frac{M_2 - M_{y_2}}{E_c I_{t_{py2}}} + \phi_{in_2} \quad (postyielding) \qquad \textbf{Eq. 5-53}$$

$$\phi_3 = \frac{M_3}{E_c I_{gt}} + \phi_{in_3} \qquad (uncracked) \qquad \textbf{Eq. 5-54}$$

$$\phi_3 = \frac{M_3 - M_{cr_3}}{E_c I_{t_{pc3}}} + \phi_{in_3} \quad (postcracking) \qquad \textbf{Eq. 5-55}$$

$$\phi_3 = \frac{M_3 - M_{y_3}}{E_c I_{t_{py3}}} + \phi_{in_3} \quad (postyielding) \qquad \textbf{Eq. 5-56}$$

5.3.3.3 Cubic curvature distribution

To refine the accuracy of the curvature distribution, four sections (three segments) as shown in Figure 5-6Eq. 5-7 is examined.

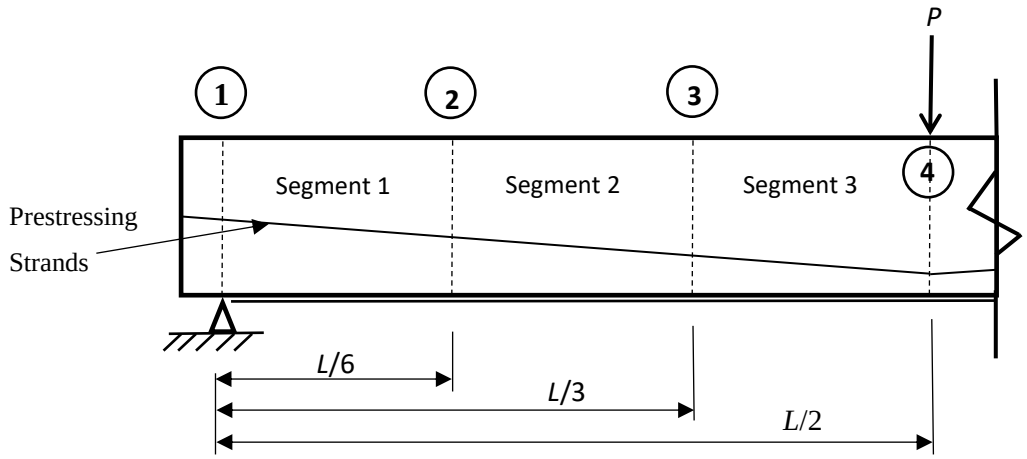

Figure 5-6: Profile of four section, half span of the FRP strengthened, harped strand pretensioned beam

Beam theory using a cubic function to define the curvature of the beam divided into four sections:

$$\phi(x) = a_0 + a_1 x + a_2 x^2 + a_3 x^3 \qquad \textbf{Eq. 5-57}$$

The first constant, a_0, is the initial curvature, $\phi_{in,1}$, as defined by Eq. 5-38. The other constants, a_1, a_2, and a_3, define the curvature at Section 2 (ϕ_2), Section 3 (ϕ_3), and Section 4 (ϕ_4), correspondingly. These are given by Eq. 5-58 through 5-60.

$$\phi_2 = a_0 + a_1 \frac{L}{6} + a_2 \left(\frac{L}{6}\right)^2 + a_3 \left(\frac{L}{6}\right)^3 \qquad \textbf{Eq. 5-58}$$

$$\phi_3 = a_0 + a_1 \frac{L}{3} + a_2 \left(\frac{L}{3}\right)^2 + a_3 \left(\frac{L}{3}\right)^3 \qquad \textbf{Eq. 5-59}$$

$$\phi_4 = a_0 + a_1 \frac{L}{2} + a_2 \left(\frac{L}{2}\right)^2 + a_3 \left(\frac{L}{2}\right)^3 \qquad \textbf{Eq. 5-60}$$

Since a_0 is at the support, the curvature equals the initial curvature as indicated in Eq. 5-38. Considering the set of simultaneous linear algebraic equations aforementioned, the other constants, a_1, a_2, and a_3, are solved for by matrix methods. The curvature distribution in matrix form is shown in Eq. 5-61.

$$\begin{bmatrix} \frac{L}{6} & \frac{L^2}{36} & \frac{L^3}{216} \\ \frac{L}{3} & \frac{L^2}{9} & \frac{L^3}{27} \\ \frac{L}{2} & \frac{L^2}{4} & \frac{L^3}{8} \end{bmatrix} \begin{Bmatrix} a_1 \\ a_2 \\ a_3 \end{Bmatrix} = \begin{Bmatrix} \phi_2 - \phi_{in_1} \\ \phi_3 - \phi_{in_1} \\ \phi_4 - \phi_{in_1} \end{Bmatrix}$$

Eq. 5-61

The determinant of a matrix is a scalar value computed from the elements of a square matrix and encodes certain properties of the linear transformation described by the matrix. The determinant of the Eq. 5-61 is:

$$Det = \frac{L}{6}\left(\frac{L^5}{72} - \frac{L^5}{108}\right) - \frac{L^2}{36}\left(\frac{L^4}{24} - \frac{L^4}{54}\right) + \frac{L^3}{216}\left(\frac{L^3}{12} - \frac{L^3}{18}\right) = \frac{L^6}{3888}$$

Eq. 5-62

To isolate the constants, the curvatures are multiplied by the inverse of the matrix of constants. In order to find the inverse, the Gauss reduction or the adjoint formula is used.

$$L^{-1} = \frac{1}{L^6/3888}\begin{bmatrix} \frac{L^5}{216} & -\frac{5L^4}{216} & \frac{L^3}{36} \\ -\frac{L^5}{432} & \frac{L^4}{54} & -\frac{L^3}{36} \\ \frac{L^5}{1944} & -\frac{L^4}{216} & \frac{L^3}{108} \end{bmatrix}^T$$

Eq. 5-63

And simplifying produces:

$$L^{-1} = \begin{bmatrix} \frac{18}{L} & -\frac{9}{L} & \frac{2}{L} \\ -\frac{90}{L^2} & \frac{72}{L^2} & -\frac{18}{L^2} \\ \frac{108}{L^3} & -\frac{108}{L^3} & \frac{36}{L^3} \end{bmatrix}$$

Eq. 5-64

The matrix equation for the curvatures is therefore:

$$\begin{Bmatrix} a_1 \\ a_2 \\ a_3 \end{Bmatrix} = \begin{bmatrix} \frac{18}{L} & -\frac{9}{L} & \frac{2}{L} \\ -\frac{90}{L^2} & \frac{72}{L^2} & -\frac{18}{L^2} \\ \frac{108}{L^3} & -\frac{108}{L^3} & \frac{36}{L^3} \end{bmatrix} \begin{Bmatrix} \phi_2 - \phi_{in_1} \\ \phi_3 - \phi_{in_1} \\ \phi_4 - \phi_{in_1} \end{Bmatrix}$$ **Eq. 5-65**

Solving for a_1 constant from

Eq. 5-65 and simplifying produces Eq. 5-66.

$$a_1 = \frac{18\phi_2 - 9\phi_3 + 2\phi_4 - 11\phi_{in_1}}{L}$$ **Eq. 5-66**

Similarly, determining a_2 constant from

Eq. 5-65 and abridging gives Eq. 5-67

$$a_2 = \frac{-90\phi_2 + 72\phi_3 - 18\phi_4 + 36\phi_{in_1}}{L^2}$$ **Eq. 5-67**

Lastly, the a_3 constant is calculated from

Eq. 5-65 and shortening creates Eq. 5-68

$$a_3 = \frac{108\phi_2 - 108\phi_3 + 36\phi_4 - 36\phi_{in_1}}{L^3}$$ **Eq. 5-68**

The load-deflection behavior is examined and can be expressed by

Eq. 5-69 and Eq. 5-70.

$$\Delta_{mid} = \delta_1 = \int_{L_y}^{\frac{L}{2}} x\phi(x)dx$$

$$= \int_0^{\frac{L}{2}} x[a_0 + a_1 x + a_2 x^2 + a_3 x^3]dx$$

$$= \int_0^{\frac{L}{2}} (a_0 x + a_1 x^2 + a_2 x^3 + a_3 x^4)dx$$

$$= \left[a_0 \frac{x^2}{2} + a_1 \frac{x^3}{3} + a_2 \frac{x^4}{4} + a_3 \frac{x^5}{5} \right]_0^{\frac{L}{2}} \quad \textbf{Eq. 5-69}$$

$$\Delta_{mid} = a_0 \frac{L^2}{8} + a_1 \frac{L^3}{24} + a_2 \frac{L^4}{64} + a_3 \frac{L^5}{160} \quad \textbf{Eq. 5-70}$$

Substituting the equations (Eq. 5-38, Eq. 5-66 through Eq. 5-68) for the coefficients into Eq. 5-70 creates:

$$\Delta_{mid_{3pt}} = \phi_{in_1} \frac{L^2}{8} + \left(\frac{18\phi_2 - 9\phi_3 + 2\phi_4 - 11\phi_{in_1}}{L} \right) \frac{L^3}{24} \quad \textbf{Eq. 5-71}$$

$$+ \left(\frac{-90\phi_2 + 72\phi_3 - 18\phi_4 + 36\phi_{in_1}}{L^2} \right) \frac{L^4}{64}$$

$$+ \left(\frac{108\phi_2 - 108\phi_3 + 36\phi_4 - 36\phi_{in_1}}{L^3} \right) \frac{L^5}{160}$$

$$= -\frac{269}{240} L^2 \phi_{in_1} + \frac{3}{160} L^2 \phi_2 + \frac{3}{40} L^2 \phi_3 + \frac{13}{480} L^2 \phi_4$$

Simplifying Eq. 5-71 produces:

$$\Delta_{mid_{3pt}} = \frac{L^2}{480}\left[2\phi_{in_1} + 9\phi_2 + 36\phi_3 + 13\phi_4\right] \quad \textbf{Eq. 5-72}$$

The initial curvature at section 1, $\phi_{in,1}$, is defined by Eq. 5-38. At the other sections, the initial curvatures are defined by Eq. 5-73 through Eq. 5-75, respectively. These curvature equations use the specific gross transformed moment of inertia of the given section, Section 2, Section 3, and Section 4. Additionally, the moment of inertia of post-cracking for each given section is based on

$$\phi_{in_2} = -\frac{P_{e_2} e_2}{E_c I_{gt_2}} \quad \textbf{Eq. 5-73}$$

$$\phi_{in_3} = -\frac{P_{e_3} e_3}{E_c I_{gt_3}} \quad \textbf{Eq. 5-74}$$

$$\phi_{in_4} = -\frac{P_{e_4} e_4}{E_c I_{gt_4}} \quad \textbf{Eq. 5-75}$$

The curvature at Section 2 for the uncracked, post-cracking, and post-yielding regions are defined by Eq. 5-76 through Eq. 5-78.

$$\phi_2 = \frac{M_2}{E_c I_{gt_2}} + \phi_{in_2} \qquad (uncracked) \quad \textbf{Eq. 5-76}$$

$$\phi_2 = \frac{M_2 - M_{cr_2}}{E_c I_{t_{pc2}}} + \phi_{cr_2} \qquad (postcracking) \quad \textbf{Eq. 5-77}$$

$$\phi_2 = \frac{M_2 - M_{y_2}}{E_c I_{t_{py2}}} + \phi_{y_2} \qquad (postyielding) \quad \textbf{Eq. 5-78}$$

Similarly, the curvature at Section 3 for the uncracked, post-cracking, and post-yielding regions are defined by Eq. 5-79 through Eq. 5-81.

$$\phi_3 = \frac{M_3}{E_c I_{gt_3}} + \phi_{in_3} \qquad (uncracked) \quad \textbf{Eq. 5-79}$$

$$\phi_3 = \frac{M_3 - M_{cr_3}}{E_c I_{t_{pc3}}} + \phi_{cr_3} \qquad (postcracking) \quad \textbf{Eq. 5-80}$$

$$\phi_3 = \frac{M_3 - M_{y_3}}{E_c I_{t_{py3}}} + \phi_{y_3} \qquad (postyielding)$$ **Eq. 5-81**

Eq. 5-82 through Eq. 5-84 define the curvature at Section 4 for the uncracked, post-cracking, and post-yielding regions.

$$\phi_4 = \frac{M_4}{E_c I_{gt_4}} + \phi_{in_4} \qquad (uncracked)$$ **Eq. 5-82**

$$\phi_4 = \frac{M_4 - M_{cr_4}}{E_c I_{t_{pc4}}} + \phi_{cr_4} \qquad (postcracking)$$ **Eq. 5-83**

$$\phi_4 = \frac{M_4 - M_{y_4}}{E_c I_{t_{py4}}} + \phi_{y_4} \qquad (postyielding)$$ **Eq. 5-84**

For the specific load condition of three-point bending, the moments at Section 2, Section 3, and Section 4 are defined by Eq. 5-48, Eq. 5-85 and Eq. 5-86Eq. 5-49, separately.

$$M_2 = \frac{PL}{12}$$ **Eq. 5-85**

$$M_3 = \frac{PL}{6}$$ **Eq. 5-86**

Once the incremental analysis is developed, the moment at each critical section, defined by Eq. 5-48, Eq. 5-85 and Eq. 5-86, will be compared with $M_{cr,i}$, $M_{y,i}$, and $M_{n,i}$ to determine the appropriate stage, uncracked, post-cracking or post-yielding occurring at the given section. Once the stage of each section is determined, the suitable curvature equations are selected (Eq. 5-76 through Eq. 5-84). The resulting curvatures at these selected sections will be substituted in the deflection expression (Eq. 5-72) at that stage of loading to produce corresponding level of deflection.

5.4 Numerical formulation

The numerical analysis is performed using the incremental deformation approach using an excel program that Calvin Reed developed. Moment-curvature is defined by increasing the extreme compression fiber of concrete from zero to the ultimate value (e.g. 0.003 in case of concrete crushing failure). For every strain value, a neutral axis depth is assumed, which completely defines the strain, stress, and force profile. An iterative loop, using the Goal Seek function in Excel, is made to converge at the neutral axis depth that satisfies the force equilibrium equation. Once the correct neutral axis depth is found, the corresponding moment and curvature are computed for that extreme strain step. This is repeated until all the moment-curvature response is specified.

The present analysis is applicable to PRC-FRP girders with harped tendons, the moment curvature response is different for all sections along the span. Therefore, the shear span is divided into 50 segments with the moment-curvature determined at the end of each segment; the moment at the end of each segment (M_i) is evaluated first then the corresponding curvature value is extracted from the moment curvature curve (ϕ_i) obtained previously. By substituting the curvatures into the deflection expression from moment-area theorem, the mid-span deflection is numerically evaluated by

Eq. 3-107. This numerical integrates each of these different moment-curvature variations along the specific segments to generate the deflection at each load level.

5.5 Comparison of three-segment and four-segment approach with experimental results

Limited studies are available to address the deflection analysis of PRC-FRP beams with harped tendons. Therefore, the three-point bending equations derived in this chapter are validated by analyzing static experiment results of beams tested by Reed and Peterman (2004) and Rosenboom and Rizkalla (2006), also published as Rosenboom, Hassan and Rizkalla (2006), studied the behavior of PRC beams strengthened with various FRP systems.

The beams that Rosenboom, Hassan and Rizkalla (2006) studied were from a dismantled bridge consisting of C-Channel type PRC bridge girders with two different prestressing strand configurations, noted as Type C1 and Type C2. Type C1 prestressing strand configuration used ten 1724 MPa stress-relieved 7-wire prestressing strands, with five strands in each web, three of which were harped at midspan and the bottom two were straight. Type C2 prestressing strand configuration using eight 1862 MPa stress-relieved 7-wire prestressing strands. The strand configuration consisted of four strands in each web, three of which were harped with a hold down at midspan and the bottom strand was straight. The girders were all tested with a clear span of 9.14 m (30 ft). Four beams were strengthened externally with CFRP and are used for this study. The notation for the beams was different in Rosenboom, Hassan, and Rizkalla (2006) than given notation in Rosenboom and Rizkalla (2006). Therefore, the notation specified in Rosenboom, Hassan, and Rizkalla (2006) is used and the notation from Rosenboom and Rizkalla (2006) is given in parenthesis: EB1S (EB1), EB2S (EB4), EB3S (EB5), and EB4S (EB6). EB1S (EB1) was strengthened with Sika CarboDur pre-cured laminate and SikaDur 30 epoxy by using one strip of CFRP, 1.5 mm thickness x 50 mm width (0.059-inch x 2.0 inch), on the bottom of the webs of the C-Channel girders. EB2S (EB4) was strengthened using Fyfe SCH-41 wet lay-

up sheets and Tyfo Type S epoxy with four plies of EB CFRP having a sheet thickness 2.4 mm x 100 mm wide (0.095-inch x 3.9 inch). EB3S (EB5) is strengthened with 3 plies of EB CFRP (VSL- C-200 wet lay-up sheets with MBrace epoxy system) with a 1.0 mm thickness x 100 mm width (0.039-inch x 3.9 inch) for each ply. EB4S (EB6) is strengthened with 5 plies of EB CFRP (Mitsubishi wet lay-up sheets F637400 and MBrace epoxy system) with a 1.0 mm sheet thickness x 125 mm width (0.039-inch x 4.9 inch). The four specimens are identified as Rosenboom EB1S through Rosenboom EB4S in Table 5-1 and Table 5-2, where additional specifics are given.

The Rosenboom, Hassan, and Rizkalla (2006) specimens were loaded in three-point loading using a hydraulic actuator mounted to a steel frame at midspan. Load and midspan deflection were recorded while loading the beams to failure. Rosenboom EB1S, Rosenboom EB2S, Rosenboom EB3S, and Rosenboom EB4S failure modes are debonding of CFRP, rupture of CFRP, crushing of concrete, and rupture of CFRP, respectively. Graphs indicating experimental applied load versus experimental deflection for the specimens were digitized and this data is used to create Figure 5-7, Figure 5-8, Figure 5-9, and Figure 5-10. This experimental data is used to compare the analytical formula presented herein of the load versus deflection of the four PRC-FRP beams.

Additionally, Reed and Peterman (2004) evaluated PRC-FRP girders. The specimens for the study were taken from a damaged, decommissioned bridge originally built in the 1960's. Three damaged prestressed double tees were saw cut in half longitudinally to provide a total of six symmetric 915 mm (36 inch) wide by 12.2 m (40 ft) long single-tee specimens. The specimens were 585 mm (23 inch) deep, with a pre-topped 127 mm (5 inch) thick flange. All specimens had four rows of prestressing reinforcement, each row consisting of a single 13 mm

(0.5 inch) diameter strand. The strands were single-point depressed at the midspan to a height of 50 mm (2 inch) form the bottom face. Additionally, two rows of mild-steel reinforcement placed longitudinally and two rows placed laterally in the flange were provided. Specimen 2 (Reed B2) was strengthened for flexure while Specimen 3 (Reed B3) was strengthened for flexure and shear. Both beams were strengthened in flexure with two layers, 305 mm (12 inch) wide sections, of CFRP (M-Brace 1998) wrapped around the bottom of the web. Refer to Table 5-1 and Table 5-2 for more specifics.

A hydraulic actuator was used to load the Reed and Peterman (2004) specimens at the midspan to failure. Reed B2 failed at an ultimate load of 160 kN (36 kips) corresponding to an ultimate moment capacity of 535 kN-m (393 kip-ft) at a deflection of 260 mm (10.25 inch). This specimen failed when a horizontal shear crack occurred in the tension zone near midspan. Reed B3 failed by FRP rupture at an ultimate load of 162 kN-m (393 kip-ft) at a deflection of 345 mm (13.5 inch). The load-deflection response for each of these specimens were digitized for comparison.

Table 5-1: Database collected from literature for PRC-FRP beams with harped strands

Beam ID	h	h_f	b_w^+	b_f^+	A_{ps}^+	A_f^+	d_{ps}	d_f^{++}	f'_c	E_c	f_{ps}	E_{ps}	f_f	E_f	L
	mm	*mm*	*mm*	*mm*	*mm²*	*mm²*	*mm*	*mm*	*MPa*	*MPa*	*MPa*	*MPa*	*MPa*	*MPa*	*mm*
Roseboom EB1S	432	127	60	387.5	348.4	65	**	250.1	61.3	36798	1723	196165	2758	160444	9140
Rosenboom EB2S	432	127	60	387.5	348.4	416	**	250.2	67.8	38700	1723	196500	1123	96000	9140
Rosenboom EB3S	432	127	60	387.5	278.7	690	**	250.1	57.5	35640	1862	196165	600	45087	9140
Rosenboom EB4S	432	127	60	387.5	278.7	972	**	425	50.9	33532	1862	200412	393	132000	9140
Reed B2	585	125	115	915	394.8	101	**	554.5	49	32900	1862	196500	3792	227500	11600
Reed B3	585	125	115	915	394.8	101	**	554.5	49	32900	1862	196500	3192	227500	11600

***non-prestressed reinforcement (compression or tension) is not shown**

****see Table 5.2**

$^+$ for ½ of C-Channel

$^{++}$ average depth shown

Table 5-2: Prestressing strand layout for harped beams

Beam ID	Number of strands	Depth of prestressing at support					Depth of prestressing at midspan				
		$d_{Layer\ 1}$	$d_{Layer\ 2}$	$d_{Layer\ 3}$	$d_{Layer\ 4}$	$d_{Layer\ 5}$	$d_{Layer\ 1}$	$d_{Layer\ 2}$	$d_{Layer\ 3}$	$d_{Layer\ 4}$	$d_{Layer\ 5}$
		mm	*mm*	*mm*	*mm*	*mm*	*mm*	*mm*	*mm*	*mm*	*mm*
Rosenboom EBS1 & EB2S	5	148	192	236	280	394	223	234	245	280	394
Rosenboom EB3S & EB4S	4	-	140	178	254	394	-	258	269	280	394
Reed B2	4	-	285	335	435	485	-	535	535	535	535
Reed B3	4	-	285	335	435	485	-	535	535	535	535
Layers start from the top of the beam											

As indicated in Table 5-1 and Table 5-2, Rosenboom EB1S was externally strengthened with one 1.2 mm by 50 mm wide (0.047 inch by 1.97 inch) strip of CFRP on its bottom web. Figure 5-7 represents the comparison of the load-deflection response of one-half of the C-shaped Rosenboom Beam EB1S from experimental (solid green line), four-section analytical (short-dashed red line) and three-section analytical (long-dashed blue line) results. From the experimental results of the full Rosenboom Beam EB1S, the cracking load, prestress yielding load, and ultimate load for one-half of the C-shaped beam were 26.4 kN (5.9 kips), 72.1 kN (16.2 kips), and 88 kN (19.8 kips), respectively. The three-section and four-section analytical curves are identical until cracking occurs, at approximately 25 kN (5.6 kips), and match the experimental load-deflection curve well up to cracking. After cracking and until prestressing yielding, the three-section analytical curve, shown as the long-dashed line, follows the experimental load-deflection curve well, but underestimates the deflection after cracking until yielding of the prestressing steel at a load of approximately 70 kN (15.7 kips). After yielding of the prestressing steel, the three-section analytical curve slightly overestimates the deflection until failure. The four-section analytical curve, shown as a short-dashed line, closely matches the experimental load-deflection curve to failure. The experimental half-beam Rosenboom Beam EB1S failed due to debonding of the CFRP strips at a load level of 88 kN (19.8 kips). The analytical failure load was 85 kN (19.1 kips).

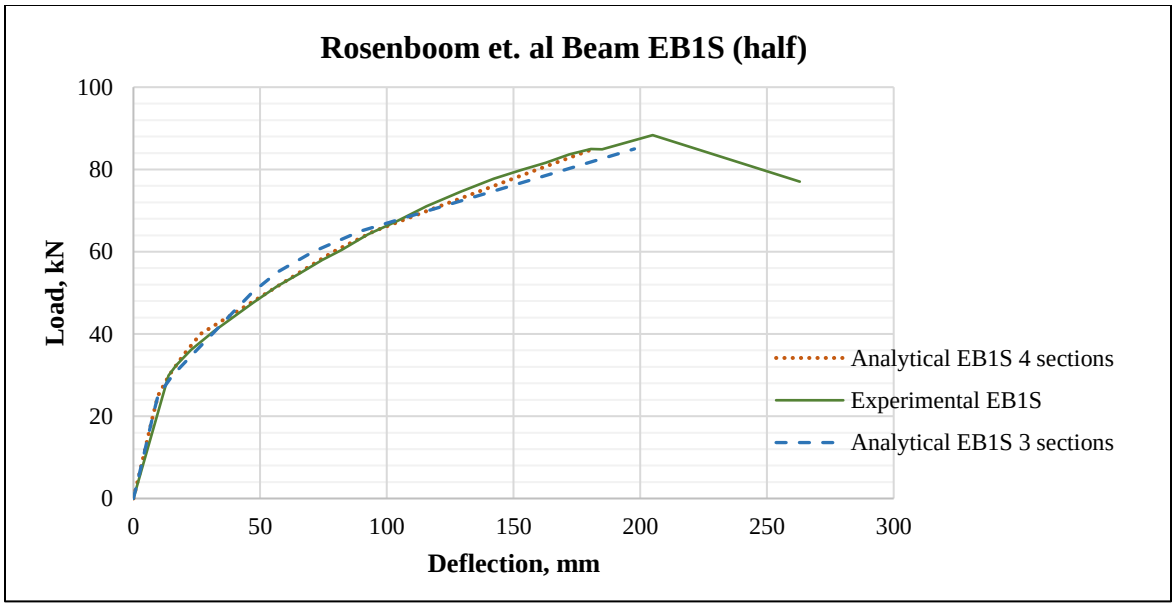

Figure 5-7: Rosenboom EB1S experimental comparison to analytical three-section and four-section methods

Rosenboom EB1S and EB2S had the same prestressing configurations and concrete geometry. The difference between EB1S and EB2S is the amount and type of external strengthening. Rosenboom EB2S was strengthened with four-plies of EB CFRP sheets, 2.4 mm by 100 mm wide (0.095 inch by 3.94 inch) that wraps up the sides of the web. Figure 5-8 signifies the comparison of the load-deflection response of one-half of the C-shaped Rosenboom Beam EB2S from experimental (solid green line), four-section analytical (short-dashed red line) and three-section analytical (long-dashed blue line) results. From the experimental results of the full Rosenboom Beam EB2S, the cracking load, prestress yielding load, and ultimate load for one-half of the C-shaped beam was 28.9 kN (6.5 kips), 69.4 kN (15.6 kips), and 118 kN (26.5 kips), respectively. The three-section and four-section analytical curves are indistinguishable until cracking occurs and match the experimental load-deflection curve as well. After cracking, the three-section analytical curve, shown as the long-dashed line, underestimates the deflection after cracking until failure. The four-section analytical curve, shown as a short-dashed line,

closely matches the experimental load-deflection curve to yielding of the prestressing steel and increasingly underestimates the deflection until failure. One contributing difference between the analytical four-section and experimental curves is the calculated prestressing steel yield point is higher than the experimental. The experimental half-beam Rosenboom Beam EB2S failed due to rupture of the CFRP strips at a load level of 118 kN (26.5 kips). The analytical failure load was 120 kN (27.0 kips).

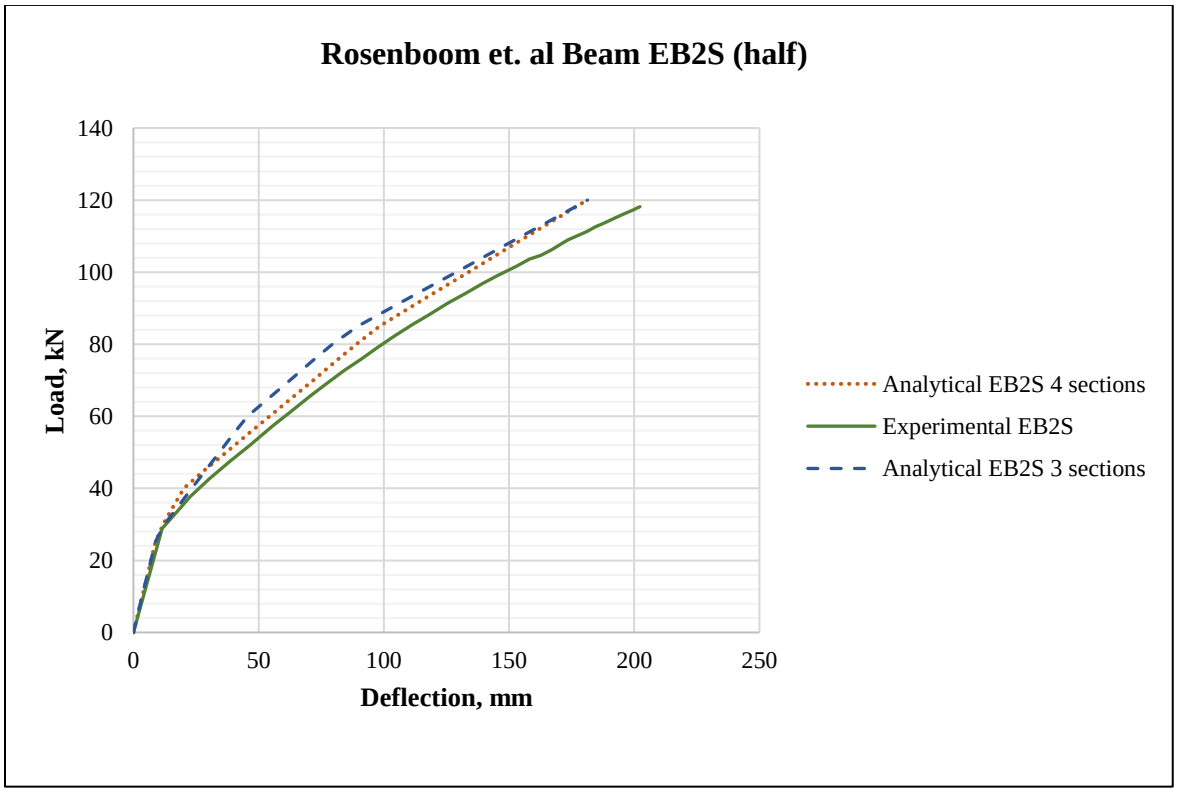

Figure 5-8: Rosenboom EB2S experimental comparison to analytical three-section and four-section methods

Rosenboom beams EB1S and EB2S have the same prestressing configuration while Rosenboom EB3S and EB4S have a different strand layout. All four beams have the same concrete geometry. As indicated in Table 5-1 and Table 5-2, Rosenboom EB3S was externally strengthened with three plies, 1.0 mm by 100 mm wide (0.039 inch by 3.94 inch) sheets of EB CFRP on the bottom of the web and wrapping the sides of the web. Figure 5-9 characterizes the

contrast of the load-deflection response of one-half of the C-shaped Rosenboom Beam EB3S from experimental (solid green line), four-section analytical (short-dashed red line) and three-section analytical (long-dashed blue line) results. From the experimental results of the full Rosenboom Beam EB3S, the cracking load, prestress yielding load, and ultimate load for one-half of the C-shaped beam were 30.9 kN (6.0 kips), 83.2 kN (18.7 kips), and 123 kN (27.7 kips), respectively. The three-section, four-section analytical curves and experimental curve are matching until the cracking load is reached. The three-section and four-section analytical curves are in close agreement with the experimental load-deflection curve until 95 kN (21.4 kips), approximate load of the prestressing steel yielding in the bottom layer. After this point and to failure, the analytical curves underestimate the deflection. The experimental half-beam Rosenboom Beam EB3S failed due to crushing of the concrete at a load level of 123 kN (27.7 kips). The analytical failure load was 130 kN (29.2 kips).

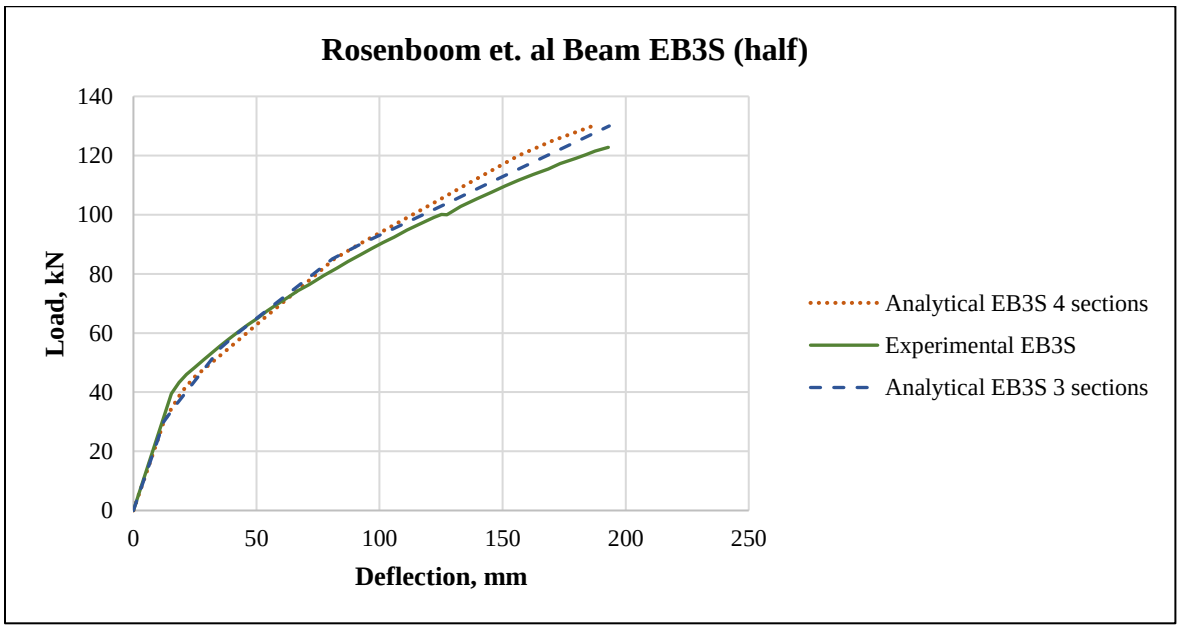

Figure 5-9: Rosenboom EB3S experimental comparison to analytical three-section and four-section methods

As indicated in Table 5-1 and Table 5-2, Rosenboom EB4S was externally strengthened with five plies, 1.0 mm by 125 mm wide (0.039 inch by 4.92 inch) sheets of EB CFRP on the bottom of the web and wrapping the sides of the web. Figure 5-10 characterizes the contrast of the load-deflection response of one-half of the C-shaped Rosenboom Beam EB4S from experimental (solid green line), four-section analytical (short-dashed red line) and three-section analytical (long-dashed blue line) results. From the experimental results of the full Rosenboom Beam EB3S, the cracking load, prestress yielding load, and ultimate load for one-half of the C-shaped beam were 31.8 kN (7.1 kips), 81.8 kN (18.4 kips), and 75 kN (16.9 kips), respectively. The three-section, four-section analytical curves and experimental curve are matching until the cracking load is reached. The three-section and four-section analytical curves are in close agreement with the experimental load-deflection curve until cracking. After this point and to failure, the analytical curves overestimate the deflection. As shown in Figure 5-10, Rosenboom EB4S exhibited a high flexural stiffness up to failure. The experimental half-beam Rosenboom Beam EB4S failed due to rupture of CFRP at a load level of 75 kN (16.9 kips).

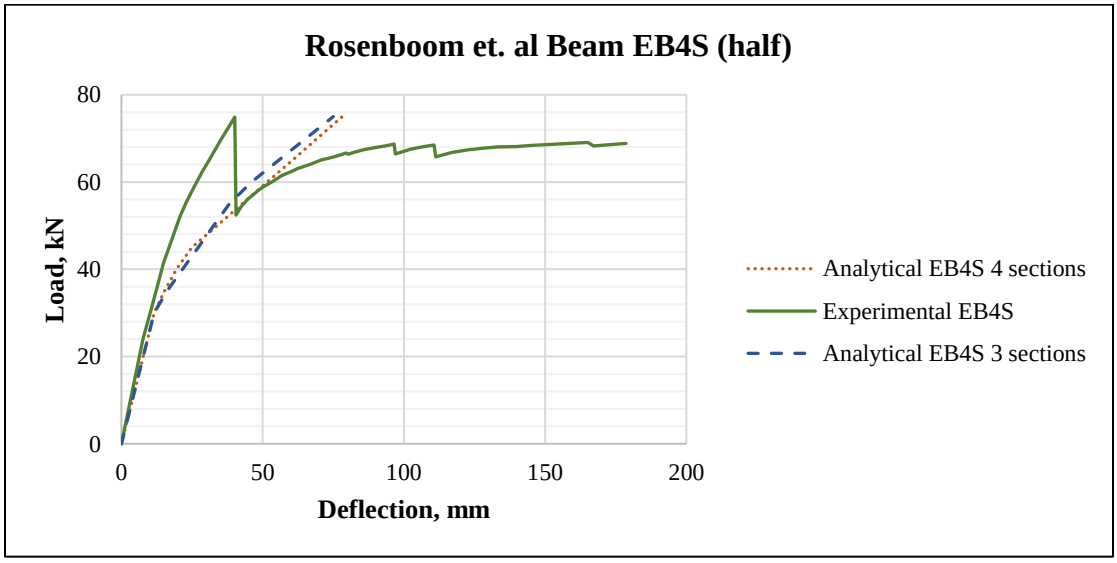

Figure 5-10: Rosenboom EB4S experimental comparison to analytical three-section and four-section methods

The unstrengthened beam properties of Reed B2 and Reed B3 are similar as indicated in Table 5-1 and Table 5-2. Both beams were strengthened for flexure with two layers, 305 mm (12 inch) wide sections, of CFRP (M-Brace 1998) wrapped around the bottom of the web. Specimen 2 (Reed B2) was strengthened for flexure while Specimen 3 (Reed B3) was strengthened for flexure and shear. Comparing Reed B2 and Reed B3 experimental beams to the three-section and four-section analytical methods indicates that the analytical methods match the experimental well until cracking. The analytical methods determined a cracking load higher than the experimental member this could be due to the age of the specimens and use prior to strengthening. After the experimentally defined cracking load and the analytical cracking load, the three-section and four-section analytical methods underestimate the deflection. Once the analytical cracking load is reached, the four-section analytical method closely matches the experimental until failure of Reed B2. Reed B3 beam exhibits a loss of flexural stiffness, greater deflection, after prestressing yielding. Reed B2 failed at an ultimate load of 160 kN (36 kips) when a horizontal shear crack occurred in the tension zone near midspan. Reed B3 failed by FRP rupture at an ultimate load of 162 kN-m (393 kip-ft).

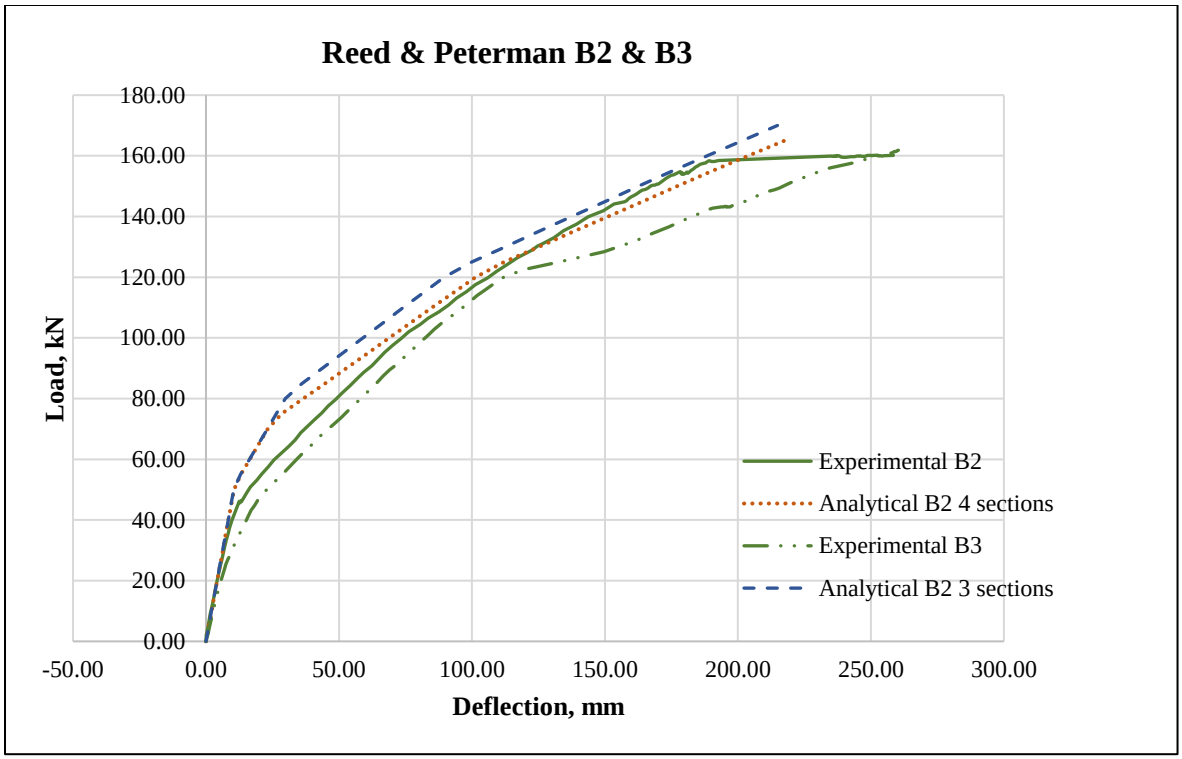

Figure 5-11: Reed & Peterman B2 and B3 experimental comparison to analytical three-section and four-section methods

Similar to Chapter 4, a comparison with different procedures to calculate instantaneous deflections of pretensioned PRC-FRP strengthened C-, L-, or T-beams is presented. Three different sets of deflection prediction equations are examined for deflections within service limits, post-cracking to first yield of the prestressing steel. Some of the equations in this section have been previously presented but are shown here for clarity.

The first set of equations, Eq. 2-46 and Eq. 2-47, is Branson equation used by ACI 318-19 with PCI-10 modifications recommended by Branson and Trost (1982) for the prestressing and currently used by ACI 440.2R-17. This set of equations computes the beam effective moment of inertia after cracking (I_e) as follows:

$$I_e = \left(\frac{M_{cr}}{M_a}\right)^3 I_{gt} + \left[1 - \left(\frac{M_{cr}}{M_a}\right)^3\right] I_{cr} \leq I_{gt} \qquad \textbf{Eq. 2-46}$$

With the cracking moment:

$$M_{cr} = \frac{f_r I_{gt}}{y_{bot}} + \frac{P_e I_{gt}}{A_{gt} y_{bot}} \quad \textbf{Eq. 2-47}$$

The second set equations, Bischoff for three point bending (Eq. 3-5, Eq. 5-87, and Eq. 3-7), is developed by Bischoff and Gross (2011) for FRP reinforced beams with four-point bending and it is implemented by ACI 440.1R-15.

$$I_e = \frac{I_{cr}}{1 - \gamma \chi \eta \left(\frac{M_{cr}}{M_a}\right)^2} \leq I_{gt} \quad \textbf{Eq. 3-5}$$

With chi, $\chi = 0.45$ for steel reinforcement and gamma for three-point bending as given in Eq. 5-87 (Bischoff and Gross 2011).

$$\gamma = 3 - 2\left(\sqrt{\chi}\frac{M_{cr}}{M_a}\right) \quad \textbf{Eq. 5-87}$$

$$\eta = 1 - \frac{I_{cr}}{I_{gt}} \quad \textbf{Eq. 3-7}$$

Further refinement using the parametric study set of equations (Eq. 3-3, **Error! Reference source not found.**, and Eq. 4-42) is studied herein.

$$I_e = \left(\frac{M_{cr}}{M_a}\right)^3 I_{gt} + \left[1 - \left(\frac{M_{cr}}{M_a}\right)^3\right] I_{ey} \leq I_{gt} \quad \textbf{Eq. 3-3}$$

$$\lambda = \frac{A_{ps} E_{ps}}{A_f E_f} \quad \textbf{Eq. 4-36}$$

$$I_{ey} = 1.21 I_{cr} + 0.029 I_{gt} \lambda \quad \textbf{Eq. 4-42}$$

A comparison between the load-deflection prediction from the three sets of equations for the effective moment of inertia is given in Figure 5-12. The experimental curve is shown in the

solid grey line. The first set of equations, Eq. 2-46 and Eq. 2-47, are the Branson and Trost (1982) equations, indicated as the blue long-dashed and two short-dashed lines and labeled 'Branson'. The second set of equations (Eq. 3-5, Eq. 5-87, and Eq. 3-7) are the Bischoff and Gross (2011) equations shown as a medium-dashed, green line that is labeled 'Bischoff'. The third set of equations (Eq. 3-3, **Error! Reference source not found.**, and Eq. 4-42) is indicated by a long-dashed and short-dashed dark yellow line are from this study, hence labeled 'Kramer & Rasheed'. The first yield of prestressing is indicated by a horizontal, solid, orange line in the figures. Figure 5-12 through Figure 5-15 use the same notation.

In Figure 5-12, Set 1 and Set 2 equations, Branson and Bischoff, respectively, extremely over-estimate the deflection after cracking occurring at a load of 25 kN (5.6 kips). Equation Set 3 accurately predicts the deflection up to a load of 50 kN (11.2 kips), which is approximately 70% of the prestressing first yield load of 70 kN (15.7 kips). After a load of 50 kN (11.2 kips), the third set of equations under-estimate the deflection.

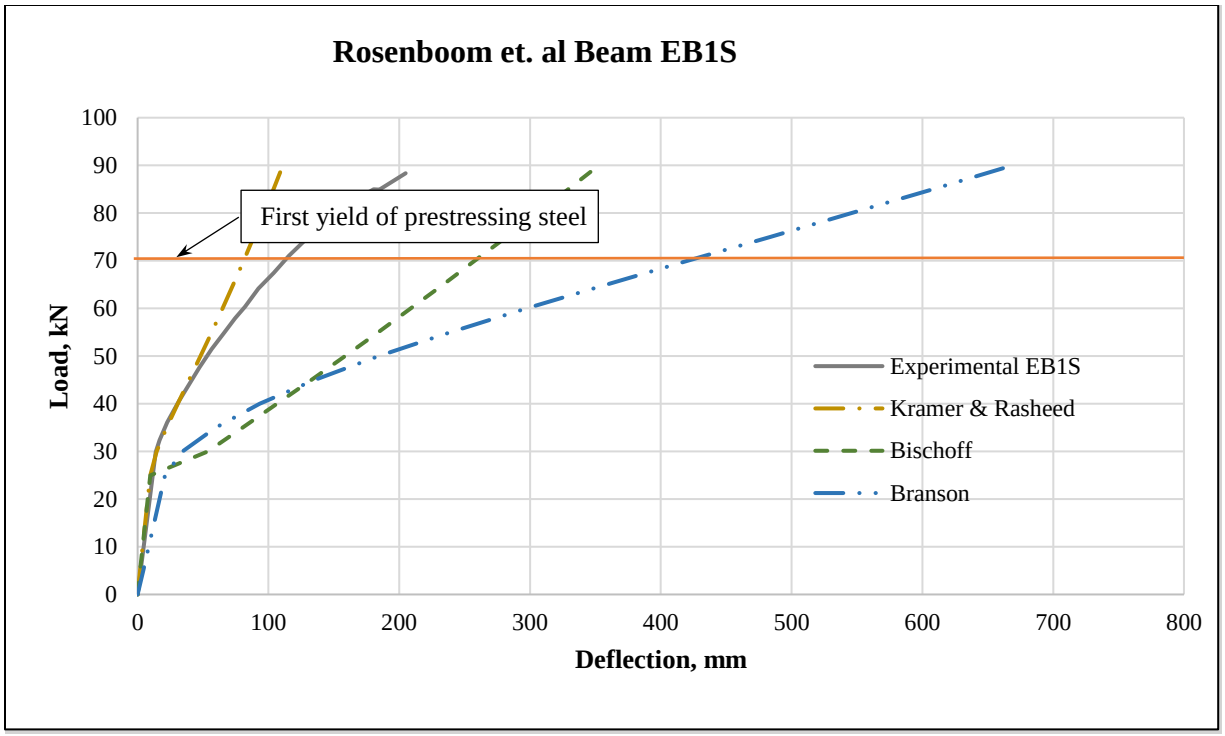

Figure 5-12: Rosenboom et. al beam EB1S load-deflection comparison

Examining Figure 5-13, Set 1 equations, Branson, grossly over-estimates the deflection after cracking occurring at a load of 29 kN (6.5 kips). While Set 2 equations, Bischoff, over-estimates the deflection behavior of Rosenboom et. al beam EB2S. Equation Set 3 accurately predicts the deflection up to a load of 60 kN (13.5 kips), which is approximately 85% of the prestressing first yield load of 70 kN (15.7 kips). After a load of 60 kN (13.5 kips), the third set of equations under-estimate the deflection.

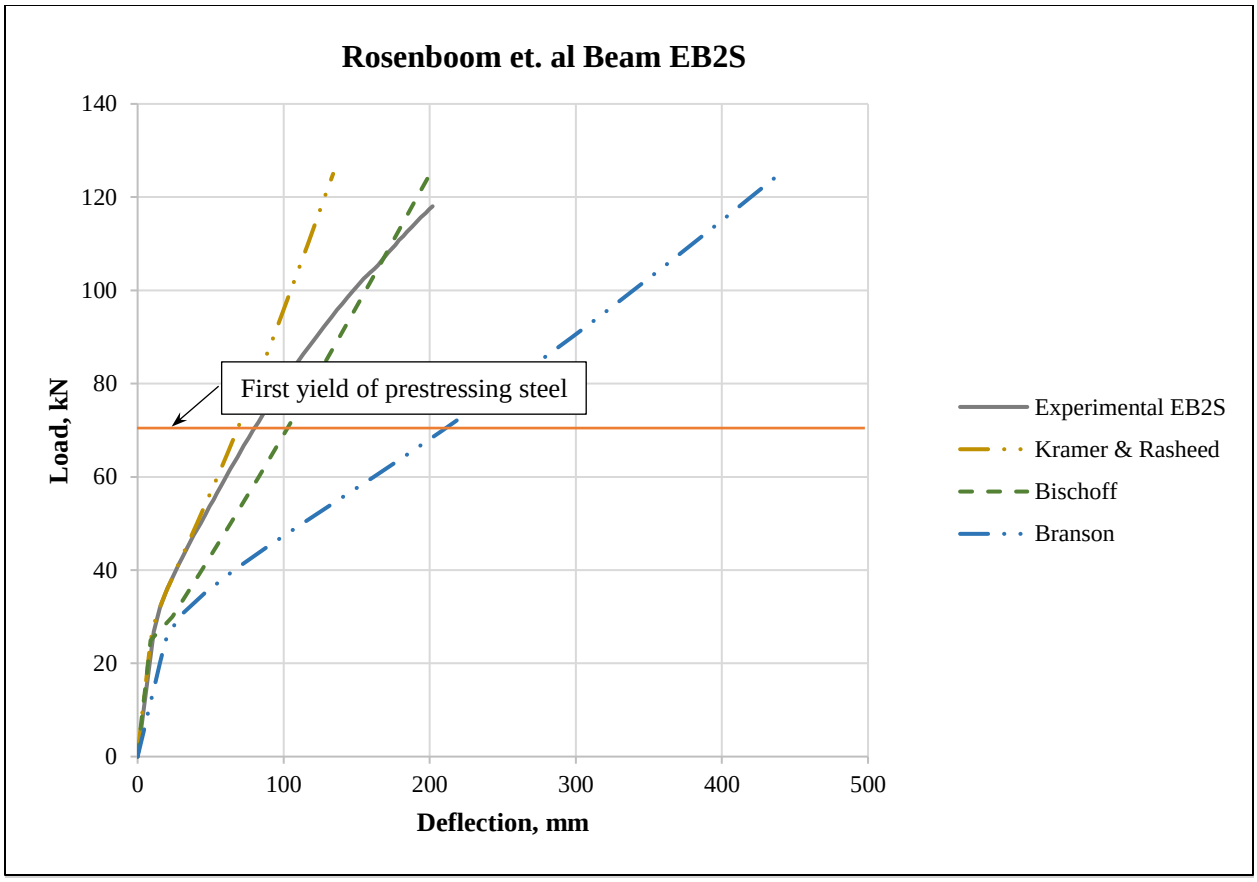

Figure 5-13: Rosenboom et. al beam EB2S load-deflection comparison

Figure 5-14 shows the comparison of the three sets of equations for Rosenboom et. al beam EB3S. Set 1 equations, Branson, grossly over-estimates the deflection after cracking occurring at a load of 31 kN (7.0 kips). Set 2 equations, Bischoff, also over-estimates the deflection behavior of Rosenboom et. al beam EB3S. Equation Set 3 slightly over-estimates the deflection from cracking to first yield of prestressing steel at approximately 83 kN (18.7 kips).

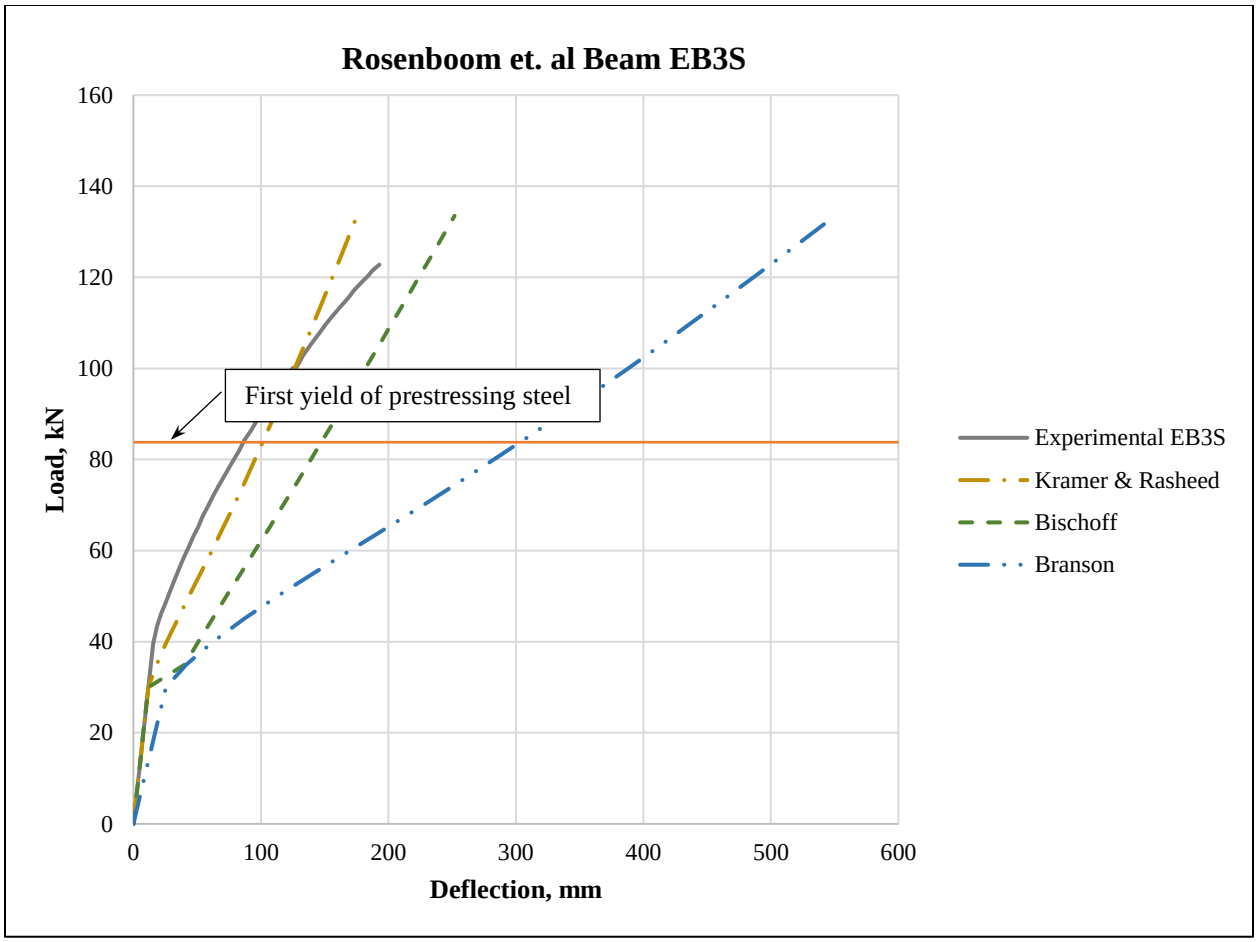

Figure 5-14: Rosenboom et. al beam EB3S load-deflection comparison

Reed & Peterman experimental beams B2 and B3 results are indicated in Figure 5-15. Additionally, a comparison of the three sets of equations is given. Set 1 and Set 2 equations, Branson and Bischoff, respectively, both highly over-estimates the deflection after possible cracking. The experimental beams were pre-cracked prior to testing. Therefore, Reed and Peterman (2005) did not indicate a defined cracking load. The analytical cracking load is roughly 70 kN (15.7 kips), while the experimental exhibits change in stiffness at 45 kN (10.1 kips). Branson equations correlate well up to a load of approximately 75 kN (16.9 kips). As the load increases beyond this, Set 1 equations progressively over-estimates the deflection. Bischoff equations highly over-estimate the deflection after apparent cracking. Set 1 and Set 2 equations

converge at first yield of the prestressing. Equation Set 3 consistently under-estimates the deflection from cracking to first yield of prestressing steel at approximately 145 kN (32.6 kips).

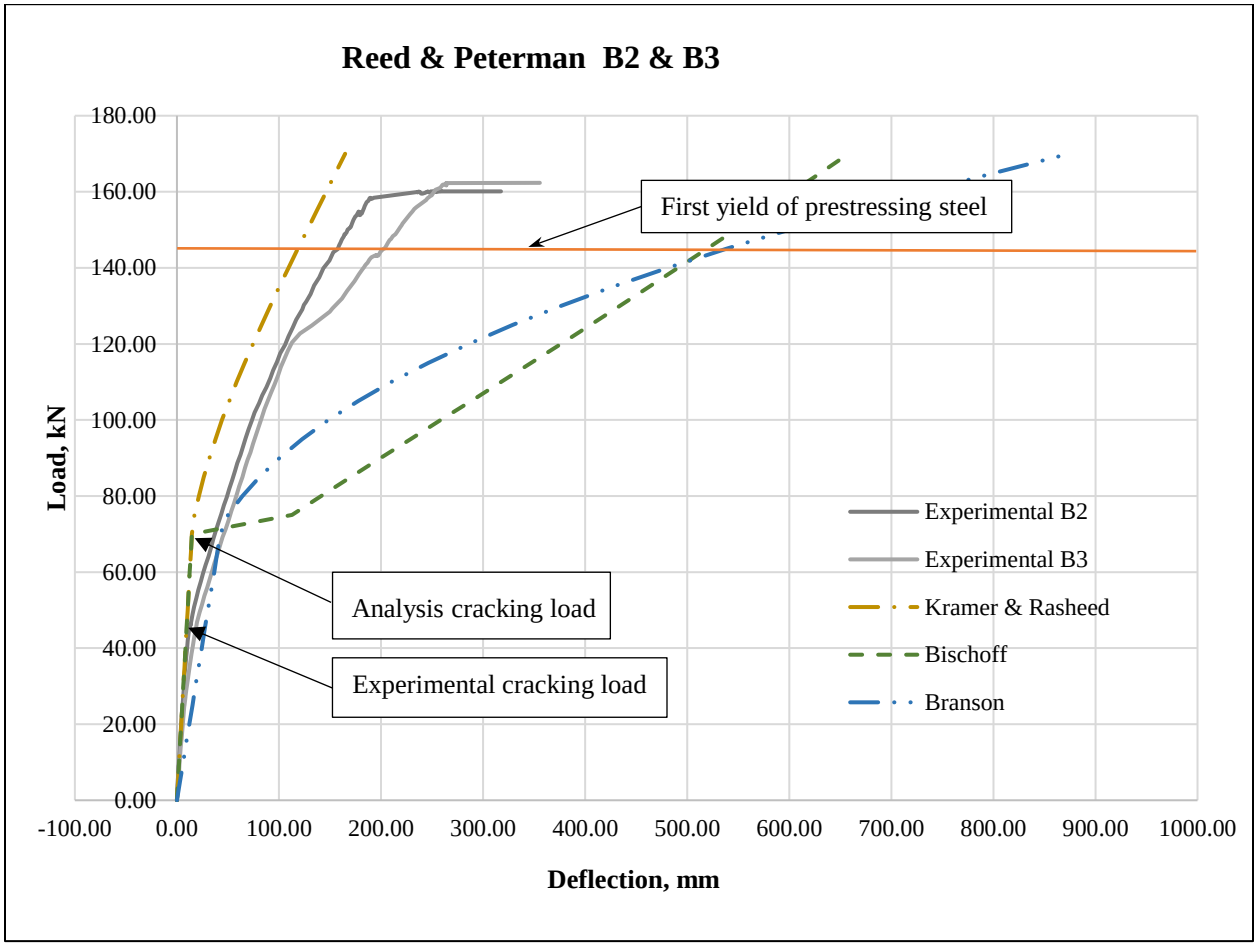

Figure 5-15: Reed & Peterman beams B2 and B3 load-deflection comparison

The analytical cracking moment was examined more closely by modifying the modulus of rupture to account for being pre-cracked beams and the percent of prestressing losses to determine the effective prestressing stress. Estimating prestress loss at any given time during the life of a prestressed concrete member is a complex issue. Since Reed & Peterman B2 and B3 beams were from decommissioned bridges, additional prestressing losses due to steel relaxation, concrete cracking, and fatigue may have occurred. Therefore, the effective prestressing was reduced by an additional 10 percent. With this reduction in effective prestressing force and

modified modulus of rupture to account for pre-cracked beams, a cracking load of approximately 45 kN (10.1 kips) was found by analysis which matches the experimental. Using this modified analysis, the three sets of effective moment of inertia equations were examined and are shown in Figure 5-16, which indicates the Kramer & Rasheed method of calculating the effective moment of inertia correlates well with the experimental response.

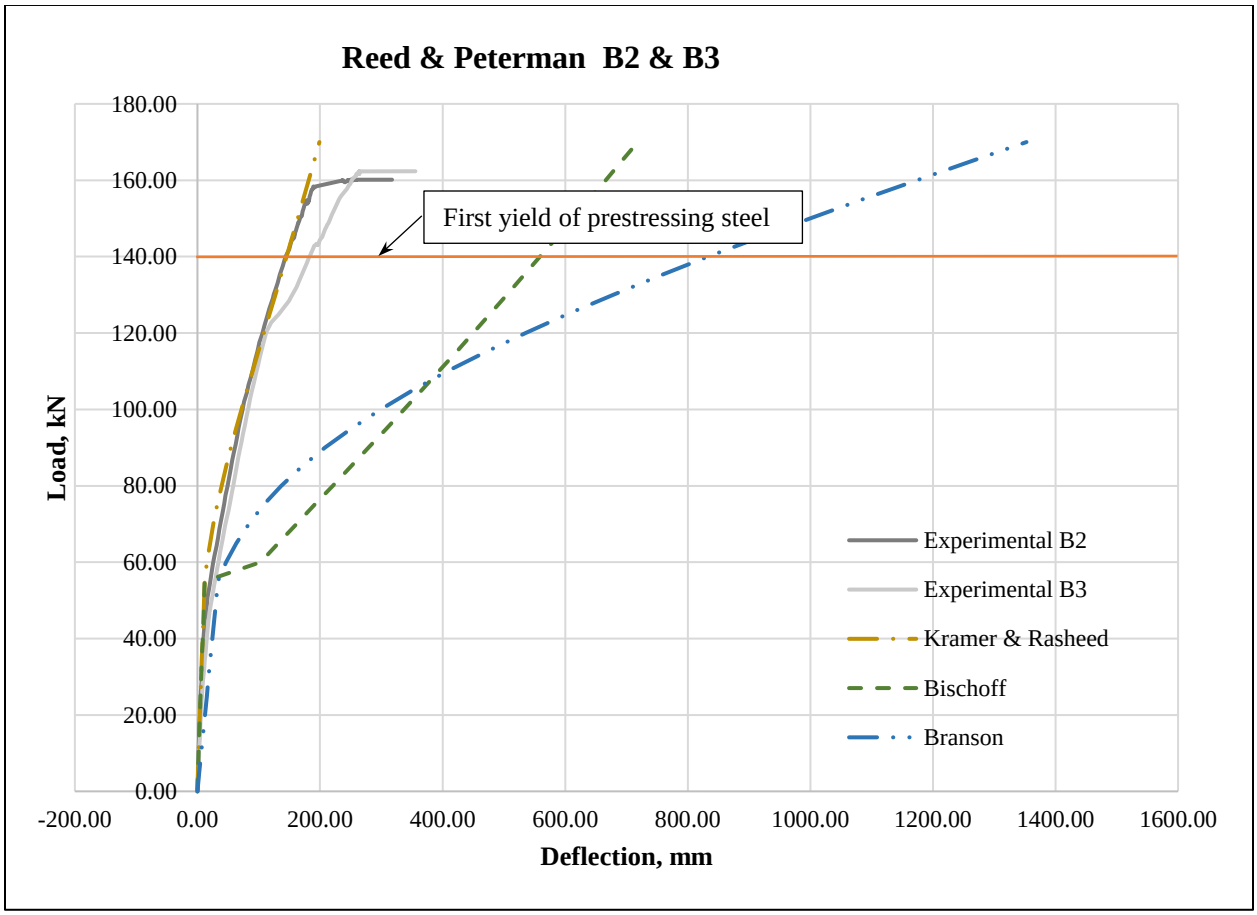

Figure 5-16: Reed & Peterman beams B2 and B3 load-deflection comparison with modified effective prestressing stress

Chapter 6 - Summary, conclusions, and recommendations

6.1 Load-deflection behavior of prestressed reinforced concrete members with straight strands and externally strengthened with FRP

6.1.1 Summary

Serviceability, deflection, is an important criterion when strengthening a PRC member. High strength materials that result in slender members are more susceptible to large deflections. This is especially true in prestressed members when members are allowed to develop cracks. Cracking can cause a sizable drop in member stiffness and increased deflections. Calculating member deflection with a high degree of accuracy is difficult due to the random variations of concrete modulus of elasticity, creep, shrinkage, duration of loading and seasonal thermal variations. Calculated deflections should be viewed as an 'estimate'. Acceptable deflection analysis should not be highly complicated mathematically, which would give a false impression of exactness, nor should it be over simplified which would compound the probable errors resulting from uncertainties in material properties and loading variations. A simplified approach to computing instantaneous deflection of PRC-FRP flexural members is proposed. The approach rationally accounts for all the important parameters, yet it involves certain approximations that make it suitable for manual computations.

In this study, the comparison between the analytical and numerical moment-curvature response for bonded PRC rectangular, and T-beams externally strengthened with FRP is presented. The comparison indicates the high accuracy of the analytically assumed trilinear moment-curvature function, which represents the foundation for establishing the short-term deflection expressions. The proposed method produced accurate predictions for moment-curvature and short-term load-deflection responses of prestressed flexural members with bonded

and straight strands strengthened with externally bonded FRP. This procedure defines the moment-curvature relationship, through key section parameters determined from standard section calculations. The moment-curvature relationship is used to express the curvature distribution along the beam, which is integrated analytically for closed form midspan deflection expressions. The results of present procedure, compares very well with experimental findings and numerical predictions for six, four rectangular-shaped and two T-shaped, PRC-FRP members. All six members were tested in four-point bending, contained pretensioned prestressing steel and non-pretensioned steel, and were strengthened with CFRP materials. The number of CFRP layers varied from one to three. The concrete compressive strength varied from 37.0 MPa (5,366 psi) to 69.54 MPa (10,086 psi). The prestressed steel was seven-wire strand with a nominal diameter of 10 mm (3/8 inch) and an ultimate strength of 1862 MPa (270 ksi).

Initially, the experimental post-cracking response of two T-shaped members were used to qualify the current deflection equations chosen by the deflection task group for ACI 440 subcommittee F on strengthening, Eq. 3-3 and Eq. 4-30. A parametric study of 6,325 load-deflection solutions with varying concrete compressive strength, amount of pretensioned prestressing steel, type of CFRP, number of layers, compression block width-to-depth ratios, and shear span-to-span ratios was performed and compared to six experimental PRC-FRP members. The flexural stiffness of PRC-FRP members varies depending a large number of variables: concrete compressive strength, pre-cracked section prior to strengthening, amount of tension stiffening after cracking, shrinkage restraint, amount of prestressing losses, pretensioned prestress reinforcement ratio, FRP reinforcement ratio, the modulus of elasticity of the prestressing steel, the modulus of elasticity of the FRP, the shear-span-to-span ratio, and the cracked moment of inertia-to-the gross moment of inertia ratio.

A generalized design approach is presented using an alternative effective moment of inertia equation to calculate instantaneous deflection of PRC-FRP flexural members. Realistic estimates are obtained by accounting for area of prestressing steel-to-area of FRP and the modulus of elasticity of the prestressing steel-to-the modulus of elasticity of the FRP. Since tension stiffening is directly related to applied moment via M_{cr}/M_a, then reducing this ratio will also reduce the tension stiffening effect in the cracking stage of the beam behavior. This is achieved by considering the effect of the cracked moment of inertia-to-gross moment of inertia ratio.

6.1.2 Conclusions

The analytical formulation developed in this study was shown to compare favorably to a wide range of experimental results. This clearly supports the accuracy of the assumed trilinear moment-curvature response and the integration of the resulting curvature distribution in integrating for accurate short-term deflections. The resulting closed form deflection expressions are used to extract an effective moment of inertia equation since experimental results are not available to capture all the parameters impacting the behavior. Therefore, the verified analytical deflection expressions are used in place of the exact deflection estimates to calibrate the more simplified effective moment of inertia equation.

The approach presented in this research uses a rational expression for the effective moment of inertia by modifying the well-known Branson effective moment of inertia equation. The analytical solution captured the load-deflection behavior well for the experimental pre-tensioned prestressed beams strengthened externally with FRP. Using this analytical procedure for engineering design and analysis is recommended.

As presented in this research, numerous factors affect the load-deflection response for PRC-FRP members after the flexural member cracks. Capturing the effect of each factor on the load-deflection response individually is extremely tedious if all variables are given from the research. Practicing engineers typically will not have all of this data for existing members. Therefore, design equations need simplification. The use of Kramer-Rasheed model (Eq. 3-3, Eq. 4-36, and Eq. 4-42) is proposed for use in determination of the effective moment of inertia of PRC-FRP beams based on the successful comparison with experiments.

Additionally, accurately calculating some of these influencing factors is not possible for existing PRC members that are strengthened with FRP after constructed in the built environment. For example, the exact amount of prestress losses at the time of strengthening is almost impossible to calculate in exact sense. When using these equations, the effective prestressing stress, f_{se}, should not be greater than sixty percent of the ultimate strength, $0.6f_{pu}$, to account for prestress losses.

6.1.3 Recommendations

Supplementary research in the load-response behavior of PRC-FRP is recommended as additional physical experimentation occurs. Furthermore, the presence of non-prestressed reinforcement in a pretensioned concrete member has an important effect on the time-dependent stresses and deformations caused by shrinkage and creep of concrete and relaxation of prestressing steel. This is particularly true in partially prestressed members where the area of non-prestressed reinforcement can be relatively large (Tadros, Ghali, & Dilger, 1977). In a prestressed simple beam, bottom non-prestressed steel restrains the deformations of concrete and results in reduction of prestress and camber. As concrete shrinks and creeps under compression, the non-prestressed steel continues to pick up compression and consequently increases the loss of

precompression in concrete. Therefore, a general study on the flexural stiffness effects of the presence of non-tensioned steel in PRC-FRP is recommended.

6.2 Load-deflection behavior of prestressed reinforced concrete members with harped strands and externally strengthened with FRP

6.2.1 Summary

As previously indicated, to limit anchorage stresses, the eccentricity of the prestressing tendon profile is often made less at the support section than at the midspan section or eliminated altogether by harping the strands. By varying the location of the prestressing strands along the length of the member, the sectional moment of inertia varies along the length of the member. Since the prestressing tendon location varies along the length of the beam, the approach used for straight strands cannot be used. The beams are analyzed using a finite number of sections along the half span of the beam due to symmetric loading.

In this study, the comparison between the analytical and numerical moment-curvature response for bonded PRC L- and T-shaped beams externally strengthened with FRP is presented. The comparison indicates the high accuracy of the analytically assumed trilinear moment-curvature function with four segments, which represents the foundation for establishing the short-term deflection expressions. The proposed method produced very accurate predictions for moment-curvature responses of prestressed flexural members with bonded, harped strands strengthened with externally bonded CFRP. The proposed method produces accurate predictions for short-term load-deflection up to seventy percent of the first yield of prestressing nearest the tension face of the beam. Loaded beyond this, the proposed method slightly underestimates the short-term deflection of PRC-FRP with harped bonded tendons at midspan.

6.2.2 Conclusions

This research is the first to derive equations to predict the load-deflection response for PRC-FRP with harped strands. The equations presented produce a very reliable approach to predict the response of PRC-FRP members with harped strands when compared to experiments. The use of Kramer-Rasheed model (Eq. 3-3, Eq. 4-36, and Eq. 4-42) PRC-FRP members derived for straight strands compares favorably and sometimes gives slightly stiffer response than the experimental load-deflection response for the post-cracking region. Another parametric study specific for harped strands is intended to be developed in future work.

References

AASHTO. (1973). *Standard Specificatoins for Highway Bridges, Section 5 - Reinforced Concrete.* Washington, D.C.: American Association of State Highway and Transportation Officials.

AASHTO. (2017). *LRFD Bridge Design Specifications.* Washington, D.C.: American Association of State Highway and Transpotation Officials.

Abeles, P. (1963). Partial Prestressing in England. *PCI Journal, 8*(1), 51-72.

Abeles, P. W. (1945, January). Fully and Partly Prestressed Concrete. *Structural Engineer, 16*(3).

Abeles, P. W. (1959). Partially Prestressing and Possibilites for its Practical Application. *PCI Journal, 4*(1), 35-51.

Abeles, P. W. (1966). Introduction to Prestressed Concrete. *Concrete Publications Ltd, 2,* 457-462.

Abeles, P. W. (1979). Philosophy of Design of Partial Prestressing. *ACI Special Publication, 59,* 287-304.

ACI Committee 318. (1963). *Building Code Requirements for Reinforced Concrete.* Farminton Hills, MI: American Concrete Institute.

ACI Committee 318. (1971). *ACI 318-71: Building Code Requirements for Structural Concrete.* Farmington: American Concrete Institute.

ACI Committee 318. (2019). *ACI 318-19: Building Code Requirements for Structural Concrete and Commentary.* Farmington: American Concrete Institute.

ACI Committee 435. (2003). *Deflection in Concrete Structures.* Farmington: American Concrete Institute.

ACI Committee 440. (2007). *ACI 440R-07 Report on Fiber-Reinforced Polymer (FRP) Reinforcement for Concrete Structures.* Farmington Hills: American Concrete Institute.

ACI Committee 440. (2015). *ACI 440.1R-15: Guide for the Design and Construction of Structural Concrete Reinforced with Fiber-Reinforced Polymer Bars.* Detroit: American Concrete Institute.

ACI Committee 440. (2017). *ACI 440.2R-17: Guide for the Design and Construction of Externally Bonded FRP Systems for Srengthening Concrete Structures.* Farmington Hills: American Concrete Institute.

ACI-ASCE Committee 323. (1958). Tentative Recommendations for Prestressed Concrete. *ACI Journal Proceedings*, 1-34.

Alwis, W. (1990). Trilinear moment-curvature relationship for reinforced concrete beams. *ACI Structural Journal, 87*(3), 276-282.

America Society of Civil Engineers. (2019, 12 10). *2017 Infrastructure Report Card*. Retrieved from https://www.infrastructurereportcard.org/wp-content/uploads/2017/01/Bridges-Final.pdf

ASTM A416. (1980). *Standard Specificatoin for Steel Strand, Uncoated Seven-Wire Stress-Relieved for Prestressed Concrete.* Philadelphia: American Society for Testing and Materials.

ASTM A886. (2017). *Standard Specification for Steel Strand, Indented, Seven-Wire Stress-Relieved for Prestressed Concrete.* Philadelphia : American Society for Testing and Materials.

ASTM D3039. (2017). *Standard Test Method for Tensile Properties of Polymer Matrix Composite Materials.* Philadelphia: American Society for Testing and Materials.

Barnes, R. A., & Mays, G. C. (1999). Fatigue Performance of Concrete Beams Strengthened with CFRP Plates. *Journal of Composites for Construction, 3*(2), 63-72.

Batal, R., & Huang, T. (1971). *Relaxation Losses in Sress-Relieved Special Grade Prestressing Strands.* Lehigh University, Civil Engineering. Lehigh: Fritz Engineering Laboratory. Retrieved February 24, 2020, from https://preserve.lehigh.edu/cgi/viewcontent.cgi?article=1355&context=engr-civil-environmental-fritz-lab-reports

Beeby, A. (1968). *Short-term Defromations of Reinforced Concrete Members.* London: Cement and Concrete Association.

Bennett, E. W., & Veerasubramanian, N. (1972, September). Behavior of Nonrectangular Beams with Limited Prestress After Flexural Cracking. *ACI Journal, Proceedings, 69*(9), 533-542.

Billet, D. F., & Appleton, J. H. (1954, June). Flexural Strength of Prestressed Concrete Beams. *ACI Journal, 50,* 837-854.

Billington, D. P. (2004). Historical Perspective on Prestressed Concrete. *PCI Journal, 49*(1), 14-30.

Bischoff, P. H., & Darabi, M. (2012, March). Unified Approach for Computing Deflection of Steel and FRP Reinforced Concrete. *ACI Special Publication, 284,* 16-1 thru 16-20.

Bischoff, P. H., & Gross, S. P. (2011). Equivalent moment of inertia based on integration of curvature. *Journal of Composites for Construction, 15*(3), 263-273.

Branson, D. E. (1963). *Report No. 7, Instantaneous and Time-Dependent Deflections of Simple and Continuous Reinforced Cocnrete Beams.* Alabama Highway Research Report, Bureau of Public Roads.

Branson, D. E. (1972). Short-time deflections of beams under single and repeated load cycles. *ACI Journal*, 110-117.

Branson, D. E., & Kripanarayanan, K. M. (1971). Loss of Prestress, Camber and Deflection of Non-composite and Composite Prestressed Concrete Structures. *PCI Journal, 16*(5), 22-52.

Branson, D. E., & Shaikh, A. F. (1985). Deflection of Partially Prestressed Members. *ACI SP-086: Deflections of Concrete Structures*, 323-363.

Branson, D. E., & Trost, H. (1982). Unified Procedures for Predicting Centroidal Axis Location of Partially Cracked Nonprestressed and Prestressed Concrete Member. *ACI Journal*, 119-130.

Brena, S. F., Bramblett, R. M., Wood, S. L., & Kreger, M. E. (2003). Increasing flexural capacity of reinforced concrete beams using carbon fiber-reinforced polymer composites. *ACI Structural Journals, 100*(1), 36-46.

Brenkus, N., & Hamilton, H. R. (2014). Proposed minimum steel provisions for prestressed and nonprestressed reinforced sections. *ACI Structural Journal, 111*(2), 431-440.

Bureau of Public Roads. (1954). *Criteria for Prestressed Concrete Bridges.* Washington, D.C.: U.S. Government Printing Office.

Burns, N. (1964, February). Moment Curvature Relationships for Partially Prestressed Concrete Beams. *PCI Journal, 9*(1), 52-63.

Cha, J. Y. (2001). Analysis of Prestressed Concrete Beams Strengthened with Carbon Fiber Composites. New Brunswick: New Brunswick Rutgers, The State University of New Jersey.

Charkas, H., Rasheed, H. A., & Melhem, H. (2003). Rigorous Procedure for Calculating Deflections of Fiber-Reinforced Polymer-Strengthed Reinforced Concrete Beams. *ACI Structural Journal, 100*(4), 529-539.

Czkwianianc, A., & Kaminska, M. (1993). Method of nonlinear analysis of one-dimensional reinforced concrete members. *PAN-IPPT, No. 36*. Warsaw.

Czkwianianc, A., & Kaminska, M. (2005). Analysis of structure in: plain, reinforced and prestressed concrete structures. *Scientific commentary for PN-B-03264:2002, t. l, Building Research Institute*. Warsaw.

Dill, R. E. (1925). *United States of America Patent No. 1684663.*

Dunker, K. F., & Rabbat, B. G. (1992). Performance of Prestressed Concrete Highway Bridges in the United States - the First 40 Years. *PCI Journal, 37*, 48-64.

El-Mihilmy, M., & Tedesco, J. (2000). Analysis of reinforced concrete beams strengthened with FRP laminates. *Journal of Structural Engineering*, 684-691.

El-Mihilmy, M., & Tedesco, J. W. (2000). Deflection of Reinforced Concrete Beams Strengthened with Fiber-Reinofrced Polymer Plates. *ACI Structural Journal, 97*(5), 679-688.

Emperger, F. (1935). Die Rissfragge beihohen Stahlspannunge und die zulassige Blosslegung des Stahl. *Miteilungen d. Oesterr. Eisenbeon Aussch., H., 16.*

Estrada, H., & Lee, L. S. (2014). *The International Handbook of FRP Composie in Civil Engineering.* Boca Raton: CRC Press Taylor & Francis Group.

GangaRao, H. V., & Vijay, P. V. (1998). Bending Behavior of Concrete Beams Wrapped with Carbon Fabric. *Journal of Structural Engineering, 124*(1), 3-10.

Garber, D., Gallardo, J., Deschenes, D., Dunkman, D., & Bayrak, O. (2013). *Effect of New Prestress Loss Estimates on Pretensioned Concrete Bridge Girder Design.*

Ghali, A. (1993). Deflection of Reinforced Concrete Members: A Critical Review. *ACI Structural Journal*, 364-373.

Gibson, R. F. (1994). *Principles of composite material mechanics.* New York: McGraw Hill.

Grelle, S. V., & Sneed, L. H. (2013). Review of Anchorage Systems for Externally-Bonded FRP Laminates. *International Journal of Concrete Structures and Materials, 7*(1), 17-33.

Hamilton, H. R. (2011). *Damage Detection and Repair Methods for GRFP Bridge Decks.* Gainsville: University of Florida.

Hassan, T. (2002). Flexural performance and bond characteristics of FRP strengthening techniques for concrete structures. *Ph.D Thesis*. Winnipeg, Man., Canada: University of Manitoba.

Hassan, T., & Rizkalla, S. (2002). Flexural strengthening of prestressed bridge slabs with FRP systems. *PCI Journal, 47*(1), 76-93.

Heffernan, P. J., & Erki, M. A. (2005). Discussion of "Fatigue Behavior of Reinforced Concrete Beams Strengthened with Carbon Fiber Reinforced Plastic Laminates". *Journal of Composites for Construction, 9*(2), 202-202.

Hognestad, E. (1952, June). Fundamental Concepts in Ultimate Load Design of Reinforced Concrete Members. *ACI Journal, 48*, 809-830.

Janney, J. R., Hognestad, E., & McHenry, D. (1956). Ultimate Flexural Strength of Prestressed and Conventionally Reinforced Concrete Beams. *ACI Journal Proceedings, 52*(2), 601-620.

Johnson, A. L. (1906). Some Notes on Reinforced Concrete. *ACI Journal Proceedings, 2*(1), 121-129.

Jones, R. M. (1976). *Nonlinear Multiaxial Modeling of Graphitc and Carbon-Carbon Materials.* Southern Methodist University,. Dallas, TX: Air Force Materials Laboratory Technical Report AFML-TR-76-215.

Kassem, C., Farghaly, A. S., & Benmokrane, B. (2011). Evaluation of flexural behavior and serviceability performance of concrete beams reinforced with FRP bars. *Journal of Composites for Construction, 15*(5), 682-695.

Kassimali, A. (1995). *Structural Analysis.* Boston, MA: PWS Publishing.

Kelley, G. S. (2000, September). Prestress Losses in Post-tensioned Structures. *PTI Technical Note(10)*, 6. Post-Tension Institute.

Khachaturian, N., & Gurfinkel, G. (1969). *Prestressed Concrete.* New York: McGraw-Hill.

Khalifa, A., Alkhrdaji, T., Nanni, A., & Lansburg, S. (1999). Anchorage of Surface-Mounted FRP Reinforcement. *Concrete International, 21*(10), 49-54.

Khan, A. A., Cook, W. D., & Mitchell, D. (1996, Sept. - Oct.). Tensile Strength of Low, Medium, and Hisgh-Strength Concretes at Early Ages. *ACI Materials Journal, 93*(5), 487-493.

Kim, Y. J., Shi, C., & Green, M. F. (2008). Ductility and cracking behavior of prestressed concrete beams strengthened with prestressed CFRP sheets. *Journal of Composites for Construction*, 274-283.

Kramer, K. W., & Rasheed, H. A. (2018). Analytical Load Deflection Behavior of Prestressed Concrete Girders Strengthened With FRP. *ACI SP Journal 327*.

Larson, K. H., Peterman, R. J., & Rasheed, H. A. (2005). Strength-fatigue Behavior of Fiber Reinforced Polymer Strengthened Prestressed Concrete T-brams. *Journal of Composites for Construction, 9*(4), 313-326.

Libby, J. (1971). *Modern Prestressed Concrete: Design Principles and Construction Methods.* New York: Van Nostrand Reinhold Co.

Lin, T. (1958). *Design of Prestressed Concrete Structures* (2nd ed.). John Wiley & Sons.

Magnel, G. (1954). *Presressed Concrete.* New York, NY: McGraw Hill.

Mandl, J. (1896). *Journal Austria Association of Engineering & Architecture*.

Martin, L., & Pellow, D. L. (1983, July-August). Low-Relaxation Strand - Practical Applications in Precast Prestressed Concrete. *PCI Journal*, 84-101.

Mattock, A. H., Kritz, L. B., & Hognestad, E. (1961, February). Rectangular Concrete Stress Distribution in Ultimate Strength Design. *ACI Journal, Proceedings, 57*, 877-928.

Meier, U. (1987). *Bridge repair with high performance composite materials.* Materials Technik.

Meier, U., Deuring, H., Meier, H., & Schwegler, G. (1993). Fiber-Reinforced-Plastic (FRP) Reinforcement for Concrete Structures. *Properties and Applications*(Developments in Civil Engineering), 423-434.

Naaman, A. E. (1977). Ultimate analysis of prestressed and partially prestressed sections by strain compatibility. *PCI Journal*, 32-51.

Nawy, E. G. (2009). *Prestressed Concrete A Fundamental Approach* (5th ed.). Upper Saddle River: Prentice Hall.

Nawy, E. G., & Huang, P. T. (1977). Crack and Deflection Control of Pretensioned Prestressed Beams. *Journal, Prestressed Concrete Instittute*, 30-47.

Nawy, E. G., & Polyondy, J. G. (1971, May). Flexural Cracking Behavior of Prestensioned I- and T-Beams. *ACI Journal, Proceedings*, pp. 355-360.

Nawy, E. G., & Potyondy, J. G. (1970). *Engineering Research Bulletin No. 51, Moment Rotation, Cracking, and Deflection of Spirally Bound, Presentionsed Prestressed Concrete Beams.* New Brunswick: Rutgers University.

Nowak, A. S., & Szerszen, M. M. (2003). Calibration of Design Code for Buildings (ACI 318): Part 1 - Statistical Models for Resistance. *ACI Structural Journal, 100*(3), 377-382.

Okeil, A. M., Bingol, Y., & Alkhrdaji, T. (2007). Analyzing model uncertainties for concrete beams flexurally strengthened with FRP laminates. *Proceedings of the Transportation Research Board 86th Annual Meeting.* Washington, DC.

Park , R., & Paulay, T. (1975). *Reinforced Concrete Structures.* New York: Wiley & Sons.

Peterson, S. (2007). *Short Term Deflection Analysis of Prestressed Concrete Beams with Straight, bonded strands using a tri-linear moment-curvature response.* Manhattan: Kansas State University.

Podolny, W. (1967, October). Understanding the Steel in Prestressing. *PCI Journal*, 54-66.

Popovics, S. (1970, March). A review of Stress-Strain Relationships for Concrete. *ACI Journal Proceedings, 67*(3), 243-248.

Popovics, S. (1973). A Numerical Approach to the Complete Stress-Strain Curve of Concrete. *Cement and Concrete Research, 3*(5), 583-598.

Precast/Prestressed Concrete Institute. (2017). *PCI Design Handbook* (8th ed.). Chicago, IL: PCI.

Preston, H. K. (1985, May-June). Testing 7-wire Strand for Prestressed Concrete - The State of the Art. *PCI Journal*, 134-155.

Rao, P. (1966). Die Grundlagen zur Berechnung der bei statishch unbestimmten Stahlbeton-konstruktionen im plastichen Bereich aufttretenden Umlagerungen der Schnittkrafte (Basic laws governing moment redistrubtion in statically indeterminate reinforced concrete structure). *DAfStb, 177*.

Rasheed, H. A. (2015). *Strengthening Design of Reinforced Concrete with FRP*. Boca Raton: CRC Press Taylor & Francis Group.

Rasheed, H. A., & Charkas, H. (2009). Modified Branson's Formula for Deflection of FRP Strengthened Concrete Brams. *ACI SP Journal 264*, 111-127.

Rasheed, H. A., Charkas, H., & Melhem, H. (2004). Simplified Nonlinear Analysis of Strengthened Concrete Beams Based on a Rigorous Approach. *Journal of Structural Engineering, 130*(7), 1087-1096.

Reed, C. E., & Peterman, R. (2004). Evalutation of Prestressed Concrete Girders Strengthened with Carbon Fiber Reinforced Polymer Sheets. *Journal of Bridge Engineering, 9*(2), 185-192.

Reed, C. E., Peterman, R. J., & Rasheed, H. A. (2005). *Evaluating FRP Repair Method for Cracked Prestressed Concrete Bridge Members Subjected to Repeated Loading Phase 1*. Manhattan: K-TRAN.

Rosenboom, O., & Rizkalla, S. (2006, November/December). Behavior of Prestressed Concrete Strengthened with Various CRFP Systems Subjected to Fatgue Loading. *Journal of Composite for Construction, 10*(6), 492-502.

Rosenboom, O., Hassan, T. K., & Rizkalla, S. (2006). Flexural behavior of aged prestressed concrete girders strengthened with various FRP systems. *Construction and Building Materials*, 764-776.

Ross, C. A., Jerome, D. M., Tedesco, J. W., & Hughes, M. N. (1999). Stregnthening of reinforced concrete beams with externally bonded composites laminates. *ACI Structural Journal, 96*, 212-220.

Ruan, F., Xu, Z., Hou, D., Li, Y., & Chu, C. (2018). Enhancing longitudinal compressive properties of unidirectional FRP based on microbuckling compression failure mechanism. *Jounral of Engineered Fibers and Fabrics, 13*(1), 84-89.

Ruan, F., Xu, Z., Hou, D., Li, Y., & Chu, C. (2018). Enhancing Longitudinal compressive Properties of Unidirectional FRP Based on Microbuckling Compression Failure Mechanism. *Journal of Engineered Fibers and Fabrics*, 84-89.

Sato, Y., & Vecchio, F. J. (2003, June). Tension Stiffening and Crack Formation in Reinforced Concrete Members with Fiber-Reinforced Polymer Sheets. *Journal of Structural Engineering*, 717-724.

Schwartz, M. M. (1984). *Composites materials handbook.* New York: McGraw-Hill.

Seguirant, S. J., & Anderson, R. G. (1985, April). Prestress Losses (Phase I). *Technical Bulletin 84-B2*. Tacoma, WA: Concrete Technology Associates.

Shaikh, A. F., & Branson, D. E. (1970). Nontensioned Steel in Prestressed Concrete Beams. *PCI Journal, 15*(1), 14-36.

Tadros, M. K., Al-Omaishi, N., Seguirant, S. J., & Gallt, J. G. (2003). *Prestress Losses in Pretensioned High-Strength Concrete Bridge Girders.* Washington, D.C.: Transportation Reserch Board, National Academy of Sciences.

Tadros, M. K., Ghali, A., & Dilger, W. H. (1977). Effect on Non-Prestressed Steel on Loss and Deflection. *PCI Journal, 22*(2), 50-63.

Tadros, M. K., Ghali, A., & Meyer, A. W. (1985). Prestressed Loss and Deflection of Precast Concrete Members. *PCI Journal, 30*(1), 114-141.

Takacs, P. F., & Kanstad, T. (2002). Strengthened Prestressed Concrete Beams with Carbon Fiber Reinforced Polymer Plates. Retrieved 2020, from https://www.researchgate.net/publication/228541900_Strengthening_prestressed_concrete_beams_with_Carbon_Fiber_Reinforced_Polymer_plates

Triantafillou, T. C., & Plevris, N. (1992). Strengthening of RC beams with epoxy-bonded fibre-composite materials. *Materials and Structures, 25*(4), 201-211.

Triantafillou, T., & Plevris, N. (1991). Post-strengthening of R/C beams with epoxy-bonded fiber composite materials. *Specialty Conference Advanced Composite MAterials in Civil Engineering Structures* (pp. 245-256). New Yoork, New York: American Society of Civil Engineers.

Walker, S., & Bloem, D. L. (1960, March). Effects of Aggregate Size on Properties of Concrete. *ACI Journal, 32*(3), 283-298.

Warwaruk, J. (1965, October). Deformation Analysis for Prestressed Concrete Beams. *PCI Journal, 10*(5), 67-80.

Warwaruk, J., Sozen, M., & Siess, C. P. (1962). *Investigation of Prestressed Reinforced Concrete for Highway Bridges: Part 3: Strength and Behavior in Flexure of Prestressed Concrete Beams.* Urbana: Engineering Experiment Station, University of Illinois.

Winnicki, A., Cichon, C., & Waszczyszyn, Z. (1990). Nonlinear analysis of reinforced concrete bar members using FEM. *Archiwum Inzynierii Ladowej, 36*, 29-61.

Yamaguchi, T. Y., Kato, T., Nishimura, T., & Uomoto, T. (1997). Creep rupture of FRP rods made of aramid, carbon and glass fibers. *Third international symposium on non-metallic (FRP) reinforcements for concrete structures (FRPRCS-3). 2*, pp. 179-186. Tokyo: Japan Concrete Institute.

Youakim, S. A., Ghali, A., Hida, S. E., & Karbhari, V. M. (2007). Elasticity Modulus, Shrinkage, and Creep of High-Strength Concrete as Adopted by AASHTO. *PCI Journal, 54*(3), 44-63.